ISTANBUL TECHNICAL UNIVERSITY ★ GRADUATE SCHOOL

MODELING AND ANALYSIS OF TERAHERTZ NON-TERRESTRIAL NETWORKS UNDER HARDWARE IMPERFECTIONS

M.Sc. THESIS

Evla Safahan AHRAZOĞLU

Department of Electronics and Communication Engineering

Telecommunication Engineering Programme

JUNE 2025

ISTANBUL TECHNICAL UNIVERSITY ★ GRADUATE SCHOOL

MODELING AND ANALYSIS OF TERAHERTZ NON-TERRESTRIAL NETWORKS UNDER HARDWARE IMPERFECTIONS

M.Sc. THESIS

Evla Safahan AHRAZOĞLU
(504221312)

Department of Electronics and Communication Engineering

Telecommunication Engineering Programme

Thesis Advisor: Prof. Dr. İbrahim ALTUNBAŞ
Co-advisor: Assoc. Prof. Dr. Eylem ERDOĞAN

JUNE 2025

İSTANBUL TEKNİK ÜNİVERSİTESİ ★ LİSANSÜSTÜ EĞİTİM ENSTİTÜSÜ

DONANIM BOZUKLUKLARI ALTINDA TERAHERTZ KARASAL OLMAYAN AĞLARIN MODELLEMESİ VE ANALİZİ

YÜKSEK LİSANS TEZİ

Evla Safahan AHRAZOĞLU
(504221312)

Elektronik ve Haberleşme Mühendisliği Anabilim Dalı

Telekomünikasyon Mühendisliği Programı

Tez Danışmanı: Prof. Dr. İbrahim ALTUNBAŞ
Eş Danışman: Doç. Dr. Eylem ERDOĞAN

HAZİRAN 2025

Evla Safahan AHRAZOĞLU, a M.Sc. student of ITU Graduate School student ID 504221312, successfully defended the thesis entitled "MODELING AND ANALYSIS OF TERAHERTZ NON-TERRESTRIAL NETWORKS UNDER HARDWARE IMPERFECTIONS", which he prepared after fulfilling the requirements specified in the associated legislations, before the jury whose signatures are below.

Thesis Advisor :	**Prof. Dr. İbrahim ALTUNBAŞ** Istanbul Technical University	....
Co-advisor :	**Assoc. Prof. Dr. Eylem ERDOĞAN** Izmir Institute of Technology	....
Jury Members :	**Assoc. Prof. Dr. Mehmet Nuri AKINCI** Istanbul Technical University	....
	Asst. Prof. Dr. Ertuğrul GÜVENKAYA Istanbul Technical University	....
	Assoc. Prof. Dr. Erdoğan AYDIN Istanbul Medeniyet University	....

Date of Submission : 17 May 2025
Date of Defense : 20 June 2025

To my beloved family,

FOREWORD

First and foremost, I would like to express my deepest gratitude to my thesis advisors, Prof. Dr. İbrahim ALTUNBAŞ and Assoc. Prof. Dr. Eylem ERDOĞAN, for their invaluable guidance, patience, and encouragement throughout my undergraduate and graduate studies. Their expertise and experience have been the most significant source of inspiration for my improvement. I am particularly grateful for the research freedom they have provided, which allowed me to present my own ideas and further develop them with their constructive feedback and insightful suggestions. This empowering environment enabled me to take significant steps toward becoming an independent researcher. Thus, I am more than glad to have the opportunity to work with them in the early stages of my academic career.

Secondly, I would like to thank Assoc. Prof. Dr. Mehmet Nuri AKINCI, Res. Asst. Mehmet CAN, and Res. Asst. Ahmet Caner GÜL for their valuable discussions and contributions to this thesis.

I would like to thank all faculty members of the Electronics and Communication Engineering Department at Istanbul Technical University for the education they have provided and the research assistants for creating an enjoyable and stimulating work environment.

I sincerely thank my brother Mehmet Akif AHRAZOĞLU and my dear friends Kutay BÖLAT and Okan ERTÜRK for taking the time to guide me whenever I reached out to them. Their experience and advice have been a great help in giving me a clearer direction throughout this process.

I also would like to thank my friends Mehmet Alperen BALTACI and Sema ALTUN for their constant support, encouragement, and companionship throughout this journey. Their presence has made the challenging times more bearable and the successes even more meaningful.

Last but not least, I sincerely thank my mother, father, and brother for their unconditional love and unwavering support throughout my life. Their belief in me has been my greatest source of strength and motivation.

June 2025

Evla Safahan AHRAZOĞLU
(Research and Teaching Assistant)

TABLE OF CONTENTS

Page

FOREWORD ... **ix**
TABLE OF CONTENTS ... **xi**
ABBREVIATIONS ... **xv**
SYMBOLS ... **xvii**
LIST OF TABLES ... **xix**
LIST OF FIGURES ... **xxi**
SUMMARY ... **xxv**
ÖZET ... **xxix**
1. INTRODUCTION ... **1**
1.1 Objective of the Thesis ... 2
1.2 Literature Review ... 3
1.3 Contribution of the Thesis ... 6
1.4 Notation ... 8
2. FUNDAMENTAL CONCEPTS OF WIRELESS COMMUNICATIONS ... **9**
2.1 Additive Gaussian Noise Channel ... 9
2.2 Fading Channel ... 11
2.2.1 Rayleigh channel ... 12
2.2.2 Rician channel ... 13
2.2.3 α-μ channel ... 13
2.3 Performance Analyses for Wireless Channels ... 14
2.3.1 BER analysis for wireless channels ... 14
2.3.2 Outage analysis for wireless channels ... 17
2.3.3 Ergodic capacity analysis for wireless channels ... 18
2.4 The Concepts of Diversity and Combining ... 20
2.4.1 Diversity techniques ... 20
2.4.2 Combining techniques ... 22
2.4.3 BER performance ... 24
2.5 Cooperative Communications ... 24
2.6 Hardware Considerations ... 28
2.6.1 Hardware impairment noise ... 29
2.6.2 I/Q imbalance ... 30
3. THz COMMUNICATIONS ... **33**
3.1 Necessity and Potential of THz Communication in 6G Networks ... 33
3.2 Large-Scale Channel Effects in THz Communications ... 34

3.2.1 Free-space loss ... 34
3.2.2 Atmospheric absorption loss ... 34
3.2.3 Weather-dependent effects ... 36
3.2.4 Ionospheric loss ... 36
3.3 Small-Scale Channel Effects in THz Communications ... 37
3.3.1 Multipath fading ... 37
3.3.2 Pointing error ... 37
4. IMPACT OF ANTENNA AND ARRAY DESIGN ON POINTING ERROR CHARACTERISTICS IN THz CHANNELS ... 39
4.1 System Model ... 40
4.2 Array Pattern and Pointing Error Modeling ... 41
4.2.1 Antenna array element ... 41
4.2.2 Array factor ... 41
4.2.3 Gain of the antenna array ... 43
4.2.4 Pointing error ... 45
4.3 Outage Analysis ... 46
4.4 Numerical Results ... 47
4.5 Concluding Remarks ... 49
5. LINK BUDGET ANALYSIS FOR NTNs IN THE THz BAND ... 51
5.1 Main Channel Effects and Transceiver Requirements ... 51
5.1.1 Free-space loss ... 52
5.1.2 Atmospheric absorption loss ... 52
5.1.3 Loss due to weather conditions ... 54
5.1.4 Ionospheric effects ... 56
5.1.5 Additional loss factors ... 57
5.1.6 Antenna requirements ... 57
5.1.7 Fading and pointing error ... 57
5.2 Noise Characteristics and Achievable Data Rate ... 58
5.2.1 Noise characteristics ... 58
5.2.2 Received power and achievable data rate ... 60
5.3 Numerical Results ... 61
5.4 Concluding Remarks ... 68
6. INTER-SATELLITE COMMUNICATIONS IN THE THz BAND ... 71
6.1 System Model ... 72
6.1.1 Path-loss factor ... 72
6.1.2 Fading and pointing error ... 73
6.2 Performance Analyses ... 74
6.2.1 Outage probability analysis ... 75
6.2.2 Asymptotic outage probability analysis ... 76
6.2.3 SER analysis ... 77
6.3 Numerical Results ... 78
6.4 Concluding Remarks ... 80

7. NTNs IN THE THz BAND WITH TRANSCEIVER NOISE **83**
7.1 System Model 83
7.1.1 Path-loss 85
7.1.2 Fading and pointing error 86
7.2 Statistics of the End-to-End SNR 86
7.2.1 PDF of the end-to-end SNR for the k-th branch 87
7.2.2 CDF of the end-to-end SNR for the k-th branch 89
7.2.3 Asymptotic CDF of the end-to-end SNR for the k-th branch 90
7.3 Performance Analyses 93
7.3.1 Outage probability analysis 93
7.3.2 High SNR analysis 93
7.3.3 Capacity analysis 94
7.4 Numerical Results 95
7.5 Concluding Remarks 99
8. NTNs IN THE THz BAND WITH I/Q IMBALANCE **103**
8.1 System Model 103
8.1.1 I/Q imbalance at the destination 105
8.1.2 Attenuation 105
8.1.3 Fading and pointing error 106
8.2 Performance Analyses 107
8.2.1 Error analysis 107
8.2.1.1 Exact SER 107
8.2.1.2 SER lower bound 109
8.2.1.3 High SNR analysis 110
8.2.1.4 Impact of I/Q imbalance on SER 111
8.2.2 Capacity analysis 111
8.3 Numerical Results 112
8.3.1 Attenuation in dry and humid atmosphere 113
8.3.2 Verification of the theoretical results 114
8.3.3 Impact of humidity 116
8.3.4 Impact of I/Q imbalance on SER 118
8.3.5 Ergodic capacity 119
8.3.6 Impact of I/Q imbalance on capacity 121
8.4 Concluding Remarks 121
9. CONCLUSION **123**
REFERENCES **127**
APPENDICES **139**
APPENDIX A 141
APPENDIX B 142
CURRICULUM VITAE **147**

ABBREVIATIONS

6G	:	Sixth-Generation
AF	:	Amplify-and-Forward
AGN	:	Additive Gaussian Noise
AWGN	:	Additive White Gaussian Noise
BER	:	Bit Error Rate
BPSK	:	Binary Phase Shift Keying
CDF	:	Cumulative Distribution Function
DF	:	Decode-and-Forward
EGC	:	Equal Gain Combining
EM	:	Electromagnetic
FSO	:	Free-Space Optical
GEO	:	Geostationary Orbit
HAPS	:	High-Altitude Platform Station
HEO	:	Highly Elliptical Orbit
ISC	:	Inter-Satellite Communications
ITU	:	International Telecommunication Union
LAPS	:	Low-Altitude Platform Station
LBLRTM	:	Line-by-Line Radiative Transfer Model
LEO	:	Low Earth Orbit
LOS	:	Line-of-Sight
M-ASK	:	M-ary Amplitude Shift Keying
MEO	:	Medium Earth Orbit
MGF	:	Moment Generating Function
MIMO	:	Multiple Input Multiple Output
ML	:	Maximum Likelihood
mmWave	:	Millimeter Wave
M-PSK	:	M-ary Phase Shift Keying
MRC	:	Maximal Ratio Combining
M-QAM	:	M-ary Quadrature Amplitude Modulation
NLOS	:	Non-Line-of-Sight
NTN	:	Non-Terrestrial Networks
PDF	:	Probability Density Function
RF	:	Radio Frequency
SatCom	:	Satellite Communication
SC	:	Selection Combining
SER	:	Symbol Error Rate
SNR	:	Signal-to-Noise Ratio
THz	:	Terahertz
UAV	:	Unmanned Aerial Vehicle

SYMBOLS

$\lvert\cdot\rvert$	: Absolute value
$\angle(\cdot)$	: Angle operator
$(\cdot)^*$	: Complex conjugate operator
$\mathcal{R}\{\cdot\}$	: Real part operator
$\mathcal{L}\{\cdot\}$	: Laplace transform operator
gcd(z, υ)	: Greatest common divisor of integers z and υ
$\mathbb{R}$	: Set of real numbers
$\mathbb{C}$	: Set of complex numbers
$\mathbb{X}$	: Set of all possible symbols
$\mathcal{N}(\mu, \sigma^2)$	: Gaussian distribution with mean μ and variance σ^2
$\mathcal{CN}(\mu, \sigma^2)$	: Complex Gaussian distribution with mean μ and variance σ^2
$E[Z]$	: Expectation of the random variable Z
$f_Z(\cdot)$	: Probability density function of the random variable Z
$F_Z(\cdot)$	: Cumulative distribution function of the random variable Z
$\mathcal{M}_Z(\cdot)$	: Moment generating function of the random variable Z
log$(\cdot)$	: Natural logarithm function
$Q(\cdot)$	: Q function
$I_0(\cdot)$	: Zeroth order modified Bessel function of the first kind
$\Gamma(\cdot)$	: Gamma function
$\gamma(\cdot,\cdot)$	: Lower incomplete Gamma function
$\Gamma(\cdot,\cdot)$	: Upper incomplete Gamma function
erf$(\cdot)$	: Error function
$\mathrm{G}^{\cdot,\cdot}_{\cdot,\cdot}\left[\cdot \,\middle\vert\, \begin{matrix}\cdots\\ \cdots\end{matrix}\right]$	: Uni-variate Meijer-G function
$\mathrm{H}^{\cdot,\cdot}_{\cdot,\cdot}\left[\cdot \,\middle\vert\, \begin{matrix}\cdots\\ \cdots\end{matrix}\right]$	: Uni-variate Fox-H function
$\mathrm{H}^{\cdot,\cdot:\cdot,\cdot:\cdot,\cdot}_{\cdot,\cdot:\cdot,\cdot:\cdot,\cdot}\left[\begin{matrix}\cdot\\ \cdot\end{matrix} \,\middle\vert\, \begin{matrix}\cdots\\ \cdots\end{matrix}\right]$	: Bi-variate Fox-H function

LIST OF TABLES

Page

Table 8.1 : Parameters for the proposed system **113**
Table 8.2 : Free-space loss and absorption loss values for $\zeta_{2k} = 30°, 60°, 75°$, $\forall k$, under dry and humid atmospheric conditions **114**

LIST OF FIGURES

Page

Figure 2.1 : Additive Gaussian noise channel model. **10**

Figure 2.2 : Fading channel model. **15**

Figure 2.3 : The BPSK BER curves for Rician ($\mathcal{K} = 0,3,10$) and AGN channels. **16**

Figure 2.4 : The BPSK BER curves for α-μ ($\alpha = 2,4,8,\ \mu = 1$) and AGN channels. **17**

Figure 2.5 : The BPSK BER curves for α-μ ($\alpha = 2,\ \mu = 1,2,4$) and AGN channels. **18**

Figure 2.6 : The outage performance for Rayleigh, Rician ($\mathcal{K} = 3,10$), and α-μ ($\alpha = 4,8$ and $\mu = 1$) channels. **19**

Figure 2.7 : The ergodic capacity performance for α-μ ($\alpha = 4,\ \mu = 1$) channel. .. **20**

Figure 2.8 : The BPSK BER performance of MRC and SC for Rayleigh channel. **24**

Figure 2.9 : A multi-relay cooperative communication system model. **25**

Figure 2.10 : Comparison of outage performance of variable-gain AF and fixed-gain AF multi-relay communication systems. **28**

Figure 2.11 : A model for a communication system in the presence of hardware impairment noise. **30**

Figure 2.12 : The BPSK BER performance in the presence of hardware impairment noise. **31**

Figure 2.13 : The BPSK BER performance in the presence of I/Q imbalance. **32**

Figure 3.1 : The specific attenuation due to absorption under dry and humid atmospheric conditions at 0 km of altitude. **35**

Figure 4.1 : (a) Normalized pattern of an array of lens antennas, with element spacing $d_{\mathrm{x}} = d_{\mathrm{y}} = 10\lambda$. (b) Beam divergence and maximum array gain for with different antennas (isotropic and horn) and element spacing $d = d_{\mathrm{x}} = d_{\mathrm{y}}$. **44**

Figure 4.2 : (a) The PDF of h^{p} for $\sigma_\theta = 0.15°$ and $N = 8,12,16$. (b) The CDF of h^{p} for $N = 12$ and $\sigma_\theta = 0.1°, 0.15°, 0.25°$. **48**

Figure 4.3 : Outage probability curves for $N = 12$, (a) $\sigma_\theta = 0.12°$ and $d_{\mathrm{e}} = 0.5\lambda, 4\lambda, 5\lambda$ (b) $\sigma_\theta = 0.05°, 0.1°, 0.12°$ and $d_{\mathrm{e}} = 5\lambda$. **49**

Figure 5.1 : Specific attenuation due to absorption at different altitudes for dry and humid standard atmospheric conditions. **53**

Figure 5.2 : (a) Specific attenuation due to rain for different rainfall rates. (b) Attenuation due to cloud/fog for different integrated cloud liquid water content levels and $90°$ elevation angle. **56**

Figure 5.3 : Upwelling and downwelling brightness temperatures and the single-sided noise power spectral density for a link between 0 km and 100 km altitudes with 0° zenith angle. **60**
Figure 5.4 : Achievable data rate in ground-to-satellite link for fixed antenna physical aperture (25×25 cm^2) and fixed antenna gain (50 dBi) under dry and humid atmospheric conditions. **62**
Figure 5.5 : Achievable data rate in aerial-to-ground link for different antenna physical apertures (5×5 cm^2, 10×10 cm^2, and 25×25 cm^2) and gains (40 dBi, 50 dBi, and 60 dBi) under humid atmospheric conditions. **63**
Figure 5.6 : Achievable data rate in uplink/downlink ground-aerial, ground-satellite, aerial-satellite links for fixed antenna physical aperture of 25×25 cm^2. .... **64**
Figure 5.7 : Achievable data rate in intra-layer communication on the ground and aerial altitudes for fixed antenna physical aperture of 10×10 cm^2 under humid atmosphere. **65**
Figure 5.8 : Achievable data rate in inter-satellite link between two LEO satellites equipped with antennas of 25×25 cm^2 physical aperture operating at 30 GHz, 100 GHz, 200 GHz, 300 GHz, and 1 THz operating frequencies. **66**
Figure 5.9 : Impact of rainfall rate on the achievable data rate in uplink/downlink ground-aerial communication with $d_{\text{eff}} = 5$ km and circularly polarized antenna of 25×25 cm^2 physical aperture under humid atmosphere. **67**
Figure 5.10 : The total loss in ground-to-aerial link for different elevation angles $\theta = 90^\circ, 30^\circ$ and integrated cloud liquid water contents $\mathcal{W}_{\text{cf}} = 0, 25$ [kg/m^2]. **68**
Figure 6.1 : Dual-hop inter-satellite THz communication system. **73**
Figure 6.2 : Outage performance of the system for $\alpha = 3, 4, 5$ and $\mu = 2.5$. **79**
Figure 6.3 : Outage performance of the system for $\alpha = 3$ and $\mu = 2, 3.5, 5$. **80**
Figure 6.4 : SER performance of the system for $\alpha = 1.5, 2.5, 6$ and $\mu = 2$ where BPSK modulation is used. **81**
Figure 7.1 : Multi-HAPS aided THz NTN. **84**
Figure 7.2 : The PDF and CDF curves for $\gamma_{e2e,k}$ and $\gamma^u_{e2e,k}$ for $\kappa^2_{ik} = 0.01$ under dry atmospheric conditions. **96**
Figure 7.3 : Outage probability curves for ideal hardware and non-ideal hardware ($\kappa^2_{ik} = 0.05$) for $K = 1, 2, 3$ and dry atmosphere. **97**
Figure 7.4 : Outage probability with respect to zenith angle in the second hop for $K = 1, 2, 3$, $P = 10$ dBm, and $\kappa^2_{ik} = 0.001$ under dry and humid atmospheric conditions. **98**
Figure 7.5 : Outage probability curves under dry atmospheric conditions for $K = 1, 2$ and $P = 10, 15$ dBm for different κ_{ik} values. **99**
Figure 7.6 : Ergodic capacity curves for $K = 2$ and humid atmosphere. **100**

Figure 7.7 : Ergodic capacity curves under humid atmospheric conditions for $P = 10, 20, 30$ dBm, $K = 2$, and different κ_{ik} values. **101**
Figure 8.1 : Multi-HAPS aided THz NTN. **104**
Figure 8.2 : Comparison of BPSK and 8-PSK SER performance of the proposed system (for $K = 1, 3$ and $\zeta_{2k} = 60°$) and dual THz/Ka band transmission (direct communication from S to D) under humid atmosphere. **115**
Figure 8.3 : BPSK SER performance of the system with respect to zenith angle in the second hop for $P = 20$ dBm and $K = 1, 2, 3$ under humid atmosphere. **116**
Figure 8.4 : BPSK SER curves for $\zeta_{2k} = 30°, 75°$ under dry and humid atmospheric conditions for $K = 2$. **117**
Figure 8.5 : BPSK SER curves with respect to the zenith angle in the second hop for different satellite altitudes under dry and humid atmospheric conditions for $K = 2$ and $P = 20$ dBm. **118**
Figure 8.6 : 8-PSK SER curves in the presence of I/Q imbalance ($g_D = 0.75$ and $\theta_D = 10°$) and ideal hardware ($g_D = 1$ and $\theta_D = 0$) for $K = 1, 2$. **119**
Figure 8.7 : Ergodic capacity curves for $\zeta_{2k} = 75°$ under dry and humid atmospheric conditions for $K = 1, 2, 3$. **120**
Figure 8.8 : Ergodic capacity curves with respect to the zenith angle in the second hop for $K = 1, 2$ and $P = 30$ dBm under humid atmospheric conditions. **121**
Figure 8.9 : Ergodic capacity curves in the presence of I/Q imbalance ($g_D = 0.75$ and $\theta_D = 10°$) and ideal hardware ($g_D = 1$ and $\theta_D = 0$) for $K = 1, 2$ and $\zeta_{2k} = 75°$. **122**

MODELING AND ANALYSIS OF TERAHERTZ NON-TERRESTRIAL NETWORKS UNDER HARDWARE IMPERFECTIONS

SUMMARY

With the recent advances in space and aerial technologies, integrating satellites, aerial vehicles, and ground stations within the non-terrestrial network (NTN) architecture has emerged as a promising solution for the global coverage requirement of the sixth-generation (6G) communication systems. To provide extreme data rates globally with NTNs, the utilization of high frequencies can be considered, among which the millimeter wave (mmWave) and terahertz (THz) bands arise as prominent candidates since they demonstrate certain advantages over their counterparts. Though mmWave/THz transmission is sensitive to atmospheric conditions and weather-dependent effects, the multi-layer structure of the NTN architecture and high-gain directional antennas/arrays enable reliable communication in the mmWave and THz bands. Hence, the mmWave/THz NTNs have gathered considerable interest from the academic community.

Within the scope of this thesis, the channel characteristics, feasibility, and statistical performance of THz NTNs are investigated and analyzed. Throughout the thesis, a statistical model for the impact of antenna misalignment is proposed, and performance analyses for various communication scenarios are presented by taking the hardware imperfections into consideration.

First, the influence of antenna misalignment on the mmWave and THz communications is investigated. Since highly directional antennas/arrays with pencil-sharp beams are utilized in mmWave/THz transmission, the perfect alignment between transmitter and receiver is critically important. When the antennas/arrays are misaligned due to non-stable positioning, moving platforms, or jitters, the received power significantly reduces, referred to as pointing errors. To characterize this phenomenon, a simple analytical model for the pointing error in mmWave/THz links is proposed. Unlike the existing models, the proposed model incorporates the antenna element radiation pattern and the array design. To accomplish this, the main lobes of the antenna element radiation pattern and the array factor are modeled as Gaussian beams. Then, the main lobe of the array pattern is formulated by accounting for the maximum gain and 3 dB beamwidth of the antenna element and number of array elements, element spacing, and 3 dB beamwidth of the array factor, which is validated via electromagnetic simulations in CST Microwave Studio. By using the main lobe of the array pattern, the statistics of the pointing error are derived, and it is shown that the pointing error follows a special case of the negative log-Gamma distribution with the shape parameter of 2 and the scale parameter depending on the antenna/array designs and jitter variance. To examine the impact of the antenna and array design parameters on the system

performance through pointing errors, outage probability of a horizontal high-altitude platform station (HAPS)-to-HAPS communication scenario is analyzed. The results have revealed that antenna/array designs are as influential as the jitter variance, and they cannot be neglected.

Secondly, link budget analysis for mmWave/THz NTNs is presented to investigate their feasibility by considering all possible uplink/downlink inter-layer and intra-layer communication scenarios. With this objective, large- and small-scale channel effects are taken into account to obtain the received power in various channel conditions. Afterwards, the received signal-to-noise ratio (SNR) is evaluated by considering the frequency-dependent noise characteristics. Then, the maximum achievable data rate is found for a wide range of system and channel parameters to quantify the performance in inter-layer and intra-layer links. The results have illustrated that the extreme losses in ground-satellite links can be reduced to a compensable level owing to the multi-layer structure of the NTN architecture, enabling multi-gigabit links. More precisely, the total propagation distance in ground-satellite links can be divided into two distinct segments by utilizing aerial nodes. The first segment spans the distance between satellites and aerial nodes in the upper atmospheric layers where the atmosphere remains sufficiently thin to meet negligible absorption. In contrast, the second layer lies within the lower atmospheric layer. Here, even though the distance is shorter, the denser concentration of absorber particles combined with weather-dependent effects lead to more frequent absorption.

Thirdly, a dual-hop inter-satellite THz communication system's outage and symbol error rate (SER) performance are examined. In the system of interest, it is assumed that the direct line-of-sight (LOS) is not available between the source and destination low earth orbit (LEO) satellites, and the communication is established with the aid of another LEO satellite at a higher altitude that employs the variable-gain amplify-and-forward (AF) relaying. To assess the performance of the system, the statistics of the end-to-end SNR are derived in the presence of free-space loss, absorption loss, ionospheric loss, fading, and pointing errors. Moreover, the asymptotic outage analysis is performed to gain insights about the system performance. It is shown that reliable inter-satellite communication links can be established with feasible transmit power levels.

Fourthly, a dual-hop multi-HAPS THz NTN is considered under hardware impairment noise. In this setup, the HAPS system that provides the maximum SNR utilize the variable-gain AF relaying to aid the transmission from the satellite to the ground station. To obtain the outage probability, asymptotic outage probability, and ergodic capacity expressions, the statistics of the end-to-end SNR are obtained. The impacts of hardware impairment levels, zenith angles, and atmospheric conditions on the system performance are illustrated by using these statistics. The findings reveal that hardware impairment noise results in a power loss in the outage performance and reduces the overall system capacity. This adverse effect can be mitigated by increasing the number of HAPS systems. Furthermore, the results have shown that the system performance is determined by either fading or pointing error characteristics in high SNR region.

Finally, the SER and ergodic capacity performance of a dual-hop THz NTN are investigated under in-phase (I)/quadrature (Q) imbalance. In the considered system model, multiple HAPS systems act as relays to assist transmission by utilizing the variable-gain AF relaying. At the ground station, the received signals from all HAPS systems are combined by using the maximal ratio combining technique. To quantify the performance, the statistics of the received SNR are derived in the presence of free-space loss, absorption loss, fading, pointing errors, and receiver I/Q imbalance. The impacts of various satellite and HAPS deployments and amplitude/phase mismatch levels are illustrated. It is demonstrated that error floors and lower capacity limits are observed due to I/Q imbalance. High SNR analysis have shown that the system performance depends on either fading or pointing error parameters in the case of perfect hardware. In addition, the results have revealed that the SER performance remains almost the same regardless of the atmospheric conditions for low zenith angles in HAPS-to-ground station link.

The main contributions of this thesis to the current literature can be summarized as follows: First, to characterize the impact of antenna and array designs on the pointing error characteristics in mmWave/THz transmission, a simple analytical model is proposed. By using this model, the variation in the system performance in the presence of different types of antenna elements and/or different array configurations can be investigated, enabling more realistic performance analysis and system design. Secondly, the feasibility assessment of mmWave/THz NTNs is performed by considering various channel conditions. It is demonstrated that reliable mmWave/THz communication links can be achieved in NTNs owing to the multi-layer structure of the NTN architecture. Afterwards, the performance analysis for a dual-hop inter-satellite THz communication system is presented. The results have revealed that satisfactory performance can be achieved with feasible transmit power levels. As the fourth contribution, the performance of a dual-hop multi-HAPS NTN is analyzed in the presence of hardware impairment noise. The performance limits due to the noise caused by non-ideal equipment are illustrated. Finally, the influence of I/Q imbalance led by the amplitude/phase mismatches in the local oscillators on a dual-hop multi-HAPS NTN is examined. From the results, it is inferred that receiver I/Q imbalance leads to error floors and lower capacity limits, deteriorating the system performance.

DONANIM BOZUKLUKLARI ALTINDA TERAHERTZ KARASAL OLMAYAN AĞLARIN MODELLEMESİ VE ANALİZİ

ÖZET

Uzay ve havacılık teknolojilerindeki son gelişmelerle birlikte, uydu, hava araçları ve yer istasyonlarının karasal olmayan ağlar (non-terrestrial networks, NTNs) mimarisi çarısı altında birleştirilmesi altıncı nesil (sixth-generation, 6G) haberleşme sistemlerinin küresel kapsama ihtiyacını karşılamak için umut verici bir çözüm olarak ortaya çıkmıştır. NTN'ler ile dünya genelinde çok yüksek veri hızları sağlamak için, atıl durumdaki frekansların kullanılması değerlendirilebilir. Bu bağlamda, milimetre dalga (millimeter wave, mmWave) ve terahertz (THz) bantları diğer frekans bantlarına kıyasla sunduğu belirli avantajlar sebebiyle öne çıkmaktadır. mmWave/THz iletimi atmosferik koşullara ve hava durumu etkilerine karşı oldukça duyarlı olsa da, NTN mimarisinin çok katmanlı yapısı ve yüksek kazançlı antenler/diziler, mmWave ve THz bantlarında güvenilir haberleşmeyi mümkün kılmaktadır. Bu nedenle, mmWave/THz NTN'ler akademik camiada önemli bir ilgi görmüştür.

Bu tez kapsamında, THz NTN'lerin kanal özellikleri, gerçeklenebilirliği ve istatistiksel performansları incelenmiştir. Tez boyunca, anten hizalama hatası için istatistiksel bir model önerilmiş ve donanım bozuklukları dikkate alınarak çeşitli haberleşme senaryoları için performans analizleri sunulmuştur.

İlk olarak, anten hizalama hatasının mmWave ve THz iletimleri üzerindeki etkisi incelenmiştir. mmWave/THz iletiminde, keskin hüzmelere sahip yüksek kazançlı antenler/diziler kullanıldığından, verici ve alıcı arasındaki mükemmel hizalama kritik öneme sahiptir. Antenler/diziler sabit olmayan konumlandırma, hareketli platformlar veya titremeler nedeniyle hizalanamadığında, alınan güç önemli ölçüde azalır ve bu durum hizalama hatası olarak adlandırılır. Bu olguyu karakterize etmek için, mmWave/THz hatlarında hizalama hatası için basit bir analitik model önerilmiştir. Mevcut modellerin aksine, önerilen model anten elemanlarının ışıma paternlerini ve dizi tasarımını içermektedir. Bu amaçla, anten elemanlarının ışıma paterni ve dizi faktörünün ana lobları Gauss hüzme olarak modellenmiştir. Daha sonra, anten elemanlarının maksimum kazancı, 3 dB hüzme genişliği, dizi elemanlarının sayısı, eleman aralığı ve dizi faktörünün 3 dB hüzme genişliği dikkate alınarak dizi ışıma paterninin ana lobu formüle edilmiş ve bu yaklaşım CST Microwave Studio'da yapılan elektromanyetik simülasyonlarla doğrulanmıştır. Dizi modelinin ana lobu kullanılarak, hizalama hatasının istatistikleri türetilmiş ve hizalama hatasının, şekil parametresi 2 ve ölçek parametresi anten/dizi tasarımlarına ve titreşim varyansına bağlı olacak biçimde, negatif log-Gamma dağılımının özel bir durumuna uyduğu gösterilmiştir. Anten ve dizi tasarım parametrelerinin sistem performansına hizalama hatası üzerinden etkilerini incelemek için iki yüksek irtifa platformu (high-altitude platform station, HAPS)

arasındaki yatay haberleşme senaryosuna ilişkin kesinti olasılığı analiz edilmiştir. Sonuçlar, anten/dizi tasarımlarının en az titreşim varyansı kadar etkili olduğunu ve ihmal edilemeyeceğini ortaya koymuştur.

İkinci olarak, mmWave/THz NTN'lerin gerçeklenebilirliğini incelemek amacıyla tüm olası aşağı yönlü ve yukarı yönlü katman içi ve katmanlar arası iletişim senaryoları dikkate alınarak bağlantı bütçe analizi sunulmuştur. Bu amaçla, farklı kanal koşullarında alınan gücü hesaplayabilmek için büyük ölçekli ve küçük ölçekli kanal etkileri hesaba katılmıştır. Burada büyük ölçekli etkiler, serbest uzay kaybı, kuru/nemli atmosfer koşullarında soğurulma kaybı, hava olaylarından kaynaklı kayıplar, iyonosferik etkiler, antenler arasındaki polarizasyon uyumsuzlukları ve besleme kayıpları olarak gruplanabilirken, küçük ölçekli etkiler ise sönümleme ve hizalama hataları olarak ayrılabilir. Daha sonra, frekansla değişen gürültü özellikleri göz önünde tutularak alınan işaret-gürültü oranı (signal-to-noise ratio, SNR) hesaplanmıştır. Ardından, sistem ve kanal parametrelerinin geniş bir aralığı için maksimum erişilebilir veri hızı bulunup katman içi ve katmanlar arası bağlantıların performansı değerlendirilmiştir. Sonuçlar, NTN mimarisinin çok katmanlı yapısı sayesinde yer-uydu bağlantılarındaki aşırı kayıpların telafi edilebilir bir seviyeye indirgenebildiğini ve yüksek veri hızına sahip bağlantıların mümkün olduğunu göstermiştir. Daha net ifade etmek gerekirse, yer-uydu bağlantılarındaki toplam iletim mesafesi hava platformları kullanılarak iki farklı bölüme ayrılabilir. İlk bölüm, atmosferin üst katmanlarında yer alan uydular ile hava platformları arasındaki mesafeyi kapsar; bu bölgede atmosfer yeterince seyrek olduğundan soğurulma ihmal edilebilir düzeydedir. Buna karşılık, ikinci bölüm alt atmosfer katmanında yer alır. Bu katmanda mesafe daha kısa olmasına rağmen, soğurucu parçacıkların daha yoğun olması ve hava koşullarına bağlı etkiler nedeniyle soğurulma daha yoğun gerçekleşir.

Üçüncü olarak, iki atlamalı uydular arası THz haberleşme sisteminin kesinti olasılığı ve sembol hata oranı (symbol error rate, SER) performansları analiz edilmiştir. İncelenen sistemde, kaynak ve hedef alçak dünya yörüngesi (low earth orbit, LEO) uyduları arasında doğrudan görüş (line-of-sight, LOS) hattının bulunmadığı varsayılmaktadır. Bu nedenle haberleşme, değişken kazançlı kuvvetlendir-ve-aktar (amplify-and-forward, AF) kullanan, daha yüksek irtifadaki başka bir LEO uydusunun yardımıyla sağlanmaktadır. Sistem performansını değerlendirmek için, serbest uzay kaybı, soğurulma kaybı, iyonosferik kayıp, sönümleme ve hizalama hatalarının varlığında uçtan uca SNR'ın istatistikleri türetilmiştir. Ayrıca, sistem performansı hakkında öngörüler elde etmek için asimptotik kesinti olasılığı analizi yapılmıştır. Kabul edilebilir iletim güç seviyeleri ile güvenilir uydular arası haberleşme bağlantılarını mümkün kılınabildiği gösterilmiştir.

Dördüncü olarak, donanım bozukluğu gürültüsü altında iki atlamalı çok HAPS'lı THz NTN ele alınmıştır. Bu yapıda, en yüksek SNR'ı sağlayan HAPS sistemi, uydu ile yer istasyonu arasındaki iletimi desteklemek amacıyla değişken kazançlı AF röle görevi görmektedir. Kesinti olasılığı, asimptotik kesinti olasılığı ve ergodik kapasite ifadelerini elde etmek için uçtan uca SNR'ın istatistikleri türetilmiştir. Bu istatistikler kullanılarak donanım bozukluğu seviyesinin, zenit açılarının ve atmosferik koşulların sistem performansı üzerindeki etkileri gösterilmiştir. Sonuçlar, donanım bozukluklarından kaynaklanan gürültünün kesinti performansında güç kaybına yol açtığını ve sistemin toplam kapasitesini azalttığını ortaya koymaktadır. Bu olumsuz etki, HAPS sistemlerinin sayısının artırılmasıyla azaltılabilir. Ek olarak, sonuçlar, yüksek SNR bölgesinde sistem performansının sönümleme veya hizalama hatası karakteristiği tarafından belirlendiğini göstermiştir.

Son olarak, iki atlamalı bir THz NTN'in eş fazlı (in-phase, I)/dik (quadrature, Q) bileşenlerin dengesizliği altında SER ve ergodik kapasite performansları araştırılmıştır. İncelenen sistem modelinde, birden fazla HAPS sistemi, değişken kazançlı AF kullanarak iletimi desteklemek için röle olarak görev yapmaktadır. Yer istasyonunda, tüm HAPS sistemlerinden alınan işaretler en büyük oranlı birleştirme tekniği ile birleştirilmektedir. Performansı ölçmek için serbest uzay kaybı, soğurulma kaybı, sönümleme, hizalama hataları ve alıcı I/Q dengesizliğinin varlığında alınan SNR'ın istatistikleri türetilmiştir. Çeşitli uydu ve HAPS yerleşimlerinin ve genlik/faz uyumsuzluğu seviyelerinin etkileri incelenmiştir. I/Q dengesizliğinin hata katına ve düşük kapasite sınırlarına yol açarak sistem performansını kötüleştirdiği gösterilmiştir. Yüksek SNR analizleri, mükemmel donanım durumunda sistem performansının sönümleme veya hizalama hatası parametrelerine bağlı olduğunu ortaya koymuştur. Ayrıca, sonuçlar, HAPS-yer istastonu arasındaki zenit açısının düşük değerlerinde atmosferik koşullardan bağımsız olarak SER performansının neredeyse aynı kaldığını göstermiştir.

Bu tezin mevcut literatüre katkıları şu şekilde özetlenebilir: mmWave/THz iletiminde hizalama hatası üzerindeki anten ve dizi tasarımlarının etkisini karakterize etmek için basit bir analitik model önerilmiştir. Bu model kullanılarak, farklı türde anten elemanları ve/veya farklı dizi konfigürasyonları varlığında sistem performansındaki değişim incelenebilir; böylece daha gerçekçi performans analizleri ve sistem tasarımı yapılabilir. mmWave/THz NTN'lerin uygulanabilirliği gerçekçi kanal koşulları dikkate alınarak değerlendirilmiştir. NTN mimarisinin çok katmanlı yapısı sayesinde güvenilir mmWave/THz bağlantılarının sağlanabileceği gösterilmiştir. İki atlamalı uydular arası THz haberleşme sistemi için performans analizi sunulmuştur. Sonuçlar, makul iletim güç seviyeleriyle tatmin edici performans elde edilebileceğini ortaya koymuştur. Donanım bozukluğu gürültüsü varlığında iki atlamalı çok HAPS'lı NTN'in performansı analiz edilmiştir. İdeal olmayan ekipmanlardan kaynaklanan gürültü nedeniyle oluşan performans sınırları gösterilmiştir. Lokal osilatörlerdeki genlik/faz uyumsuzluklarının neden olduğu I/Q dengesizliğinin iki atlamalı çok HAPS'lı NTN'e etkisi incelenmiştir. Sonuçlardan, alıcı I/Q dengesizliğinin hata katına ve düşük kapasite sınırlarına yol açtığı ve sistem performansını kötüleştirdiği anlaşılmıştır.

1. INTRODUCTION

Considering the growing demand for data transfer driven by an increasing number of users and proliferation of a wide variety of applications, the sixth-generation (6G) communication networks aim to provide global coverage, low latency, extremely broad bandwidths, and high data rates [1]. With this objective, satellite communication systems are expected to be one of the key enablers of 6G networks [2]. To satisfy the requirements of the next-generation communication systems, integration of high-altitude platform station (HAPS) systems and unmanned aerial vehicles (UAVs) with satellite networks can be considered as a promising solution, contributing to the versatility of 6G networks [3]. In this context, the non-terrestrial network (NTN) architecture has gathered great interest from the academic community [4].

The NTN architecture integrates space, aerial, and terrestrial layers. Satellites operate within the space layer in different orbits, such as highly elliptical orbit (HEO), geostationary orbit (GEO), medium earth orbit (MEO), and low earth orbit (LEO). In the aerial layer, HAPS systems and UAVs are employed to assist transmission, facilitating a reliable communication between the space and terrestrial networks [5]. In this architecture, the line-of-sight (LOS) link between the communicating nodes might be infeasible due to long transmission distance or adverse weather conditions. In such cases, information can be relayed from one node to another by decoding and re-transmitting in decode-and-forward (DF) protocol or by amplifying and re-transmitting in amplify-and-forward (AF) protocol [6]. Owing to the capability of offering service to a larger number of users, global coverage with 6G networks becomes attainable [7]. However, providing extreme data rates in NTNs is still an open problem. In order to achieve this as required in the next-generation networks, the system capacity must be increased. To enhance the capacity and to utilize idle frequencies, terahertz (THz) communication can be considered as one of the most effective methods [8].

THz communication is basically defined as utilizing THz frequencies (0.1-10 THz) to provide incredibly wide bandwidths and exceptional data rates [9]. In addition, miniaturization of antennas, improved beamforming, and enhanced security can be listed as other advantages owing to very short wavelengths [10]. However, shorter wavelengths can lead to significant attenuation primarily caused by free-space propagation and molecular absorption [11], which results in the LOS link requirement since the reflected waves are severely attenuated. To combat with the excessive loss levels observed in THz channels, highly directional antennas are used. Yet, this leads to the utilization of very narrow pencil-sharp beams, which requires perfect antenna alignment. In the case of antenna misalignment due to non-stable positions of the communicating nodes or antenna jitters, significant reduction is observed in the received signal power, referred to as pointing error. Fortunately, the NTN architecture has important advantages in overcoming these drawbacks by providing LOS connectivity with reduced pointing errors through quasi-stationary intermediate nodes [12]. Moreover, it also benefits from the decreased absorption loss since the density of the absorbers decrease at higher altitudes in the atmosphere [13].

Therefore, the NTNs operating in the THz band can help achieving the objectives of the next-generation communication systems. In this perspective, it is important to model the THz channel characteristics and to analyze the system performance under realistic scenarios. Moreover, the effects of imperfect hardware and the limits introduced by them must be explored accordingly.

1.1 Objective of the Thesis

The main objectives of this thesis are in-depth investigation and analysis of the utilization of THz frequencies in NTNs considering various deployment and communication scenarios. To quantify the system performance, comprehensive analyses, including the outage probability, asymptotic outage probability, symbol error rate (SER), and ergodic capacity, are performed for different system configurations under realistic conditions in the presence of ideal and non-ideal equipment. The relationship between the system performance and parameters, such as the transceiver altitudes, atmospheric humidity, temperature, pressure, and parameters related to the fading characteristics and pointing acquisition, are presented. The derived theoretical expressions are validated via Monte-Carlo simulations.

1.2 Literature Review

In recent years, THz communications have attracted significant attention from the academic community. Numerous works in the current literature have focused on the feasibility assessments, system design, and performance analyses. Several studies examine the link performance of the short range THz indoor/outdoor communication systems to investigate their feasibility under various channel conditions. The link budget analysis for an indoor communication scenario at a distance of 1-100 m can be found in [14]. In [15], the achievable data rate is analyzed in the presence of the absorption loss and fog/rain-induced losses for link distances up to 1 km. The maximum data rate for a short range THz communication system is examined by accounting for the multipath fading effect in [16] for link distances below 60 m. In addition, [17] provides a comprehensive analysis of how number of antennas and transmission distance affect the achievable data rate. The maximum data rate and achievable error performance of a fixed millimeter wave (mmWave) and THz communications under extreme weather conditions are studied in [18]. The link budget evaluation for an objective data rate is performed in [19] by taking the modulation order and channel coding rate into account for link distances from 10 m to 1 km.

Relying on the link performance presented in the aforementioned works, numerous papers focus on the statistical analyses of single-hop terrestrial THz communication systems. In [20], the ergodic capacity and outage capacity analyses for a terrestrial THz communication system are performed by considering the absorption loss, pointing errors, and turbulence-induced fading for weak-to-strong turbulence regimes. A compound channel model to incorporate the multipath fading, shadowing, and absorption loss via a composite distribution is proposed in [21], where the outage probability is derived for a single-hop communication system. The outage probability, SER, and ergodic capacity analyses for a THz communication system under random fog conditions are obtained in [22].

To combat with the excessive loss levels in THz links and to enhance the system performance, relay-assisted communication scenarios are considered. A dual-hop THz communication system's performance is examined in terms of the outage probability in [23]. In [24], the impact of the number of relays on the outage performance of communication between mobile users and the base station is examined by considering the users' mobility range, the outage threshold, and the distance between relays and the base station. The performance losses due to different fading, pointing error, or fog conditions in a dual-hop THz system are presented in [25]. The authors in [26] have presented the performance analyses for a multi-hop THz communication system in the presence of fading, shadowing, and antenna misalignment. The bit error rate (BER) and ergodic capacity expressions for a dual-hop THz backhaul link are obtained in [27] by accounting for the absorption loss, fading, and pointing errors. A comprehensive statistical analysis of a dual-hop THz system can be found in [28], where the outage, ergodic capacity, and BER performance are examined. The performance enhancement due to the employment of both the relay-aided and direct links between the source and the destination is explored in [29]. A relay-based blockage and antenna misalignment technique is proposed in [30], and the throughput performance of the best relay selection and random relay selection mechanisms are compared. Two-way relaying in a multiple input multiple output (MIMO) THz system to overcome the blockage problem is introduced in [31], and a multi-hop THz system's BER performance is analyzed in the presence of the absorption loss, turbulence-induced fading, and pointing errors under adverse weather conditions in [32].

So far, all the mentioned works primarily focus on the terrestrial communication systems. However, THz transmission can also be considered in aerial communications [33, 34], in satellite networks [35, 36], and in NTNs to provide connectivity between ground, air, and space [37]. In this regard, analyzing the feasibility of all possible communication scenarios regarding these applications is critically important. In this context, a few works focus on the link analyses for NTN applications. In [38], the link budget analysis is performed for an Earth-satellite communication system in Tanggula, Tibet, where massive antenna arrays are employed to combat with excessive loss levels due to absorption, rain, cloud, and spreading. The achievable BER for a THz-enabled intra-orbit link of 1000 km distance in a satellite constellation is evaluated in [39]. Moreover, the maximum throughput of a near-Earth inter-satellite THz communication link is obtained by accounting for the ionospheric effects, absorption, and noise temperature caused by the cosmic microwave background radiation and the sun in [40].

Based on the above-mentioned feasibility assessments, the performance analyses for various scenarios regarding aerial and satellite communications can be found in the literature. A drone-to-drone THz link is considered in [41], and the outage probability, BER, capacity, and diversity order analyses are presented. In [42], a vertical drone-to-ground THz communication system is analyzed in terms of the outage probability for various transmission windows and drone altitudes up to 100 m. The outage probability for a UAV-assisted THz communication between a base station and a mobile user is analyzed in [43], where the UAV has a fixed position and extends the coverage area of the base station. The system model in this work is generalized in [44] to a scenario where the UAV has a dynamic position to enhance the system flexibility and performance. The statistical analyses for a drone-aided dual-hop mixed THz/radio frequency (RF) communication system between a ground station and a drone can be found in [45]. Moreover, in [46], the usable bandwidths for a reliable communication in different scenarios in NTNs, such as low-altitude platform station (LAPS)-to-HAPS, HAPS-to-HAPS, and HAPS-to-satellite communications, are obtained for different transmission windows from sub-THz to THz bands. The impact of adverse weather conditions, such as rain and snow, on the capacity of a THz link between a GEO satellite and a ground station located in mid-latitude regions is investigated in [47]. A multiple reconfigurable intelligent surface-enabled inter-satellite THz communication system's performance is analyzed in terms of BER and achievable data rate in [48].

Together with the above-mentioned works focusing on terrestrial and non-terrestrial THz systems, the effect of non-ideal equipment is of crucial importance in high frequency communications. In practical implementations, the hardware impairment noise, in-phase (I)/quadrature (Q) imbalance, and phase noise can be observed due to the non-linearity of the power amplifiers, mismatch in the I and Q components of the local oscillators, and poor-quality oscillators, respectively [49]. In the literature, limited research progress has been made in analyzing the impact of hardware imperfections on THz terrestrial or non-terrestrial systems. In [50], the outage probability and ergodic capacity performance of a single-hop THz communication system are analyzed in the presence of multipath fading, pointing errors, absorption, and hardware impairment noise. A comprehensive statistical analysis of a THz communication system is presented in [51], where the outage probability, BER, and ergodic capacity performance are obtained by considering the performance degradation induced by the hardware impairment noise. The I/Q imbalance effect and precompensation technique for THz transmitters is presented in [52]. In [53], the influences of hardware impairment noise and I/Q imbalance on the performance of a THz beamforming system are analyzed, and a theoretical framework for the performance assessment for a THz link in the presence of pointing errors and phase noise is presented in [54].

1.3 Contribution of the Thesis

Throughout the thesis, five different works are presented, focusing on the modeling of the channel characteristics and on the performance of THz NTNs under various conditions. The contributions of the thesis can be listed as follows:

- Firstly, the impact of antenna and array designs on the pointing error characteristics in mmWave and THz communications is investigated. Considering the utilization of highly directional antenna elements and antenna arrays, the radiation pattern of the antenna array is modeled to examine the influence of single antenna element and array configuration. Then, based on this pattern, a simple statistical model for the pointing error is proposed. By using this model, the closed-form expressions for the statistics of the joint fading and pointing error coefficient and signal-to-noise ratio (SNR) for highly directional mmWave/THz transmission are derived. The outage probability analysis for a HAPS-to-HAPS communication system is performed to examine the performance variation due to different antenna/array designs.

- Secondly, the link budget analysis for the NTN architecture operating in mmWave/THz frequencies is presented. By taking the varying channel characteristics for all possible communication scenarios in THz NTNs into account, including the dry/humid atmospheric conditions, rain- and fog-induced attenuation, uplink/downlink noise characteristics, etc., the achievable data rates in ground-aerial, aerial-satellite, ground-satellite, inter-aerial, and inter-satellite links are obtained to assess the feasibility of THz NTNs.

- Thirdly, the performance of a dual-hop inter-satellite THz link is examined. In the system of interest, it is considered that the communication between two LEO satellites is established with the aid of another relay satellite orbiting at a higher altitude since the direct link between the source and the destination LEO satellites is not available. The statistics of the end-to-end SNR are derived for this setup, and the system performance is analyzed in terms of the outage probability and SER for various channel parameters.

- Fourthly, the performance of a multi-HAPS NTN is analyzed in the presence of hardware impairment noise. In the considered system, multiple HAPS systems assist the transmission from a LEO satellite to a ground station. The statistics of the end-to-end SNR are obtained, and the outage probability, asymptotic outage probability, and ergodic capacity are analyzed. The system performance is illustrated for different number of HAPS systems under various channel conditions, hardware impairment levels, and HAPS deployment scenarios.

- Finally, an NTN consisting of a LEO satellite, multiple HAPS systems, and a ground station is considered, where HAPS systems act as relays. Here, it is assumed that the ground station suffers from I/Q imbalance. The statistics of the end-to-end SNR are derived for this scenario. To quantify the system performance, two different theoretical bounds for the SER and a tight ergodic capacity bound are obtained. The SER and capacity performance of the system are presented for different number of HAPS systems, atmospheric conditions, HAPS and satellite deployments scenarios, and amplitude/phase mismatch levels at the ground station.

1.4 Notation

Throughout the thesis, $|\cdot|$ shows the absolute value, $\angle(\cdot)$ is the angle operator, $(\cdot)^*$ denotes the complex conjugate, and $z = \mathrm{gcd}(z, v)$ is the greatest common divisor of the integers z and v. $\mathcal{R}\{\cdot\}$ is the real part operator, and $\mathcal{L}\{\cdot\}$ denotes the Laplace transform operator. $\mathbb{R}$ and $\mathbb{C}$ show the set of real numbers, the set of complex numbers, respectively. $f_Z(\cdot)$, $F_Z(\cdot)$, and $\mathcal{M}_Z(\cdot)$ denote the probability density function (PDF), cumulative distribution function (CDF), and moment generating function (MGF) of the random variable Z, respectively. $E[\cdot]$ is the expectation operator. $\mathcal{CN}(\mu, \sigma^2)$ represents the complex Gaussian distribution, where μ and σ^2 are the mean value and the variance, respectively. $\log(\cdot)$ represents the natural logarithm function. $\Gamma(\cdot)$, $\gamma(\cdot,\cdot)$, $\Gamma(\cdot,\cdot)$, $I_0(\cdot)$, erf$(\cdot)$, and $Q(\cdot)$ denote the Gamma function [55, Eq. (8.310.1)], lower incomplete Gamma function [55, Eq. (8.350.1)], upper incomplete Gamma function [55, Eq. (8.350.2)], zeroth order modified Bessel function of the first kind [55, Eq. (8.406.1)], error function [55, Eq. (8.250.1)], and Q function, respectively. $\mathrm{G}_{\cdot,\cdot}^{\cdot,\cdot}\left[\cdot\left|\begin{matrix}\cdots\\ \cdots\end{matrix}\right.\right]$, $\mathrm{H}_{\cdot,\cdot}^{\cdot,\cdot}\left[\cdot\left|\begin{matrix}\cdots\\ \cdots\end{matrix}\right.\right]$, and $\mathrm{H}_{\cdot,\cdot:\cdot,\cdot:\cdot,\cdot}^{\cdot,\cdot:\cdot,\cdot:\cdot,\cdot}\left[\begin{matrix}\cdot\\ \cdot\end{matrix}\left|\begin{matrix}\cdots\\ \cdots\end{matrix}\right.\right]$ are the Meijer-G function [55, Eq. (9.301)], uni-variate Fox-H function [56, Eq. (1.1)], and bi-variate Fox-H function [56, Eq. (2.55)], respectively.

2. FUNDAMENTAL CONCEPTS OF WIRELESS COMMUNICATIONS

Communication is the process of conveying information from its source to the destination. In the communications engineering perspective, this is accomplished by converting information into electrical signals of the form which is suitable for the communication scenario of interest and by transmitting electromagnetic (EM) waves to transfer the information to the destination. In this context, a communication system comprises of three main parts, namely, the transmitter, the receiver, and the channel between them. Unfortunately, the channel exhibits certain characteristics that degrades the quality of the communication, which primarily arise from the distance between transmitter and receiver, the nature of the transmission medium, relative movements of the communicating units, etc. In the subsequent sections, the key channel characteristics are obtained with the mathematical frameworks used to model them, and relevant mitigation techniques are introduced to establish a solid foundation for the modeling and analysis of THz NTNs throughout the thesis.

2.1 Additive Gaussian Noise Channel

In the simplest case of a communication scenario as depicted in Fig. 2.1, e.g. a wireline communication, a noise signal is added to the transmitted signal. Here, the noise originates from the thermal motions of the electrons in the receiver circuits, and the variation in the received signal level is modeled by the Gaussian distribution. Such communication channels are called additive Gaussian noise (AGN) channels.[1] Mathematically, the received signal over an AGN channel can be written as

$$y = \sqrt{P}x + n, \tag{2.1}$$

[1] Since the bandwidth is limited in a practical communication system, the noise is band-limited and non-white. Therefore, the term AGN channel is intentionally used instead of the term additive white Gaussian noise (AWGN) channel.

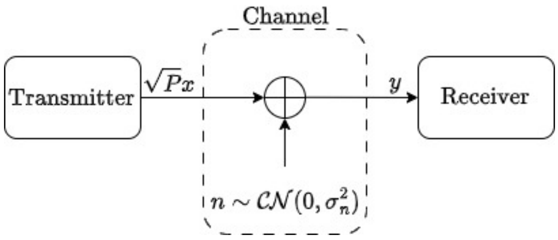

Figure 2.1 : Additive Gaussian noise channel model.

where P is the transmit power, $x \in \mathbb{X}$ is the modulated complex message signal with $E[|x|^2] = 1$, $\mathbb{X} = \{X_m\}_{m=1}^{M}$ is the set of equiprobable symbols X_m for $m = 1, 2, \ldots, M$, and M is the modulation order. Here, different modulation schemes can be considered for transmission, such as binary phase shift keying (BPSK), M-ary phase shift keying (M-PSK), M-ary quadrature amplitude modulation (M-QAM), etc. Moreover, $n \sim \mathcal{CN}(0, \sigma_n^2)$ the complex Gaussian noise with zero mean and variance σ_n^2. In a conventional communication system of bandwidth W performing coherent demodulation with a matched filter, the noise power (or variance of the zero mean noise) is found as $\sigma_n^2 = k_\mathrm{B} T W$, where $k_\mathrm{B} = 1.38 \times 10^{-23}$ m^{2}kgs^{-2}K^{-1} is the Boltzmann's constant, and T is the temperature in Kelvin.

The noise n can be decomposed as $n = n_\mathrm{I} + j n_\mathrm{Q}$, where $n_\mathrm{I} \sim \mathcal{N}(0, \frac{\sigma_n^2}{2})$ and $n_\mathrm{Q} \sim \mathcal{N}(0, \frac{\sigma_n^2}{2})$ are in-phase and quadrature components, respectively, and their PDFs are given as

$$f_{n_\mathrm{I}}(z) = f_{n_\mathrm{Q}}(z) = \frac{1}{\sqrt{\pi \sigma_n^2}} \exp\left(-\frac{z^2}{\sigma_n^2}\right), \quad z \in \mathbb{R}, \tag{2.2}$$

where $\mathbb{R}$ is the set of real numbers. Hence, the conditional PDF of y given $x = X_m$ is written as

$$f_{y|x=X_m}(z|x = X_m) = \frac{1}{\sqrt{2\pi \sigma_n^2}} \exp\left(-\frac{|z - \sqrt{P} X_m|^2}{2\sigma_n^2}\right), \quad z \in \mathbb{C}, \tag{2.3}$$

where $\mathbb{C}$ is the set of complex numbers. The receiver estimates the symbol index m as $\hat{m}$ based on the received signal y by the maximum-likelihood (ML) rule, which can be mathematically stated as

$$\hat{m} = \underset{1 \le m \le M}{\arg\max} \left(f_{y|x=X_m}(z|x = X_m) \right). \tag{2.4}$$

By substituting (2.3) into the above-equation, the ML rule can be simplified after some manipulations as

$$\hat{m} = \underset{1 \leq m \leq M}{\arg\min} \left(|y - \sqrt{P} X_m|^2 \right). \tag{2.5}$$

In other words, the receiver estimates the transmitted symbol index according to the minimum squared distance between the received signal and all possible symbols. For the BPSK modulation, the probability of estimating the symbol or bit index erroneously, i.e. BER, is expressed as

$$P_e = Q\left(\sqrt{\frac{2P}{\sigma_n^2}}\right). \tag{2.6}$$

2.2 Fading Channel

In a wireless communication system, the transmitted EM wave interacts with the transmission medium, which affects the received signal in several ways. The objects in the transmission medium and the transmission medium itself in certain cases lead EM waves to be reflected, scattered, diffracted, and refracted. While a wireless channel exhibits such a complex nature, it is important to characterize it in order to analyze the performance of a communication system. In this regard, the channel effects can be grouped under three main items:

- Path-loss: It refers to the level of attenuation, and it is related to the operating frequency, distance, content of the transmission medium, weather events, etc. Usually, deterministic models are preferred to characterize the path-loss as it remains constant for very long periods of time compared to communication periods.
- Shadowing: The signal attenuates due to the obstacles between the transmitter and receiver, such as buildings, hills, or trees. Unlike path-loss, shadowing introduces random variations. Hence, it is modeled as a slow-varying component in the received signal.
- Fading: The EM waves arrive at the destination from different paths, some from direct or LOS paths and some from indirect or non-line-of-sight (NLOS) paths.

These components are detected at the receiver, and they have constructive and destructive effects based on the random amplitude and phase of each component, which results in rapid fluctuations in the received signal level, referred to as fading. This effect can be categorized based on channel behaviour in the time domain (slow and fast channels) and in the frequency domain (frequency-selective and frequency-flat channels).

In the following subsections, some of the most commonly adopted fading models are presented with the corresponding statistics, and the system performance is illustrated in the next section.

2.2.1 Rayleigh channel

When the LOS link between the transmitter and receiver is not available and communication is established via reflections, the Rayleigh fading model can be used to characterize the fading channel. In this model, the fading coefficient can be decomposed into in-phase and quadrature components as

$$h = h_{\mathrm{I}} + j h_{\mathrm{Q}}, \tag{2.7}$$

where $h_{\mathrm{I}} \sim \mathcal{N}(0, \frac{\Omega}{2})$ and $h_{\mathrm{Q}} \sim \mathcal{N}(0, \frac{\Omega}{2})$ are the in-phase and quadrature components, respectively, and $\Omega = E[|h|^2]$ is the power of the channel coefficient. The PDF of the envelope of h is given by [57]

$$f_{|h|}(z) = \frac{2z}{\Omega} \exp\left(-\frac{z^2}{\Omega}\right), \quad z \geq 0. \tag{2.8}$$

Assuming $\Omega = 1$, the PDF and the CDF of the instantaneous SNR $\gamma = \bar{\gamma}|h|^2$ are given by

$$f_{\gamma}(z) = \frac{1}{\bar{\gamma}} \exp\left(-\frac{z}{\bar{\gamma}}\right), \quad z \geq 0, \tag{2.9}$$

and

$$F_{\gamma}(z) = 1 - \exp\left(-\frac{z}{\bar{\gamma}}\right), \quad z \geq 0, \tag{2.10}$$

respectively, where $\bar{\gamma} = \frac{P}{\sigma_n^2}$ is the average SNR. By using these statistics, the MGF of the SNR can be expressed as

$$\mathcal{M}_\gamma(s) = E\left[e^{-s\gamma}\right] = \int_0^\infty e^{-sz} f_\gamma(z) dz = (1+s\bar{\gamma})^{-1}. \tag{2.11}$$

2.2.2 Rician channel

In the presence of a LOS link between the transmitter and receiver, the fading channel is modeled by incorporating both the dominant LOS component and the scattered NLOS components, as characterized by the Rician fading distribution. In this case, the fading channel coefficient can be decomposed as

$$h = h_\mathrm{I} + jh_\mathrm{Q} + h_\mathrm{LOS}, \tag{2.12}$$

where $h_\mathrm{I} \sim \mathcal{N}(0, \sigma_h^2)$ and $h_\mathrm{Q} \sim \mathcal{N}(0, \sigma_h^2)$ are the in-phase and quadrature NLOS components, respectively, and h_LOS is the constant representing the LOS component. Here, the power of the fading channel coefficient is expressed as $\Omega = |h_\mathrm{LOS}|^2 + 2\sigma_h^2$, and the Rician factor $\mathcal{K} = \frac{|h_\mathrm{LOS}|^2}{2\sigma_h^2}$ denotes the ratio of LOS power to NLOS power. The PDF of the SNR for a Rician channel is given as [57]

$$f_\gamma(z) = \frac{(1+\mathcal{K})e^{-\mathcal{K}}}{\bar{\gamma}} \exp\left(-\frac{(1+\mathcal{K})z}{\bar{\gamma}}\right) I_0\left(2\sqrt{\frac{(1+\mathcal{K})\mathcal{K}z}{\bar{\gamma}}}\right), \quad z \geq 0, \tag{2.13}$$

and the MGF of the SNR can be written as [57]

$$\mathcal{M}_\gamma(s) = \frac{1+\mathcal{K}}{1+\mathcal{K}+s\bar{\gamma}} \exp\left(-\frac{s\mathcal{K}\bar{\gamma}}{1+\mathcal{K}+s\bar{\gamma}}\right). \tag{2.14}$$

2.2.3 α-μ channel

To model a wide range of communication channel characteristics, α-μ distribution can be used, which can describe the fading channel in the presence or absence of the LOS link and in the case of severer characteristics compared to the Rayleigh channel. The α-μ channel can be reduced to other well-known models, such as Gamma, Nakagami-m, exponential, Weibull, one-sided Gaussian, and Rayleigh. The envelope of the α-μ distributed fading coefficient h can be generated for integer μ

as [58][2]

$$|h| = \sqrt[\alpha]{\sum_{i=1}^{\mu} X_i^2 + Y_i^2}, \tag{2.15}$$

where X_i and Y_i are zero mean mutually independent Gaussian random variables with $E[X_i^2] = E[Y_i^2] = \frac{\hat{h}^\alpha}{2\mu}$. Here, $\hat{h} = \sqrt[\alpha]{E[|h|^\alpha]}$ represents the α-root mean value of the fading coefficient. The PDF and CDF of the envelope of h are given as [58]

$$f_{|h|}(z) = \frac{\alpha \mu^\mu z^{\alpha\mu-1}}{\hat{h}^{\alpha\mu}\Gamma(\mu)} \exp\left(-\mu \frac{z^\alpha}{\hat{h}^\alpha}\right), \quad z \geq 0, \tag{2.16}$$

and

$$F_{|h|}(z) = \frac{\gamma\left(\mu, \mu \frac{z^\alpha}{\hat{h}^\alpha}\right)}{\Gamma(\mu)}, \quad z \geq 0, \tag{2.17}$$

respectively. Therefore, the CDF of the SNR for α-μ channel is written as

$$F_\gamma(z) = \frac{\gamma\left(\mu, \mu \frac{z^{\alpha/2}}{\bar{\gamma}^{\alpha/2}\hat{h}^\alpha}\right)}{\Gamma(\mu)}, \quad z \geq 0. \tag{2.18}$$

Subsequently, the MGF of the SNR can be obtained as[3]

$$\mathcal{M}_\gamma(z) = \frac{1}{\Gamma(\mu)} \mathrm{H}_{2,2}^{1,2}\left[\frac{\mu}{\bar{\gamma}^{\alpha/2}\hat{h}^\alpha s^{\alpha/2}} \,\middle|\, \begin{matrix}(1,1),(0,\frac{\alpha}{2})\\(\mu,1),(0,1)\end{matrix}\right]. \tag{2.19}$$

2.3 Performance Analyses for Wireless Channels

This section of the thesis focuses on the impact of slow and frequency-flat fading on communication system's performance and elaborates on the performance analysis. First, the BER performance of wireless channels are presented for the statistical channel models described in the previous section. Then, the outage and ergodic capacity performance are analyzed and illustrated.

2.3.1 BER analysis for wireless channels

In a flat fading channel as depicted in Fig. 2.2, the received signal can be expressed as

[2]For non-integer values of μ, the fading coefficient of unit power can be generated by the α-root of a Gamma distributed random variable with shape parameter of μ and scale parameter of $\frac{1}{\mu}$.

[3]Since this chapter provides a smooth introduction to the channel effects in wireless communications, the derivation of (2.19) is skipped. Please refer to [59, Eqs. (39a), (40), and (41)] for detailed derivation of (2.19).

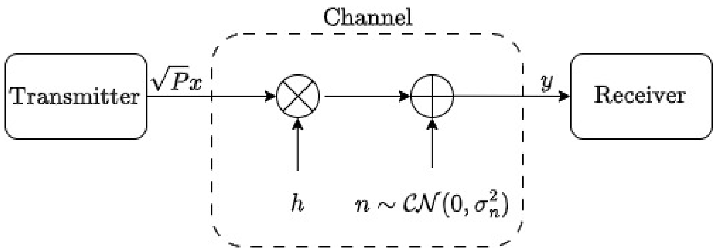

Figure 2.2 : Fading channel model.

$$y = \sqrt{P}hx + n, \tag{2.20}$$

where h is the complex fading coefficient. Contrary to AGN channels, the receiver estimates the transmitted symbol index by the ML rule as

$$\hat{m} = \underset{1 \le m \le M}{\arg\min} \left(|y - h\sqrt{P}X_m|^2 \right). \tag{2.21}$$

For the BPSK modulation, the BER can be found by averaging the error probability in AGN channel over the channel coefficient as

$$P_e = \int_0^\infty Q\left(\sqrt{2\frac{P|z|^2}{\sigma_n^2}}\right) f_{|h|}(z)dz. \tag{2.22}$$

The error probability can also be evaluated in terms of the SNR $\left(\gamma = \frac{P|h|^2}{\sigma_n^2}\right)$ as

$$P_e = \int_0^\infty Q\left(\sqrt{2z}\right) f_\gamma(z)dz, \tag{2.23}$$

or equivalently, it can be obtained by applying partial integration to (2.23) as

$$P_e = \frac{1}{\sqrt{4\pi}} \int_0^\infty F_\gamma(z) \frac{e^{-z}}{\sqrt{z}} dz, \tag{2.24}$$

where $F_\gamma(z)$ is the CDF of the SNR. Alternatively, by using the Craig's formula, the BER can be found as [57]

$$P_e = \frac{1}{\pi} \int_0^{\pi/2} \mathcal{M}_\gamma\left(\frac{1}{\sin^2(\theta)}\right) d\theta, \tag{2.25}$$

where $\mathcal{M}_\gamma(s) = E[e^{-s\gamma}]$ is the MGF of the SNR. In different communication scenarios, various channel characteristics can be observed. For example, the presence or absence of the LOS link changes the statistics of the channel coefficient. There are numerous statistical models to represent these kind of behaviours properly.

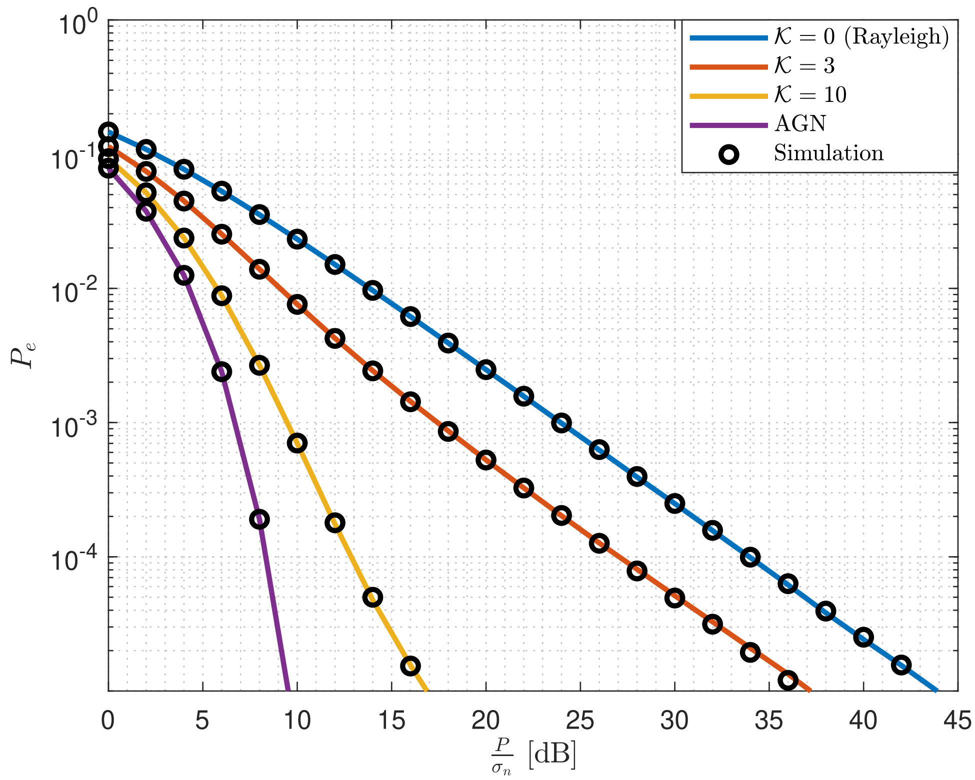

Figure 2.3 : The BPSK BER curves for Rician ($\mathcal{K}=0,3,10$) and AGN channels.

The BER performance of a wireless communication system is illustrated for the fading channel models presented in the previous section for different channel parameters. It is assumed that the BPSK modulation is used in the system, and the results are obtained via Monte-Carlo simulations and the theoretical expressions in (2.23)-(2.25).

In Fig. 2.3, the BPSK BER curves for the Rician ($\mathcal{K}=0,3,10$) and AGN channels are shown. Here, recalling that the Rician factor is the ratio of LOS power to NLOS power, it can be said that $\mathcal{K}=0$ is the Rayleigh channel, and it exhibits a poor error performance compared to that for AGN channel due to severe fading. Moreover, it can be observed that for higher $\mathcal{K}$, the BER performance enhances owing to the increased LOS power. It is worth mentioning that in theory, the slope of the BER curves in high SNR region are the same for Rician and Rayleigh channels, however, it is only observable at very low error rates for high $\mathcal{K}$ values. Moreover, as $\mathcal{K}$ approaches to infinity, the fading effect diminishes, and the channel reduces to the AGN channel.

In Fig. 2.4, the BPSK error performance of a wireless system is illustrated for the α-μ ($\alpha=2,4,8,\ \mu=1$) and AGN channels. It is evident that higher α leads to improved

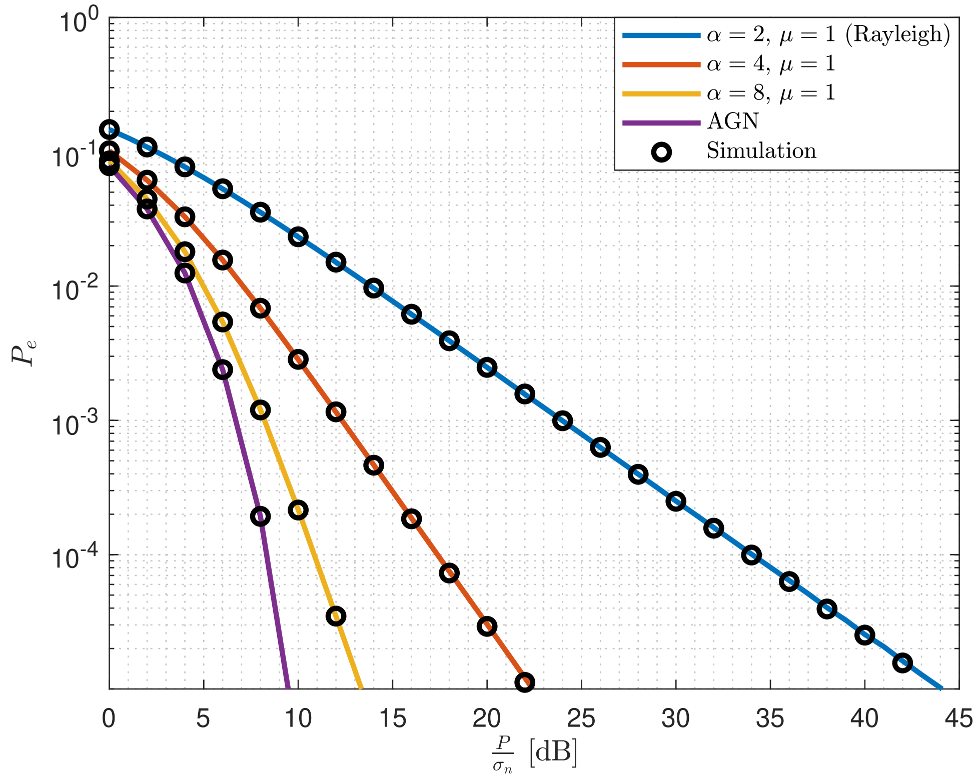

Figure 2.4 : The BPSK BER curves for α-μ ($\alpha = 2,4,8$, $\mu = 1$) and AGN channels.

error performance because of favorable fading channel characteristics. Contrary to the Rician channel, the slope of the curves for α-μ channel is higher, thus, the system performance is enhanced for all SNR values. The BPSK BER curves for the α-μ ($\alpha = 2$, $\mu = 1,2,4$) and AGN channels are presented in Fig. 2.5. It can be seen that increased μ results in lower BER. Also, it is inferred from both figures that as α or μ approaches to infinity, less fading effect is observed, hence, the channel characteristics reduces to that of the AGN channel.

2.3.2 Outage analysis for wireless channels

Another performance metric for wireless communications is the outage probability, which is defined as the probability that the received SNR falls below a predefined threshold γ_{th}. The outage probability can be formulated as

$$P_{\text{out}} = \Pr\left[\gamma \leq \gamma_{th}\right] = F_{\gamma}(\gamma_{th}), \tag{2.26}$$

where $\gamma = \frac{P|h|^2}{\sigma_n^2}$ is the instantaneous SNR according to the signal model given in (2.20). The outage probability can be easily evaluated by using the statistics of γ.

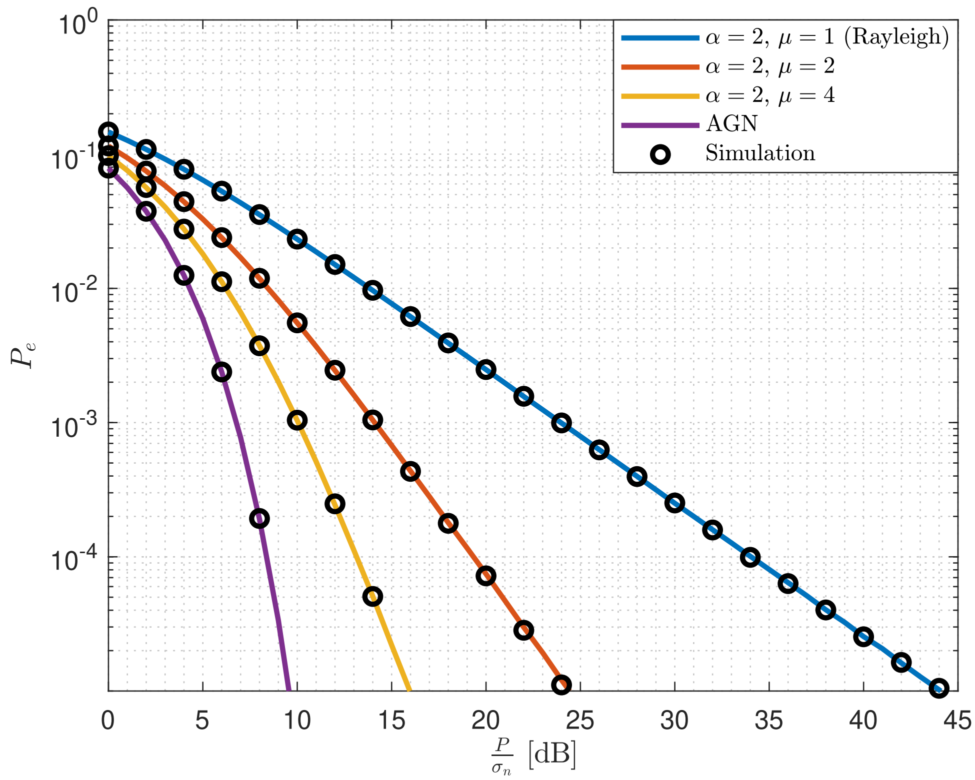

Figure 2.5 : The BPSK BER curves for α-μ ($\alpha = 2$, $\mu = 1,2,4$) and AGN channels.

In Fig. 2.6, the outage performance of a wireless system is shown for Rayleigh, Rician ($\mathcal{K} = 3,10$), and α-μ ($\alpha = 4,8$ and $\mu = 1$) channels. It can be inferred from the figure that the most degraded performance is observed in the Rayleigh channel case which can also be denoted as $\mathcal{K} = 0$ as in the Rician channel or $\alpha = 2$ and $\mu = 1$ as in the α-μ channel. For a higher value of the Rician factor $\mathcal{K}$, the outage performance enhances since the contribution of the LOS link rises. Similarly, as α increases, the outage performance is improved since it provides more favorable channel characteristics.

2.3.3 Ergodic capacity analysis for wireless channels

Ergodic capacity of a wireless channel is the maximum data rate at which the information can be transferred over the channel with a given bandwidth. Mathematically, the ergodic capacity is formulated as [57]

$$C_{erg} = E\left[W \log_2 (1+\gamma)\right], \tag{2.27}$$

where W is the system bandwidth. Obtaining the exact form of the ergodic capacity might be involved. Fortunately, employing the Jensen's inequality provides a tight

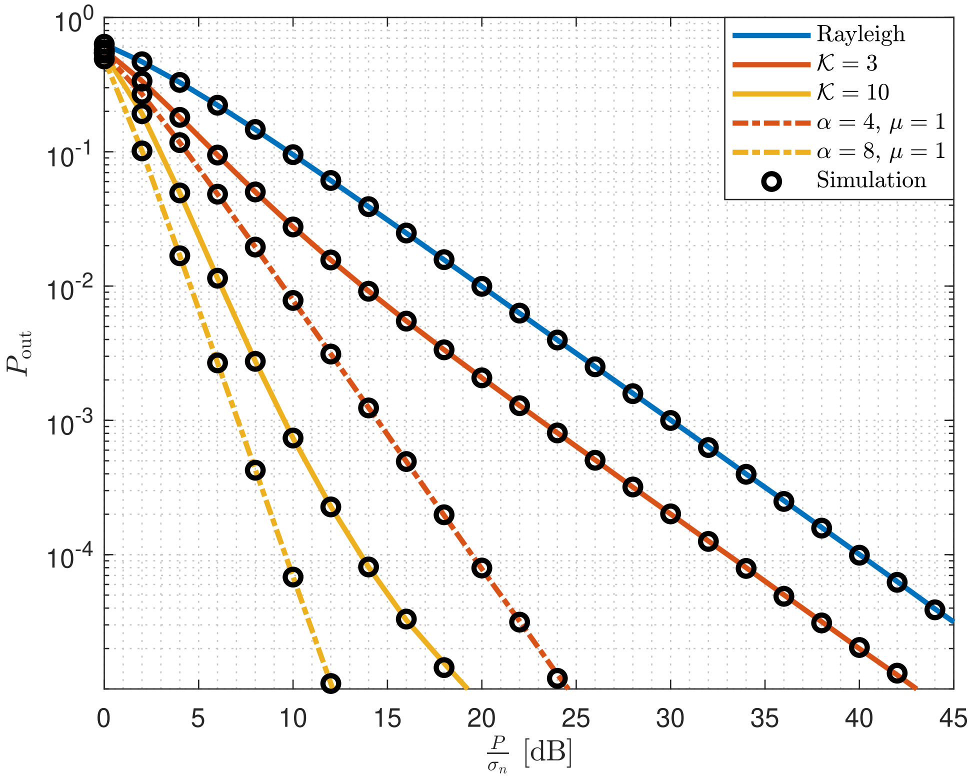

Figure 2.6 : The outage performance for Rayleigh, Rician ($\mathcal{K}=3,10$), and α-μ ($\alpha=4,8$ and $\mu=1$) channels.

upper bound for C_{erg}, which can be expressed as [60]

$$C_{erg} \leq W \log_2 \left(1+E\left[\gamma\right]\right). \tag{2.28}$$

Here, the expected value of the SNR, i.e. $E\left[\gamma\right]=\frac{P}{\sigma_n^2}E\left[|h|^2\right]$, can be found by using the statistics of γ or the square of the envelope of the channel coefficient for the adopted channel model.

The ergodic capacity performance of a wireless system is illustrated in Fig. 2.7 for the α-μ channel model with $\alpha=4$ and $\mu=1$. It can be observed from the figure that the ergodic capacity increases with the increasing $\frac{P}{\sigma_n^2}$. Also, the Jensen's inequality provides a tight upper bound for the ergodic capacity. Though only one channel model is presented in this figure very similar ergodic capacity curves can be obtained for the Rayleigh and Rician channel models since the expected value of $|h|^2$, i.e. the power of the channel, is fixed to unity in Section 2.2. However, the tightness of the Jensen's inequality might slightly change for different statistical models.

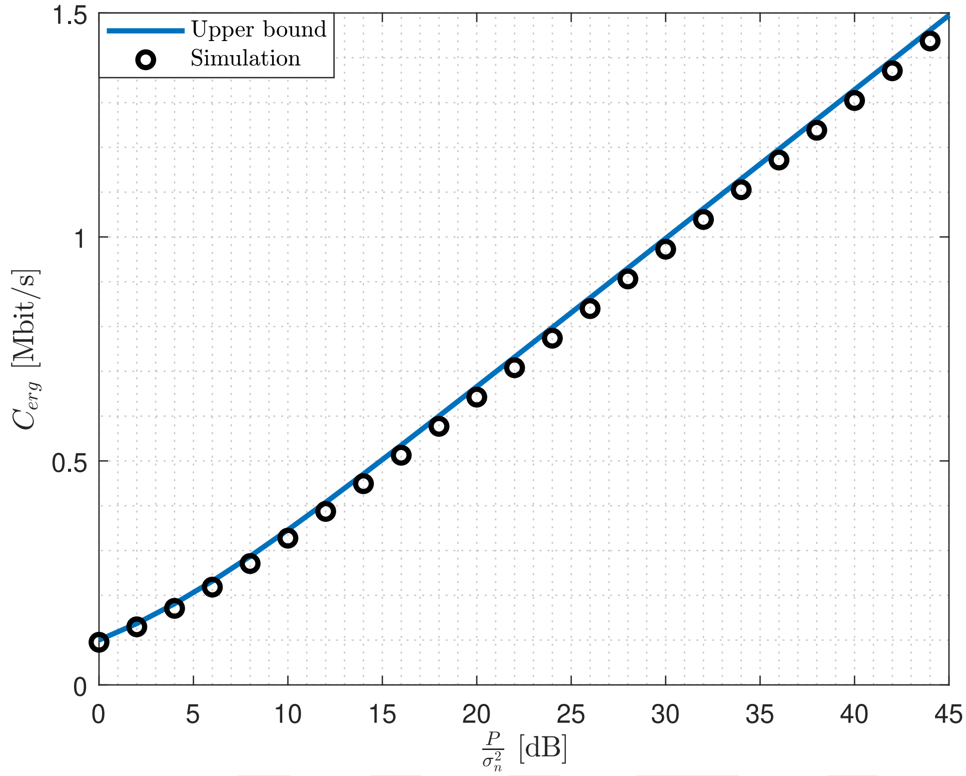

Figure 2.7 : The ergodic capacity performance for α-μ ($\alpha = 4$, $\mu = 1$) channel.

2.4 The Concepts of Diversity and Combining

So far, the adverse effects of fading channels are summarized, and significant performance losses are illustrated in different channel conditions. In the literature, several techniques to mitigate the fading effects can be found, and in this section, the most commonly used techniques are presented. First, the diversity concept is introduced in time, frequency, and spacial domains. Thereafter, the combining methods are explained, and their advantages and disadvantages are discussed.

2.4.1 Diversity techniques

When the received signal is of poor quality, meaning that it is affected by the severe fading conditions, the system performance is deteriorated. This stems from the rapidly changing amplitude/phase of the received signal. In such cases, transmitting orthogonal copies of the message signal reduces the probability that all received copies are of poor quality, which is the primary principle of the diversity techniques. In the following, diversity in the time, frequency, and spacial domains are introduced.

- *Time diversity:* This technique is basically described as transmitting the same message signal in the same frequency band from the same antenna but in different time intervals. Here, it is assumed that the channel state is changing fast enough to make consecutive time intervals independent of each other. In this way, the copies of the received signal become independent also, and the probability of all copies experiencing severe fading is reduced compared to transmitting only one copy. Thus, the error performance of the system enhances. However, since this technique utilizes more than one time interval to transmit a single message, the transmittable data in a unit time using unit frequency, i.e. the spectral efficiency, reduces [61].

- *Frequency diversity:* This technique can be expressed as transmitting the same message signal in the same time interval from the same antenna but in different frequency bands. Similar to the time diversity technique, the independence of the channel state in utilized frequency bands must be ensured to observe improved error performance. Once these bands are separated enough, the channel states are independent of each other, making the received copies in different bands independent also. Therefore, the probability of different copies being of poor quality reduces, enhancing the error performance of the system. However, this improvement comes with the costs of decreased spectral efficiency due to larger bandwidth and complex transceiver design to support different bands allocated to introduce diversity [61].

- *Space diversity:* In this technique, the message signal is transmitted (or received) in single time interval and frequency band but from different antennas. To achieve a satisfactory performance enhancement, the transmitter (or receiver) antennas must be physically separated such that the channel states are independent of each other, leading to reduced probability of receiving all copies of poor quality. Though this technique does not compromise in the spectral efficiency [61], it causes more complex transceiver design. [4]

[4]Alternatively, space diversity can also be achieved by utilizing different polarizations, leading to less complex hardware design.

2.4.2 Combining techniques

Theoretically, diversifying the received signal by using time, frequency, or spacial diversity improves the system performance. However, the combining technique also plays critical role in determining the performance enhancement, efficiency, and hardware complexity. In this context, several combining techniques are briefly introduced in this subsection. The k-th copy of the received signal in any of the above-mentioned diversity schemes can be written as

$$y_k = \sqrt{P_k} h_k x + n_k, \tag{2.29}$$

where x denotes the information signal of unit power. Here, P_k, h_k and $n_k \sim \mathcal{CN}(0, \sigma_n^2)$ for $1 \leq k \leq K$ represent the the transmit power, fading channel coefficient, and the zero mean Gaussian noise with variance σ_n^2, respectively. Furthermore, the K number of copies are received, and k is the index corresponding to the k-th copy of the received signal. The instantaneous SNR of the k-th copy can be expressed as

$$\gamma_k = \bar{\gamma} |h_k|^2, \tag{2.30}$$

where $\bar{\gamma} = \frac{P}{\sigma_n^2}$ is the average SNR.

- *Selection combining (SC):* This is the simplest method to combine the received copies. In this technique, the receiver measures the SNR values for all copies and selects the one which provides the maximum [57]. Mathematically, the SC rule can be given as

  $$k^\dagger = \arg\max_{1 \leq k \leq K} \gamma_k, \tag{2.31}$$

  where $k^\dagger$ is the index of the selected copy. The overall SNR can be written as

  $$\gamma_{\mathrm{SC}} = \max_{1 \leq k \leq K} \gamma_k. \tag{2.32}$$

  However, this technique requires frequent channel measurements, which reduces the efficiency.

- *Switch combining:* To mitigate the inefficiency of frequent channel measurements in SC, the switch combining performs measurements only if needed. In this regard, the receiver selects a new copy if the previously selected one falls below a predefined threshold. This enables less channel estimation, increasing the efficiency [61].

- *Equal gain combining (EGC):* The above-mentioned combining techniques consider only one copy to decode the received signal, which is selected among all possible copies. However, in the EGC technique, all copies are taken into consideration in the decoding. To do that, the EGC combines the copies as in the following:

$$y_{\text{EGC}} = \sum_{k=1}^{K} u_k y_k, \tag{2.33}$$

  where $u_k = e^{-j\angle(h_k)}$ is the weighting coefficient which is used to correct the phase of the k-th copies. In this technique, only the phase of the received signals are corrected by the weighting coefficient u_k [61].[5]

- *Maximal ratio combining (MRC):* Contrary to the EGC method, both the amplitude and phase are corrected in the MRC technique [57]. The combined signal is expressed as

$$y_{\text{MRC}} = \sum_{k=1}^{K} u_k y_k. \tag{2.34}$$

  In this case, the weighting coefficients are determined to maximize the overall SNR γ_{MRC} as $u_k = \frac{h_k^*}{|h_k|}$ [57]. Hence, γ_{MRC} is written as

$$\gamma_{\text{MRC}} = \sum_{k=1}^{K} \gamma_k. \tag{2.35}$$

  The MRC technique is the optimum combining method since it provides the maximum possible overall SNR. However, it requires frequent channel measurement that increases receiver complexity.

[5]It is important to note here that the EGC technique can only be used when the information is conveyed solely in the phase of the modulated signal. In 16-QAM or M-ary amplitude shift keying (ASK) modulation for example, the EGC technique cannot be utilized since the amplitude of the modulated signal also carries information, which requires correction in the amplitudes of the received copies.

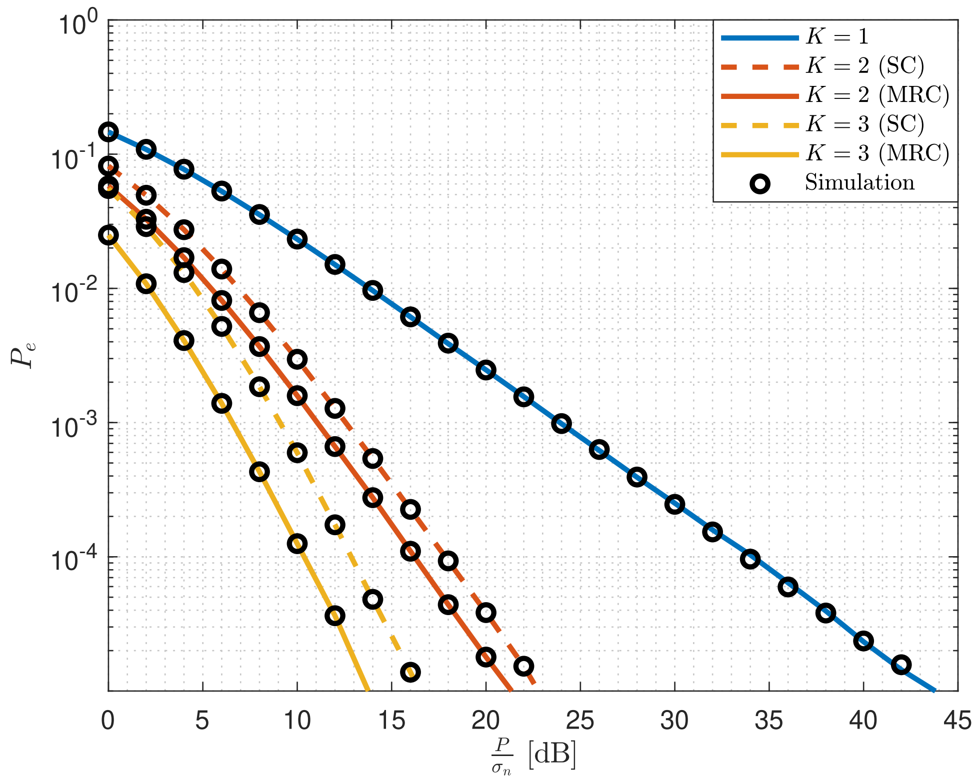

Figure 2.8 : The BPSK BER performance of MRC and SC for Rayleigh channel.

2.4.3 BER performance

In this subsection, the BPSK BER performance of a multi-antenna communication system is presented. Here, it is assumed that K number of antennas are used at the receiver, and the channels are characterized by the Rayleigh fading model.

In Fig. 2.8, the BPSK BER curves for the MRC and SC techniques and $K = 1,2,3$ are shown. It can be observed from the figure that for higher K, the slope of the curves (diversity orders) increase, and the system performance enhances significantly. This stems from the diversity introduced by the increased number of copies. Additionally, the MRC technique slightly outperforms the SC. For $K = 2$, the MRC technique provides ~ 1 dB SNR gain compared to the SC, whereas for $K = 3$, the MRC introduces ~ 2 dB SNR gain.

2.5 Cooperative Communications

In wireless communications, the performance of the LOS link between the transmitter and receiver might be deteriorated by obstacles, severe fading environment, or

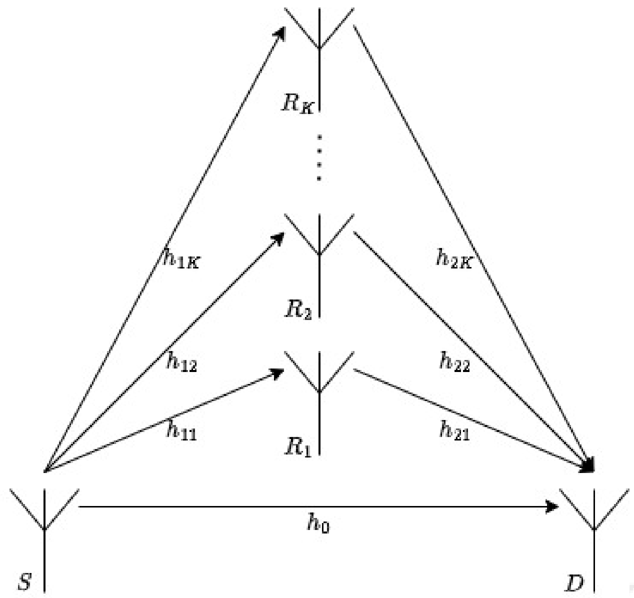

Figure 2.9 : A multi-relay cooperative communication system model.

extreme path-loss. In such scenarios, employing multiple relays enhances the system performance both by reducing the large-scale effects and by providing diversity gain. This transmission strategy is called cooperative communication since the received signals from both the transmitter and relays are incorporated at the receiver.

In Fig. 2.9, a multi-relay cooperative communication system model is depicted. Here, K number of relays, R_k for $1 \leq k \leq K$, are employed to assist the transmission from the source S to the destination D. In this system, the transmission is completed in $K+1$ orthogonal time intervals. In the first one, S transmits information to both the destination and relays. The received signals at the destination and relays can be expressed as

$$y_0 = \sqrt{P_0} h_0 x + n_0 \tag{2.36}$$

and

$$y_{1k} = \sqrt{P_{1k}} h_{1k} x + n_{1k},\ 1 \leq k \leq K, \tag{2.37}$$

where P_0 and P_{1k} are the transmit powers of S in S-to-D and S-to-R_k links, respectively. In this formulation, h_0 and h_{1k} denote the channel coefficients, and $n_0 \sim \mathcal{CN}(0, \sigma_n^2)$ and $n_{1k} \sim \mathcal{CN}(0, \sigma_n^2)$ are the receiver thermal noise signal with zero mean and variance σ_n^2 in S-to-D and S-to-R_k links, respectively. After the first time interval, while S remains silent, each relay transmits its data to D by using the variable-gain AF or fixed-gain AF relaying protocol which are defined as follows:[6]

- *Variable-gain AF relaying:* In this protocol, the k-th relay amplifies the received signal y_{1k} depending on the channel coefficient h_{1k} between S and R_k by the amplification factor [6]

$$G_k^{\mathrm{VG}} = \frac{1}{\sqrt{P_{1k}|h_{1k}|^2 + \sigma_n^2}}. \tag{2.38}$$

  Afterwards, R_k transmits the amplified signal. Then, the received signal from R_k at D is written as

$$\begin{aligned} y_{2k} &= \sqrt{P_{2k}} h_{2k} G_k^{\mathrm{VG}} y_{1k} + n_{2k} \\ &= \sqrt{P_{1k}P_{2k}} h_{1k} h_{2k} G_k^{\mathrm{VG}} x + \sqrt{P_{2k}} h_{2k} G_k^{\mathrm{VG}} n_{1k} + n_{2k}. \end{aligned} \tag{2.39}$$

  By substituting G_k^{VG} into the above-equation, the end-to-end SNR for the S-R_k-D link can be obtained after some manipulations as [6]

$$\gamma_{e2e,k}^{\mathrm{VG}} = \frac{\gamma_{1k}\gamma_{2k}}{\gamma_{1k} + \gamma_{2k} + 1}, \tag{2.40}$$

  where $\gamma_{ik} = \bar{\gamma}_{ik}|h_{ik}|^2$, $\bar{\gamma}_{ik} = \frac{P_{ik}}{\sigma_n^2}$, $E\left[|h_{ik}|^2\right] = 1$, $i \in \{1,2\}$, and $1 \leq k \leq K$.

- *Fixed-gain AF relaying:* Contrary to the variable-gain counterpart, in the fixed-gain AF relaying, the k-th relay amplifies the received signal y_{1k} depending on the power of the channel coefficient h_{1k} between S and R_k. Here, the amplification factor is given as [6]

$$G_k^{\mathrm{FG}} = \frac{1}{\sqrt{P_{1k}E[|h_{1k}|^2] + \sigma_n^2}}. \tag{2.41}$$

  Following the similar steps, the received signal from R_k at D can be expressed as

$$y_{2k} = \sqrt{P_{1k}P_{2k}} h_{1k} h_{2k} G_k^{\mathrm{FG}} x + \sqrt{P_{2k}} h_{2k} G_k^{\mathrm{FG}} n_{1k} + n_{2k}. \tag{2.42}$$

[6] The relays can also utilize the DF relaying protocol, in which the received signal is decoded and re-modulated for transmission at the relay nodes. Throughout the thesis, the AF relaying is considered. Hence, the performance of AF relaying technique is discussed in this section.

Here, the end-to-end SNR for the S-R_k-D link can be found as [6]

$$\gamma_{e2e,k}^{\mathrm{FG}} = \frac{\gamma_{1k}\gamma_{2k}}{\gamma_{2k} + C}, \tag{2.43}$$

where $C = 1 + \bar{\gamma}_{1k} E[|h_{1k}|^2]$.

For either of the above-mentioned protocols, the receiver can utilize the combining techniques presented in Section 2.4.2. In case the SC technique, the overall SNR can be expressed as [57]

$$\gamma_{\mathrm{SC}} = \max\left(\gamma_0, \gamma_{e2e,1}, \gamma_{e2e,2}, \cdots, \gamma_{e2e,K}\right), \tag{2.44}$$

where $\gamma_{e2e,k} = \gamma_{e2e,k}^{\mathrm{VG}}$ for variable-gain AF relaying and $\gamma_{e2e,k} = \gamma_{e2e,k}^{\mathrm{FG}}$ for fixed-gain AF relaying. In this formulation, $\gamma_0 = \bar{\gamma}_0 |h_0|^2$ is the SNR for the direct S-to-D link, where $\bar{\gamma}_0 = \frac{P_0}{\sigma_n^2}$ for $E\left[|h_0|^2\right] = 1$. On the other hand, the overall SNR can be written for the MRC technique as [57]

$$\gamma_{\mathrm{MRC}} = \gamma_0 + \sum_{k=1}^{K} \gamma_{e2e,k}. \tag{2.45}$$

The impacts of the diversity introduced by employing multiple relays and the utilized combining technique can be investigated by considering the outage probability, which is defined as the probability that the overall SNR falls below a predefined threshold SNR value γ_{th}. Mathematically, it is formulated as

$$P_{\mathrm{out}} = \Pr\left[\gamma \leq \gamma_{th}\right] = F_\gamma(\gamma_{th}), \tag{2.46}$$

where $\gamma \in \{\gamma_{\mathrm{SC}}, \gamma_{\mathrm{MRC}}\}$.

In Fig. 2.10, outage performance of the variable-gain AF and fixed-gain AF multi-relay communication systems is illustrated. Here, K number of variable-gain or fixed-gain AF relays are employed in addition to the direct link between S and D to enhance the system performance. Furthermore, the Rayleigh channel model is considered for all links in the system, and $P_0 = P_{1k} = P_{2k}$, $\forall k$. For a fair comparison, it is assumed that total transmit power at S is equally divided among the direct path and relay-assisted links. It can be observed from the figure that the system performance

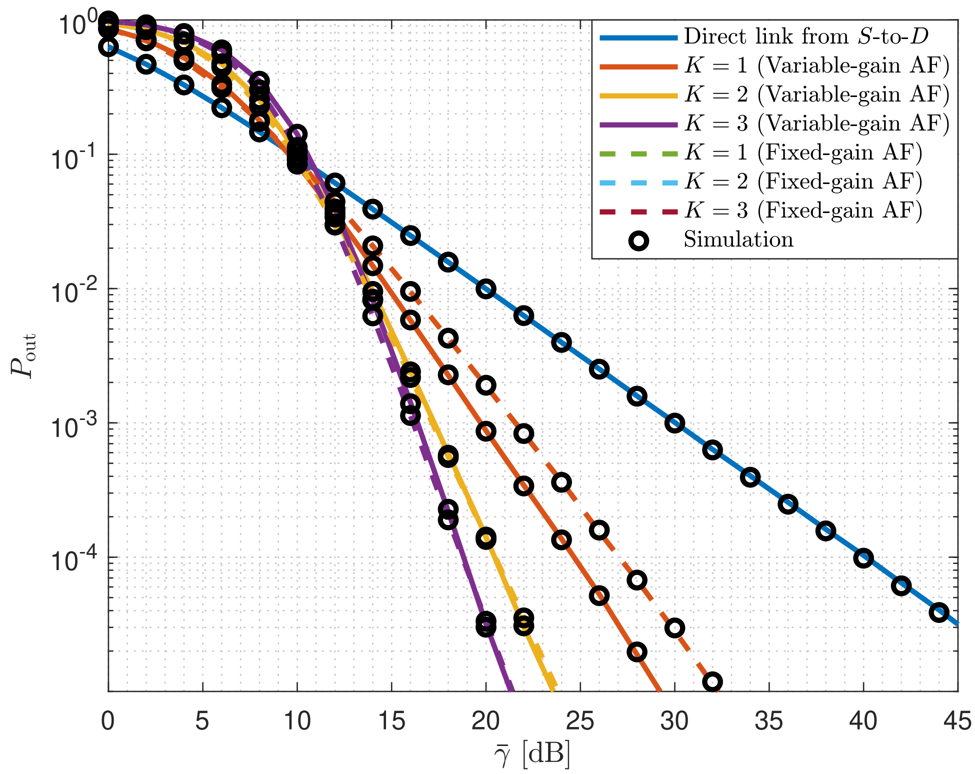

Figure 2.10 : Comparison of outage performance of variable-gain AF and fixed-gain AF multi-relay communication systems.

can be improved for high SNR values by employing relays as it introduces diversity. For low SNR values, the outage performance slightly degraded since the total power is equally divided and transmit power per link decreases. Moreover, it is evident that the variable-gain AF technique outperforms the fixed-gain counterpart for $K = 1$. For higher K, the two relaying protocols provide almost the same performance.

2.6 Hardware Considerations

Up to this point, the receiver's thermal noise and multipath fading effect are discussed as performance degrading factors observed in a communication system. However, in real-world applications, non-ideal equipment is used, which may further degrade the system performance. For example, the power amplifiers operate linearly below a certain input amplitude limit. If the peak amplitude of the input signal (the modulated signal in this case) is near this limit, not only the output changes non-linearly, but also the device introduces an additional noise, referred to as hardware impairment noise. This phenomenon can be considered as the non-linearity. Additionally, the in-phase (I) and quadrature (Q) components of the local oscillator at the transmitter or receiver might not be matched in phase and/or amplitude. In such a scenario, I and Q components of the received signal are not balanced, resulting in a performance degradation due to I/Q imbalance. Furthermore, due to the utilization of poor-quality oscillators, the phase noise can also be observed. To realistically analyze the system performance, these effects must be accounted for. In this section, the mathematical models for two of the most commonly addressed hardware considerations in the literature, namely hardware impairment noise and I/Q imbalance, are presented, and the performance limits caused by these imperfections are illustrated.

2.6.1 Hardware impairment noise

In the presence of hardware impairment noise, the system model can be depicted as in Fig. 2.11. Here, the received signal is expressed as

$$y = \sqrt{P}h(x + w^{\mathrm{t}}) + w^{\mathrm{r}} + n, \tag{2.47}$$

where P, h, x, and $n \sim \mathcal{CN}(0, \sigma_n^2)$ are the transmit power, fading channel coefficient, modulated signal of unit power, and zero mean Gaussian noise with variance σ_n^2, respectively. In this formulation, $w^{\mathrm{t}} \sim \mathcal{CN}(0, \kappa_{\mathrm{t}}^2)$ and $w^{\mathrm{r}} \sim \mathcal{CN}(0, P|h|^2\kappa_{\mathrm{r}}^2)$ denote the hardware impairment noise terms at the transmitter and receiver, where κ_{t}^2 and κ_{r}^2 represent the hardware impairment levels, respectively [62]. Furthermore, $\kappa^2 = \kappa_{\mathrm{t}}^2 + \kappa_{\mathrm{r}}^2$ shows the total hardware impairment level, and $\kappa^2 = 0$ is the ideal hardware case without impairments. Relying on (2.47), the SNR of the received signal can be written as

$$\gamma = \frac{\bar{\gamma}|h|^2}{\bar{\gamma}|h|^2\kappa^2 + 1}, \tag{2.48}$$

where $\bar{\gamma} = \frac{P}{\sigma_n^2}$. It can be understood from the above-equation that as $\bar{\gamma}$ approaches to infinity, γ approaches to $\frac{1}{\kappa^2}$. In other words, in the presence of hardware impairment noise, the SNR has an achievable limit determined by the total hardware impairment level. Moreover, the CDF of γ can be expressed in terms of the statistics of the envelope

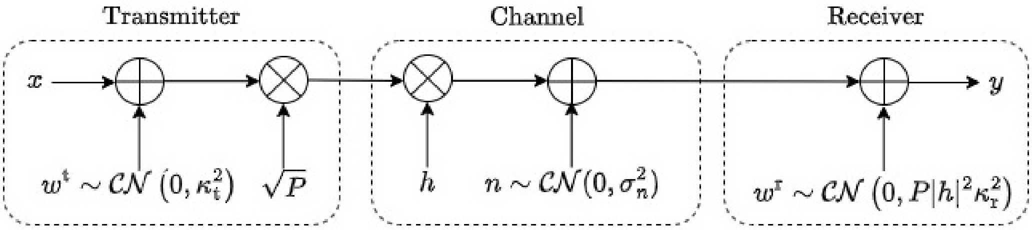

Figure 2.11 : A model for a communication system in the presence of hardware impairment noise.

of h as

$$F_{\gamma}(z) = \begin{cases} F_{|h|}\left(\sqrt{\frac{z/\bar{\gamma}}{1-\kappa^2 z}}\right), & z < \frac{1}{\kappa^2} \\ 1, & z \geq \frac{1}{\kappa^2} \end{cases}. \tag{2.49}$$

The BPSK BER performance of a single-hop communication system in the presence of hardware impairment noise can be found by inserting (2.49) into (2.24).

To illustrate the performance limits introduced by the hardware impairment noise, the BER performance of the system depicted in Fig. 2.11 can be investigated. In Fig. 2.12, the BPSK BER curves for a wireless communication system in α-μ channel are shown in the presence of hardware impairment noise for $\kappa^2 = 0, 0.1, 0.15$. Here, the fading channel parameters are taken as $\alpha = 3$ and $\mu = 2$. It can be inferred from the figure that the hardware impairment noise severely deteriorates the system performance by causing error floors. In this case, the minimum achievable error rates are $\sim 4 \times 10^{-6}$ and $\sim 10^{-4}$ for $\kappa^2 = 0.1$ and $\kappa^2 = 0.15$, respectively.

2.6.2 I/Q imbalance

In the presence of amplitude and/or phase mismatch between I and Q components of the local oscillators, I/Q imbalance is observed. In this case, the received signal under receiver I/Q imbalance can be written as

$$\begin{aligned} y &= U_1\left(\sqrt{P}hx + n\right) + U_2\left(\sqrt{P}hx + n\right)^* \\ &= \underbrace{U_1\sqrt{P}hx}_{\text{Signal term}} + \underbrace{U_1 n + U_2\sqrt{P}(hx)^* + U_2 n^*}_{\text{Noise term}}. \end{aligned} \tag{2.50}$$

Here, $U_1 = \frac{1+ge^{-j\theta}}{2}$ and $U_2 = \frac{1-ge^{j\theta}}{2}$, where g and θ are the amplitude and phase mismatches, respectively [63]. In this formulation, P is the transmit power, h denotes

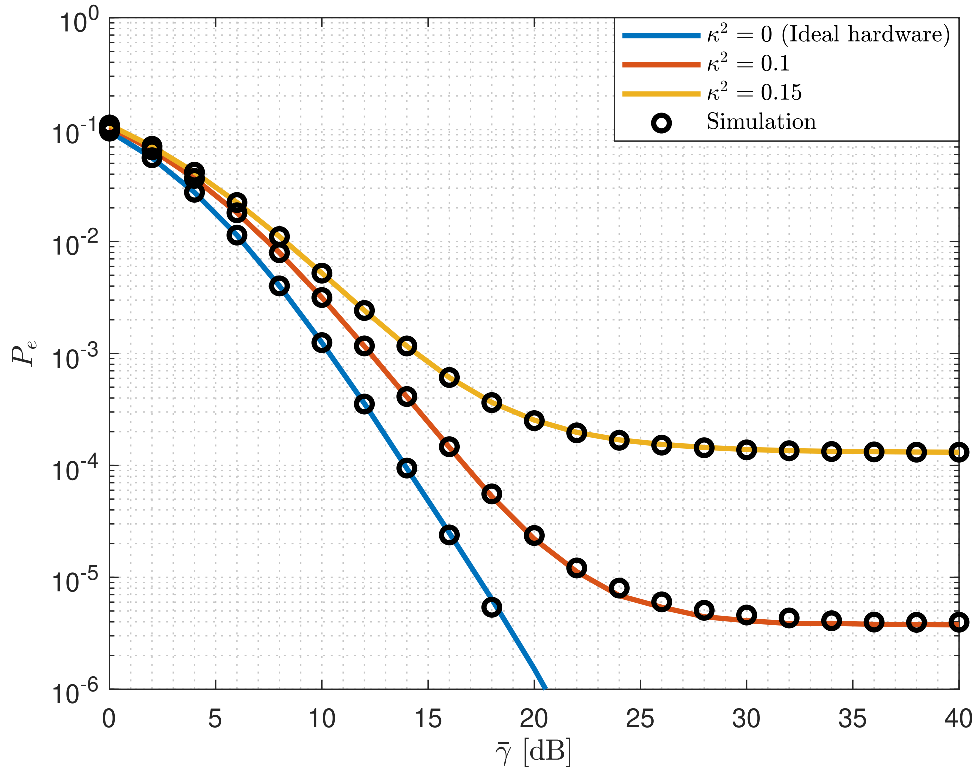

Figure 2.12 : The BPSK BER performance in the presence of hardware impairment noise.

the fading channel coefficient, x stands for the modulated signal of unit power, and $n \sim \mathcal{CN}(0, \sigma_n^2)$ shows the zero mean thermal noise of power σ_n^2. From (2.50), the SNR of the received signal can be obtained as

$$\gamma = \frac{P|h|^2}{\frac{|U_2|^2}{|U_1|^2} P|h|^2 + \frac{|U_1|^2+|U_2|^2}{|U_1|^2}\sigma_n^2}. \tag{2.51}$$

By using (2.51), the CDF of the SNR can be written as

$$F_\gamma(z) = \begin{cases} F_{|h|}\left(\sqrt{\frac{\frac{|U_1|^2+|U_2|^2}{|U_1|^2}\frac{z}{\bar{\gamma}}}{1-\frac{|U_2|^2}{|U_1|^2}z}}\right), & z < \frac{|U_1|^2}{|U_2|^2} \\ 1, & z \geq \frac{|U_1|^2}{|U_2|^2} \end{cases}. \tag{2.52}$$

where $\bar{\gamma} = \frac{P}{\sigma_n^2}$ Then, the BPSK BER performance under receiver I/Q imbalance can be found by substituting $F_\gamma(z)$ into (2.24).

In Fig. 2.13, the BPSK BER performance is illustrated under ideal hardware ($g = 1$ and $\theta = 0°$) and I/Q imbalance ($g = 0.6$ and $\theta = 10°$). In this analysis, α-μ channel

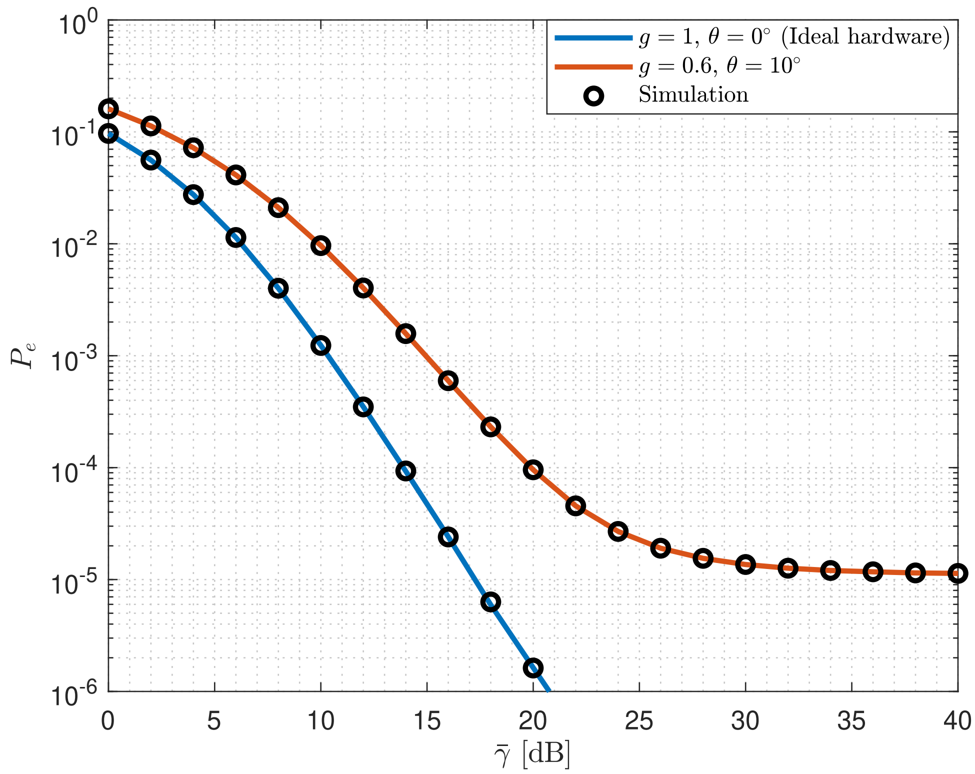

Figure 2.13 : The BPSK BER performance in the presence of I/Q imbalance.

is considered with the fading channel parameters $\alpha = 3$ and $\mu = 2$. As can be seen, the system performance is significantly degraded in the presence I/Q imbalance as it introduces an error floor at $\sim 10^{-5}$ error rate. Hence, it can be said that I/Q imbalance limits the system performance similar to the hardware impairment noise.

3. THz COMMUNICATIONS

After elaborating the fundamental concepts of wireless communications, THz communications is introduced in this chapter as the main topic of the thesis. Before delving deeper into the applications of THz communications within the NTN architecture in the scope of the thesis, it is essential to understand the main channel effects in THz links and the underlying physical phenomena behind them. In the following, the necessity of the utilization of the THz bands, the advantages and disadvantages of it, and the primary considerations about the channel characteristics in THz communications are presented.[1]

3.1 Necessity and Potential of THz Communication in 6G Networks

The exploration and investigation of novel methods to accomplish the objectives of 6G communications are currently under development [64]. In order to achieve enhanced data rates and throughput in 6G networks, it is mandatory to surpass the existing limitations on the system capacity. One of the important factors that contributes to the restrictions in the system capacity is the inadequacy of the current spectrum. To cope with this problem, current literature mainly focuses on the utilization of idle frequencies [65]. Among them, THz communication has emerged as a prominent area of research and has attracted considerable interest from the academic community due to its ability to provide extremely wide bandwidths [8]. By utilizing THz frequencies (0.1-10 THz) to offer incredibly broad bandwidths, high data rates can be achievable to meet the requirements of the next-generation communication systems [9]. However, high frequencies (or short wavelengths) bring some disadvantages, such as high level

[1]It is important to note here that this chapter provides conceptual explanations about the channel characteristics in THz transmission. Hence, the mathematical frameworks to model the channel effects are skipped for brevity and are presented in the next chapters in detail.

of losses caused by spreading, absorption, and weather events as the large-scale effects, along with fading and antenna misalignment as the small-scale effects.

3.2 Large-Scale Channel Effects in THz Communications

One of the most important concerns in THz communications is the excessive loss factor caused by free-space propagation, atmospheric absorption, adverse weather conditions, and interactions between charged particles in the transmission medium and EM waves. All these adverse factors are discussed below in detail.

3.2.1 Free-space loss

As the EM wave is transmitted from an antenna and is propagating through free-space, the radiated power intensity spreads out, and the energy on a unit area decreases, causing a reduction in the received power. The attenuation in the received power due to spreading or free-space loss has a well-known mathematical model, which is given by the Friis formula [66, Sec. 2.17.1]. This model suggests that the received power quadratically reduces with the increasing frequency or transmission distance. Since very high frequencies are utilized in THz communications, severe free-space loss is encountered.

3.2.2 Atmospheric absorption loss

At higher frequencies, the EM wave interacts with the absorber particles present in the transmission medium, such as water vapour and oxygen molecules. In the literature, several models can be found for the atmospheric absorption loss for different scenarios and considerations. For example, transmittance data can be extracted by using line-by-line radiative transfer model (LBLRTM) [67] or an atmospheric model [68] considering the weather profile and altitude for the atmospheric absorption loss calculation. Moreover, International Telecommunication Union (ITU) provides estimation data in [13] for the absorption loss up to 1000 GHz for both horizontal and slant paths. It is shown in [69] that the results obtained by the ITU recommendation [13], LBLRTM [67], and the atmospheric model tool given in [68] are consistent.

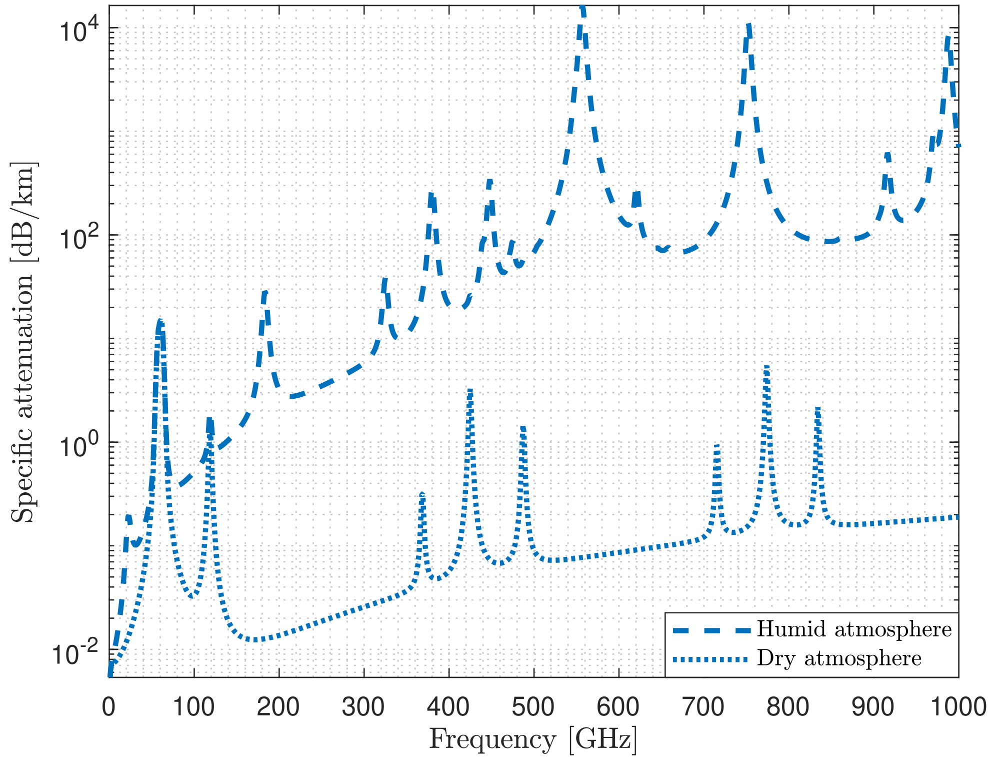

Figure 3.1 : The specific attenuation due to absorption under dry and humid atmospheric conditions at 0 km of altitude.

However, these models do not offer tractable expressions. To accomplish this, a few models are proposed in the literature. In [70], an analytical model for the absorption loss for the frequency bands 0.79-0.91 THz and 0.93-0.94 THz is presented for altitudes up to 1 km and distances from 1 m to 100 m. Another absorption loss model valid from 275 GHz to 400 GHz and transmission distances below 1 km is presented in [71]. Moreover, a mathematical model characterizing the THz band aerial-to-satellite communications is proposed in [72]. All these models have different validity criteria, and thus, they are applicable to certain scenarios.

Despite the lack of analytical tractability, the ITU recommendation [13] is followed throughout the thesis due to its applicability to a wide range of communication systems, including terrestrial, aerial, and satellite communications. In Fig. 3.1, the specific attenuation due to atmospheric absorption is shown up to 1000 GHz. Here, [13] is followed for dry and humid atmospheric conditions at 0 km altitude specified in [73]. It is evident that under dry atmospheric conditions, the absorption loss levels are relatively low in the transmission windows between the peak frequencies. However, in humid atmosphere, excessive absorption loss values are observed due to significant increment in the absorber densities and more frequent absorption.

3.2.3 Weather-dependent effects

THz communication systems are also prone to weather events, such as rain, cloud and fog formations, etc., as they increase the density of the absorber particles in the transmission medium [74, 75]. The loss factor is highly dependent on specific parameters related to the weather conditions. For example, the rainfall rate plays a critical role while determining the loss factor. Moreover, the operating frequency, polarization of the antennas, and positioning of the transmitter and receiver also affect the loss due to rain [76]. In addition, cloud and fog formations lead to a dramatic increment in the absorber densities in the transmission medium [77]. The liquid water content, operating frequency, and elevation angle determine the level of absorption, and thus, the attenuation. Fortunately, weather events mostly occur in the lower layers of the atmosphere, making the THz communications suitable especially for aerial and satellite communications.

3.2.4 Ionospheric loss

Besides absorption loss and weather-dependent effects, THz communications may also suffer from the interactions between the EM wave and the ions and charged particles in the ionosphere. While propagating through plasma in the ionosphere, the EM wave causes free electrons and ions to oscillate, which is measured by the plasma frequency [78]. As the operating frequency increases, the impact of plasma frequency decreases. This stems from the free electrons and ions falling short compared to the frequency of the EM wave [40]. Moreover, the collisions between charged particles in the ionosphere lead to attenuation [79]. Also, depolarization introduced by Faraday rotation in the ionosphere causes attenuation [80], however, it is inversely related to the square of the operating frequency. Hence, it has negligible impact in the THz band [40]. Considering all the above-mentioned ionospheric effects, it is shown in [40] that ionospheric loss is on the order of 10^{-4} dB/km in sub-THz region and decreases at higher frequencies.

3.3 Small-Scale Channel Effects in THz Communications

Other than the loss factors mentioned above, THz channels also experience rapid fluctuations in the received signal level, referred to as small-scale effects, which can be decomposed into two primary factors, namely fading and pointing errors.

3.3.1 Multipath fading

At low frequencies, small-scale fading originates from reception of the reflected waves and their constructive/destructive effects [57]. However, the reflected waves are severely attenuated at higher frequencies because of the loss factors [81]. Hence, in THz communications, small-scale fading primarily emerges from the scattering due to the aerosols present in the transmission medium. This results in multipath components of non-negligible power being detected even if they arrive from NLOS directions [82]. In [83], THz fading channel coefficient is modeled based on measurements conducted in a shopping mall, an airport check-in area, and an entrance hall of a university by α-μ, Rician, Nakagami-m, and log-normal distributions, and it is shown that the α-μ distribution provides an almost excellent fit for the envelope of the fading channel coefficient.[2]

3.3.2 Pointing error

To combat with the extreme loss levels, the utilization of highly directional transmission is considered in THz systems. This can be achieved by using high-gain antennas/arrays, which results in pencil-sharp beams. In this case, the perfect alignment between the transmitter and receiver antennas/arrays becomes critically

[2]It is important to note here that the reflected waves might have detectable power, specifically in short range applications or indoor scenarios as examined in [83]. However, since the focus of this thesis is on THz NTNs, where all links have very long link distances, it is assumed that the reflected waves are severely attenuated, and the primary cause of the fading is the scattering due to aerosols in the transmission medium, resulting in a minimal fading effect [37]. Hence, throughout the thesis, the α-μ channel model is adopted with high values of the distribution parameters to account for weak multipath fading in LOS dominant THz channels.

important [84]. When the antennas are misaligned, the received power rapidly fluctuates, degrading the system performance. One of the early attempts to characterize the pointing error is presented in [84]. However, this model is proposed for free-space optical (FSO) communications. Hence, it only accounts for the jitters at the transmitter and cannot capture the THz transmission characteristics. In [85], a pointing error model is proposed for highly directional THz communication considering square arrays of isotropic antennas, and this model is generalized in [86] to the cases where the jitters in different directions are not identical.[3]

By taking all the above-mentioned large- and small-scale channel effects, the THz links can be modeled for a wide range of communication scenarios, and the performance analyses can be conducted to explore the performance limits and to develop novel architectures to improve the system capabilities.

[3]In Chapter 4 of this thesis, a new pointing error model is proposed for mmWave and THz links. The pointing error model adopted in the Chapters 6, 7, and 8 is described in the respective chapters in detail.

4. IMPACT OF ANTENNA AND ARRAY DESIGN ON POINTING ERROR CHARACTERISTICS IN THz CHANNELS

As mentioned in the previous chapter, highly directional antenna arrays are used to cope with the high levels of attenuation in mmWave and THz communications [87]. However, this leads to the utilization of very narrow pencil-sharp beams, which requires perfect antenna alignment. In the case of antenna misalignment due to non-stable positions of the communicating nodes or antenna jitters, significant reduction is observed in the received signal power, referred to as pointing error.[1]

In the literature, numerous works ([23, 50, 89–91], among others) include the effects of pointing errors for a wide range of communication scenarios. Most of these studies use the pointing error model proposed in [84]. Yet, this model is proposed for FSO communications, and it only accounts for the pointing error due to jitters at the transmitter. Additionally, mmWave/THz transmitters have very different structures and characteristics due to massive arrays, which cannot be captured by this model. More recently, the authors in [85] proposed a pointing error model for mmWave to THz transmission. In this model, the Gaussian approximation is used for the radiated beam from a square antenna array. In [86], the model is extended to the cases where the jitters in different directions are not identical. However, both models are limited the to standard uniform antenna array. In other words, the spacing between array elements is fixed to half-wavelength, which might not always be practically implementable.[2] Also, the effects of array element radiation pattern are not considered. It is demonstrated later in this chapter that both element spacing and array element radiation pattern, i.e. array design and antenna design, significantly impact the radiated beam from the array, thus, the pointing error characteristics.

---

[1]This chapter is based on the paper entitled "An improved pointing error model for mmWave and THz links: Antenna and array design impact" published in *IEEE Communications Letters* [88].

[2]The physical dimensions of highly directional array elements utilized in mmWave/THz communications usually exceed half-wavelength, e.g. horn antennas. Therefore, the element spacing in antenna arrays might be greater than half-wavelength in practical implementations.

Therefore, in this chapter, a simple analytical pointing error model for highly directional mmWave/THz transmission is presented. By utilizing the Gaussian beam approximation for both the array element radiation pattern and the array factor, the presented model incorporates antenna design parameters (maximum gain and 3 dB beamwidth) and array design parameters (number of array elements, element spacing, and 3 dB beamwidth). To examine the effects of antenna and array designs, the outage probability analysis for a horizontal communication between two HAPS systems is conducted.[3] The results have shown that design parameters are as influential as the jitters variance and cannot be ignored.

4.1 System Model

In the system of interest, communication between the transmitter (t) and the receiver (r) is established in the mmWave/THz band. It is assumed that both the transmitter and receiver are equipped with $N \times N$ planar antenna arrays and that the LOS link is available between them. In this case, the received signal can be written as

$$y = \sqrt{\frac{P\mathcal{G}^{\mathrm{t}}(\theta_{\mathrm{t}},\phi_{\mathrm{t}})\mathcal{G}^{\mathrm{r}}(\theta_{\mathrm{r}},\phi_{\mathrm{r}})}{L^{\mathrm{abs}}L^{\mathrm{fsl}}}}h^{\mathrm{f}}x + n, \tag{4.1}$$

where P, L^{abs}, and $L^{\mathrm{fsl}} = \left(\frac{4\pi d}{\lambda}\right)^2$ are the transmit power, atmospheric absorption loss, and free-space loss, respectively. Here, λ is the operating wavelength, d stands for the link distance, x is the transmitted signal of unit power, and $n \sim \mathcal{CN}(0,\sigma_n^2)$ denotes the additive Gaussian noise, where σ_n^2 shows the noise power. Moreover, h^{f} represents the α-μ distributed fading coefficient [58], where α and μ are the distribution parameters. The PDF of the envelope of h^{f} is given as

$$f_{|h^{\mathrm{f}}|}(z) = \frac{\alpha\mu^{\mu}z^{\alpha\mu-1}}{\left(\hat{h}^{\mathrm{f}}\right)^{\alpha\mu}\Gamma(\mu)}\exp\left(-\mu\frac{z^{\alpha}}{\left(\hat{h}^{\mathrm{f}}\right)^{\alpha}}\right). \tag{4.2}$$

Here, $\hat{h}^{\mathrm{f}} = \sqrt[\alpha]{E\left[|h^{\mathrm{f}}|^{\alpha}\right]}$ is the α-root mean value of the envelope of the fading coefficient h^{f}. Additionally, $\mathcal{G}^{\mathrm{q}}(\theta_{\mathrm{q}},\phi_{\mathrm{q}})$ for $\mathrm{q} \in \{\mathrm{t},\mathrm{r}\}$ is the gain of the antenna array in

[3] A HAPS system is defined as a network node that operates at an altitude of 20-50 km [92]. Due to the possible non-stable positioning and antenna jitters, HAPS-to-HAPS communication is prone to pointing errors [5].

the direction of the elevation angle $\theta_{\mathrm{q}} \in [0, \pi]$ and the azimuth angle $\phi_{\mathrm{q}} \in [0, 2\pi)$. The gain of the antenna array $\mathcal{G}^{\mathrm{q}}(\theta_{\mathrm{q}}, \phi_{\mathrm{q}})$ depends on the gain of the antenna array element $\mathcal{G}_{\mathrm{e}}^{\mathrm{q}}(\theta_{\mathrm{q}}, \phi_{\mathrm{q}})$ and the normalized array factor $A_{\mathrm{n}}^{\mathrm{q}}(\theta_{\mathrm{q}}, \phi_{\mathrm{q}})$ as follows [93, Eq. (2.30)]:

$$\mathcal{G}^{\mathrm{q}}(\theta_{\mathrm{q}}, \phi_{\mathrm{q}}) = N^2 \mathcal{G}_{\mathrm{e}}^{\mathrm{q}}(\theta_{\mathrm{q}}, \phi_{\mathrm{q}}) \left(A_{\mathrm{n}}^{\mathrm{q}}(\theta_{\mathrm{q}}, \phi_{\mathrm{q}})\right)^2. \tag{4.3}$$

In the presence of antenna jitters, θ_{q} and ϕ_{q} fluctuate randomly, following the Gaussian distribution, which results in a reduction in the received power. To describe this, $G^{\mathrm{q}}(\theta_{\mathrm{q}}, \phi_{\mathrm{q}})$ is modeled by the Gaussian beam approximation, and pointing error statistics are derived accordingly in the next section.

4.2 Array Pattern and Pointing Error Modeling

4.2.1 Antenna array element

For antennas with pencil beam radiation patterns in the far-field, the radiation pattern can be approximated by a Gaussian beam. Here, it is assumed that the array element has a symmetrical radiation pattern in the azimuth direction, i.e. $\mathcal{G}_{\mathrm{e}}^{\mathrm{q}}(\theta, \phi) = \mathcal{G}_{\mathrm{e}}^{\mathrm{q}}(\theta)$. To model such a Gaussian beam pointed to $\theta = 0°$, first, the radiation pattern function is defined as $g(\theta) = e^{-\theta^2/2\sigma_{\mathrm{e}}^2}$, where the Gaussian spread parameter σ_{e} is determined by 3 dB beamwidth of the antenna array element as $\sigma_{\mathrm{e}} \approx 0.6\theta_{\mathrm{e,3dB}}$ [94, Eq. (8.1.12)]. By using the radiation pattern function, the gain of the antenna array element can be written as [94, Eq. (8.1.10)]

$$\mathcal{G}_{\mathrm{e}}^{\mathrm{q}}(\theta) = \mathcal{G}_{\mathrm{e,max}}^{\mathrm{q}} g^2(\theta) = \mathcal{G}_{\mathrm{e,max}}^{\mathrm{q}} e^{-\theta^2/\sigma_{\mathrm{e}}^2}. \tag{4.4}$$

4.2.2 Array factor

The normalized array factor for $N \times N$ antenna array can be formulated as $A_{\mathrm{n}}^{\mathrm{q}}(\theta, \phi) = A_{\mathrm{nx}}^{\mathrm{q}}(\theta, \phi) A_{\mathrm{ny}}^{\mathrm{q}}(\theta, \phi)$, where $A_{\mathrm{nx}}^{\mathrm{q}}(\theta, \phi)$ and $A_{\mathrm{ny}}^{\mathrm{q}}(\theta, \phi)$ are the normalized array factors of the arrays on the x-axis and y-axis, respectively, and they are defined as

$$A_{\mathrm{nx}}^{\mathrm{q}}(\theta, \phi) = \frac{1}{N} \sum_{p=1}^{N} I_{p\mathrm{x}} e^{j k_{\mathrm{w}} \mathrm{x}_p \sin\theta \cos\phi + \beta_{p\mathrm{x}}}, \tag{4.5a}$$

$$A_{\mathrm{ny}}^{\mathrm{q}}(\theta, \phi) = \frac{1}{N} \sum_{m=1}^{N} I_{m\mathrm{x}} e^{j k_{\mathrm{w}} \mathrm{y}_m \sin\theta \sin\phi + \beta_{m\mathrm{y}}}. \tag{4.5b}$$

In this formulation, $I_{p\mathrm{x}}$, x_p, and $\beta_{p\mathrm{x}}$ are amplitude excitation, x coordinate of the array element, and phase excitation along the x-axis, respectively. The same quantities for the y-axis are denoted as $I_{m\mathrm{y}}$, y_m, and $\beta_{m\mathrm{y}}$. Moreover, $k_\mathrm{w} = 2\pi/\lambda$ is the wave number. For $N \times N$ uniform planar arrays, $A^\mathrm{q}_\mathrm{nx}(\theta,\phi)$ and $A^\mathrm{q}_\mathrm{ny}(\theta,\phi)$ can be written in closed-form as [66, Eq. (6.91)]

$$A^\mathrm{q}_\mathrm{nx}(\theta,\phi) = \frac{1}{N}\frac{\sin\left(\frac{N}{2}k_\mathrm{w}d_\mathrm{x}\sin\theta\cos\phi+\beta_\mathrm{x}\right)}{\sin\left(\frac{1}{2}k_\mathrm{w}d_\mathrm{x}\sin\theta\cos\phi+\beta_\mathrm{x}\right)}, \tag{4.6a}$$

$$A^\mathrm{q}_\mathrm{ny}(\theta,\phi) = \frac{1}{N}\frac{\sin\left(\frac{N}{2}k_\mathrm{w}d_\mathrm{y}\sin\theta\sin\phi+\beta_\mathrm{y}\right)}{\sin\left(\frac{1}{2}k_\mathrm{w}d_\mathrm{y}\sin\theta\sin\phi+\beta_\mathrm{y}\right)}, \tag{4.6b}$$

where d_x and d_y are the spacing between array elements, and β_x and β_y show the uniform phase excitation values. Assuming symmetric behaviour of the array factor along ϕ direction due to square array, i.e. $A^\mathrm{q}_\mathrm{n}(\theta,\phi) = A^\mathrm{q}_\mathrm{n}(\theta)$, half-power beamwidth of the array factor for broadside radiation, i.e. $\beta_\mathrm{x} = \beta_\mathrm{y} = 0$, is given by $\theta_\mathrm{a,3dB} = 2\left|\frac{\pi}{2} - \frac{\lambda}{2\pi d_\mathrm{x}}\frac{2.782}{N}\right|$ [66, Eq. (6.14c)]. The main lobe of $A^\mathrm{q}_\mathrm{nx}(\theta,\phi)$ and $A^\mathrm{q}_\mathrm{ny}(\theta,\phi)$ can be approximated by a Gaussian beam as [95]

$$A^\mathrm{q}_\mathrm{nx}(\theta,\phi) = \exp\left(-\frac{k_\mathrm{w}^2\sin^2\theta\cos^2\phi}{2\sigma_\mathrm{a}^2}\right), \tag{4.7a}$$

$$A^\mathrm{q}_\mathrm{ny}(\theta,\phi) = \exp\left(-\frac{k_\mathrm{w}^2\sin^2\theta\sin^2\phi}{2\sigma_\mathrm{a}^2}\right). \tag{4.7b}$$

In the above-equations, σ_a is the mean-square deviation which can be found by

$$\sigma_\mathrm{a} = k_\mathrm{w}\sqrt{\frac{10}{b\log 10}}\sin\left(\frac{\theta_\mathrm{a,3dB}}{2}\right), \tag{4.8}$$

where $b = 3$. Hence, $A^\mathrm{q}(\theta)$ can be written as

$$A^\mathrm{q}_\mathrm{n}(\theta,\phi) = A^\mathrm{q}_\mathrm{n}(\theta) = \exp\left(-\frac{k_\mathrm{w}^2\sin^2\theta}{2\sigma_\mathrm{a}^2}\right). \tag{4.9}$$

In practice, non-uniform arrays and optimized amplitude/phase excitations can be utilized to reduce the undesired grating lobe levels and to produce pencil beam array factor [95]. In such a case, the whole main lobe can be approximated by a Gaussian beam, and its corresponding mean square deviation can be found as in (4.8) by replacing $\theta_\mathrm{a,3dB}$ by the desired b dB beamwidth $\theta_{\mathrm{a},b\mathrm{dB}}$, where b is any positive real number.

4.2.3 Gain of the antenna array

By substituting (4.4) and (4.9) in (4.3), the gain of the antenna array can be written as

$$\mathcal{G}^{\mathrm{q}}(\theta)=\mathcal{G}^{\mathrm{q}}_{\max}\exp\left(-\frac{\theta^2}{\sigma_{\mathrm{e}}^2}\right)\exp\left(-\frac{k_{\mathrm{w}}^2\sin^2\theta}{\sigma_{\mathrm{a}}^2}\right), \tag{4.10}$$

where $\mathcal{G}^{\mathrm{q}}_{\max}=N^2\mathcal{G}^{\mathrm{q}}_{\mathrm{e},\max}$ denotes the maximum array gain. For small values of θ, the above-expression can be further simplified by using $\sin\theta\approx\theta$ as

$$\mathcal{G}^{\mathrm{q}}(\theta)=\mathcal{G}^{\mathrm{q}}_{\max}\exp\left(-\frac{\theta^2}{\sigma_{\mathrm{e}}^2}-\frac{k_{\mathrm{w}}^2\theta^2}{\sigma_{\mathrm{a}}^2}\right). \tag{4.11}$$

After some manipulations, the gain of the antenna array can be obtained as

$$\mathcal{G}^{\mathrm{q}}(\theta)=\mathcal{G}^{\mathrm{q}}_{\max}\exp\left(-\frac{\theta^2}{\sigma^2}\right), \tag{4.12}$$

where $\sigma=\sqrt{\frac{\sigma_{\mathrm{e}}^2\sigma_{\mathrm{a}}^2}{\sigma_{\mathrm{a}}^2+k_{\mathrm{w}}^2\sigma_{\mathrm{e}}^2}}$ is the beam divergence of the array pattern. By using (4.12), the gain of antenna array can be accurately approximated by taking antenna array element pattern ($\mathcal{G}^{\mathrm{q}}_{\mathrm{e},\max}$ and 3 dB beamwidth through σ_{e}^2) and array factor (number of array elements N^2 and 3 dB beamwidth through σ_{a}^2) into consideration.

In Fig. 4.1a, array pattern normalized to its maximum is illustrated for $N=8,12,16$. Here, a 300 GHz lens antenna with $\theta_{\mathrm{e,3dB}}=6.8^\circ$ and $G^{\mathrm{q}}_{\mathrm{e},\max}=28.1$ dBi is used [96], and it is assumed that the spacing between the array elements is $d_{\mathrm{x}}=d_{\mathrm{y}}=10\lambda$. Also, for the dashed curves, the original array factor in (4.6) is considered, whereas the Gaussian approximated array factor in (4.9) is used for the dotted curves. The figure shows that the main lobe of the array pattern is well-approximated. While the Gaussian model tends to underestimate the side lobes and grating lobes, this model is still valid for small orientation fluctuations as it tightly approximates the array pattern for small θ values.[4,5] Therefore, the Gaussian approximation for the array pattern is well-suited for pointing error modeling in mmWave/THz links. In Fig. 4.1b, the beam divergence (σ) and the maximum array gain ($\mathcal{G}^{\mathrm{q}}_{\max}$) values are shown with respect to N. It can be inferred that the radiated beam gets narrower as the array size increases. Additionally,

[4]By utilizing the beam tracking mechanisms [97], orientation fluctuation can be reduced to a certain level at which the communication is predominantly established via the main lobe.

[5]The side and grating lobes are different types of radiation lobes: the former naturally arises in any antenna or array pattern, while the latter is distinct high-energy lobe that originates from the array geometry.

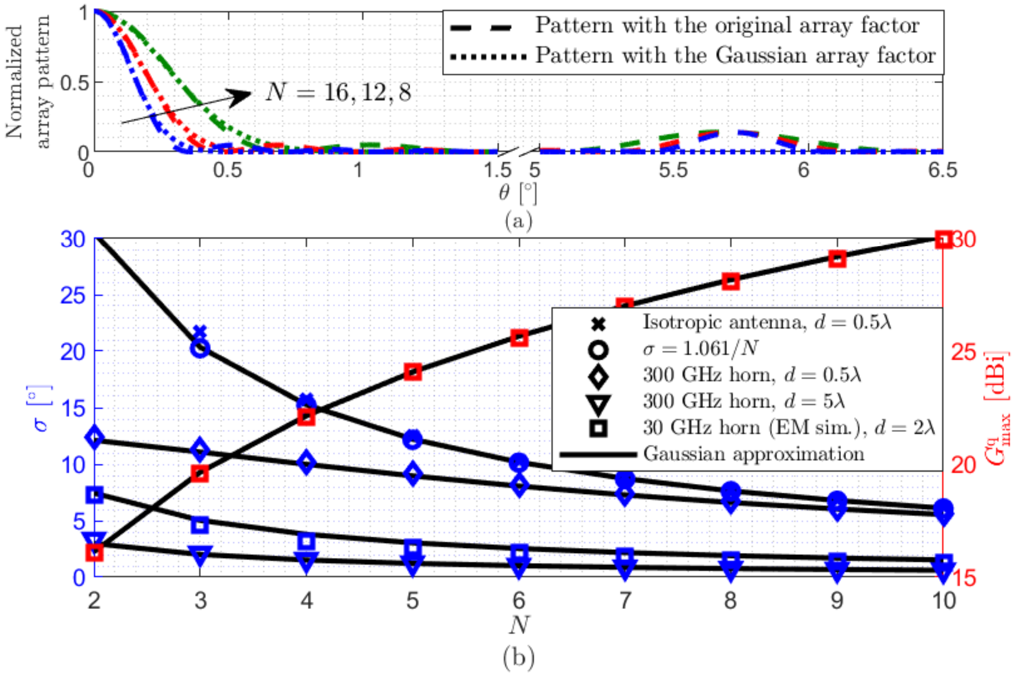

Figure 4.1 : (a) Normalized pattern of an array of lens antennas [96] with element spacing $d_{\mathrm{x}} = d_{\mathrm{y}} = 10\lambda$. (b) Beam divergence and maximum array gain for with different antennas (isotropic and horn) and $d = d_{\mathrm{x}} = d_{\mathrm{y}}$.

it can be observed that the model proposed in [85] and [86] is valid only for an array of isotropic antennas and element spacing of $d_{\mathrm{x}} = d_{\mathrm{y}} = 0.5\lambda$. This originates from the fact that the beam divergence expression $\sigma = 1.061/N$ in [85] and [86] does not take antenna radiation pattern and array design into consideration. Hence, they cannot capture the variations due to antenna and/or array design parameters. On the contrary, the proposed model in this chapter is valid for a wide range of antenna types (e.g. horn, lens, etc.) with different element spacing values. Here, horn antennas (diamond, triangular, and square markers in Fig. 4.1b) are considered as an example. Comparing the curves for isotropic and 300 GHz horn antennas ($\theta_{\mathrm{e,3dB}} = 22°$ and $G^{\mathrm{q}}_{\mathrm{e,max}} = 17$ dBi [98]) for $d_{\mathrm{e}} = 0.5\lambda$, it can be deduced that the array element radiation pattern has an impact on σ for small arrays. Furthermore, the Gaussian approximation is validated via EM simulations in CST Microwave Studio for 30 GHz horn antenna with $\theta_{\mathrm{e,3dB}} = 56.1°$ and $G^{\mathrm{q}}_{\mathrm{e,max}} = 10.1$ dBi (square markers in Fig. 4.1b), and the theoretical results are perfectly matched with the EM simulations. Moreover, for larger element spacing, σ decreases. In other words, the radiated beam gets narrower, making the system more susceptible to orientation fluctuations.

4.2.4 Pointing error

In the case of imperfect alignment between the transmitter and receiver antenna arrays, the radiation direction of $\mathrm{q} \in \{\mathrm{t},\mathrm{r}\}$ can be given as $\theta_{\mathrm{q}} = \tan^{-1}\left(\sqrt{\tan^2\theta_{\mathrm{qx}} + \tan^2\theta_{\mathrm{qy}}}\right)$, where $\theta_{\mathrm{qx}} \sim \mathcal{N}(0,\sigma_\theta^2)$ and $\theta_{\mathrm{qy}} \sim \mathcal{N}(0,\sigma_\theta^2)$ are the orientation fluctuation in the x-z plane and y-z plane, respectively. For small values of θ_{qx} and θ_{qy}, the radiation direction can be written as $\theta_{\mathrm{q}} \approx \sqrt{\theta_{\mathrm{qx}}^2 + \theta_{\mathrm{qy}}^2}$, where θ_{q} is Rayleigh distributed with the distribution parameter σ_θ^2. By substituting (4.12) in (4.1), the received signal can be rewritten as $y = \sqrt{\frac{P}{L}} h^{\mathrm{fp}} x + n$, where $h^{\mathrm{fp}} = h^{\mathrm{f}} h^{\mathrm{p}}$, $h^{\mathrm{p}} = \exp\left(-\frac{\theta_{\mathrm{t}}^2+\theta_{\mathrm{r}}^2}{2\sigma^2}\right)$, and $L = \frac{L^{\mathrm{abs}} L^{\mathrm{fsl}}}{\mathcal{G}_{\mathrm{e,max}}^{\mathrm{t}} \mathcal{G}_{\mathrm{e,max}}^{\mathrm{r}} N^4}$ are the joint channel coefficient, the pointing error coefficient, and the total path-loss, respectively. Here, θ_{t}^2 and θ_{r}^2 are exponential distributed random variables with the distribution parameter $\frac{1}{2\sigma_\theta^2}$. The pointing error coefficient can be expressed as $h^{\mathrm{p}} = \exp\left(-\frac{\theta_{\mathrm{tr}}^2}{2\sigma^2}\right)$, where $\theta_{\mathrm{tr}}^2 = \theta_{\mathrm{t}}^2 + \theta_{\mathrm{r}}^2$ is Gamma distributed with the shape parameter 2 and the scale parameter $2\sigma_\theta^2$. Finally, h^{p} is negative log-Gamma distributed with the shape parameter 2 and scale parameter σ_θ^2/σ^2, and its PDF is given as [99][6]

$$
\begin{aligned}
f_{h^{\mathrm{p}}}(z) &= -\psi^2 z^{\psi-1} \log z && \text{(4.13a)}\\
&\approx \psi^2 c z^{\psi-1} - \psi^2 c z^{\psi-1+\frac{1}{c}}, \; 0 \le z \le 1, && \text{(4.13b)}
\end{aligned}
$$

where $\psi = \sigma^2/\sigma_\theta^2$. Invoking the approximate formula for the natural logarithm function, i.e. $\log x \approx c x^{1/c} - c$, in (4.13a) implies (4.13b), where c is a large real number [55, Eq. (1.512.4)]. Throughout this work $c = 1000$ is used to enhance the accuracy of the derived expression. Integrating (4.13b) with respect to z, the CDF of h^{p} can be derived as

$$F_{h^{\mathrm{p}}}(z) \approx \psi c z^{\psi} - \psi^2 c \frac{z^{\psi+\frac{1}{c}}}{\psi+\frac{1}{c}}, \; 0 \le z \le 1. \tag{4.14}$$

For $z > 1$, $F_{h^{\mathrm{p}}}(z) = 1$. By using these statistics, the outage performance of a mmWave/THz system can be analyzed to assess the impact of antenna/array design.

[6] Here, (4.13a) is the same as given in [85, Eq. (11)] with the main difference in the definition of σ incorporating the antenna/array parameters in the pointing error statistics, which is the primary objective of this chapter.

4.3 Outage Analysis

In the presence of antenna misalignment, received power reduces, causing outages. The outage probability can be defined as the probability that the received SNR $\gamma = \frac{P}{L\sigma_n^2}\left|h^{\mathrm{fp}}\right|^2$ falls below a predefined threshold γ_{th}, i.e. $P_{\mathrm{out}} = \Pr\left[\gamma \leq \gamma_{th}\right]$. Mathematically, it can be expressed as

$$P_{\mathrm{out}} = \Pr\left[\left|h^{\mathrm{fp}}\right| \leq \sqrt{\frac{L\sigma_n^2\gamma_{th}}{P}}\right] = F_{\left|h^{\mathrm{fp}}\right|}\left(\sqrt{\frac{L\sigma_n^2\gamma_{th}}{P}}\right), \tag{4.15}$$

where the CDF of the joint channel coefficient h^{fp} can be obtained as[7]

$$F_{\left|h^{\mathrm{fp}}\right|}(z) = \int_0^\infty F_{h^{\mathrm{p}}}\left(\frac{z}{\upsilon}\right) f_{\left|h^{\mathrm{f}}\right|}(\upsilon) d\upsilon. \tag{4.16}$$

Substituting (4.2) and (4.13b) into the above-equation yields

$$F_{\left|h^{\mathrm{fp}}\right|}(z) = \frac{I_1}{\Gamma(\mu)} + \frac{\psi c \alpha A^\mu z^\psi}{\Gamma(\mu)} I_2 - \frac{\psi^2 c}{\psi + \frac{1}{c}} \frac{\alpha A^\mu z^{\psi + \frac{1}{c}}}{\Gamma(\mu)} I_3, \tag{4.17}$$

where $A = \frac{\mu}{\left(\hat{h}^{\mathrm{f}}\right)^\alpha}$. Here, I_1, I_2, and I_3 are given by

$$I_1 = \alpha A^\mu \int_0^z \upsilon^{\alpha\mu - 1} \exp\left(-A\upsilon^\alpha\right) d\upsilon, \tag{4.18a}$$

$$I_2 = \int_z^\infty \upsilon^{\alpha\mu - 1 - \psi} \exp\left(-A\upsilon^\alpha\right) d\upsilon, \tag{4.18b}$$

$$I_3 = \int_z^\infty \upsilon^{\alpha\mu - 1 - \psi - \frac{1}{c}} \exp\left(-A\upsilon^\alpha\right) d\upsilon, \tag{4.18c}$$

respectively. By changing the variables $t_1 = A\upsilon^\alpha$ and after employing the definition of lower incomplete Gamma function [55, Eq. (8.350.1)] in (4.18a), I_1 can be found as

$$I_1 = \int_0^{Az^\alpha} t_1^{\mu - 1} e^{-t_1} dt_1 = \gamma\left(\mu, Az^\alpha\right). \tag{4.19}$$

Thereafter, utilizing the variable change $t_2 = A\upsilon^\alpha$ in (4.18b) together with the definition of upper incomplete Gamma function [55, Eq. (8.350.2)] yields

$$I_2 = \frac{A^{\frac{\psi}{\alpha} - \mu}}{\alpha} \int_{Az^\alpha}^\infty t_2^{\mu - \frac{\psi}{\alpha} - 1} e^{-t_2} dt_2 = \frac{A^{\frac{\psi}{\alpha} - \mu}}{\alpha} \Gamma\left(\mu - \frac{\psi}{\alpha}, Az^\alpha\right). \tag{4.20}$$

[7] Notice here that the pointing error coefficient h^{p} is defined as a positive real-valued random variable since it represents the fraction of the received power in the presence of antenna misalignment. However, the fading coefficient h^{f} is complex. Hence, the derived statistics in this section is related to the envelope of the joint fading and pointing error coefficient, i.e. $\left|h^{\mathrm{fp}}\right| = \left|h^{\mathrm{f}}\right| h^{\mathrm{p}}$.

Similarly, I_3 can be obtained by changing the variables $t_3 = Av^{\alpha}$ and by invoking [55, Eq. (8.350.2)] as

$$I_3 = \frac{A^{\frac{\psi}{\alpha}-\mu+\frac{1}{c\alpha}}}{\alpha}\int_{Az^{\alpha}}^{\infty} t_3^{\mu-\frac{\psi}{\alpha}-\frac{1}{c\alpha}-1} e^{-t_3} dt_3 = \frac{A^{\frac{\psi}{\alpha}-\mu+\frac{1}{c\alpha}}}{\alpha}\Gamma\left(\mu-\frac{\psi}{\alpha}-\frac{1}{c\alpha}, Az^{\alpha}\right). \tag{4.21}$$

By inserting I_1, I_2, and I_3 into (4.17), the CDF of the joint channel coefficient can be expressed as

$$\begin{aligned} F_{|h^{\mathrm{fp}}|}(z) = \frac{\gamma(\mu, Az^{\alpha})}{\Gamma(\mu)} + \frac{\psi c A^{\frac{\psi}{\alpha}} z^{\psi}}{\Gamma(\mu)}\Gamma\left(\mu-\frac{\psi}{\alpha}, Az^{\alpha}\right) \\ - \frac{\psi^2 c}{\psi+\frac{1}{c}}\frac{A^{\frac{\psi}{\alpha}+\frac{1}{c\alpha}} z^{\psi+\frac{1}{c}}}{\Gamma(\mu)}\Gamma\left(\mu-\frac{\psi}{\alpha}-\frac{1}{c\alpha}, Az^{\alpha}\right). \end{aligned} \tag{4.22}$$

Finally, by substituting (4.22) in (4.15), the outage probability can be obtained.

4.4 Numerical Results

In this section, theoretical findings are validated via Monte-Carlo simulations. Throughout the section, horizontal HAPS-to-HAPS communication scenario at 30 km of altitude is considered based on the International Telecommunication Union Radio Regulations [92]. The distance between transmitter and recevier HAPS systems is taken as $d = 10$ km.[8] For such a setup, the fading parameters are assumed as $\alpha = 6$ and $\mu = 4$. Additionally, carrier frequency is set to 300 GHz. The absorption loss is evaluated as shown in [13] for dry standard atmospheric conditions specified in [73], and it is found as $L^{\mathrm{abs}} = 8.74\times10^{-5}$ dB. The noise power is given as $\sigma_n^2 = -80$ dBm. Moreover, it is considered that an array of horn antennas ($\theta_{\mathrm{e,3dB}} = 22^\circ$ and $G^{\mathrm{q}}_{\mathrm{e,max}} = 17$ dBi [98]) are used at both transmitter and receiver. To run the simulations 10^4 independent random variables (θ_{qx}, θ_{qy}, and $\theta_{\mathrm{q}} = \tan^{-1}\left(\sqrt{\tan^2\theta_{\mathrm{qx}}+\tan^2\theta_{\mathrm{qy}}}\right)$ for $\mathrm{q}\in\{\mathrm{t},\mathrm{r}\}$) are generated for each 10^3 Monte-Carlo runs. Then, the pointing error coefficient is generated for each run by substituting the random variable $\theta_{\mathrm{tr}}^2 = \theta_{\mathrm{t}}^2+\theta_{\mathrm{r}}^2$ in $h^{\mathrm{p}} = \exp\left(-\frac{\theta_{\mathrm{tr}}^2}{2\sigma^2}\right)$.

In Fig. 4.2a, the PDF of h^{p} is illustrated for different values of σ_θ and N. Here, horn antenna ($\theta_{\mathrm{e,3dB}} = 22^\circ$ and $G^{\mathrm{q}}_{\mathrm{e,max}} = 17$ dBi [98]) is considered with element spacing

[8] The link distance of $d = 10$ km can be realized in mmWave/THz communications by utilizing very high-gain antenna arrays.

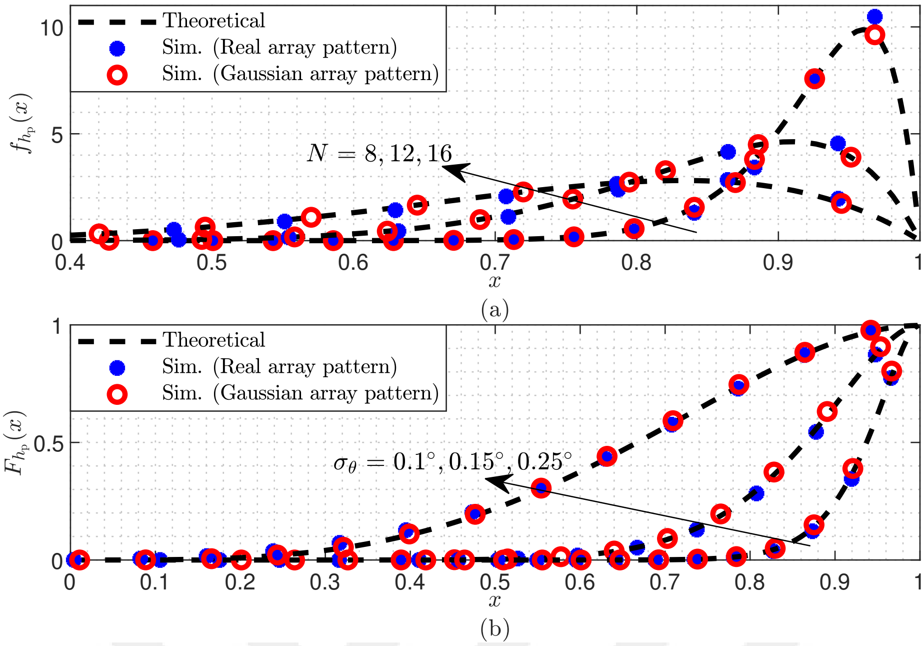

Figure 4.2 : (a) The PDF of h^{p} for $\sigma_\theta = 0.15°$ and $N = 8, 12, 16$. (b) The CDF of h^{p} for $N = 12$ and $\sigma_\theta = 0.1°, 0.15°, 0.25°$.

$d_{\mathrm{x}} = d_{\mathrm{y}} = 5\lambda$. It is shown that the PDF obtained by the Gaussian approximation is well-matched with the simulation PDF obtained by the real array pattern. It is observed from Fig. 4.2a that as the array size increase, the PDF widens, resulting in more severe pointing error. This stems from radiated beam getting narrower for larger arrays (see Fig. 4.1a), making the system more susceptible to antenna misalignment. The CDF of h^{p} is shown in Fig. 4.2b. It can be seen from Fig. 4.2b that higher σ_θ results in more significant pointing error effect as expected.

In Fig. 4.3, outage probability curves are presented for $N = 12$ and different values of element spacing $d_{\mathrm{e}} = d_{\mathrm{x}} = d_{\mathrm{y}}$ and orientation fluctuation standard deviation σ_θ. In Fig. 4.3a, fixed $\sigma_\theta = 0.12°$ is used, and the outage performance is illustrated for $d_{\mathrm{e}} = 0.5\lambda, 4\lambda, 5\lambda$. It can be observed here that as the element spacing increase, system performance degrades. More specifically, ~ 3 dBm power loss is observed at 10^{-6} outage rate when the element spacing is increased from $d_{\mathrm{e}} = 0.5\lambda$ (as modeled in [85] and [86]) to $d_{\mathrm{e}} = 5\lambda$. This performance loss originates from the fact that as the element spacing increases, the radiated beam gets narrower (see Fig. 4.1b), making the system more susceptible to the same level of orientation fluctuation. It is a very critical deduction presented in this chapter that the array design has a significant impact on

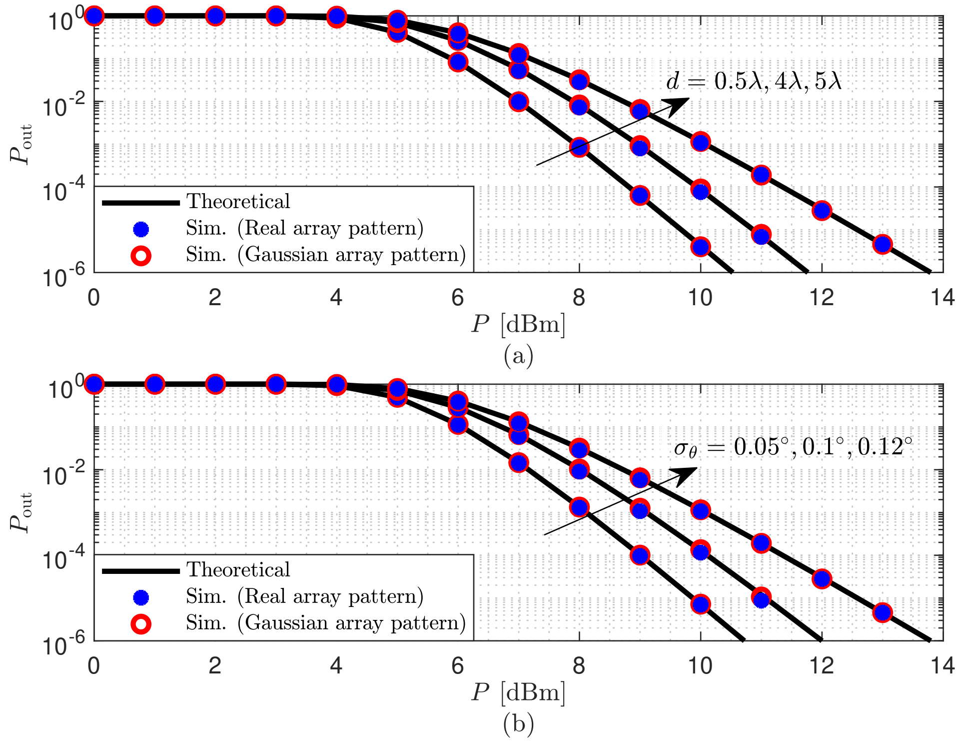

Figure 4.3 : Outage probability curves for $N = 12$, (a) $\sigma_\theta = 0.12°$ and $d_{\rm e} = 0.5\lambda, 4\lambda, 5\lambda$ (b) $\sigma_\theta = 0.05°, 0.1°, 0.12°$ and $d_{\rm e} = 5\lambda$.

the system performance through pointing errors. Furthermore, in Fig. 4.3b, outage curves are shown for $d_{\rm e} = 5\lambda$ and $\sigma_\theta = 0.05°, 0.1°, 0.12°$. It can be inferred that higher jitter variance causes higher misalignment angles, reducing the received power, thus, degrading the system performance. However, it can be understood from the figure that σ_θ has the same level of importance as the array design (through element spacing), which is captured by the developed theoretical model, emphasizing the contribution of this study.

4.5 Concluding Remarks

In this chapter, a simple analytical pointing error model for mmWave and THz communications is presented by accounting for the antenna and array design criteria. To accomplish this, the main lobe of the array is modeled by using the Gaussian beam approximation for both the array factor and the radiated beam from an antenna array element, which is verified by EM simulations in CST Microwave Studio. Once the main lobe of the array is modeled, the statistics of the pointing error are derived, showing that the pointing error follows a special case of the negative log-Gamma distribution with the shape parameter of 2 and the scale parameter depending on the 3 dB beamwidth of the array factor, antenna element radiation pattern, and jitters variance. The validity of the presented model is confirmed via computer simulations. It is demonstrated that both antenna and array designs significantly impact the radiated beam, thus, the pointing error characteristics. The outage performance of an aerial communication scenario is analyzed to examine the effects of pointing error. The results have shown that larger element spacing produces narrower beams, and the system becomes more susceptible to pointing errors. Hence, the antenna and array design parameters are as influential as the standard deviation of the orientation fluctuations.

5. LINK BUDGET ANALYSIS FOR NTNs IN THE THz BAND

In the previous chapters, the primary considerations in THz communications are introduced and discussed in detail. Before delving deeper into the statistical performance analyses for THz NTNs, it is crucial to assess the feasibility of utilizing THz frequencies in the NTN architecture. The high level of losses caused by the very long link distances, atmospheric conditions, weather events, etc. should be addressed to account for the various real-world scenarios. Several works can be found in the literature that analyzes the link performance of THz ground-satellite communications [38] and inter-satellite THz communications [39, 40]. However, the link analysis of the whole NTN architecture operating in mmWave/THz band remains unexplored in the current literature. Therefore, in this chapter, the achievable data rate in uplink/downlink communications between ground, aerial, satellite nodes are analyzed by taking the free-space loss, atmospheric absorption loss, weather-dependent losses, ionospheric effects, and additional losses caused by polarization mismatch between antennas and feeder equipment.[1] Moreover, the varying characteristics of the noise in uplink/downlink communications, the impacts of fading and pointing errors, antenna gain and aperture are considered during the analysis.

5.1 Main Channel Effects and Transceiver Requirements

To analyze the feasibility of mmWave/THz NTNs, the main channel effects should be modeled by accounting for the varying characteristics of the transmission medium with respect to altitude, atmospheric conditions, and weather events. In the following, the large-scale channel effects, such as the free-space loss, atmospheric absorption loss, attenuation due to weather conditions, ionospheric effects, polarization mismatch

[1]The work presented in this chapter is submitted to *IEEE Transactions on Vehicular Technology*.

between antennas, and feeder losses, as well as the small-scale channel effects, such as the fading and pointing errors, are presented.

5.1.1 Free-space loss

Once the EM wave is transmitted from an antenna, the transmitted power is distributed on a sphere. The power intensity on a unit area on this sphere decreases as the EM wave propagates. Thus, for a fixed receiver aperture, the received power reduces for larger link distances. This phenomenon is called the free-space loss or spreading loss, and it has a well-known mathematical model given by the Friis formula as [66, Sec. 2.17.1]

$$L^{\mathrm{fsl}} = \left(\frac{4\pi d}{\lambda}\right)^2, \tag{5.1}$$

where d and λ are the link distance and the operating wavelength, respectively. Here, it can be seen that the free-space loss increases quadratically as the operating wavelength gets smaller or the transmission distance gets larger.

5.1.2 Atmospheric absorption loss

At high frequencies, the EM wave interacts with the absorber particles in the transmission medium, leading to molecular absorption loss. In NTNs, the transmission medium is the atmosphere which contains the oxygen molecules and water vapour as the principal absorbers. The specific attenuation due to absorption up to 1000 GHz is given as [13]

$$\varphi^{\mathrm{abs}} = 0.182 f_{\mathrm{GHz}} \left(N''_{\mathrm{oxy}}(f_{\mathrm{GHz}}) + N''_{\mathrm{wv}}(f_{\mathrm{GHz}})\right) \quad \text{[dB/km]}, \tag{5.2}$$

where f_{GHz} is the operating frequency in GHz. Moreover, $N''_{\mathrm{oxy}}(f_{\mathrm{GHz}})$ and $N''_{\mathrm{wv}}(f_{\mathrm{GHz}})$ are the imaginary parts of the frequency-dependent complex refractivities of the oxygen molecules and water vapour in the atmosphere, respectively [13]. In this formulation, $N''_{\mathrm{oxy}}(f_{\mathrm{GHz}})$ and $N''_{\mathrm{wv}}(f_{\mathrm{GHz}})$ are related to the atmospheric parameters, such as pressure, humidity level, and temperature which can be found in [73] or can be extracted from the local data if available. Since the densities of the absorber particles

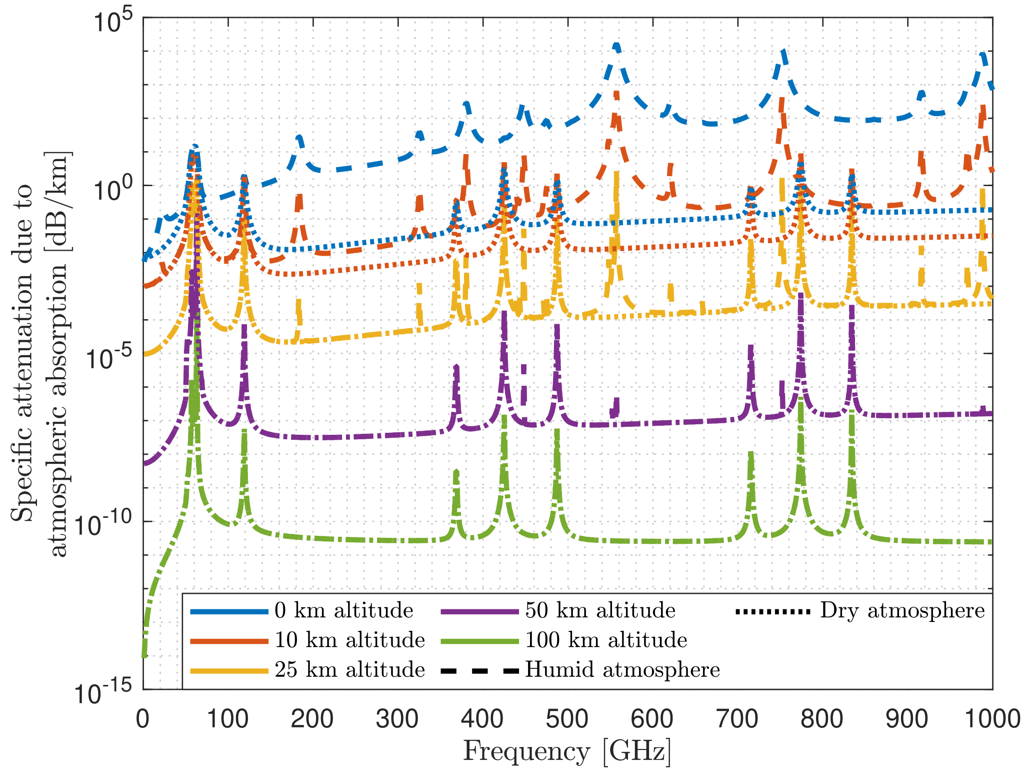

Figure 5.1 : Specific attenuation due to absorption at different altitudes for dry and humid standard atmospheric conditions.

are constant along horizontal paths, the atmospheric absorption loss is obtained by

$$L^{\text{abs}} = \varphi^{\text{abs}} d \quad [\text{dB}]. \tag{5.3}$$

On the other hand, for slant paths, the densities of the absorber particles vary along the propagation path. Thus, the atmospheric absorption loss can be approximately computed by dividing the atmosphere into exponentially increasing layers as

$$L^{\text{abs}} = \sum_{i=i_{\text{lower}}}^{i_{\text{upper}}} \varphi_i^{\text{abs}} d_i \quad [\text{dB}], \tag{5.4}$$

where i_{lower} and i_{upper} are the indexes of the lowest and the uppermost layers of the atmosphere in which the transmitter and receiver are located. Furthermore, φ_i^{abs} and d_i are the corresponding specific attenuation [dB/km] and the path length [km] of the i-th layer, respectively. Please refer to [13] for the detailed calculation of φ_i^{abs} and d_i.

In Fig. 5.1, the specific attenuation at different altitudes are shown for dry and humid standard atmospheric conditions [73]. As observed, the atmosphere introduces absorption peaks at certain frequencies, permitting signal transmission only within the communication windows between these peak values. Moreover, significant difference is observed in the specific attenuation values under dry and humid atmospheric conditions at lower altitudes, which stems from the fact that the oxygen molecules and water vapour lie mostly in the lowest layers of the atmosphere, leading to increased absorption loss in humid air. At higher altitudes, the curves for dry and humid atmospheric conditions get closer to each other. Furthermore, it can be deduced that some absorption peaks disappear at higher altitudes, e.g. at 183 GHz, 325 GHz, 557 GHz, 916 GHz, enabling larger transmission windows. Additionally, it can be inferred from the figure that the absorption loss is negligible at high altitudes, which makes the mmWave/THz transmission feasible for NTNs, especially in inter-satellite, inter-aerial, and aerial-to-satellite links.

5.1.3 Loss due to weather conditions

In addition to the free-space loss and atmospheric absorption loss, the performance of mmWave and THz communications can be degraded by the adverse weather conditions in the lower layers of the atmosphere, such as rain, clouds, and fog formations, because of the increased density of the absorber particles.

In the presence of rain, the specific attenuation due to rain is written as $\varphi^{\mathrm{rain}} = k_{\mathrm{rain}}\mathcal{R}^{\rho_{\mathrm{rain}}}$ [dB/km], where $k_{\mathrm{rain}} \in \{k_{\mathrm{H}}, k_{\mathrm{V}}, k_{\mathrm{C}}\}$ and $\rho_{\mathrm{rain}} \in \{\rho_{\mathrm{H}}, \rho_{\mathrm{V}}, \rho_{\mathrm{C}}\}$ are frequency-dependent constants which can be found in [76]. Here, k_{H} and ρ_{H} stand for the constants for horizontal polarization, whereas k_{V} and ρ_{V} denote the constants for vertical polarization. For circular polarization, k_{C} and ρ_{C} are given as [76]

$$\begin{aligned} k_{\mathrm{C}} &= \frac{k_{\mathrm{H}} + k_{\mathrm{V}} + (k_{\mathrm{H}} - k_{\mathrm{V}})\cos^2\theta\cos 2\varpi}{2}, \\ \rho_{\mathrm{C}} &= \frac{k_{\mathrm{H}}\rho_{\mathrm{H}} + k_{\mathrm{V}}\rho_{\mathrm{V}} + (k_{\mathrm{H}}\rho_{\mathrm{H}} - k_{\mathrm{V}}\rho_{\mathrm{V}})\cos^2\theta\cos 2\varpi}{2k_{\mathrm{C}}}, \end{aligned} \tag{5.5}$$

where ϖ is the polarization tilt angle ($\varpi = 45^\circ$ for circular polarization). By using the specific attenuation, the total attenuation due to rain can be found by $L^{\mathrm{rain}} = \varphi^{\mathrm{rain}} d_{\mathrm{eff}}$, where d_{eff} is the effective path length under rainy weather conditions.

In the presence of cloud/fog formations, the attenuation can be found by $L^{\mathrm{cf}} = \frac{\mathcal{K}_{\mathrm{cf}}\mathcal{W}_{\mathrm{cf}}}{\sin\theta}$ [dB] up to 200 GHz, where $\mathcal{W}_{\mathrm{cf}}$ [kg/m^2] is the integrated liquid water content, and θ is the elevation angle. Here, the cloud liquid mass absorption coefficient $\mathcal{K}_{\mathrm{cf}}$ is defined as

$$\mathcal{K}_{\mathrm{cf}} = \mathcal{K}'_{\mathrm{cf}}\left(0.1522e^{-\frac{(f_{\mathrm{GHz}}-f_1)^2}{\sigma_1}} + 11.51e^{-\frac{(f_{\mathrm{GHz}}-f_2)^2}{\sigma_2}} - 10.4912\right), \tag{5.6}$$

where $f_1 = -23.9589$, $f_2 = 219.2096$, $\sigma_1 = 3.2991\times 10^3$, $\sigma_2 = 2.7595\times 10^6$, and $\mathcal{K}'_{\mathrm{cf}} = \frac{0.819 f_{\mathrm{GHz}}}{\varepsilon''(1+\eta^2)}$ [77]. In this formulation, ε'' and ε' are given as

$$\begin{aligned}\varepsilon'' &= \frac{f_{\mathrm{GHz}}(\varepsilon_0-\varepsilon_1)}{f_{\mathrm{p}}\left[1+(f_{\mathrm{GHz}}/f_{\mathrm{p}})^2\right]} + \frac{f_{\mathrm{GHz}}(\varepsilon_1-\varepsilon_2)}{f_{\mathrm{s}}\left[1+(f_{\mathrm{GHz}}/f_{\mathrm{s}})^2\right]},\\ \varepsilon' &= \frac{\varepsilon_0-\varepsilon_1}{\left[1+(f_{\mathrm{GHz}}/f_{\mathrm{p}})^2\right]} + \frac{\varepsilon_1-\varepsilon_2}{\left[1+(f_{\mathrm{GHz}}/f_{\mathrm{s}})^2\right]} + \varepsilon_2,\end{aligned} \tag{5.7}$$

where $\varepsilon_0 = 77.66 + 103.3\left(\frac{300}{T}-1\right)$, $\varepsilon_1 = 0.0671\varepsilon_0$, $\varepsilon_2 = 3.52$, $f_{\mathrm{p}} = 20.20 - 146\left(\frac{300}{T}-1\right) + 316\left(\frac{300}{T}-1\right)^2$, $f_{\mathrm{s}} = 39.8 f_{\mathrm{p}}$, and $T = 273.75$ K [77]. By taking both attenuation due to rain and cloud/fog formations into account, the loss factor due to weather conditions can be written as $L^{\mathrm{wea}} = L^{\mathrm{rain}}L^{\mathrm{cf}}$.

In Fig. 5.2a, the specific attenuation due to rain is illustrated from 1 GHz to 1000 GHz for horizontal, vertical, and circular polarizations under several rainfall rates. At frequencies below 10 GHz, the impact of rain on signal attenuation is minimal. However, as the frequency increases, significant attenuation becomes noticeable reaching its peak at 100 GHz. In addition, it is inferred from the figure that attenuation is almost the same for different polarizations over the whole frequency range. In Fig. 5.2b, attenuation due to cloud/fog formations is shown for different integrated cloud liquid water content levels. As can be seen, higher liquid water content levels lead to severe attenuation. At 200 GHz operating frequency, very dense cloud/fog concentration $\left(\mathcal{W}_{\mathrm{cf}} = 25\ \mathrm{kg/m^2}\right)$ results in ~ 35 dB attenuation, which dramatically reduces the received power. Since both rain and cloud/fog formations are observed at lower altitudes up to a few km above ground, it can be concluded that the communication links between ground and aerial nodes, as well as those between ground and satellites, are prone to adverse weather conditions.

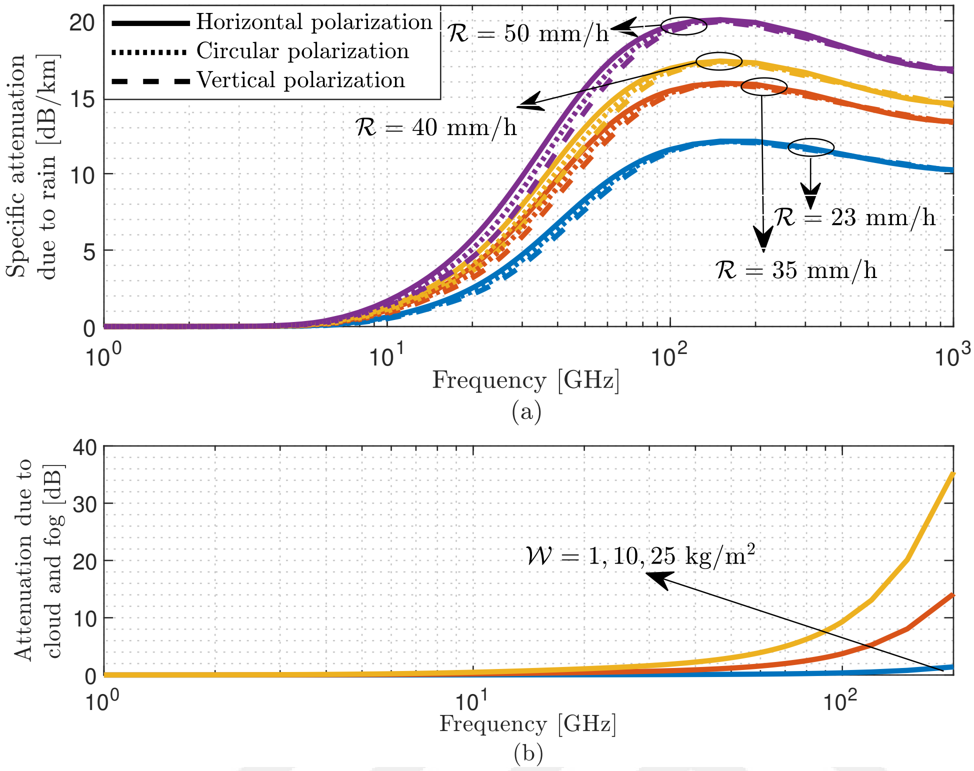

Figure 5.2 : (a) Specific attenuation due to rain for different rainfall rates. (b) Attenuation due to cloud/fog for different integrated cloud liquid water content levels and $90°$ elevation angle.

5.1.4 Ionospheric effects

The THz transmission is also affected by the ions and charged particles in the ionosphere. Three metrics can be used to describe the ionospheric effects, namely, plasma frequency, collision frequency, and depolarization due to the Faraday rotation [40]. The EM waves lead free electrons and ions to oscillate while propagating through plasma. At very high frequencies, the impact of plasma frequency diminishes, which can be interpreted as the free electrons and ions falling short compared to the frequency of the EM wave [40]. In addition to the above-given metrics, the collisions among charged particles, ions, electrons, and neutral particles may cause attenuation. Moreover, the total electron content along the transmission path leads the polarization of the EM wave to rotate [100]. These effects might be more significant especially in polar caps and when the auroras are observed. Fortunately, the loss and depolarization due to the ionosphere reduces quadratically as the frequency increases [100, Table 3], and they are negligible above 10 GHz [101, Table 1]. Since the objective of this work is to analyze the link performance of mmWave/THz NTNs, which operate above 30 GHz, the ionospheric effects are neglected.

5.1.5 Additional loss factors

Apart from the signal attenuation as described in the previous subsections, communication links in NTNs may also suffer from other losses due to polarization mismatch between antennas, feeder losses etc. The polarization mismatch occurs when the transmitter and receiver antennas do not have the same polarization, which inevitably reduce the received signal power. Moreover, the feeder loss may arise from the cables, connectors, and impedance mismatch between the connected components. In order to take these factors into account, L^{add} is taken into consideration in the link budget analysis with typical values ranging between 1-3 dB [102].

5.1.6 Antenna requirements

As explained so far, several attenuation factors are present in mmWave/THz communications, reducing the received power and degrading the performance. To compensate for the excessive loss levels, highly directional arrays are employed. By utilizing antenna arrays, higher gains at both the transmitter (t) and receiver (r) can be achieved, enabling long range links. Denoting the largest dimension of the antenna array by ℓ, the maximum gain of antenna array can be written as [66, Eq. (6.106)]

$$\mathcal{G}^{\mathrm{q}} = 4\pi \frac{\ell^2}{\lambda^2}, \quad \mathrm{q} \in \{\mathrm{t}, \mathrm{r}\}. \tag{5.8}$$

It can be inferred from the above-equation that the maximum antenna gains at both the transmitter and receiver can be increased proportionally to the square of the decreasing wavelength by keeping the physical size of the array fixed. Thus, the losses caused by spreading, atmospheric absorption, and adverse weather conditions can be tolerated.

5.1.7 Fading and pointing error

Besides loss factors, wireless channels experience rapid fluctuations in the received signal's amplitude, referred to as the small-scale effects, which can be decomposed as multipath fading and pointing errors. In mmWave/THz frequencies, fading primarily emerges from scattering due to the aerosols present in the transmission medium. This results in multipath components of significant power being detected by the receiver even if they arrive from NLOS directions. In addition to the multipath fading, the misalignment between the transmitter and receiver antennas can lead to small-scale variations, which originates from the utilization of highly directional antennas/arrays to combat with the excessive loss levels in mmWave/THz communications. Since these antennas/arrays employ pencil-sharp beams, they are very susceptible to imperfect alignment caused by the relative movements of the communicating nodes and/or the antenna jitters, leading to a reduction in the received power also known as pointing error. In the link budget calculation, these effects can be incorporated by defining a link margin L^{mar} with commonly adopted values ranging from 1 to 5 dB [18].

By taking the free-space loss, atmospheric absorption loss, weather-dependent losses, polarization mismatch, feeder losses, antenna gains, and link margin into consideration, the received power can be evaluated for a wide range of communication scenarios. To find the achievable data rate, the noise characteristics should also be modeled properly, which is elaborated in the next section.

5.2 Noise Characteristics and Achievable Data Rate

5.2.1 Noise characteristics

In most of the existing studies, the noise observed at the receiver is modeled as a thermal noise. However, in mmWave/THz bands, the noise characteristics differ from the thermal noise model because of the cosmic microwave brightness temperature, the microwave brightness temperature of the Earth, and attenuation due to atmospheric absorption. As a result, uplink and downlink communication links exhibit distinct noise profiles [13]. Specifically, downlink communications (e.g. aerial-to-ground, satellite-to-ground, satellite-to-aerial, links) are affected by the downwelling brightness temperature, while uplink communications (e.g. ground-to-aerial,ground-to-satellite, aerial-to-satellite links) are influenced by the upwelling brightness temperature. The downwelling brightness temperature $T_{\mathrm{Br,down}}$ is the sum of cosmic microwave brightness temperature attenuated by the atmospheric absorption and downwelling atmospheric microwave brightness temperature [13, Sec. 4.1]. On the contrary, the upwelling brightness temperature $T_{\mathrm{Br,up}}$ is slightly different as it consists of the upwelling atmospheric microwave brightness temperature, the downwelling atmospheric microwave brightness temperature reflected by the Earth's surface attenuated by the net atmospheric absorption, and upwelling microwave brightness temperature of the Earth's surface attenuated by the atmospheric absorption [13, Sec. 4.2]. Once the brightness temperature is calculated as shown in [13], the single-sided noise power spectral density can be written as

$$S_n = k_{\mathrm{B}}(T_0 + T_{\mathrm{Br}}), \tag{5.9}$$

where T_0 is the receiver thermal noise temperature and k_{B} represents the Boltzmann's constant. Here, $T_{\mathrm{Br}} = T_{\mathrm{Br,down}}$ for downlink and $T_{\mathrm{Br}} = T_{\mathrm{Br,up}}$ for uplink communications. In Fig. 5.3, the brightness temperature and the single-sided noise power spectral density are illustrated for $T_0 = 300$ K for a link between 0 km and 100 km altitudes with zenith angle of 0° under humid atmospheric conditions. It can be deduced from the figure that the brightness temperature varies with operating frequency due to the frequency selectivity of the absorption affected on the cosmic microwave brightness temperature and the brightness temperature of the Earth's surface. Thus, the noise power is non-white. For the analysis, it is assumed that the system bandwidth, denoted as W, is divided into small sub-bands of width ΔW and that the noise power spectral density is constant within each sub-band. Hence, the noise power observed in each sub-band can be expressed as [38]

$$P_{n,l} = k_{\mathrm{B}}(T_0 + T_{\mathrm{Br}})\Delta W \mathcal{F}_n, \tag{5.10}$$

where $\mathcal{F}_n$ is the receiver's noise figure and l is the sub-band index. Throughout this work, $\Delta W = 100$ MHz is considered. After obtaining the noise power in uplink/downlink communications, achievable data rate can be found for various communication scenarios in mmWave/THz NTNs.

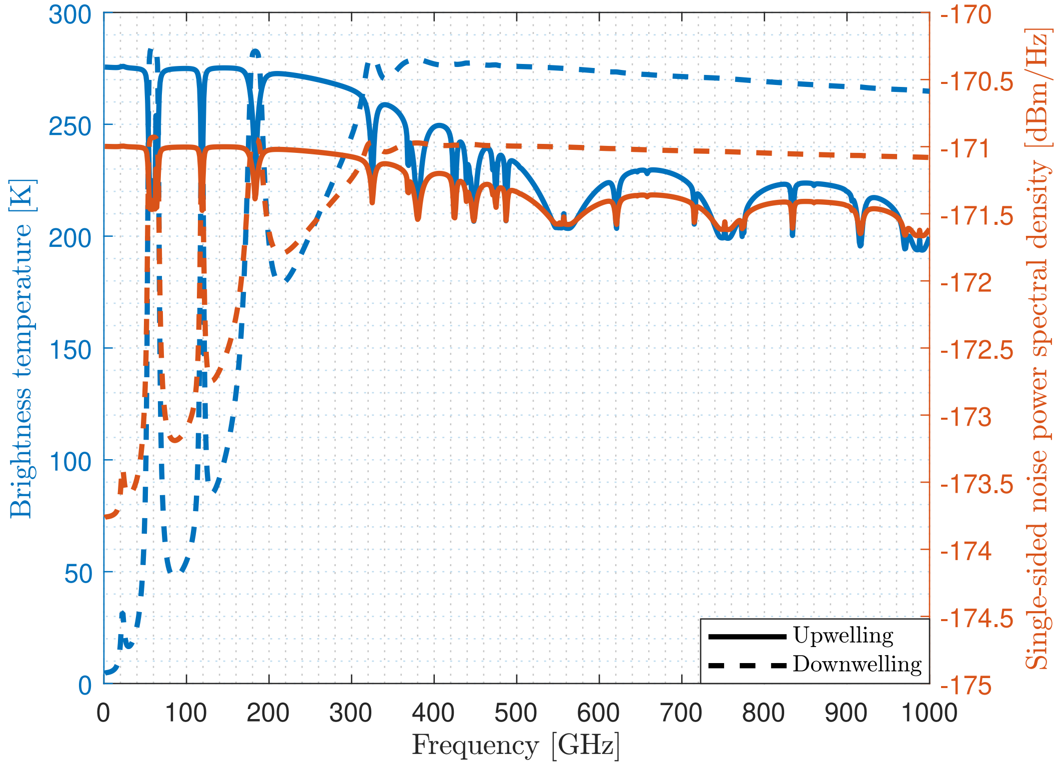

Figure 5.3 : Upwelling and downwelling brightness temperatures and the single-sided noise power spectral density for a link between 0 km and 100 km altitudes with 0° zenith angle.

5.2.2 Received power and achievable data rate

Recalling that the system bandwidth is divided into small sub-bands of width ΔW, the received power in each sub-band is evaluated as

$$P_{\mathrm{r},l} = \frac{P_{\mathrm{t},l}\mathcal{G}^{\mathrm{t}}\mathcal{G}^{\mathrm{r}}}{L_l^{\mathrm{tot}}}, \tag{5.11}$$

where $P_{\mathrm{t},l}$ is the transmit power of the l-th sub-band, and it is assumed that P_{t} is equally divided across each sub-band. In this formulation, the total loss $L_l^{\mathrm{tot}} = L_l^{\mathrm{fsl}} L_l^{\mathrm{abs}} L_l^{\mathrm{wea}} L_l^{\mathrm{add}} L_l^{\mathrm{mar}}$ is calculated for the center frequency of the l-th sub-band as shown in Section 5.1. Therefore, the achievable data rate can be expressed as the sum of data rates in each sub-band as

$$C = \sum_l \Delta W \log_2\left(1 + \frac{P_{\mathrm{r},l}}{P_{n,l}}\right) = \sum_l \Delta W \log_2\left(1 + \frac{P_{\mathrm{t},l}\mathcal{G}^{\mathrm{t}}\mathcal{G}^{\mathrm{r}}}{L_l^{\mathrm{fsl}} L_l^{\mathrm{abs}} L_l^{\mathrm{wea}} L_l^{\mathrm{add}} L_l^{\mathrm{mar}} P_{n,l}}\right). \tag{5.12}$$

Based on the above-equation, all possible inter-layer and intra-layer communication scenarios in mmWave/THz NTNs can be analyzed in terms of the achievable data rate.

5.3 Numerical Results

In this section, the feasibility assessment of the mmWave/THz NTNs is performed by considering the achievable data rates in inter- and intra-layer communication scenarios. The altitudes of the ground, aerial, and satellite nodes are assumed as 0 km, 30 km, and 700 km above mean sea level, respectively. Unless otherwise stated, 0° zenith angle (or equivalently 90° elevation angle) is considered for all inter-layer communication links, and identical antennas/arrays are used at the transmitter and receiver of each link. Moreover, the transmission bandwidth is taken as the 2% of the operating frequency. Furthermore, relying on the most recent advances in the mmWave and THz electronics, the transmit power of $P_{\mathrm{t}} = 20$ dBm ([103–105] and references therein) and noise figure of $\mathcal{F}_n = 10$ dB ([106–108] and references therein) are considered. In addition, $L^{\mathrm{mar}} = 6$ dB and $L^{\mathrm{add}} = 3$ dB are included in the analysis, where the former accounts for the fading and pointing errors, and the latter is related with additional loss factors, such as polarization mismatch and feeder losses.

In Fig. 5.4, the achievable data rate is illustrated up to 1 THz for a ground-to-satellite link under dry/humid atmospheric conditions. Here, fixed physical aperture (25×25 cm^2) and fixed gain (50 dBi) antennas are used. As can be seen, fixed gain antenna outperforms fixed physical aperture antenna below 120 GHz operating frequency. At high frequencies, the achievable data rate for fixed gain antenna tends to reduce, and fixed physical aperture provides enhanced data rates, which originates from the fact that the realized gain increases with the increasing frequency for a fixed physical aperture. Moreover, in dry air, the atmospheric absorption loss levels are significantly lower compared to those in humid air. Thus, fixed physical aperture can tolerate the loss values under dry atmospheric conditions as the operating frequency increases. However, the absorption loss is incredibly high under humid atmospheric conditions due to the increased densities of the absorber particles in the lower layers of the atmosphere. Hence, both fixed physical aperture and fixed gain antennas perform

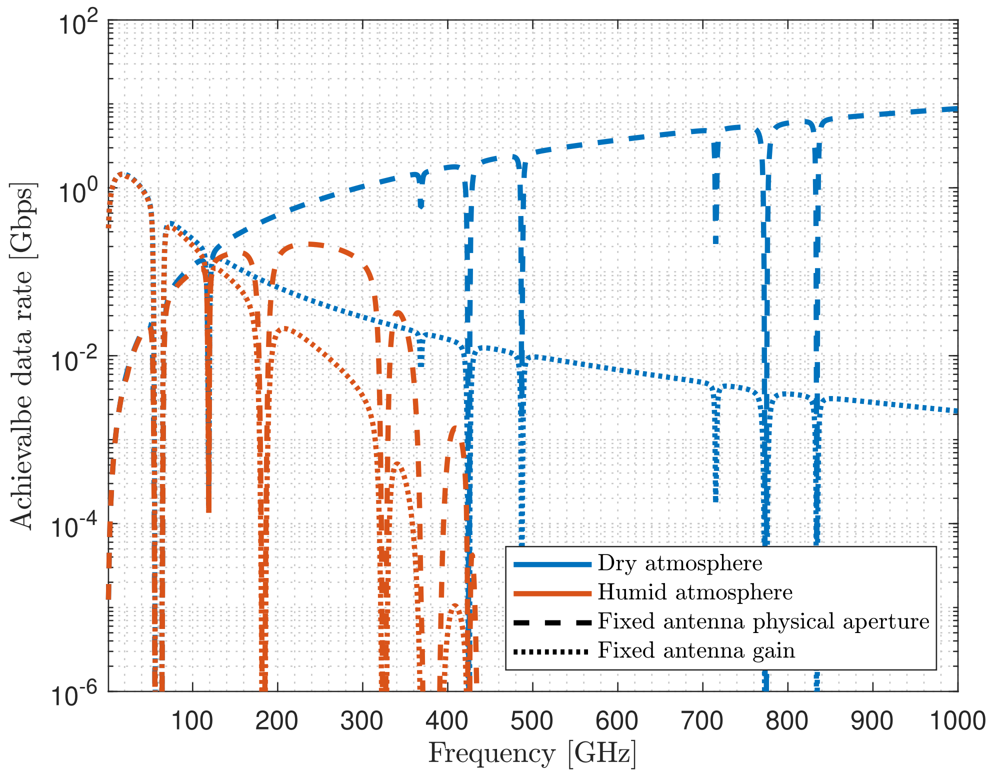

Figure 5.4 : Achievable data rate in ground-to-satellite link for fixed antenna physical aperture (25×25 cm^2) and fixed antenna gain (50 dBi) under dry and humid atmospheric conditions.

poorly above 435 GHz operating frequency in ground-to-satellite links under humid atmospheric conditions.

The achievable date rates in an aerial-to-ground link under humid atmospheric conditions for different antenna physical aperture sizes (5×5 cm^2, 10×10 cm^2, and 25×25 cm^2) and antenna gains (40 dBi, 50 dBi, and 60 dBi) are shown in Fig. 5.5. It can be inferred from the figure that both enlarging the physical aperture and increasing antenna gain improve the system performance. In addition, satisfactory data rates are not achievable above 450 GHz operating frequency, as also observed in Fig. 5.4, even though the aerial-to-ground communication link has much shorter propagation distance. This stems from the severe absorption loss observed due to the dense atmosphere at low altitudes.

The achievable uplink/downlink data rates in ground-aerial, ground-satellite, and aerial-satellite links under humid atmospheric conditions are presented in Fig. 5.6. Here, antennas with fixed physical aperture of 25×25 cm^2 are considered. It

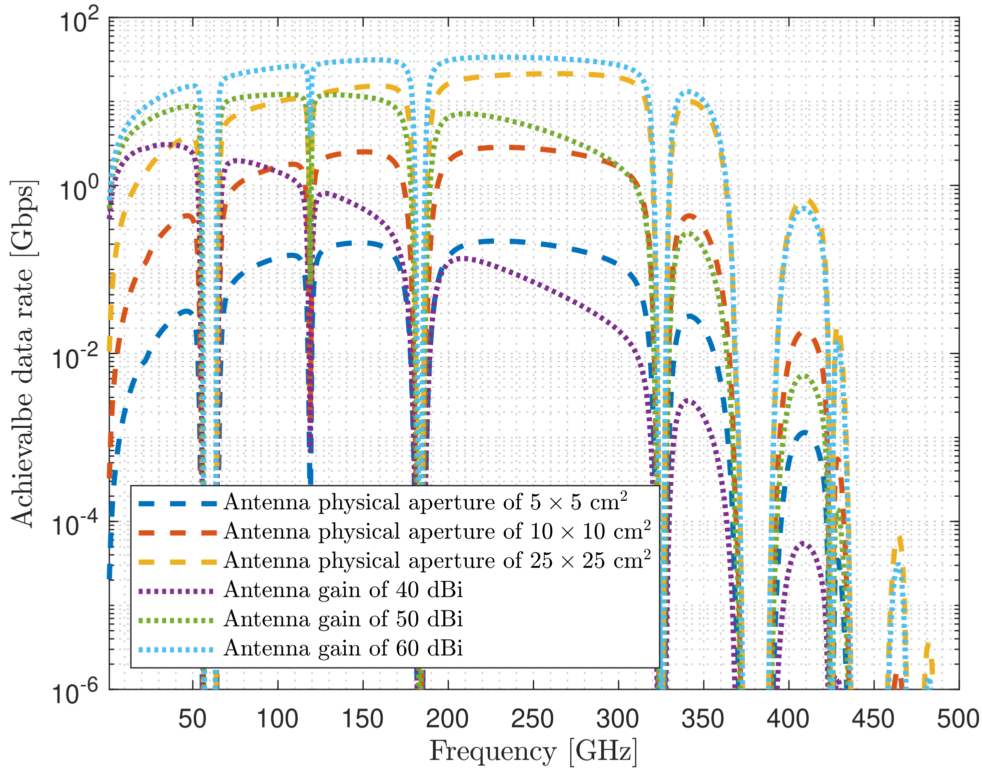

Figure 5.5 : Achievable data rate in aerial-to-ground link for different antenna physical apertures (5×5 cm^2, 10×10 cm^2, and 25×25 cm^2) and gains (40 dBi, 50 dBi, and 60 dBi) under humid atmospheric conditions.

is deduced from the figure that ground-aerial and ground-satellite links experience frequency-selective nature of the atmosphere as the propagating EM waves pass through the lowest layers of the atmosphere in which the absorption occurs frequently. The variation between the curves for ground-aerial and ground-satellite links originates from the longer propagation path and increased free-space loss. On the contrary, aerial-satellite link has negligible frequency selectivity since it is almost unaffected by the absorption owing to the very thin atmosphere above the troposphere. It can be concluded that data rates around 10 Gbps are achievable in both ground-aerial and aerial-satellite links since either the free-space loss or the absorption determines the performance in these links, where ground-satellite link suffers from both the free-space loss and absorption loss. This suggests that the utilization of mmWave/THz frequencies in NTNs can be a strong enabler for future communication systems as it reduces the attenuation owing to the multi-layer structure. Additionally, slight differences are observed between the uplink and downlink curves, which stems from

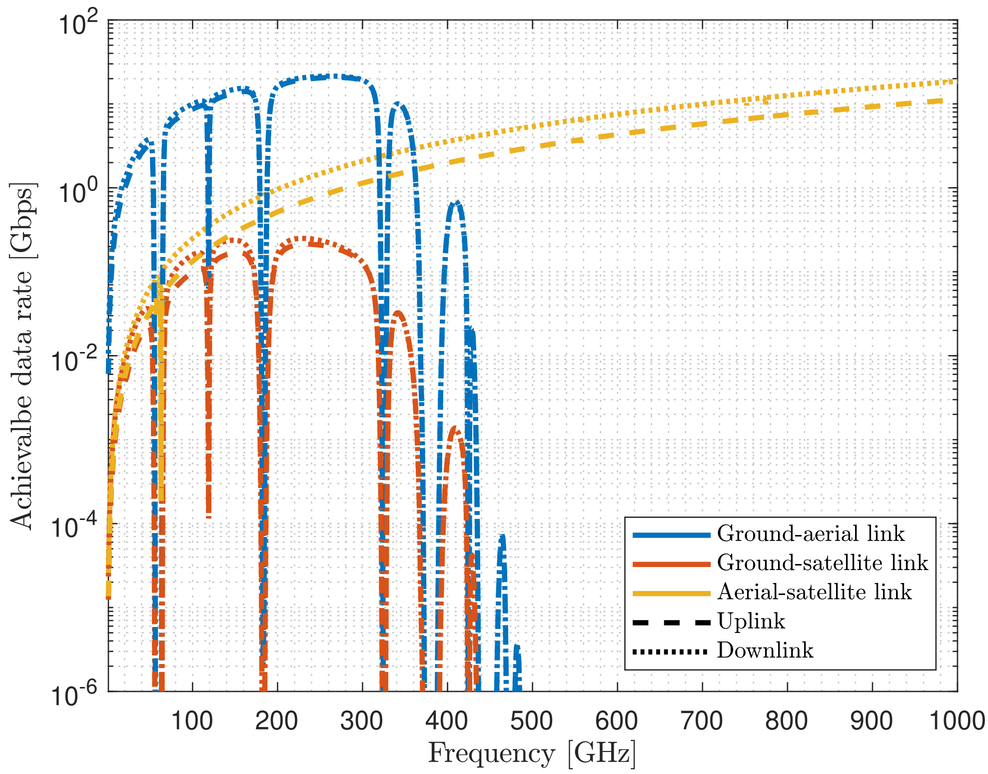

Figure 5.6 : Achievable data rate in uplink/downlink ground-aerial, ground-satellite, aerial-satellite links for fixed antenna physical aperture of 25×25 cm^2.

the disparity between the upwelling and downwelling brightness temperatures (see Fig. 5.3).

In Fig. 5.7, the achievable data rates in intra-layer communication under humid atmospheric conditions are shown with respect to the link distance at operating frequencies 100 GHz and 300 GHz. Here, the transmitter and receiver with fixed physical apertures of 10×10 cm^2 are located at altitudes of 0 km, 0.5 km, 10 km, and 30 km. For link distances up to a few km at lower altitudes, enhanced data rates are achievable at 300 GHz operating frequency owing to wider bandwidth (2% of the operating frequency) and high antenna gain due to fixed physical aperture. However, for larger link distances at lower altitudes, the absorption and free-space loss grow significantly at 300 GHz operating frequency, and the system performance deteriorates. As a result, 100 GHz operating frequency outperforms 300 GHz for longer ranges at low altitudes. On the other hand, at 10 km and 30 km of altitude, 300 GHz operating frequency offers enhanced data rates. This arises from the absorption loss being

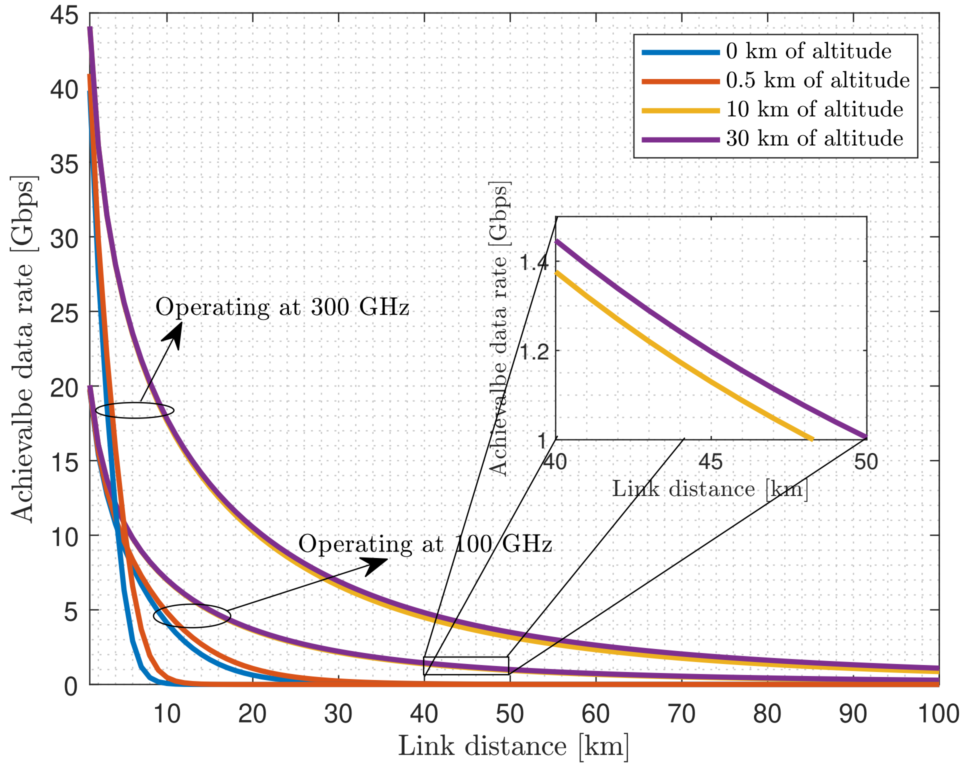

Figure 5.7 : Achievable data rate in intra-layer communication on the ground and aerial altitudes for fixed antenna physical aperture of 10×10 cm^2 under humid atmosphere.

insignificant at higher altitudes (see Fig. 5.1), hence, the free-space loss becomes the only limiting factor, which is compensated for with the fixed physical antenna aperture. Therefore, it can be said that utilizing higher frequencies enhances the achievable data rate in communication links at higher altitudes.

The achievable data rate in an inter-satellite link between two LEO satellites orbiting at 700 km of altitude and equipped with antennas of 25×25 cm^2 physical aperture is shown in Fig. 5.8 for 30 GHz, 100 GHz, 200 GHz, 300 GHz, and 1 THz operating frequencies. It can be observed from the figure that for all operating frequencies, the achievable data rate reduces for longer transmission distance because of the increasing free-space loss. In addition, the achievable data rate significantly enhances for higher operating frequency. This can be attributed to the increasing antenna gain and the wider available bandwidth at higher frequencies. Since the communication is established above 100 km of altitude in inter-satellite links, the atmospheric absorption

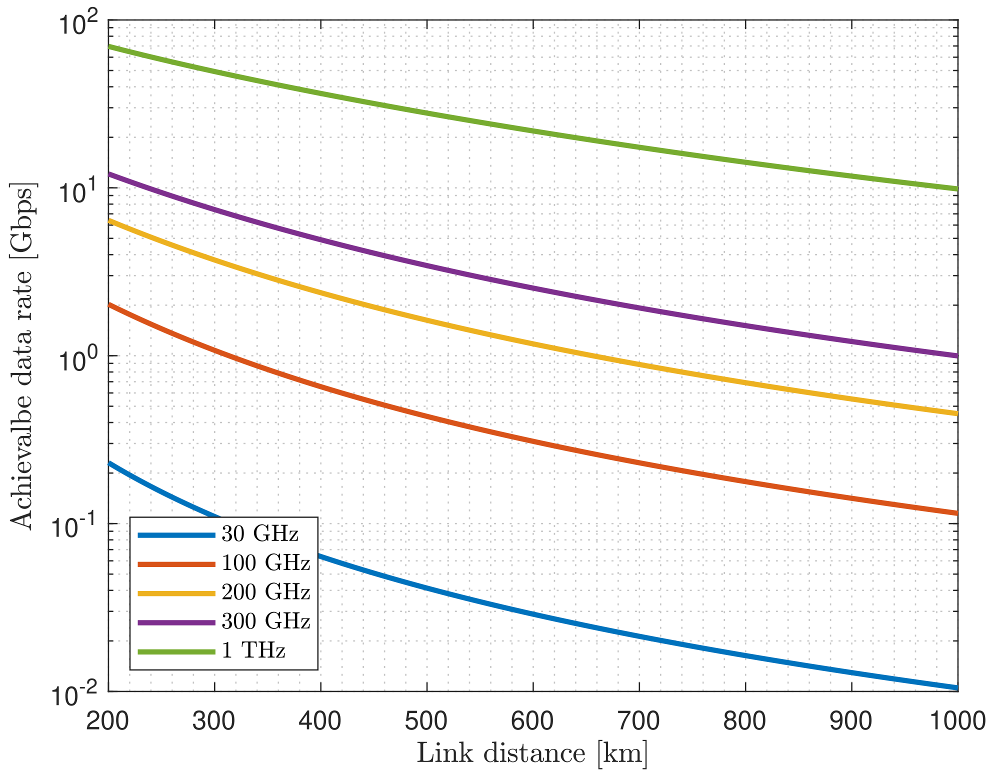

Figure 5.8 : Achievable data rate in inter-satellite link between two LEO satellites equipped with antennas of 25×25 cm^2 physical aperture operating at 30 GHz, 100 GHz, 200 GHz, 300 GHz, and 1 THz operating frequencies.

is negligible (see Fig. 5.1). Here, the dominant loss factor is the free-space loss which can be compensated for by using fixed physical aperture antennas. This allows improved performance in inter-satellite links owing to the utilization of high frequencies.

The achievable data rate in uplink/downlink ground-aerial communications under humid atmosphere are provided in the presence of rain for $\mathcal{R} = 0, 23, 35, 40, 50$ mm/h and $d_{\text{eff}} = 5$ km in Fig. 5.9. In this figure, it is considered that circularly polarized antennas with fixed physical apertures of 25×25 cm^2 are used. As can be inferred, the rainy weather does not have significant impact on the system performance below ~ 6 GHz. As the frequency increases, higher rainfall rate leads to a poorer performance. At some frequencies, the absorption peaks (e.g. at 60 GHz) form transmission windows.[2]

[2]Please note here that the influence of some of the previously observed absorption peaks in the humid atmosphere are not present in Fig. 5.9. This is due to the lack of samples at high frequencies in [76, Table V].

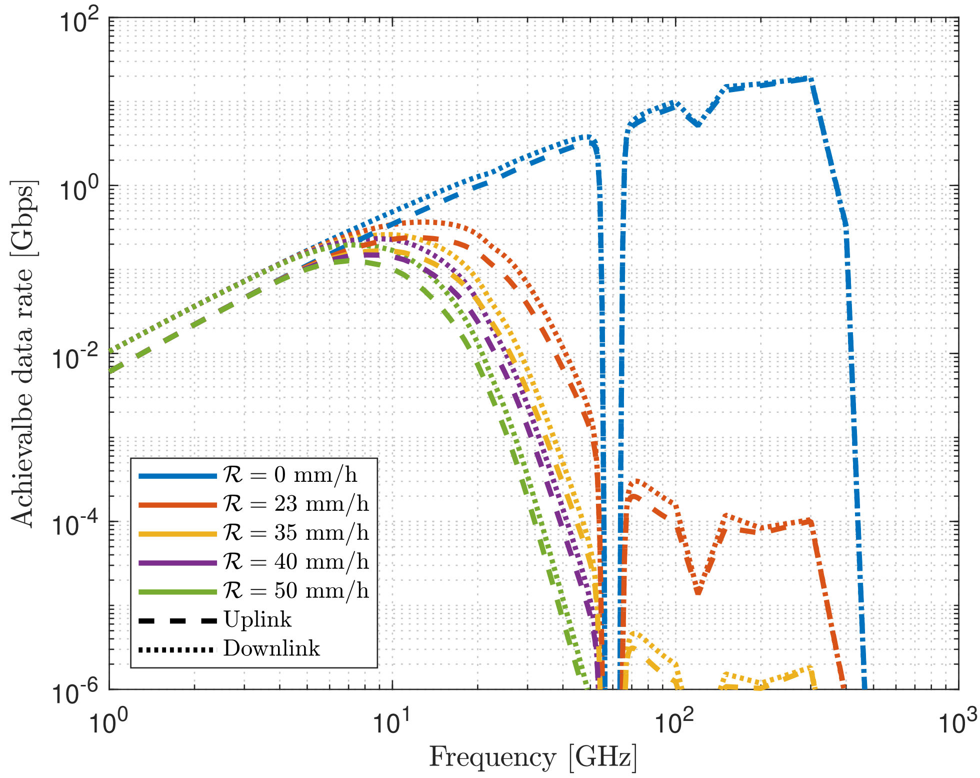

Figure 5.9 : Impact of rainfall rate on the achievable data rate in uplink/downlink ground-aerial communication with $d_{\text{eff}} = 5$ km and circularly polarized antenna of 25×25 cm^2 physical aperture under humid atmosphere.

Furthermore, satisfactory performance cannot be achieved at operating frequencies higher than ~ 400 GHz under rainy weather conditions.

In Fig. 5.10, the impact of cloud/fog on total loss in ground-to-aerial link is presented for elevation angles $\theta = 90°, 30°$ and integrated cloud liquid water contents $\mathcal{W}_{\text{cf}} = 0, 25$ [kg/m^2]. The method in [77] is followed to compute cloud/fog-induced attenuation up to 200 GHz. Several transmission windows are observed due to absorption peaks around 60, 120, and 180 GHz. It can be inferred that higher aerial altitude results in greater total loss due to longer link distance. The curves for $\mathcal{W}_{\text{cf}} = 0$ [kg/m^2] show that loss increases with decreasing elevation angle, caused by longer path length. Moreover, higher integrated liquid water content leads to more severe attenuation. As also shown in Fig. 5.2, $\mathcal{W}_{\text{cf}} = 25$ [kg/m^2] causes ~ 35 dB loss for $\theta = 90°$, increasing up to ~ 70 dB for $\theta = 30°$.

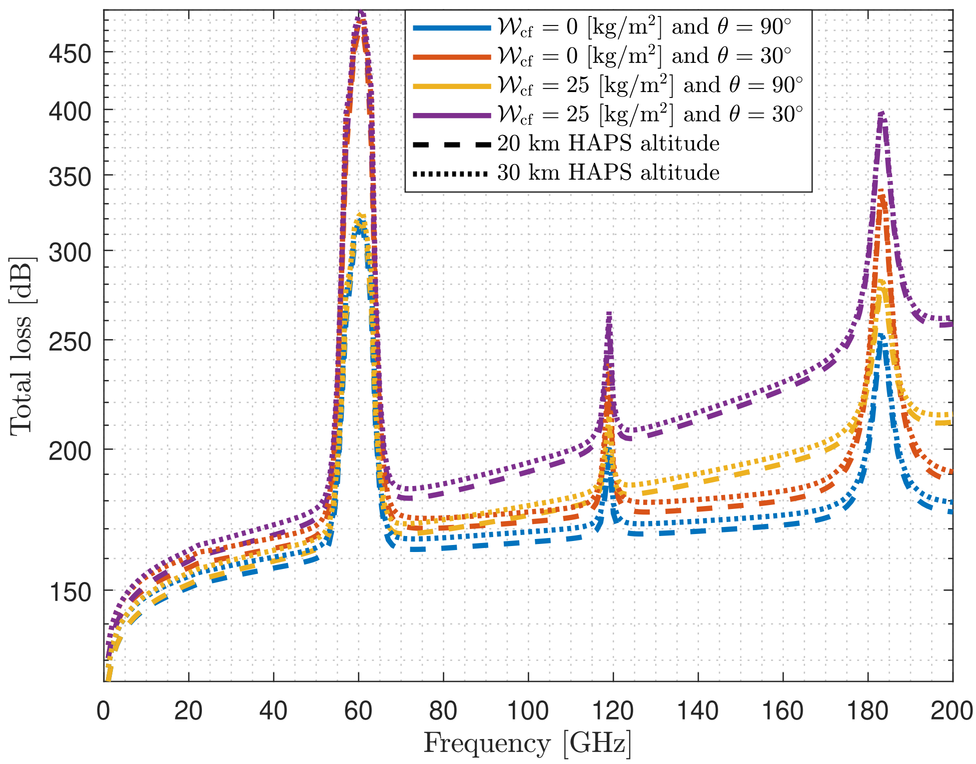

Figure 5.10 : The total loss in ground-to-aerial link for different elevation angles $\theta = 90°, 30°$ and integrated cloud liquid water contents $\mathcal{W}_{cf} = 0, 25$ [kg/m^2].

5.4 Concluding Remarks

In this chapter, the feasibility of utilizing THz frequencies in the NTN architecture is examined by considering the link budget analysis. First, the models for the main channel effects, including the free-space loss, absorption loss, weather-dependent losses, polarization mismatch and feeder losses, fading and pointing errors, are presented. Afterwards, by taking the varying noise characteristics in uplink and downlink communications due the brightness temperature and absorption into consideration, the noise power and the received signal power are found. Based on the aforementioned channel effects and noise characteristics, the achievable data rate is obtained for various communication scenarios within the NTN architecture. The results have shown that high loss levels can be compensated for by using fixed physical aperture antenna under dry atmospheric conditions. In addition, it is illustrated that the absorption and weather events have significant impacts only at low altitudes, making the THz band advantageous especially for the links at higher altitudes. Leveraging the multi-layer structure of the NTN architecture, both the free-space loss values in aerial-satellite links due to long distance and the absorption loss values in ground-aerial links due to denser atmosphere can be tolerated with high-gain directional antennas/arrays, enabling multi-gigabit links while connecting the ground, air, and space as targeted in the next-generation communication systems.

6. INTER-SATELLITE COMMUNICATIONS IN THE THz BAND

As demonstrated in the previous chapter, the THz NTNs have significant potential to provide extreme system capacity on a global scale as required in 6G networks [109]. A key aspect of this architecture is the deployment of satellites at different orbits, such as HEO, GEO, MEO, and LEO [110]. In this context, the inter-satellite communication (ISC) plays an important role in reducing the latency and dependence on the terrestrial infrastructures [111]. In certain scenarios where the direct connection between two LEO satellites cannot be provided, ISC can be established with the aid of another LEO satellite at higher altitude by using AF or DF protocol. Despite those advantages, satellite mega-constellations may still suffer from the congestion in the current spectrum due to microwave communication (in L-band, Ka-band, V-band) especially when thousands of satellites are deployed. To cope with this problem, utilization of THz frequencies can be considered to improve system capacity for 6G systems.[1]

In the literature, there are a few works which investigate performance of THz NTNs. However, performance of dual-hop inter-satellite THz communication system that utilizes variable-gain AF protocol remains unexplored. Therefore, in this chapter, a dual-hop THz ISC link is considered.[2] In this setup, it is assumed that communication between two LEO satellites is established with the aid of another LEO satellite at higher altitude that uses variable-gain AF protocol. In order to quantify the overall system performance, statistics of the end-to-end SNR are derived. By using these statistics, outage probability, asymptotic outage probability, and SER analyses are performed.

---

[1] Optical communication can also be considered to improve system capacity, however, it poses a great challenge due to the strict requirement of pointing accuracy [112].

[2] This chapter is based on the conference paper entitled "Outage and SER analyses for dual-hop inter-satellite THz communication" presented at *2024 6th International Conference on Communications, Signal Processing, and their Applications (ICCSPA)* [113].

6.1 System Model

As depicted in Fig. 6.1, in the system of interest, communication between two LEO satellites is established through another LEO satellite which acts as a relay. Here, it is assumed that direct connection between the LEO satellites can not be provided since they are deployed in different orbits at the same altitudes. In this system, transmission is completed in two phases. In the first phase, source LEO satellite (S) transmits modulated signal to the relay LEO satellite (R) in the THz band. Thereafter, in the second phase, R re-transmits the signal to the destination LEO satellite (D) by using variable-gain AF protocol. In the i-th phase, $i \in \{1,2\}$, received signal can be written as

$$y_i = \sqrt{\frac{P_i}{L_i}} h_i^{\mathrm{fp}} x_i + n_i, \tag{6.1}$$

where P_i and L_i represent transmit power and path-loss factor, respectively. h_i^{fp} is the channel coefficient which models the joint fading and pointing error. $n_i \sim \mathcal{CN}(0, \sigma_{n_i}^2)$ denotes the additive Gaussian noise where $\sigma_{n_i}^2$ shows the noise power, and x_i stands for the transmitted signal. For S-to-R link ($i = 1$), x_1 is the modulated signal with unit power and for R-to-D link ($i = 2$), $x_2 = G y_1$ is the amplified signal with the amplification factor $G = 1/\sqrt{\frac{P_1}{L_1}\left|h_1^{\mathrm{fp}}\right|^2 + \sigma_{n_i}^2}$. The end-to-end SNR is given by

$$\gamma_{e2e} = \frac{\gamma_1 \gamma_2}{\gamma_1 + \gamma_2 + 1}. \tag{6.2}$$

Here, $\gamma_i = \frac{\bar{\gamma}_i^{\mathrm{t}}}{L_i}\left|h_i^{\mathrm{fp}}\right|^2$ represents the SNR for the i-th phase where $\bar{\gamma}_i^{\mathrm{t}} = \frac{P_i}{\sigma_{n_i}^2}$ is the average transmit SNR.

6.1.1 Path-loss factor

In THz frequencies, EM waves interact with the particles in the atmosphere such as water vapour and oxygen, which results in atmospheric absorption loss. Additionally, free-space loss is observed due to the propagation of the EM wave. Furthermore, it is worth mentioning that EM waves can interact with the plasma in the ionosphere, which also introduces attenuation. By taking the transmitter and receiver antenna gains ($\mathcal{G}_i^{\mathrm{t}}$ and $\mathcal{G}_i^{\mathrm{r}}$, respectively) into account on the top of the mentioned loss factors, the total

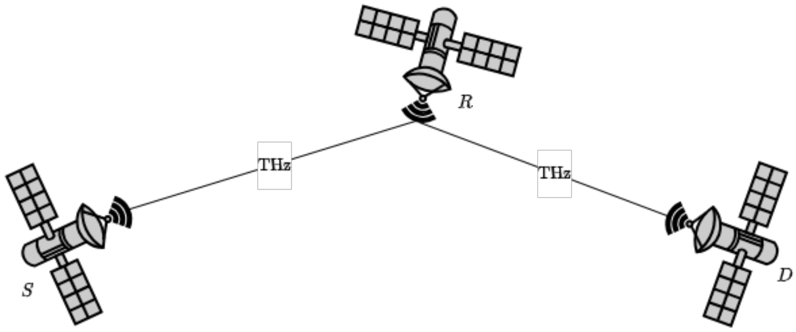

Figure 6.1 : Dual-hop inter-satellite THz communication system.

path-loss in the i-th phase can be formulated as

$$L_i = L_i^{\mathrm{fsl}} L_i^{\mathrm{abs}} L_i^{\mathrm{ion}} / \left(\mathcal{G}_i^{\mathrm{t}} \mathcal{G}_i^{\mathrm{r}}\right). \tag{6.3}$$

Here, $L_i^{\mathrm{fsl}} = \left(\frac{4\pi d_i}{\lambda}\right)^2$ is the free-space loss, where d_i and λ stand for the transmission distance and the operating wavelength, respectively. In this formulation, d_i can be found as a function of zenith angle and the altitude difference between transmitter and receiver, where the zenith angle is defined as the angle between the transmission path and the vertical axis. Moreover, L_i^{abs} denotes the atmospheric absorption loss and it is related to the atmospheric temperature, pressure and humidity level [13]. However, for an ISC, absorption loss is negligibly small since the atmosphere is thinner at LEO altitudes and densities of the absorber particles are very low [40]. Furthermore, L_i^{ion} represents the ionospheric loss, and it is shown in [40] that attenuation factor due to the ionospheric layer is on the order of 10^{-4} dB/km for sub-THz region and even lower at higher frequencies. Hence, throughout this chapter, the atmospheric absorption loss and the ionospheric loss are assumed to be $L_i^{\mathrm{abs}} = 0$ dB/km and $L_i^{\mathrm{ion}} = 0$ dB/km, respectively.

6.1.2 Fading and pointing error

Since LOS connectivity is required for THz communication systems, pencil-sharp radiation patterns are considered. However, due to the orbital movements of the satellites, perfect alignment between transmitter and receiver antennas might not be established, resulting in a decrement in the received power. Consequently, pointing error is observed in addition to small-scale fading. Therefore, the channel coefficient can be denoted as $h_i^{\mathrm{fp}} = h_i^{\mathrm{f}} h_i^{\mathrm{p}}$, where h_i^{f} and h_i^{p} are fading and pointing error coefficients, respectively. In this chapter, α-μ distribution model is used for the fading coefficient in the i-th phase h_i^{f} [58], where α and μ stand for the distribution parameters. Also, the PDF of h_i^{p} is given as $f_{h_i^{\mathrm{p}}}(z) = z^{\psi^2-1}\psi^2/A_0^{\psi^2}$ for $0 \le z \le A_0$ [84]. In this formulation, $\psi = \frac{\sigma_{eq}}{2\sigma_s}$ and $A_0 = \mathrm{erf}^2(c)$ show the distribution parameter and the fraction of the received power for the perfect alignment case, respectively. Here, $\sigma_{eq} = \sqrt{\sigma_d^2 \frac{\sqrt{\pi}\mathrm{erf}(c)}{2c\exp(-c^2)}}$ denotes the equivalent beamwidth where $c = \frac{\sqrt{\pi}a}{\sqrt{2}\sigma_d}$ and σ_s stands for the distribution parameter of Rayleigh distributed pointing error vector. Additionally, a and σ_d represent the aperture of the receiver and equivalent beamwidth at the receiver plane, respectively. The PDF of the envelope of the joint α-μ fading and pointing error coefficient is found by $f_{|h_i^{\mathrm{fp}}|}(z) = \int_0^{A_0} \frac{1}{\upsilon} f_{|h_i^{\mathrm{f}}|}\left(\frac{z}{\upsilon}\right) f_{h_i^{\mathrm{p}}}(\upsilon) d\upsilon$ as [50][3]

$$f_{|h_i^{\mathrm{fp}}|}(z) = \frac{\mu^{\psi^2/\alpha}\psi^2 A_0^{-\psi^2}}{(\hat{h}_i^{\mathrm{f}})^{\psi^2}\Gamma(\mu)} z^{\psi^2-1}\Gamma\left(\mu - \frac{\psi^2}{\alpha}, \frac{\mu z^\alpha}{(\hat{h}_i^{\mathrm{f}})^\alpha A_0^\alpha}\right),\ z \ge 0, \tag{6.4}$$

where $\hat{h}_i^{\mathrm{f}} = \sqrt[\alpha]{E\left[\left|h_i^{\mathrm{f}}\right|^\alpha\right]}$ is the α-root mean of the fading coefficient. By using (6.4), the PDF of the SNR for the i-th phase can be obtained as

$$f_{\gamma_i}(z) = A_i z^{\frac{\psi^2}{2}-1}\Gamma\left(B_i, C_i z^{\frac{\alpha}{2}}\right),\ z \ge 0, \tag{6.5}$$

where $A_i = \frac{\psi^2\mu^{\psi^2/\alpha}\left(L_i/\bar{\gamma}_i^{\mathrm{t}}\right)^{\frac{\psi^2}{2}}}{2A_0^{\psi^2}(\hat{h}_i^{\mathrm{f}})^{\psi^2}\Gamma(\mu)}$, $B_i = \mu - \frac{\psi^2}{\alpha}$, $C_i = \frac{\mu\left(L_i/\bar{\gamma}_i^{\mathrm{t}}\right)^{\frac{\alpha}{2}}}{(\hat{h}_i^{\mathrm{f}})^\alpha A_0^\alpha}$. By taking the integral of the PDF in (6.5), the CDF of γ_i can be found as [114]

$$F_{\gamma_i}(z) = \frac{\gamma\left(\mu, C_i z^{\frac{\alpha}{2}}\right)}{\Gamma(\mu)} + \frac{C_i^{\frac{\psi^2}{\alpha}}}{\Gamma(\mu)} z^{\frac{\psi^2}{2}}\Gamma\left(B_i, C_i z^{\frac{\alpha}{2}}\right),\ z \ge 0. \tag{6.6}$$

6.2 Performance Analyses

In this section, system performance is analyzed in terms of outage probability, asymptotic outage probability, and SER.

[3]The pointing error coefficient h^{p} is a positive real-valued random variable since it denotes the fraction of the received power in the presence of antenna misalignment. However, the fading coefficient h^{f} is complex. Therefore, the provided statistics is related to the envelope of the joint fading and pointing error coefficient, i.e. $\left|h^{\mathrm{fp}}\right| = \left|h^{\mathrm{f}}\right| h^{\mathrm{p}}$.

6.2.1 Outage probability analysis

Outage probability can be defined as the probability that the SNR of the received signal at D falls below the predefined threshold SNR value γ_{th}, and it is formulated as

$$P_{\text{out}} = \Pr\left[\gamma_{e2e} \leq \gamma_{th}\right] = F_{\gamma_{e2e}}\left(\gamma_{th}\right). \tag{6.7}$$

However, finding the exact CDF of γ_{e2e} might pose mathematical challenges. Instead, following tight SNR upper bound can be used:

$$\gamma_{e2e} < \gamma_{e2e}^{u_1} = \left(\frac{1}{\gamma_1} + \frac{1}{\gamma_2}\right)^{-1}, \tag{6.8}$$

where $\gamma_{e2e}^{u_1}$ denotes the SNR upper bound. By using $\gamma_{e2e}^{u_1}$, outage probability can be lower bounded as

$$P_{\text{out}} \geq F_{\gamma_{e2e}^{u_1}}\left(\gamma_{th}\right). \tag{6.9}$$

To find the CDF of $\gamma_{e2e}^{u_1}$, the MGF approach can be used [115]. To do this, first, the MGF of $\frac{1}{\gamma_i}$ for $i \in \{1,2\}$ is obtained by using the Laplace transform as

$$\mathcal{M}_{\frac{1}{\gamma_i}}(s) = \int_0^{\infty} e^{-sz} f_{\frac{1}{\gamma_i}}(z)dz. \tag{6.10}$$

where $f_{\frac{1}{\gamma_i}}(z)$ can be derived from (6.5) as

$$f_{\frac{1}{\gamma_i}}(z) = A_i z^{-\frac{\psi^2}{2}-1}\Gamma\left(B_i, C_i z^{-\frac{\alpha}{2}}\right). \tag{6.11}$$

By substituting (6.11) in (6.10) together with $\Gamma(z,v) = \mathrm{G}_{1,2}^{2,0}\left[v \,\middle|\, \begin{matrix} 1 \\ z, 0 \end{matrix}\right]$ and Mellin-Barnes type integral representation of the Meijer-G function, the MGF of $\frac{1}{\gamma_i}$ can be rewritten as

$$\mathcal{M}_{\frac{1}{\gamma_i}}(s) = \frac{A_i}{2\pi j}\int_{\mathcal{L}_i} \frac{\Gamma(B_i - \xi_i)\Gamma(-\xi_i)}{\Gamma(1-\xi_i)} C_i^{\xi_i} \mathcal{I}_1 d\xi_i, \tag{6.12}$$

where $\mathcal{I}_1$ is given by [55, Eq. (17.13.3)]

$$\mathcal{I}_1 = \int_0^{\infty} z^{-\frac{\psi^2}{2}-1-\frac{\alpha}{2}\xi_i} e^{-sz} dz = s^{\frac{\psi^2}{2}+\frac{\alpha}{2}\xi_i}\Gamma\left(-\frac{\psi^2}{2} - \frac{\alpha}{2}\xi_i\right). \tag{6.13}$$

Substituting (6.13) in (6.12) and using the definition of the uni-variate Fox-H function result in

$$\mathcal{M}_{\frac{1}{\gamma_i}}(s) = A_i s^{\psi^2/2}\mathrm{H}_{1,3}^{3,0}\left[C_i s^{\frac{\alpha}{2}} \,\middle|\, \begin{matrix} (1,1) \\ (B_i,1),(0,1),(-\frac{\psi^2}{2},\frac{\alpha}{2}) \end{matrix}\right]. \tag{6.14}$$

By multiplying the MGFs of $\frac{1}{\gamma_1}$ and $\frac{1}{\gamma_2}$, the MGF of $\frac{1}{\gamma_{e2e}^{u_1}}$ can be found as

$$\mathcal{M}_{\frac{1}{\gamma_{e2e}^{u_1}}}(s) = \mathcal{M}_{\frac{1}{\gamma_1}}(s)\mathcal{M}_{\frac{1}{\gamma_2}}(s). \tag{6.15}$$

The CDF of $1/\gamma_{e2e}^{u_1}$ can be obtained by using the inverse Laplace transform as follows:

$$F_{\frac{1}{\gamma_{e2e}^{u_1}}}(z) = \mathcal{L}^{-1}\left\{\frac{1}{s}\mathcal{M}_{\frac{1}{\gamma_{e2e}^{u_1}}}(s)\right\}. \tag{6.16}$$

The above-equation can be rewritten by employing the definition of the uni-variate Fox-H function and by changing the order of integrals and the Laplace transform operator as

$$F_{\frac{1}{\gamma_{e2e}^{u_1}}}(z) = A_1A_2\frac{1}{(2\pi j)^2}\int_{\mathcal{L}_1}\int_{\mathcal{L}_2}\phi_1(\xi_1)\phi_2(\xi_2)C_1^{\xi_1}C_2^{\xi_2}\mathcal{I}_2 d\xi_1 d\xi_2, \tag{6.17}$$

where $\phi_i(\xi_i) = \frac{\Gamma(B_i-\xi_i)\Gamma(-\xi_i)\Gamma\left(-\frac{\psi^2}{2}-\frac{\alpha}{2}\xi_i\right)}{\Gamma(1-\xi_i)}$ for $i \in \{1,2\}$. $\mathcal{I}_2$ in (6.17) is given by [55, Eq. (17.13.3)]

$$\mathcal{I}_2 = \mathcal{L}^{-1}\left\{s^{\psi^2-1+\frac{\alpha}{2}\xi_1+\frac{\alpha}{2}\xi_2}\right\} = \frac{z^{-\psi^2-\frac{\alpha}{2}\xi_1-\frac{\alpha}{2}\xi_2}}{\Gamma\left(-\psi^2+1-\frac{\alpha}{2}\xi_1-\frac{\alpha}{2}\xi_2\right)}. \tag{6.18}$$

By substituting (6.18) in (6.17) and by employing the definition of the bi-variate Fox-H function, the CDF of $\frac{1}{\gamma_{e2e}^{u_1}}$ can be found. Using the identity of $F_Z(z) = 1 - F_{\frac{1}{Z}}\left(\frac{1}{z}\right)$ results in the CDF of $\gamma_{e2e}^{u_1}$ which can be obtained as

$$F_{\gamma_{e2e}^{u_1}}(z) = 1 - A_1A_2z^{\psi^2}\mathrm{H}_{1,0:1,3:1,3}^{0,0:3,0:3,0}\left[\begin{matrix}C_1z^{\frac{\alpha}{2}}\\ C_2z^{\frac{\alpha}{2}}\end{matrix}\middle|\begin{matrix}V_1\\ V_2\end{matrix}\right], \tag{6.19}$$

where $V_1 = \{(-\psi^2+1,\frac{\alpha}{2},\frac{\alpha}{2})\} : \{(1,1)\} : \{(1,1)\}$ and $V_2 = \{-\} : \{(B_1,1),(0,1),(-\frac{\psi^2}{2},\frac{\alpha}{2})\} : \{(B_2,1),(0,1),(-\frac{\psi^2}{2},\frac{\alpha}{2})\}$. By using (6.19) in (6.9), a tight lower bound for P_{out} can be obtained.

6.2.2 Asymptotic outage probability analysis

Asymptotic behaviour of the system in outage performance can be found by using another upper bound for the end-to-end SNR, i.e. $\gamma_{e2e}^{u_2} = \min(\gamma_1,\gamma_2)$. In this case, a lower bound for the asymptotic outage probability can be obtained as

$$P_{\text{out}}^{\infty} = F_{\gamma_{e2e}^{u_2}}^{\infty} \approx F_{\gamma_1}^{\infty}(\gamma_{th}) + F_{\gamma_2}^{\infty}(\gamma_{th}) \tag{6.20}$$

The asymptotic CDF of γ_i for $i \in \{1,2\}$, i.e. $F^{\infty}_{\gamma_i}(z)$, can be derived from (6.6) by employing [116, Eq. (45.9.1)] and [116, Eq. (45.9.6)] as

$$F^{\infty}_{\gamma_i}(z) = \left(\frac{C_i^{\mu}}{\Gamma(\mu+1)} - \frac{C_i^{\mu}}{\Gamma(\mu)B_i}\right) z^{\frac{\alpha\mu}{2}} + \frac{\Gamma(B_i)C_i^{\psi^2/\alpha}}{\Gamma(\mu)} z^{\frac{\psi^2}{2}}. \tag{6.21}$$

By substituting (6.21) in (6.20), the asymptotic outage probability can be obtained.

6.2.3 SER analysis

SER for M-PSK system, where M is the modulation order, can be found by the well-known formula [57]

$$P_e = \frac{1}{\pi}\int_0^{\Theta} \mathcal{M}_{\gamma_{e2e}}\left(\frac{c_{\mathrm{MPSK}}}{\sin^2(\theta)}\right) d\theta, \tag{6.22}$$

where $\Theta = \pi\frac{M-1}{M}$, $c_{\mathrm{MPSK}} = \sin^2(\pi/M)$. SER can be approximately computed by [117, Eq. (10)]

$$P_e \approx \left(\frac{\Theta}{2\pi} - \frac{1}{6}\right)\mathcal{M}_{\gamma_{e2e}}(c_{\mathrm{MPSK}}) + \frac{1}{4}\mathcal{M}_{\gamma_{e2e}}\left(\frac{4}{3}c_{\mathrm{MPSK}}\right) + \left(\frac{\Theta}{2\pi} - \frac{1}{4}\right)\mathcal{M}_{\gamma_{e2e}}\left(\frac{c_{\mathrm{MPSK}}}{\sin^2\Theta}\right). \tag{6.23}$$

Also, to simplify the calculations, instead of using the MGF of γ_{e2e}, the MGF of the upper bound $\gamma_{e2e}^{u_2}$ can be used. The CDF of $\gamma_{e2e}^{u_2}$ is given as $F_{\gamma_{e2e}^{u_2}}(z) \approx F_{\gamma_1}(z) + F_{\gamma_2}(z)$. By using this relation, the MGF of $\gamma_{e2e}^{u_2}$ can be obtained as

$$\mathcal{M}_{\gamma_{e2e}^{u_2}}(s) \approx s\mathcal{L}\{F_{\gamma_1}(z)\} + s\mathcal{L}\{F_{\gamma_2}(z)\}. \tag{6.24}$$

The Laplace transform of the CDF of γ_i for $i \in \{1,2\}$ in (6.24) can be evaluated as

$$\mathcal{L}\{F_{\gamma_i}(z)\} = \frac{\mathcal{T}_1}{\Gamma(\mu)} + C_i^{\psi^2/\alpha}\frac{\mathcal{T}_2}{\Gamma(\mu)}, \tag{6.25}$$

where $\mathcal{T}_1 = \int_0^{\infty} \gamma\left(\mu, C_i z^{\frac{\alpha}{2}}\right) e^{-sz} dz$ and $\mathcal{T}_2 = \int_0^{\infty} z^{\frac{\psi^2}{2}} \Gamma\left(B_i, C_i z^{\frac{\alpha}{2}}\right) e^{-sz} dz$. Here, by using the Meijer-G representations of the exponential function [118, Eq. (01.03.26.0004.01)] and lower incomplete gamma function [118, Eq. (06.06.26.0004.01)], [116, Eq. (45.0.1)] and by invoking [118, Eq. (07.34.21.0013.01)], $\mathcal{T}_1$ can be obtained as

$$\mathcal{T}_1 = \int_0^{\infty} \mathrm{G}_{0,1}^{1,0}\left[sz \,\middle|\, \begin{matrix} - \\ 0 \end{matrix}\right] \mathrm{G}_{1,2}^{1,1}\left[C_i z^{\frac{\ell}{\rho}} \,\middle|\, \begin{matrix} 1 \\ \mu, 0 \end{matrix}\right] dz = \frac{\rho^{\mu-0.5}\ell^{0.5}}{(2\pi)^{\frac{\ell}{2}+\frac{\rho}{2}-1} s} \mathrm{G}_{\rho+\ell,2\rho}^{\rho,\rho+\ell}\left[\frac{C_i^{\rho}\ell^{\ell}}{s^{\ell}\rho^{\rho}} \,\middle|\, \begin{matrix} V_3 \\ V_4 \end{matrix}\right], \tag{6.26}$$

where $V_3 = \left\{\frac{1}{\rho}, \frac{2}{\rho}, \cdots, 1, 0, \frac{1}{\ell}, \cdots, \frac{\ell-1}{\ell}\right\}$ and $V_4 = \left\{\frac{\mu}{\rho}, \frac{\mu+1}{\rho}, \cdots, \frac{\mu+\rho-1}{\rho}, 0, \frac{1}{\rho}, \cdots, \frac{\rho-1}{\rho}\right\}$. Here, the variables ℓ and ρ are positive integers such that $\frac{\ell}{\rho} = \frac{\alpha}{2}$ and $\gcd(\ell, \rho) = 1$. Similar to $\mathcal{T}_1$, by using [118, Eq. (07.34.21.0013.01)] together with the Meijer-G representations of the exponential function [118, Eq. (01.03.26.0004.01)] and upper incomplete Gamma function [118, Eq. (06.06.26.0005.01)], $\mathcal{T}_2$ can be found as

$$\mathcal{T}_2 = \int_0^\infty z^{\psi^2/2} \mathrm{G}_{0,1}^{1,0}\left[sz \,\middle|\, \begin{matrix} - \\ 0 \end{matrix}\right] \mathrm{G}_{1,2}^{2,0}\left[C_i z^{\frac{\ell}{\rho}} \,\middle|\, \begin{matrix} 1 \\ B_i, 0 \end{matrix}\right] dz = \frac{\rho^{B_i - 0.5} \ell^{\frac{\psi^2}{2}+0.5}}{(2\pi)^{\frac{\ell}{2}+\frac{\rho}{2}-1} s^{\frac{\psi^2}{2}+1}} \mathrm{G}_{\rho+\ell,2\rho}^{2\rho,\ell}\left[\frac{C_i^\rho \ell^\ell}{s^\ell \rho^\rho} \,\middle|\, \begin{matrix} V_5 \\ V_6 \end{matrix}\right], \tag{6.27}$$

where $V_5 = \left\{\frac{-\psi^2/2}{\ell}, \frac{1-\psi^2/2}{\ell}, \cdots, \frac{\ell-\psi^2/2-1}{\ell}, \frac{1}{\rho}, \frac{2}{\rho}, \cdots, 1\right\}$, $V_6 = \left\{\frac{B_i}{\rho}, \frac{B_i+1}{\rho}, \cdots, \frac{B_i+\rho-1}{\rho}, 0, \frac{1}{\rho}, \cdots, \frac{\rho-1}{\rho}\right\}$. By substituting (6.26) and (6.27) in (6.25) then inserting (6.25) into (6.24), $\mathcal{M}_{\gamma_{e2e}^{u_2}}(s)$ can be found. By replacing $\mathcal{M}_{\gamma_{e2e}}(s)$ in (6.23) by $\mathcal{M}_{\gamma_{e2e}^{u_2}}(s)$, the approximate SER can be obtained.

6.3 Numerical Results

In this section, outage and SER performance of the system are investigated and theoretical results are verified by Monte-Carlo simulations. It is assumed that LEO satellites (S and D) are orbiting at an altitude of 500 km and the altitude of R is taken as 1200 km. Zenith angles for both S-to-R and R-to-D links are 40° and the operating frequency is given as 295 GHz. Moreover, antenna gains for both links are assumed as $\mathcal{G}_i^{\mathrm{t}} = \mathcal{G}_i^{\mathrm{r}} = 60$ dBi. The pointing error parameters are given as $\psi = 4.422$ and $A_0 = 0.74$, whereas the several values are used for the fading parameters α and μ. Transmit powers, noise power, and transmit SNRs are taken as $P_1 = P_2 = P$, $\sigma_{n_i}^2 = -70$ dBm, and $\bar{\gamma}_1^{\mathrm{t}} = \bar{\gamma}_2^{\mathrm{t}} = \bar{\gamma}^t$, respectively.

In Fig. 6.2, outage and asymptotic outage curves are shown for $\alpha = 3, 4, 5$ and $\mu = 2.5$. It can be seen from the figure that both theoretical curves establish lower bound for simulation curves. Additionally, it can be inferred that 10^{-6} outage rate is achievable below 30 dBm transmit power. Moreover, it can be deduced that as the value of α increases, outage performance enhances, which originates from the fact that higher values of α corresponds to less severe fading channel characteristics. Also, it can be

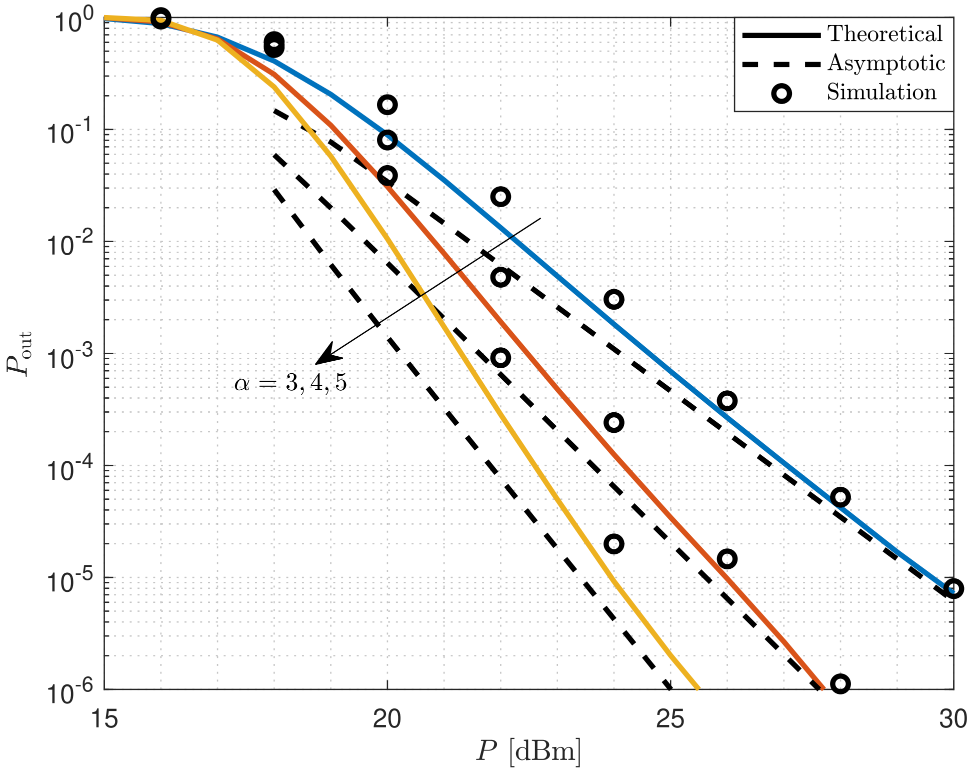

Figure 6.2 : Outage performance of the system for $\alpha = 3, 4, 5$ and $\mu = 2.5$.

observed that asymptotic curves accurately represent the high SNR behaviour of the system performance.

Outage performance of the system is illustrated for $\alpha = 3$ and $\mu = 2, 3.5, 5$ in Fig. 6.3 together with asymptotic outage performance. As in Fig. 6.2, similar deductions can be made about the impact of distribution parameter on the system performance. Outage performance is improved with increasing values of μ since higher μ corresponds to more suitable channel for communication by means of severity of the fading channel. Furthermore, it is observed that the asymptotic curves are successfully matched with the high SNR characteristics of the outage performance.

SER curves of the system are presented in Fig. 6.4. For this analysis, BPSK modulation ($M = 2$) is used, and the fading parameters are set to $\alpha = 1.5, 2.5, 6$ and $\mu = 2$. It is shown in the figure that the theoretical curves establish lower bound for the simulation curves since end-to-end SNR is upper bounded by $\gamma_{e2e}^{u2} = \min(\gamma_1, \gamma_2)$. It can be noticed that for low and medium SNR values, the theoretical results provide

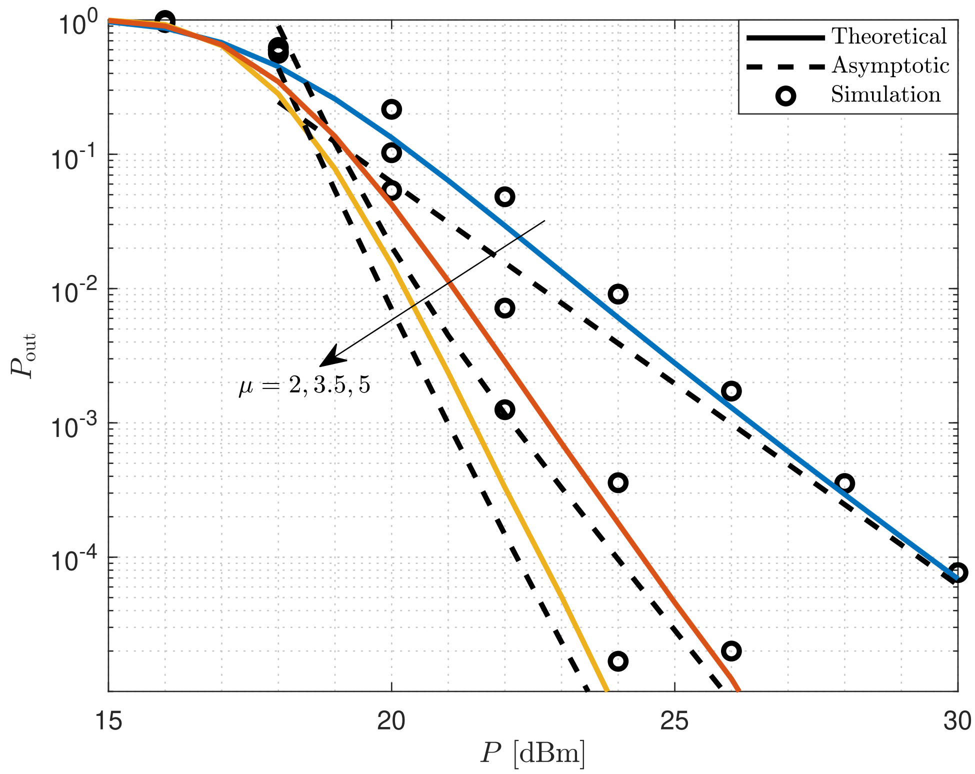

Figure 6.3 : Outage performance of the system for $\alpha = 3$ and $\mu = 2, 3.5, 5$.

a loose bound for the simulations. However, for higher transmit power (or average transmit SNR), $\gamma_{e2e}^{u_2}$ provides a tighter bound and the theoretical SER expression gives closer results to the simulations. Also, it can be observed from the figure that 10^{-5} error rate is achievable below 30 dBm transmit power.

6.4 Concluding Remarks

In this chapter, a dual-hop ISC between two LEO satellites is examined. It is assumed that in this setup, variable-gain AF protocol is utilized at the relay LEO satellite. The system performance is analyzed by means of outage probability and SER, together with the asymptotic outage probability. To evaluate the performance, statistics of the end-to-end SNR are obtained and examined in detail. The results have shown that improved system performance is observed for higher values of the fading parameters α and μ since they correspond to less severe fading channel characteristics. Moreover, it is illustrated that 10^{-6} outage probability and 10^{-5} error rate are achievable below

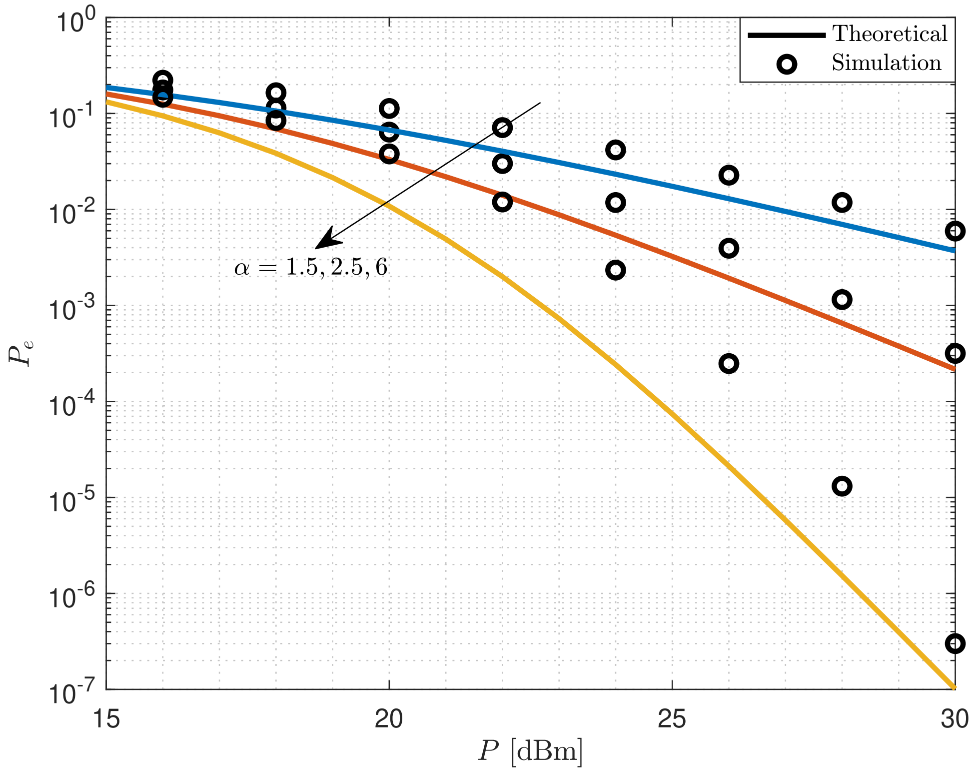

Figure 6.4 : SER performance of the system for $\alpha = 1.5, 2.5, 6$ and $\mu = 2$ where BPSK modulation is used.

30 dBm transmit power. These findings highlight the efficiency of the proposed model under realistic channel conditions.

7. NTNs IN THE THz BAND WITH TRANSCEIVER NOISE

Up to this chapter, THz NTNs are analyzed under ideal hardware consideration. However, non-ideal equipment is used in practical communication systems. In this regard, hardware impairment noise is observed besides other performance degrading factors, such as free-space loss, and atmospheric absorption loss. Hardware impairments are mainly observed due to non-linear behaviour of power amplifiers, and they are non-negligible at THz frequencies because of the noise characteristics of active circuit elements [49, 119]. In this context, additional noise signals are added to the modulated signal at the transmitter and to the received signal at the receiver, limiting the system performance [62]. However, the impact of hardware impairments on the THz-enabled HAPS-aided satellite communication scenario remains unexplored in the current literature. Hence, this chapter considers a setup where multiple HAPS systems aid the transmission of downlink satellite by using variable-gain AF protocol.[1] To evaluate the overall performance bounds in the presence of hardware impairments, pointing errors, and absorption loss, the statistics related to the upper bound of the end-to-end SNR are derived. Based on these statistics, outage probability, asymptotic outage probability, and ergodic capacity of the system are obtained.

7.1 System Model

This study considers a dual-hop THz NTN, as shown in Fig. 7.1, comprising of a LEO satellite (S), K HAPS nodes ($H_k|_{k=1}^{K}$), and a destination (D), with each node affected by hardware impairment noise caused by non-ideal equipment. In this model, S seeks to communicate with D through HAPS systems that use variable-gain AF relaying

[1] An earlier version of the work in this chapter is presented at *2023 31st Signal Processing and Communication Applications Conference (SIU)* [120], and the study presented in this chapter is submitted to *Transactions on Emerging Telecommunications Technologies*.

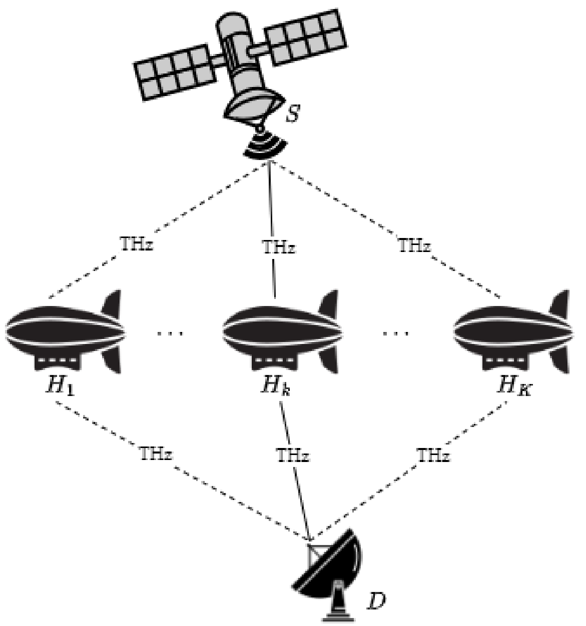

Figure 7.1 : Multi-HAPS aided THz NTN.

protocol.[2] Here, it is assumed that LOS connection cannot be established between S and D. The HAPS system (or the branch) which provides the maximum end-to-end SNR is selected for transmission.[3] Thus, in this system, the transmission is completed in only 2 time intervals. In the first time interval, S transmits its signal to the selected HAPS system H_ℓ. Thereafter, in the second time interval, H_ℓ transmits the signal to D using AF relaying, while S remains silent. In the i-th hop of the selected branch ℓ for $i \in \{1,2\}$, the received signal can be written as

$$y_{i\ell} = \sqrt{\frac{P_{i\ell}}{L_{i\ell}}} h_{i\ell}^{\mathrm{fp}} \left(x_{i\ell} + w_{i\ell}^{\mathrm{t}} \right) + w_{i\ell}^{\mathrm{r}} + n_{i\ell}. \tag{7.1}$$

Here, $P_{i\ell}$, $L_{i\ell}$, and $h_{i\ell}^{\mathrm{fp}}$ denote the transmit power, the path-loss factor, and the independent identically distributed channel coefficient in the i-th hop, respectively. $w_{i\ell}^{\mathrm{t}} \sim \mathcal{CN}\left(0, \kappa_{i\ell,\mathrm{t}}^2\right)$ and $w_{i\ell}^{\mathrm{r}} \sim \mathcal{CN}\left(0, \frac{P_{i\ell}}{L_{i\ell}} \left|h_{i\ell}^{\mathrm{fp}}\right|^2 \kappa_{i\ell,\mathrm{r}}^2\right)$ are the noise terms due to hardware impairments, where $\kappa_{i\ell,\mathrm{t}}^2$ and $\kappa_{i\ell,\mathrm{r}}^2$ are the hardware impairment levels at the

[2]For dual-hop communication systems with hardware impairments, it is shown in the literature that variable-gain AF relaying outperforms fixed-gain counterpart and also that it has similar performance with DF relaying in high SNR regime [62]. Therefore, variable-gain AF relaying is considered in this chapter.

[3]SC is utilized at the receiver since it requires lower hardware complexity.

transmitter and receiver, respectively [121]. Moreover, $\kappa_{i\ell}^2 = \kappa_{i\ell,\mathrm{t}}^2 + \kappa_{i\ell,\mathrm{r}}^2$ represents the total hardware impairment level, where $\kappa_{i\ell}^2 = 0$ shows the ideal hardware case without impairments. $n_{i\ell} \sim \mathcal{CN}\left(0, \sigma_n^2\right)$ stands for the thermal noise observed at the receiver, and σ_n^2 shows the noise power. Also, $x_{i\ell}$ denotes the transmitted signal with unit power. For the first hop, $x_{1\ell}$ is the information signal, whereas for the second hop, $x_{2\ell} = G_\ell y_{1\ell}$ is the amplified signal with the variable amplification factor $G_\ell = 1/\sqrt{\frac{P_{1\ell}}{L_{1\ell}}\left|h_{1\ell}^{\mathrm{fp}}\right|^2\left(1+\kappa_{1\ell}^2\right)+\sigma_n^2}$ as a function of the channel coefficient $h_{1\ell}^{\mathrm{fp}}$ of that time interval. Hence, end-to-end SNR is obtained as

$$\gamma_{e2e,\ell} = \frac{\gamma_{1\ell}\gamma_{2\ell}}{b_\ell\gamma_{1\ell}\gamma_{2\ell} + a_{1\ell}\gamma_{1\ell} + a_{2\ell}\gamma_{2\ell} + 1}, \tag{7.2}$$

where variables b_ℓ, $a_{1\ell}$, and $a_{2\ell}$ are expressed as $b_\ell = \kappa_{1\ell}^2 + \kappa_{2\ell}^2 + \kappa_{1\ell}^2\kappa_{2\ell}^2$, $a_{1\ell} = 1 + \kappa_{1\ell}^2$, and $a_{2\ell} = 1 + \kappa_{2\ell}^2$, respectively. Here, $\gamma_{i\ell}$ is written as

$$\gamma_{i\ell} = \frac{\frac{\bar{\gamma}_{i\ell}^{\mathrm{t}}}{L_{i\ell}}\left|h_{i\ell}^{\mathrm{fp}}\right|^2}{\frac{\bar{\gamma}_{i\ell}^{\mathrm{t}}}{L_{i\ell}}\left|h_{i\ell}^{\mathrm{fp}}\right|^2\kappa_{i\ell}^2 + 1}, \tag{7.3}$$

where $\bar{\gamma}_{i\ell}^{\mathrm{t}} \triangleq \frac{P_{i\ell}}{\sigma_n^2}$ shows the average transmit SNR in the i-th hop for $i \in \{1,2\}$. In this model, the index of the selected HAPS system is determined by the selection rule $\ell = \underset{1\le k\le K}{\arg\max}\left(\gamma_{e2e,k}\right)$, where $\gamma_{e2e,k}$ denotes the end-to-end SNR for the k-th branch.

7.1.1 Path-loss

Since absorption loss is observed at THz frequencies in addition to the free-space loss due to the water vapour and oxygen molecules in the atmosphere, the total path-loss in the i-th hop of the k-th branch can be given as $L_{ik}{=}L_{ik}^{\mathrm{fsl}}L_{ik}^{\mathrm{abs}}/\left(\mathcal{G}_{ik}^{\mathrm{t}}\mathcal{G}_{ik}^{\mathrm{r}}\right)$ for $1{\le}k{\le}K$. In this formulation, $L_{ik}^{\mathrm{fsl}} = \left(\frac{4\pi d_{ik}}{\lambda}\right)^2$ is the free-space loss where λ denotes the operating wavelength of the system. Here, d_{ik} represents link distance which depends on the zenith angle and the vertical distance between the transmitter and the receiver. The zenith angle is defined as the angle between propagation path and the vertical axis. Moreover, L_{ik}^{abs} is the absorption loss caused by water vapour and oxygen content of the atmosphere. L_{ik}^{abs} can be calculated as a function of atmospheric temperature, pressure, and humidity level. In humid atmosphere, absorption occurs more frequently compared to dry atmosphere due to increased density of absorber particles, thus, L_{ik}^{abs}

increases [13]. Lastly, $\mathcal{G}_{ik}^{\mathrm{t}}$ and $\mathcal{G}_{ik}^{\mathrm{r}}$ represent the gains of transmitter and receiver antennas, respectively. In this chapter, the absorption loss is computed as shown in ITU-Rec. 676-13 [13], which is valid up to 1 THz for both horizontal and slant Earth-space paths, under dry and humid atmospheric conditions provided in [73].

7.1.2 Fading and pointing error

In the VHetNet architecture, the establishment of precise alignment between transmitter and receiver can be hindered as the nodes are in movement. In this case, a portion of the received power is diminished, resulting in pointing error. The joint channel coefficient which models fading and pointing error in the i-th hop of the k-th branch can be expressed as $h_{ik}^{\mathrm{fp}} = h_{ik}^{\mathrm{f}} h_{ik}^{\mathrm{p}}$. Here, h_{ik}^{f} is fading coefficient which is modeled by α-μ distribution [58], where α and μ are the distribution parameters of fading coefficient. h_{ik}^{p} stands for pointing error coefficient and the PDF of h_{ik}^{p} is given as $f_{h_{ik}^{\mathrm{p}}}(z) = z^{\psi^2-1}\psi^2/A_0^{\psi^2}$, for $0 \leq z \leq A_0$ [84]. In this expression, $A_0 = \mathrm{erf}^2(c)$ denotes the fraction of the received power for perfect alignment between antennas, where $c = \frac{\sqrt{\pi}a}{\sqrt{2}\sigma_d}$. Here, a is the receiver aperture and σ_d is the equivalent beamwidth at the receiver plane. Also, $\psi = \frac{\sigma_{eq}}{2\sigma_s}$ is the parameter related to the pointing error h_{ik}^{p}, where $\sigma_{eq} = \sqrt{\sigma_d^2 \frac{\sqrt{\pi}\mathrm{erf}(c)}{2v\exp(-c^2)}}$ and σ_s are the equivalent beamwidth and the scaling parameter of the Rayleigh distributed pointing error vector, respectively. The PDF of h_{ik}^{fp} can be found by $f_{|h_{ik}^{\mathrm{fp}}|}(z) = \int_0^{A_0} \frac{1}{v} f_{|h_{ik}^{\mathrm{f}}|}\left(\frac{z}{v}\right) f_{h_{ik}^{\mathrm{p}}}(v)dv$, which is obtained as [50][4]

$$f_{h_{ik}^{\mathrm{fp}}}(z) = \frac{\mu^{\psi^2/\alpha}\psi^2 z^{\psi^2-1}}{(\hat{h}_{ik}^{\mathrm{f}})^{\psi^2}\Gamma(\mu)A_0^{\psi^2}}\Gamma\left(\mu - \frac{\psi^2}{\alpha}, \frac{\mu}{(\hat{h}_{ik}^{\mathrm{f}})^{\alpha}A_0^{\alpha}} z^{\alpha}\right). \tag{7.4}$$

Here, $\hat{h}_{ik}^{\mathrm{f}} = \sqrt[\alpha]{E\left[|h_{ik}^{\mathrm{f}}|^{\alpha}\right]}$ is the α-root mean value of the envelope of h_{ik}^{f}.

7.2 Statistics of the End-to-End SNR

In this section, the PDF and CDF expressions of the end-to-end SNR for the k-th branch are derived.

[4]The pointing error coefficient h_{ik}^{p} is a positive real-valued random variable, and the fading coefficient h_{ik}^{f} is complex. Therefore, the provided statistics is related to the envelope of the joint fading and pointing error coefficient, i.e. $|h_{ik}^{\mathrm{fp}}| = |h_{ik}^{\mathrm{f}}|h_{ik}^{\mathrm{p}}$.

7.2.1 PDF of the end-to-end SNR for the k-th branch

By using (7.4), the PDF of γ_{ik} can be written as

$$f_{\gamma_{ik}}(z)=\begin{cases}\frac{A_{ik}z^{\frac{\psi^2}{2}-1}}{\left(1-\kappa_{ik}^2 z\right)^{\frac{\psi^2}{2}+1}}\Gamma\left(B_{ik},\frac{C_{ik}z^{\frac{\alpha}{2}}}{\left(1-\kappa_{ik}^2 z\right)^{\frac{\alpha}{2}}}\right), & 0\leq z\leq\frac{1}{\kappa_{ik}^2}\\ 0, & \text{otherwise}\end{cases}, \tag{7.5}$$

where $A_{ik}=\frac{\psi^2\mu^{\psi^2/\alpha}\left(L_{ik}/\bar{\gamma}_{ik}^{\mathrm{t}}\right)^{\frac{\psi^2}{2}}}{2A_0^{\psi^2}(\hat{h}_{ik}^{\mathrm{f}})^{\psi^2}\Gamma(\mu)}$, $B_{ik}=\mu-\frac{\psi^2}{\alpha}$, $C_{ik}=\frac{\mu\left(L_{ik}/\bar{\gamma}_{ik}^{\mathrm{t}}\right)^{\frac{\alpha}{2}}}{(\hat{h}_{ik}^{\mathrm{f}})^{\alpha}A_0^{\alpha}}$. Here, obtaining the exact PDF of the end-to-end SNR might be mathematically involved. To find a tractable PDF expression, following SNR upper bound can be used [122]:

$$\gamma_{e2e,k}<\gamma_{e2e,k}^{u}=\left(b_k+\frac{a_{2k}}{\gamma_{1k}}+\frac{a_{1k}}{\gamma_{2k}}\right)^{-1}, \tag{7.6}$$

where $\gamma_{e2e,k}^{u}$ shows the SNR upper bound. The applied methodology to obtain the PDF of $\gamma_{e2e,k}^{u}$ can be summarized in four steps: (i) The MGFs of b_k and $\frac{a_{\rho k}}{\gamma_{ik}}$ for $\rho,i\in\{1,2\}$, $\rho\neq i$ are found by using the Laplace transform. (ii) The MGFs of b_k and $\frac{a_{\rho k}}{\gamma_{ik}}$ are multiplied to obtain the MGF of $(\gamma_{e2e,k}^{u})^{-1}$. (iii) The PDF of $(\gamma_{e2e,k}^{u})^{-1}$ is derived by taking the inverse Laplace transform of its MGF. (iv) Finally, the PDF of $\gamma_{e2e,k}^{u}$ can be found.

In the first step, the MGF of the constant b_k is given as $\mathcal{M}_{b_k}(s)=e^{-sb_k}$. Moreover, with the aid of (7.5), the PDF of $\frac{a_{\rho k}}{\gamma_{ik}}$ can be obtained as

$$f_{\frac{a_{\rho k}}{\gamma_{ik}}}(z)=\begin{cases}\frac{A_{ik}a_{\rho k}^{\frac{\psi^2}{2}}}{\left(z-\kappa_{ik}^2 a_{\rho k}\right)^{\frac{\psi^2}{2}+1}}\Gamma\left(B_{ik},\frac{C_{ik}a_{\rho k}^{\frac{\alpha}{2}}}{\left(z-\kappa_{ik}^2 a_{\rho k}\right)^{\frac{\alpha}{2}}}\right), & z\geq a_{\rho k}\kappa_{ik}^2\\ 0, & \text{otherwise}\end{cases}. \tag{7.7}$$

Hence, the MGF of $\frac{a_{\rho k}}{\gamma_{ik}}$ can be found by taking the Laplace transform of the PDF as follows:

$$\mathcal{M}_{\frac{a_{\rho k}}{\gamma_{ik}}}(s)=\int_{a_{\rho k}\kappa_{ik}^2}^{\infty}\frac{e^{-sz}A_{ik}a_{\rho k}^{\frac{\psi^2}{2}}}{\left(z-\kappa_{ik}^2 a_{\rho k}\right)^{\frac{\psi^2}{2}+1}}\Gamma\left(B_{ik},\frac{C_{ik}a_{\rho k}^{\frac{\alpha}{2}}}{\left(z-\kappa_{ik}^2 a_{\rho k}\right)^{\frac{\alpha}{2}}}\right)dz. \tag{7.8}$$

Here, by changing the variables as $\tau=s(z-a_{\rho k}\kappa_{ik}^2)$ and by applying $\Gamma(\upsilon,z)=G_{1,2}^{2,0}\left[z\,\middle|\,\begin{matrix}1\\ \upsilon,0\end{matrix}\right]$ together with the Mellin-Barnes type integral representation of Meijer-G function, $\mathcal{M}_{\frac{a_{\rho k}}{\gamma_{ik}}}(s)$ can be found as

$$\mathcal{M}_{\frac{a_{\rho k}}{\gamma_{ik}}}(s) = A_{ik} a_{\rho k}^{\psi^2/2} s^{\psi^2/2} e^{-s a_{\rho k}\kappa_{ik}^2} \frac{1}{2\pi j}\int_{\mathcal{L}_i} \frac{\Gamma(B_{ik}-\xi_i)\Gamma(-\xi_i)}{\Gamma(1-\xi_i)} \left(C_{ik} a_{\rho k}^{\frac{\alpha}{2}} s^{\frac{\alpha}{2}}\right)^{\xi_i} \mathcal{I}_1 d\xi_i. \tag{7.9}$$

where $\mathcal{I}_1$ in the above-equation is given as

$$\mathcal{I}_1 = \int_0^\infty \tau^{\frac{-\psi^2}{2}-1-\frac{\alpha}{2}\xi_i} e^{-\tau} d\tau = \Gamma\left(-\frac{\psi^2}{2} - \frac{\alpha}{2}\xi_i\right), \tag{7.10}$$

under the condition of $\mathcal{C}_1 : \mathcal{R}\left\{\frac{-\psi^2}{2} - \frac{\alpha}{2}\xi_i\right\} > 0$ for the convergence of the Laplace transform [55, Eq. (17.13.3)]. Please note here that $\mathcal{C}_1$ can be satisfied by choosing a proper contour $\mathcal{L}_i$ as described in [56] for the integral over ξ_i in (7.9). By substituting (7.10) in (7.9) and by using the definition of the uni-variate Fox-H function, the MGF of $\frac{a_{\rho k}}{\gamma_{ik}}$ can be written as

$$\mathcal{M}_{\frac{a_{\rho k}}{\gamma_{ik}}}(s) = A_{ik} a_{\rho k}^{\psi^2/2} s^{\psi^2/2} e^{-s a_{\rho k}\kappa_{ik}^2} \mathrm{H}_{1,3}^{3,0}\left[C_{ik} a_{\rho k}^{\frac{\alpha}{2}} s^{\frac{\alpha}{2}} \,\middle|\, \begin{matrix} V_1 \\ V_2 \end{matrix}\right], \tag{7.11}$$

where $V_1 = \{(1,1)\}$, $V_2 = \{(B_{ik},1),(0,1),(-\frac{\psi^2}{2},\frac{\alpha}{2})\}$. In the second step, by using $\mathcal{M}_{b_k}(s)$ together with (7.11), the MGF of $\frac{1}{\gamma_{e2e,k}^u}$ can be expressed as

$$\mathcal{M}_{\frac{1}{\gamma_{e2e,k}^u}}(s) = \mathcal{M}_{b_k}(s)\mathcal{M}_{\frac{a_{2k}}{\gamma_{1k}}}(s)\mathcal{M}_{\frac{a_{1k}}{\gamma_{2k}}}(s). \tag{7.12}$$

Thereafter, in the third step, the PDF of $\frac{1}{\gamma_{e2e,k}^u}$ can be found by taking the inverse Laplace transform of its MGF as $f_{\frac{1}{\gamma_{e2e,k}^u}}(z) = \mathcal{L}^{-1}\left\{\mathcal{M}_{\frac{1}{\gamma_{e2e,k}^u}}(s)\right\}$. This expression can be rewritten by using integral form of uni-variate Fox-H function as [56]

$$\begin{aligned} f_{\frac{1}{\gamma_{e2e,k}^u}}(z) &= A_{1k}A_{2k} a_{2k}^{\frac{\psi^2}{2}} a_{1k}^{\frac{\psi^2}{2}} \\ &\times \frac{1}{(2\pi j)^2}\int_{\mathcal{L}_1}\int_{\mathcal{L}_2} \phi_1(\xi_1)\phi_2(\xi_2)\left(C_1 a_{2k}^{\frac{\alpha}{2}}\right)^{\xi_1}\left(C_2 a_{1k}^{\frac{\alpha}{2}}\right)^{\xi_2} \mathcal{I}_2 d\xi_1 d\xi_2, \end{aligned} \tag{7.13}$$

where $\phi_i(\xi_i) = \frac{\Gamma(B_{ik}-\xi_i)\Gamma(-\xi_i)\Gamma\left(-\frac{\psi^2}{2}-\frac{\alpha}{2}\xi_i\right)}{\Gamma(1-\xi_i)}$. Here, $\mathcal{I}_2$ can be written as

$$\mathcal{I}_2 = \mathcal{L}^{-1}\left\{\frac{e^{-s g_k}}{s^{-\psi^2-\frac{\alpha}{2}\xi_1-\frac{\alpha}{2}\xi_2}}\right\} = \frac{(z-g_k)^{-\psi^2-1-\frac{\alpha}{2}\xi_1-\frac{\alpha}{2}\xi_2}}{\Gamma\left(-\psi^2-\frac{\alpha}{2}\xi_1-\frac{\alpha}{2}\xi_2\right)}, \tag{7.14}$$

where $g_k = b_k + a_{2k}\kappa_{1k}^2 + a_{1k}\kappa_{2k}^2$ under the condition of $\mathcal{C}_2 : \mathcal{R}\left\{-\psi^2 - \frac{\alpha}{2}\xi_1 - \frac{\alpha}{2}\xi_2\right\} > 0$ for the Laplace transform to converge [55, Eq. (17.13.3)]. It is important to note that $\mathcal{C}_1$ and $\mathcal{C}_2$ do not contradict. Finally, in the fourth step, by substituting (7.14) in (7.13) with the definition of the bi-variate Fox-H function and by using the identity of $f_Z(z) = f_{\frac{1}{Z}}(\frac{1}{z})z^{-2}$ from the probability theory, the PDF of $\gamma_{e2e,k}^u$ can be found for $z \leq \frac{1}{g_k}$ as

$$\begin{aligned} f_{\gamma_{e2e,k}^u}(z) &= A_{1k}A_{2k}\frac{a_{2k}^{\frac{\psi^2}{2}}\,a_{1k}^{\frac{\psi^2}{2}}\,z^{\psi^2-1}}{(1-g_k z)^{\psi^2+1}} \\ &\quad\times \mathrm{H}_{1,0:1,3:1,3}^{0,0:3,0:3,0}\left[\begin{matrix} C_{1k}a_{2k}^{\frac{\alpha}{2}}\left(\frac{1}{z}-g_k\right)^{-\frac{\alpha}{2}} \\ C_{2k}a_{1k}^{\frac{\alpha}{2}}\left(\frac{1}{z}-g_k\right)^{-\frac{\alpha}{2}} \end{matrix}\middle| \begin{matrix} (-\psi^2,\frac{\alpha}{2},\frac{\alpha}{2}):(1,1):(1,1) \\ -:(B_{1k},1),(0,1),(-\frac{\psi^2}{2},\frac{\alpha}{2}):(B_{2k},1),(0,1),(-\frac{\psi^2}{2},\frac{\alpha}{2}) \end{matrix}\right], \end{aligned} \tag{7.15}$$

and $f_{\gamma_{e2e,k}^u}(z) = 0$ for $z > \frac{1}{g_k}$.

7.2.2 CDF of the end-to-end SNR for the k-th branch

The CDF of $\gamma_{e2e,k}^u$, i.e. $F_{\gamma_{e2e,k}^u}(z)$, can be found by integrating its PDF. However, integrating (7.15) may not be feasible since there are no closed form expressions for the integration of bi-variate Fox-H function in the literature. Even if the integral representation of bi-variate Fox-H function is used, a closed form expression for $F_{\gamma_{e2e,k}^u}(z)$ might not be found for all values of z. Thus, the CDF of $\gamma_{e2e,k}^u$ can be obtained by using the CDF of $\frac{1}{\gamma_{e2e,k}^u}$ which can be expressed as

$$F_{\frac{1}{\gamma_{e2e,k}^u}}(z) = \mathcal{L}^{-1}\left\{\frac{1}{s}\mathcal{M}_{\frac{1}{\gamma_{e2e,k}^u}}(s)\right\}. \tag{7.16}$$

By substituting (7.12) in (7.16), $F_{\frac{1}{\gamma_{e2e,k}^u}}(z)$ can be written as

$$F_{\frac{1}{\gamma_{e2e,k}^u}}(z) = A_{1k}A_{2k}a_{2k}^{\frac{\psi^2}{2}}\,a_{1k}^{\frac{\psi^2}{2}}\frac{1}{(2\pi j)^2}\int_{\mathcal{L}_1}\int_{\mathcal{L}_2}\phi_1(\xi_1)\phi_2(\xi_2)\left(C_1a_{2k}^{\frac{\alpha}{2}}\right)^{\xi_1}\left(C_2a_{1k}^{\frac{\alpha}{2}}\right)^{\xi_2}\mathcal{I}_3 d\xi_1 d\xi_2, \tag{7.17}$$

where $\mathcal{I}_3$ can be given as

$$\begin{aligned} \mathcal{I}_3 &= \mathcal{L}^{-1}\left\{\frac{e^{-sg_k}}{s^{-\psi^2+1-\frac{\alpha}{2}\xi_1-\frac{\alpha}{2}\xi_2}}\right\} \\ &= \frac{(z-g_k)^{-\psi^2-\frac{\alpha}{2}\xi_1-\frac{\alpha}{2}\xi_2}}{\Gamma\left(-\psi^2+1-\frac{\alpha}{2}\xi_1-\frac{\alpha}{2}\xi_2\right)}, \end{aligned} \tag{7.18}$$

under the condition of $\mathcal{C}_3 : \mathcal{R}\left\{-\psi^2 - \frac{\alpha}{2}\xi_1 - \frac{\alpha}{2}\xi_2\right\} > -1$ [55, Eq. (17.13.3)]. It is worth noting that $\mathcal{C}_3$ does not contradict with $\mathcal{C}_1$ which is the only condition to obtain $\mathcal{M}_{\frac{1}{\gamma^u_{e2e,k}}}(s)$ used in (7.16). $F_{\gamma^u_{e2e,k}}(z)$ can be found in closed form for $z \leq \frac{1}{g_k}$ by substituting (7.18) in (7.17) and by using the identity $F_Z(z) = 1 - F_{\frac{1}{Z}}\left(\frac{1}{z}\right)$ together with the definition of the bi-variate Fox-H function as

$$F_{\gamma^u_{e2e,k}}(z) = 1 - \frac{A_{1k}A_{2k}a_{2k}^{\frac{\psi^2}{2}}a_{1k}^{\frac{\psi^2}{2}}}{\left(\frac{1}{z}-g_k\right)^{\psi^2}} \\ \times \mathrm{H}^{0,0:3,0:3,0}_{1,0:1,3:1,3}\left[\begin{matrix} C_{1k}a_{2k}^{\frac{\alpha}{2}}\left(\frac{1}{z}-g_k\right)^{-\frac{\alpha}{2}} \\ C_{2k}a_{1k}^{\frac{\alpha}{2}}\left(\frac{1}{z}-g_k\right)^{-\frac{\alpha}{2}}\end{matrix}\left|\begin{matrix}(-\psi^2+1,\frac{\alpha}{2},\frac{\alpha}{2}):(1,1):(1,1) \\ -:(B_{1k},1),(0,1),(-\frac{\psi^2}{2},\frac{\alpha}{2}):(B_{2k},1),(0,1),(-\frac{\psi^2}{2},\frac{\alpha}{2})\end{matrix}\right.\right], \tag{7.19}$$

and for $z > \frac{1}{g_k}$, $F_{\gamma^u_{e2e,k}}(z) = 1$.

7.2.3 Asymptotic CDF of the end-to-end SNR for the k-th branch

By using the definition of the bi-variate Fox-H function, $F_{\gamma^u_{e2e,k}}(z)$ can be expressed as

$$F_{\gamma^u_{e2e,k}}(z) = 1 - \frac{R_{1k}R_{2k}a_{2k}^{\frac{\psi^2}{2}}a_{1k}^{\frac{\psi^2}{2}}}{\left(\frac{1}{z}-g_k\right)^{\psi^2}(\bar{\gamma}^{\mathrm{t}})^{\psi^2}}\frac{1}{(2\pi j)^2}\int_{\mathcal{L}_1}\int_{\mathcal{L}_2}\phi_1(\xi_1)\phi_2(\xi_2) \\ \times \frac{\left(E_{1k}(\bar{\gamma}^{\mathrm{t}})^{-\frac{\alpha}{2}}\right)^{\xi_1}\left(E_{2k}(\bar{\gamma}^{\mathrm{t}})^{-\frac{\alpha}{2}}\right)^{\xi_2}}{\Gamma(1-\psi^2-\frac{\alpha}{2}\xi_1-\frac{\alpha}{2}\xi_2)}d\xi_2 d\xi_1, \tag{7.20}$$

where $\bar{\gamma}^{\mathrm{t}} = \bar{\gamma}^{\mathrm{t}}_{ik}$, $R_{ik} = \frac{\psi^2\mu^{\psi^2/\alpha}L_{ik}^{\psi^2/2}}{2A_0^{\psi^2}(\hat{h}^{\mathrm{f}}_{ik})^{\psi^2}\Gamma(\mu)}$, and $E_{ik} = \frac{\mu L_{ik}^{\alpha/2}a_{\rho k}^{\alpha/2}}{(\hat{h}^{\mathrm{f}}_{ik})^{\alpha}A_0^{\alpha}}\left(\frac{1}{z}-g_k\right)^{-\alpha/2}$ for $k = 1,\ldots,K$, $\rho, i \in \{1,2\}$, and $\rho \neq i$. By changing the variables $\xi_1' = \xi_1 + \frac{\psi^2}{\alpha}$ and by using [56, Eq. (1.1)] and [56, Eq. (1.60)], $F_{\gamma^u_{e2e,k}}(z)$ can be rewritten as

$$F_{\gamma^u_{e2e,k}}(z) = 1 - \frac{R_{1k}R_{2k}}{(J_{1k}J_{2k})^{\frac{\psi^2}{\alpha}}}\frac{1}{2\pi j}\int_{\mathcal{L}_1'}\frac{\Gamma(\mu-\xi_1')\Gamma(\frac{\psi^2}{\alpha}-\xi_1')\Gamma(-\frac{\alpha}{2}\xi_1')}{\Gamma(1+\frac{\psi^2}{\alpha}-\xi_1')} \\ \times \mathrm{H}^{3,0}_{2,3}\left[E_{2k}(\bar{\gamma}^{\mathrm{t}})^{-\frac{\alpha}{2}}\left|\begin{matrix}(1-\frac{\alpha}{2}\xi_1',\frac{\alpha}{2}),(1+\frac{\psi^2}{\alpha},1) \\ (\mu,1),(\frac{\psi^2}{\alpha},1),(0,\frac{\alpha}{2})\end{matrix}\right.\right]\left(E_{1k}(\bar{\gamma}^{\mathrm{t}})^{-\frac{\alpha}{2}}\right)^{\xi_1'}d\xi_1', \tag{7.21}$$

where $J_{ik} = \frac{\mu L_{ik}^{\alpha/2}}{(\hat{h}^{\mathrm{f}}_{ik})^{\alpha}A_0^{\alpha}}$. Here, as $\bar{\gamma}^{\mathrm{t}}$ goes to infinity, the Fox-H function inside the integration in (7.21) approximately approaches to [123, Eq. (1.8.4)]

$$\mathrm{H}_{2,3}^{3,0}\left[E_{2k}(\bar{\gamma}^{\mathrm{t}})^{-\alpha/2}\left|\begin{matrix}(1-\frac{\alpha}{2}\xi_1',\frac{\alpha}{2}),(1+\frac{\psi^2}{\alpha},1)\\(\mu,1),(\frac{\psi^2}{\alpha},1),(0,\frac{\alpha}{2})\end{matrix}\right.\right]\underset{\bar{\gamma}^{\mathrm{t}}\to\infty}{\approx}\frac{\Gamma(\frac{\psi^2}{\alpha}-\mu)\Gamma(-\frac{\alpha\mu}{2})}{\Gamma(1-\frac{\alpha}{2}\xi_1'-\frac{\alpha\mu}{2})\Gamma(1+\frac{\psi^2}{\alpha}-\mu)}E_{2k}^{\mu}(\bar{\gamma}^{\mathrm{t}})^{-\frac{\alpha\mu}{2}}$$
$$+\frac{\Gamma(\mu-\frac{\psi^2}{\alpha})\Gamma(-\frac{\psi^2}{2})}{\Gamma(1-\frac{\alpha}{2}\xi_1'-\frac{\psi^2}{2})}E_{2k}^{\psi^2/\alpha}(\bar{\gamma}^{\mathrm{t}})^{-\psi^2/2}$$
$$+\frac{2}{\alpha}\frac{\Gamma(\mu)\Gamma(\frac{\psi^2}{\alpha})}{\Gamma(1-\frac{\alpha}{2}\xi_1')\Gamma(1+\frac{\psi^2}{\alpha})}. \tag{7.22}$$

By inserting (7.22) into (7.21), $F_{\gamma^u_{e2e,k}}(z)$ can be approximately expressed as

$$F_{\gamma^u_{e2e,k}}(z)\approx 1-\mathcal{T}_1-\mathcal{T}_2-\mathcal{T}_3, \tag{7.23}$$

where

$$\mathcal{T}_1=\frac{R_{1k}R_{2k}}{(J_{1k}J_{2k})^{\frac{\psi^2}{\alpha}}}\frac{\Gamma(\frac{\psi^2}{\alpha}-\mu)\Gamma(-\frac{\alpha\mu}{2})}{\Gamma(1+\frac{\psi^2}{\alpha}-\mu)}E_{2k}^{\mu}(\bar{\gamma}^{\mathrm{t}})^{-\frac{\alpha\mu}{2}}$$
$$\times\mathrm{H}_{2,3}^{3,0}\left[E_{1k}(\bar{\gamma}^{\mathrm{t}})^{-\frac{\alpha}{2}}\left|\begin{matrix}(1+\frac{\psi^2}{\alpha},1),(1-\frac{\alpha\mu}{2},\frac{\alpha}{2})\\(\mu,1),(\frac{\psi^2}{\alpha},1),(0,\frac{\alpha}{2})\end{matrix}\right.\right], \tag{7.24a}$$

$$\mathcal{T}_2=\frac{R_{1k}R_{2k}}{(J_{1k}J_{2k})^{\frac{\psi^2}{\alpha}}}\Gamma\left(\mu-\frac{\psi^2}{\alpha}\right)\Gamma\left(-\frac{\psi^2}{2}\right)E_{2k}^{\frac{\psi^2}{\alpha}}(\bar{\gamma}^{\mathrm{t}})^{-\frac{\psi^2}{2}}$$
$$\times\mathrm{H}_{2,3}^{3,0}\left[E_{1k}(\bar{\gamma}^{\mathrm{t}})^{-\frac{\alpha}{2}}\left|\begin{matrix}(1+\frac{\psi^2}{\alpha},1),(1-\frac{\psi^2}{2},\frac{\alpha}{2})\\(\mu,1),(\frac{\psi^2}{\alpha},1),(0,\frac{\alpha}{2})\end{matrix}\right.\right], \tag{7.24b}$$

$$\mathcal{T}_3=\frac{R_{1k}R_{2k}}{(J_{1k}J_{2k})^{\frac{\psi^2}{\alpha}}}\frac{2}{\alpha}\frac{\Gamma(\mu)\Gamma(\frac{\psi^2}{\alpha})}{\Gamma(1+\frac{\psi^2}{\alpha})}$$
$$\times\mathrm{H}_{2,3}^{3,0}\left[E_{1k}(\bar{\gamma}^{\mathrm{t}})^{-\alpha/2}\left|\begin{matrix}(1+\frac{\psi^2}{\alpha},1),(1,\frac{\alpha}{2})\\(\mu,1),(\frac{\psi^2}{\alpha},1),(0,\frac{\alpha}{2})\end{matrix}\right.\right]. \tag{7.24c}$$

Here, $\mathcal{T}_1$ and $\mathcal{T}_2$ can be rewritten by employing [123, Eq. (1.8.7)] and [118, Eq. (06.05.17.0002.01)] as

$$\mathcal{T}_1=\frac{R_{1k}R_{2k}}{(J_{1k}J_{2k})^{\frac{\psi^2}{\alpha}}}\frac{2}{\alpha}\frac{\Gamma(\frac{\psi^2}{\alpha}-\mu)\Gamma(\mu)}{\Gamma(1+\frac{\psi^2}{\alpha}-\mu)\frac{\psi^2}{\alpha}(-\frac{\alpha\mu}{2})}E_{2k}^{\mu}(\bar{\gamma}^{\mathrm{t}})^{-\alpha\mu/2}, \tag{7.25a}$$

$$\mathcal{T}_2=\frac{R_{1k}R_{2k}}{(J_{1k}J_{2k})^{\frac{\psi^2}{\alpha}}}\frac{2}{\alpha}\frac{\Gamma\left(\mu-\frac{\psi^2}{\alpha}\right)\Gamma(\mu)}{\frac{\psi^2}{\alpha}(-\frac{\psi^2}{2})}E_{2k}^{\psi^2/\alpha}(\bar{\gamma}^{\mathrm{t}})^{-\psi^2/2}. \tag{7.25b}$$

Afterwards, $\mathcal{T}_3$ is found by invoking [123, Eq. (1.8.4)] as

$$\begin{aligned}\mathcal{T}_3 = &\frac{R_{1k}R_{2k}}{(J_{1k}J_{2k})^{\frac{\psi^2}{\alpha}}}\frac{2}{\alpha}\frac{\Gamma(\mu)}{\frac{\psi^2}{\alpha}(\frac{\psi^2}{\alpha}-\mu)(-\frac{\alpha\mu}{2})}E_{1k}^{\mu}(\bar{\gamma}^{\mathrm{t}})^{-\alpha\mu/2}\\ &+\frac{R_{1k}R_{2k}}{(J_{1k}J_{2k})^{\frac{\psi^2}{\alpha}}}\frac{2}{\alpha}\frac{\Gamma(\mu)\Gamma(\mu-\frac{\psi^2}{\alpha})}{\frac{\psi^2}{\alpha}(-\frac{\psi^2}{2})}E_{1k}^{\psi^2/\alpha}(\bar{\gamma}^{\mathrm{t}})^{-\psi^2/2}\\ &+\frac{R_{1k}R_{2k}}{(J_{1k}J_{2k})^{\frac{\psi^2}{\alpha}}}\left(\frac{2}{\alpha}\frac{\Gamma(\mu)}{\frac{\psi^2}{\alpha}}\right)^2.\end{aligned} \tag{7.26}$$

Substituting $\mathcal{T}_1$, $\mathcal{T}_2$, and $\mathcal{T}_3$ in (7.23) results in

$$\begin{aligned}F_{\gamma_{e2e,k}^u}(z)\underset{\bar{\gamma}^{\mathrm{t}}\to\infty}{\approx}1&+\frac{R_{1k}R_{2k}}{(J_{1k}J_{2k})^{\frac{\psi^2}{\alpha}}}\frac{2}{\alpha}\frac{\Gamma(\frac{\psi^2}{\alpha}-\mu)\Gamma(\mu)}{\Gamma(1+\frac{\psi^2}{\alpha}-\mu)\frac{\psi^2}{\alpha}\frac{\alpha\mu}{2}}E_{2k}^{\mu}(\bar{\gamma}^{\mathrm{t}})^{-\alpha\mu/2}\\ &+\frac{R_{1k}R_{2k}}{(J_{1k}J_{2k})^{\frac{\psi^2}{\alpha}}}\frac{2}{\alpha}\frac{\Gamma\left(\mu-\frac{\psi^2}{\alpha}\right)\Gamma(\mu)}{\frac{\psi^2}{\alpha}\frac{\psi^2}{2}}E_{2k}^{\psi^2/\alpha}(\bar{\gamma}^{\mathrm{t}})^{-\psi^2/2}\\ &+\frac{R_{1k}R_{2k}}{(J_{1k}J_{2k})^{\frac{\psi^2}{\alpha}}}\frac{2}{\alpha}\frac{\Gamma(\mu)}{\frac{\psi^2}{\alpha}(\frac{\psi^2}{\alpha}-\mu)\frac{\alpha\mu}{2}}E_{1k}^{\mu}(\bar{\gamma}^{\mathrm{t}})^{-\alpha\mu/2}\\ &+\frac{R_{1k}R_{2k}}{(J_{1k}J_{2k})^{\frac{\psi^2}{\alpha}}}\frac{2}{\alpha}\frac{\Gamma(\mu)\Gamma(\mu-\frac{\psi^2}{\alpha})}{\frac{\psi^2}{\alpha}\frac{\psi^2}{2}}E_{1k}^{\psi^2/\alpha}(\bar{\gamma}^{\mathrm{t}})^{-\psi^2/2}-\frac{R_{1k}R_{2k}}{(J_{1k}J_{2k})^{\frac{\psi^2}{\alpha}}}\left(\frac{2}{\alpha}\frac{\Gamma(\mu)}{\frac{\psi^2}{\alpha}}\right)^2.\end{aligned} \tag{7.27}$$

Notice that as $\bar{\gamma}^{\mathrm{t}}$ goes to infinity, all of the summation terms in (7.27) approaches to 0 except for the first and the last terms. In this equation, it can be shown after some algebraic manipulations that

$$\frac{R_{1k}R_{2k}}{(J_{1k}J_{2k})^{\frac{\psi^2}{\alpha}}}\left(\frac{2}{\alpha}\frac{\Gamma(\mu)}{\frac{\psi^2}{\alpha}}\right)^2=1. \tag{7.28}$$

Hence, the asymptotic CDF of the end-to-end SNR $F^{\infty}_{\gamma_{e2e,k}^u}(z)$ can be obtained as

$$\begin{aligned}F_{\gamma_{e2e,k}^u}(z)\underset{\bar{\gamma}^{\mathrm{t}}\to\infty}{\approx}F^{\infty}_{\gamma_{e2e,k}^u}(z)=&\frac{R_{1k}R_{2k}}{(J_{1k}J_{2k})^{\frac{\psi^2}{\alpha}}}\frac{2}{\alpha}\frac{\Gamma(\frac{\psi^2}{\alpha}-\mu)\Gamma(\mu)}{\Gamma(1+\frac{\psi^2}{\alpha}-\mu)\frac{\psi^2}{\alpha}\frac{\alpha\mu}{2}}E_{2k}^{\mu}(\bar{\gamma}^{\mathrm{t}})^{-\alpha\mu/2}\\ &+\frac{R_{1k}R_{2k}}{(J_{1k}J_{2k})^{\frac{\psi^2}{\alpha}}}\frac{2}{\alpha}\frac{\Gamma\left(\mu-\frac{\psi^2}{\alpha}\right)\Gamma(\mu)}{\frac{\psi^2}{\alpha}\frac{\psi^2}{2}}E_{2k}^{\psi^2/\alpha}(\bar{\gamma}^{\mathrm{t}})^{-\psi^2/2}\\ &+\frac{R_{1k}R_{2k}}{(J_{1k}J_{2k})^{\frac{\psi^2}{\alpha}}}\frac{2}{\alpha}\frac{\Gamma(\mu)}{\frac{\psi^2}{\alpha}(\frac{\psi^2}{\alpha}-\mu)\frac{\alpha\mu}{2}}E_{1k}^{\mu}(\bar{\gamma}^{\mathrm{t}})^{-\alpha\mu/2}\\ &+\frac{R_{1k}R_{2k}}{(J_{1k}J_{2k})^{\frac{\psi^2}{\alpha}}}\frac{2}{\alpha}\frac{\Gamma(\mu)\Gamma(\mu-\frac{\psi^2}{\alpha})}{\frac{\psi^2}{\alpha}\frac{\psi^2}{2}}E_{1k}^{\psi^2/\alpha}(\bar{\gamma}^{\mathrm{t}})^{-\psi^2/2}.\end{aligned} \tag{7.29}$$

7.3 Performance Analyses

7.3.1 Outage probability analysis

The probability that the SNR of the received signal falls below the predefined threshold SNR value γ_{th} is defined as the outage probability and can be found as $P_{\text{out}} = \Pr\left[\gamma_{e2e,\ell} = \max_{1\leq k\leq K}\left(\gamma_{e2e,k}\right) \leq \gamma_{th}\right]$. Since the ℓ-th branch is selected among K possible branches according to maximum end-to-end SNR criteria, by using order statistics, P_{out} can be obtained as

$$P_{\text{out}} = \Pr\left[\max_{1\leq k\leq K}\left(\gamma_{e2e,k}\right) \leq \gamma_{th}\right] = \prod_{k=1}^{K} \Pr\left[\gamma_{e2e,k} \leq \gamma_{th}\right]. \tag{7.30}$$

Here, P_{out} can be lower bounded by replacing $\gamma_{e2e,k}$ by the SNR upper bound $\gamma_{e2e,k}^{u}$ as

$$P_{\text{out}} \geq \prod_{k=1}^{K} \Pr\left[\gamma_{e2e,k}^{u} \leq \gamma_{th}\right] = \left(F_{\gamma_{e2e,k}^{u}}(\gamma_{th})\right)^{K} \tag{7.31}$$

which can be found by using (7.19).

7.3.2 High SNR analysis

To gain insights about the performance of THz NTNs, the outage probability is analyzed in high SNR region. To accomplish this, (7.29) is substituted in (7.31). Taking the most dominant terms into account after some manipulations, the asymptotic outage probability can be obtained as

$$\begin{aligned}
P_{\text{out}}^{\infty} = &\left(\frac{R_{1k}R_{2k}}{(J_1J_2)^{\frac{\psi^2}{\alpha}}}\frac{2}{\alpha}\frac{\Gamma(\frac{\psi^2}{\alpha}-\mu)\Gamma(\mu)}{\Gamma(1+\frac{\psi^2}{\alpha}-\mu)\frac{\psi^2}{\alpha}\frac{\alpha\mu}{2}}E_{2k}^{\mu}\right)^{K}(\bar{\gamma}^{\text{t}})^{-K\alpha\mu/2} \\
&+\left(\frac{R_{1k}R_{2k}}{(J_1J_2)^{\frac{\psi^2}{\alpha}}}\frac{2}{\alpha}\frac{\Gamma\left(\mu-\frac{\psi^2}{\alpha}\right)\Gamma(\mu)}{\frac{\psi^2}{\alpha}\frac{\psi^2}{2}}E_{2k}^{\psi^2/\alpha}\right)^{K}(\bar{\gamma}^{\text{t}})^{-Kq^2/2} \\
&+\left(\frac{R_{1k}R_{2k}}{(J_1J_2)^{\frac{\psi^2}{\alpha}}}\frac{2}{\alpha}\frac{\Gamma(\mu)}{\frac{\psi^2}{\alpha}(\frac{\psi^2}{\alpha}-\mu)\frac{\alpha\mu}{2}}E_{1k}^{\mu}\right)^{K}(\bar{\gamma}^{\text{t}})^{-K\alpha\mu/2} \\
&+\left(\frac{R_{1k}R_{2k}}{(J_1J_2)^{\frac{\psi^2}{\alpha}}}\frac{2}{\alpha}\frac{\Gamma(\mu)\Gamma(\mu-\frac{\psi^2}{\alpha})}{\frac{\psi^2}{\alpha}\frac{\psi^2}{2}}E_{1k}^{\psi^2/\alpha}\right)^{K}(\bar{\gamma}^{\text{t}})^{-Kq^2/2}.
\end{aligned} \tag{7.32}$$

The asymptotic outage probability can be expressed as $P_{\text{out}}^{\infty} = \mathcal{G}_c(\bar{\gamma}^{\text{t}})^{-\mathcal{G}_d}$, where $\mathcal{G}_c$ and $\mathcal{G}_d$ represent the array gain and diversity order, respectively. Here, the diversity order is found as $\mathcal{G}_d = \min\{K\frac{\alpha\mu}{2}, K\frac{\psi^2}{2}\}$, and it reveals that the system performance depends on either the fading parameters (α and μ) or the pointing error distribution parameter ψ in high SNR region. In other words, either the fading channel characteristics or the pointing accuracy determines the system performance for high SNRs. Moreover, it can be seen that the system performance is enhanced as the number of HAPS systems increase.

7.3.3 Capacity analysis

Ergodic system capacity can be defined as the average data rate achievable over a channel and for the proposed setup, it can be expressed as $C_{erg} = \frac{W}{2}E\left[\log_2\left(1+\gamma_{e2e,\ell}\right)\right]$, where W denotes the system bandwidth. By using $\gamma_{e2e,\ell} = \max\limits_{1\leq k\leq K}\left(\gamma_{e2e,k}\right)$ and the Jensen's inequality, C_{erg} can be upper bounded as

$$C_{erg} \leq C_{erg}^{u} = \frac{W}{2}\log_2\left(1+\max_{1\leq k\leq K} E\left[\gamma_{e2e,k}\right]\right). \tag{7.33}$$

Here, the first moment $E\left[\gamma_{e2e,k}\right]$ can also be tightly upper bounded by $E[\gamma_{e2e,k}^{u}]$. By using (7.15), $E[\gamma_{e2e,k}^{u}]$ can be found as follows:

$$\begin{aligned}E\left[\gamma_{e2e,k}^{u}\right] =& A_{1k}A_{2k}a_{2k}^{\psi^2/2}a_{1k}^{\psi^2/2}\\ &\times\frac{1}{(2\pi j)^2}\int_{\mathcal{L}_1}\int_{\mathcal{L}_2}\phi_0(\xi_1,\xi_2)\phi_1(\xi_1)\phi_2(\xi_2)\left(C_1 a_{2k}^{\frac{\alpha}{2}}\right)^{\xi_1}\left(C_2 a_{1k}^{\frac{\alpha}{2}}\right)^{\xi_2}\mathcal{I}_4 d\xi_1 d\xi_2,\end{aligned} \tag{7.34}$$

where $\phi_0(\xi_1,\xi_2) = \frac{1}{\Gamma\left(-\psi^2-\frac{\alpha}{2}\xi_1-\frac{\alpha}{2}\xi_2\right)}$ and $\mathcal{I}_4$ is written as

$$\begin{aligned}\mathcal{I}_4 &= \int_0^{\frac{1}{g_k}}\frac{z^{\psi^2+\frac{\alpha}{2}\xi_1+\frac{\alpha}{2}\xi_2}\left(\frac{1}{g_k}-z\right)^{-\psi^2-1-\frac{\alpha}{2}\xi_1-\frac{\alpha}{2}\xi_2}}{g_k^{\psi^2+1+\frac{\alpha}{2}\xi_1+\frac{\alpha}{2}\xi_2}}dz\\ &= \frac{\Gamma\left(-\psi^2-\frac{\alpha}{2}\xi_1-\frac{\alpha}{2}\xi_2\right)\Gamma\left(\psi^2+1+\frac{\alpha}{2}\xi_1+\frac{\alpha}{2}\xi_2\right)}{g_k^{\psi^2+1+\frac{\alpha}{2}\xi_1+\frac{\alpha}{2}\xi_2}},\end{aligned} \tag{7.35}$$

under the condition of $\mathcal{C}_4 : 1 > \mathcal{R}\left\{-\psi^2-\frac{\alpha}{2}\xi_1-\frac{\alpha}{2}\xi_2\right\} > 0$ [55, Eq. (3.191.1)]. Here, it can be seen that $\mathcal{C}_4$ does not contradict with $\mathcal{C}_1$ and $\mathcal{C}_2$ which are the conditions to evaluate the PDF of $\gamma^{u}_{e2e,k}$ in (7.15). After some mathematical manipulations, the first moment of $\gamma^{u}_{e2e,k}$ can be written in closed form as

$$E\left[\gamma^{u}_{e2e,k}\right] = \frac{A_{1k}A_{2k}(a_{2k}a_{1k})^{\frac{\psi^2}{2}}}{g_k^{\psi^2+1}} \mathrm{H}^{0,1:3,0:3,0}_{1,0:1,3:1,3}\left[\begin{array}{c|c} \frac{C_{1k}a_{2k}^{\alpha/2}}{g_k^{\alpha/2}} & V_3 \\ \frac{C_{2k}a_{1k}^{\alpha/2}}{g_k^{\alpha/2}} & V_4 \end{array}\right], \tag{7.36}$$

where $V_3=\{(-\psi^2,\frac{\alpha}{2},\frac{\alpha}{2})\}:\{(1,1)\}:\{(1,1)\}$, $V_4=\{-\}:\{(B_{1k},1),(0,1),(-\frac{\psi^2}{2},\frac{\alpha}{2})\}:\{(B_{2k},1),(0,1),(-\frac{\psi^2}{2},\frac{\alpha}{2})\}$. By replacing $E\left[\gamma_{e2e,k}\right]$ in (7.33) by $E\left[\gamma^{u}_{e2e,k}\right]$, the upper bound for ergodic capacity of the system can be obtained.

7.4 Numerical Results

In this section, outage and ergodic capacity performance of the THz NTN are illustrated and theoretical findings are validated through Monte-Carlo simulations. Altitudes of satellite, HAPS systems, and ground station receiver are assumed to be 500 km, 30 km, and 0 km, respectively. It is assumed that the zenith angles in the first and second hops of all branches are taken as $20°$ and $10°$, respectively. The operation frequency of the system is 295 GHz while the atmospheric attenuation is calculated as shown in ITU Rec. 676-13 [13] for dry and humid air under standard atmospheric conditions provided in [73]. In addition, the system bandwidth is $W=1$ GHz, and the noise power is given by $\sigma_n^2 = k_{\mathrm{B}}TW\mathcal{F}_n = -71.83$ dBm, where $k_{\mathrm{B}} = 1.38\times10^{-23}$ $\mathrm{m^2kgs^{-2}K^{-1}}$, $T=300$ K, and $\mathcal{F}_n = 12$ dB are the Boltzmann's constant, thermal noise temperature, and noise figure, respectively [46, 124]. Also, antenna gains for the first hop and the second hop are set to $\mathcal{G}^{\mathrm{t}}_{ik} = 60$ dBi and $\mathcal{G}^{\mathrm{r}}_{ik} = 60$ dBi, $i\in\{1,2\}$ [125]. The fading parameters are assumed to be $\alpha=6$ and $\mu=4$ (strong LOS), whereas the pointing error parameters are taken as $\psi=4.422$ and $A_0=0.74$. Moreover, for all branches, total hardware impairment levels are taken as $\kappa^2_{1k}=\kappa^2_{2k}$, $\forall k$. Finally, transmit powers and average transmit SNRs are taken as $P_{1\ell}=P_{2\ell}=P$ and $\bar{\gamma}^{\mathrm{t}}_{1\ell}=\bar{\gamma}^{\mathrm{t}}_{2\ell}=\bar{\gamma}^{\mathrm{t}}$, respectively.

In Fig. 7.2, the PDF and CDF curves of the end-to-end SNR for the k-th branch are illustrated under dry atmospheric conditions for total hardware impairment level $\kappa^2_{ik}=0.01$. Here, the absorption loss values are evaluated as $L^{\mathrm{abs}}_{1k}=2.885\times10^{-5}$ dB

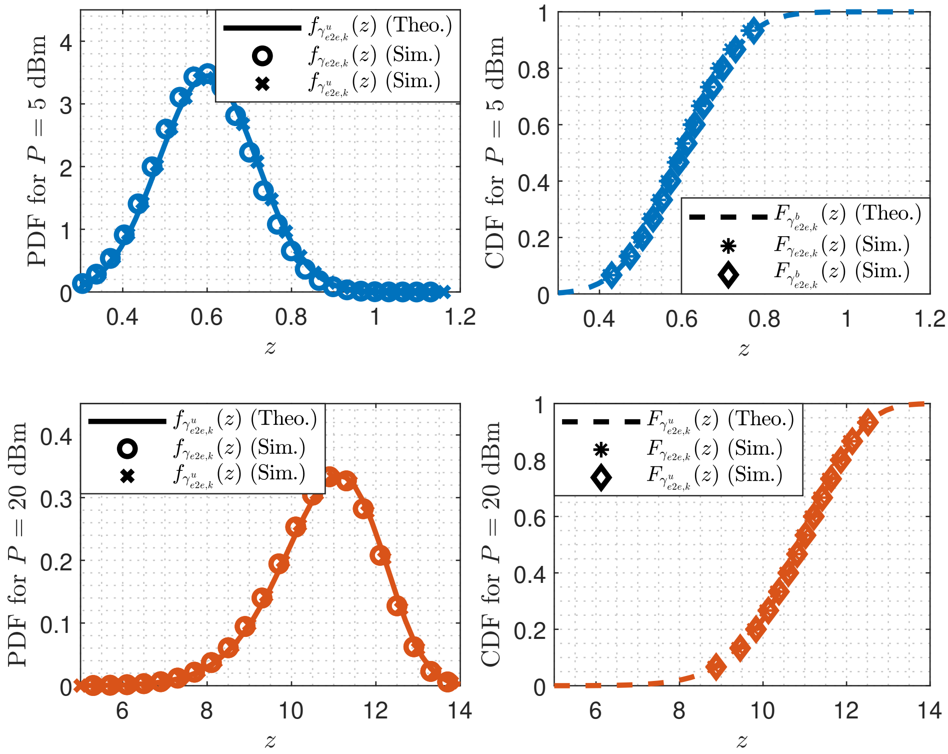

Figure 7.2 : The PDF and CDF curves for $\gamma_{e2e,k}$ and $\gamma^u_{e2e,k}$ for $\kappa^2_{ik} = 0.01$ under dry atmospheric conditions.

and $L^{\text{abs}}_{2k} = 0.14$ dB. It can be seen from the figure that simulation results match well with the theoretical results both for PDF and CDF curves of $\gamma^u_{e2e,k}$. Moreover, it can be observed that theoretical curves for $\gamma^u_{e2e,k}$ are slightly closer to the simulated PDF and CDF curves of $\gamma_{e2e,k}$ at $P = 20$ dBm transmit power. Hence, it can be concluded that $\gamma^u_{e2e,k}$ tightly upper bounds $\gamma_{e2e,k}$ for high SNR region.

The lower bound and asymptotic outage probability curves are shown in Fig. 7.3 for $K = 1,2,3$ under dry atmospheric conditions. For total hardware impairment level, two different settings are considered such as $\kappa^2_{ik} = 0$ and $\kappa^2_{ik} = 0.05$, where the first one corresponds to the ideal hardware case. It is shown that the asymptotic curves perfectly match with the theoretical ones and that the theoretical curves set lower bound to the simulation results since $\gamma_{e2e,k}$ is upper bounded by $\gamma^u_{e2e,k}$. Comparing the results for ideal hardware and non-ideal hardware, it can be observed that hardware impairment results in ~ 1 dBm power loss. Also, as the number of HAPS system increases, the system performance is enhanced since the diversity is introduced. Additionally, it can

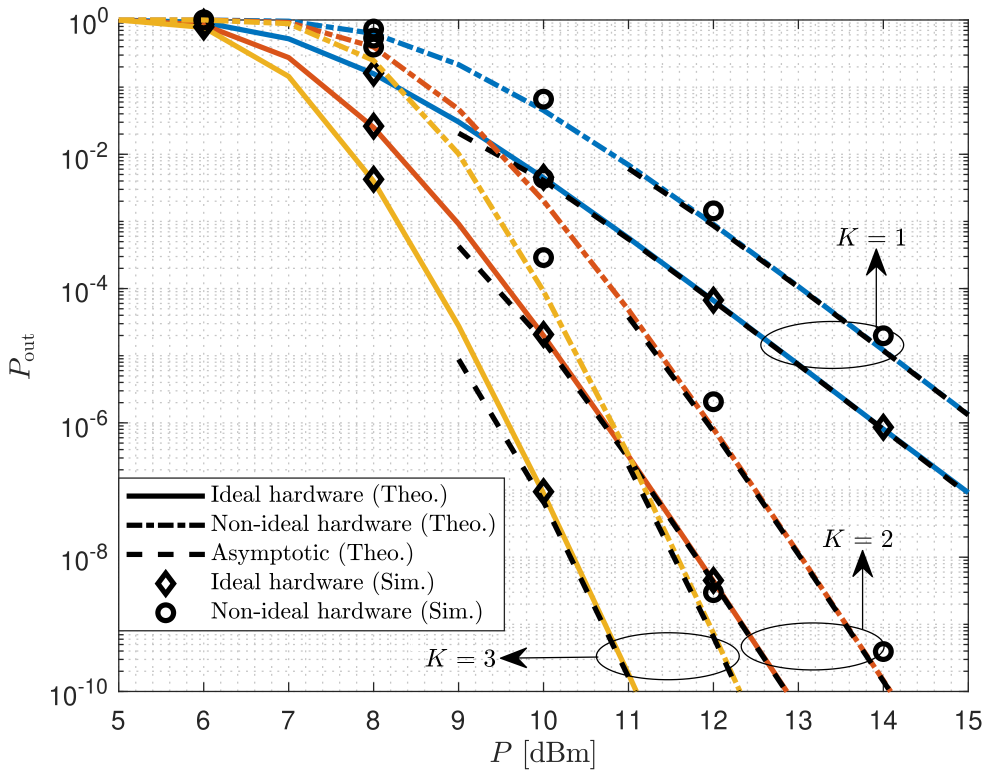

Figure 7.3 : Outage probability curves for ideal hardware and non-ideal hardware ($\kappa_{ik}^2 = 0.05$) for $K = 1, 2, 3$ and dry atmosphere.

be deduced that the power loss caused by the hardware impairment can be tolerated by increasing the number of HAPS systems.

In Fig. 7.4, outage performance of the system is illustrated with respect to the zenith angle in the second hop ζ_{2k} for $K = 1, 2, 3$, $P = 10$ dBm, and $\kappa_{ik} = 0.001$ for different atmospheric conditions. It can be inferred from the figure that the outage performance remains the same under dry atmosphere up to $\sim 70°$ of zenith angle. For $\zeta_{2k} > 70°$, outage probability increases. In contrast, under humid atmospheric conditions, outage performance deteriorates for $\zeta_{2k} > 30°$, which shows that the system performance is susceptible to zenith angle in the second hop, particularly under humid atmospheric conditions. This arises from the increased zenith angle as it extends the transmission path. and severer absorption loss due to humid air in the second hop.

Outage performance of the system with respect to κ_{ik} is illustrated in Fig. 7.5 for $K = 1, 2$ and $P = 10, 15$ dBm under dry atmospheric conditions. It can be seen that up to a certain level of impairment, increasing the number of HAPS systems improves

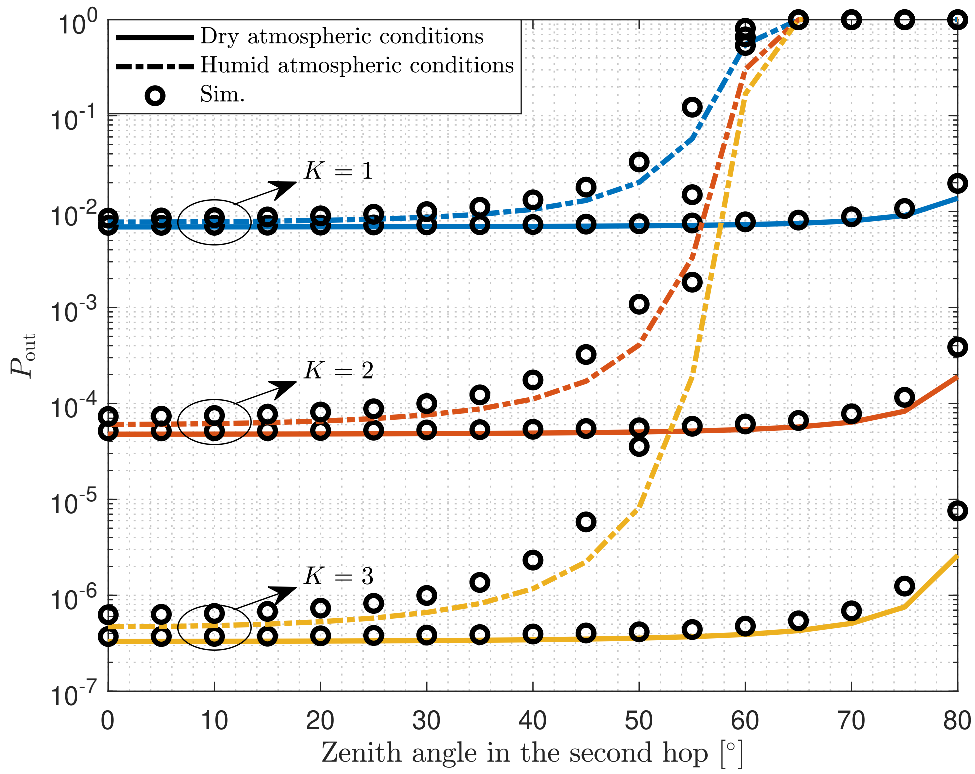

Figure 7.4 : Outage probability with respect to zenith angle in the second hop for $K = 1,2,3$, $P = 10$ dBm, and $\kappa_{ik}^2 = 0.001$ under dry and humid atmospheric conditions.

the outage performance of the system. For very high impairment levels, the system is in outage. Moreover, for $P = 10$ dBm transmit power, an outage probability about 2×10^{-5} can be achieved by employing 2 HAPS systems, whereas the minimum achievable outage probability is about 4.5×10^{-2} for single HAPS system. This performance improvement originates from diversity introduced by the multiple HAPS systems.

Ergodic capacity performance of the system under humid atmospheric conditions is illustrated in Fig. 7.6 for total hardware impairment levels $\kappa_{ik}^2 = 0.001, 0.01, 0.05$ for $K = 2$ HAPS systems. Here, the absorption loss values are found as $L_{1k}^{\text{abs}} = 2.889 \times 10^{-5}$ dB and $L_{2k}^{\text{abs}} = 9.083$ dB under humid atmospheric conditions. The figure demonstrates that the derived theoretical expression provides a tight upper bound for the simulations. It can be seen from the figure that for $\kappa_{ik}^2 = 0.001$, $\kappa_{ik}^2 = 0.01$, and $\kappa_{ik}^2 = 0.05$, maximum achievable capacity levels are almost 4 Gbit/s, 2.4 Gbit/s, and 1.3

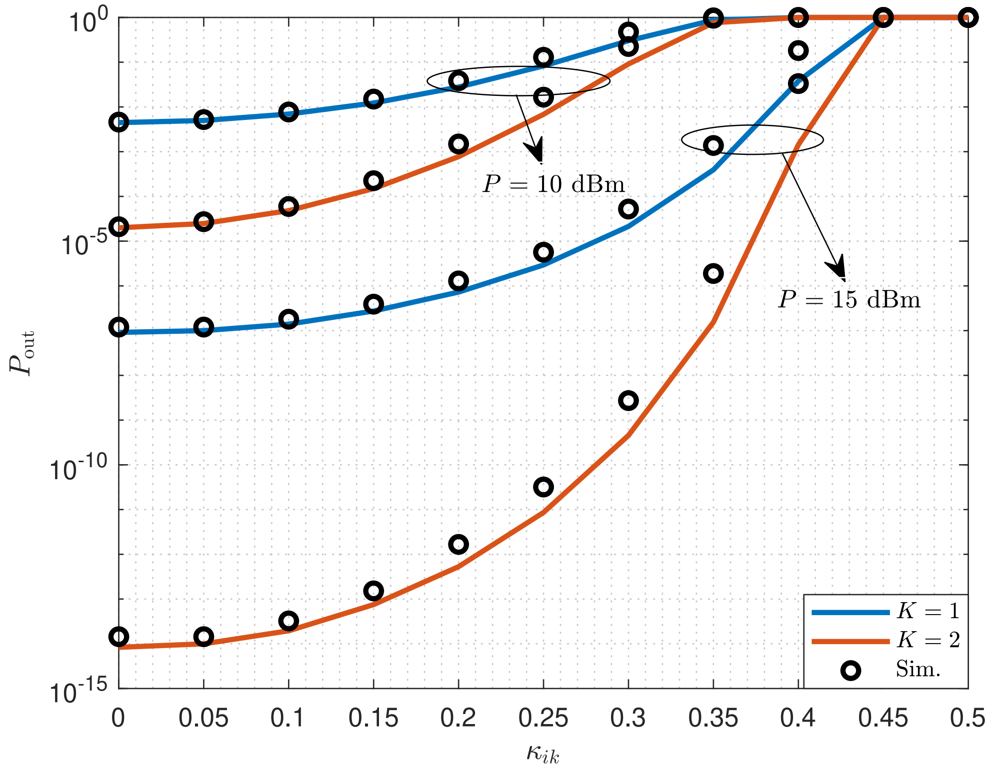

Figure 7.5 : Outage probability curves under dry atmospheric conditions for $K = 1, 2$ and $P = 10, 15$ dBm for different κ_{ik} values.

Gbit/s, respectively. Hence, it can be concluded that higher total hardware impairment level results in lower ergodic capacity.

In Fig. 7.7, ergodic capacity curves with respect to κ_{ik} are shown for $P = 20, 30$ dBm and $K = 2$ under humid atmospheric conditions. It can be observed from the figure that higher transmit power significantly enhances the system capacity especially for low κ_{ik}. Moreover, it can be seen that the curves for $P = 20$ dBm and $P = 30$ dBm meet at higher values of κ_{ik}. This originates from the fact that higher κ_{ik} results in lower capacity limit due to impairment (see Fig. 7.6), and the capacity cannot be enhanced even with higher transmit power as the system has already reached the maximum achievable capacity.

7.5 Concluding Remarks

This chapter presents the outage, asymptotic outage, and ergodic capacity analyses for a multi-HAPS THz NTN under hardware impairments. In the system model, it

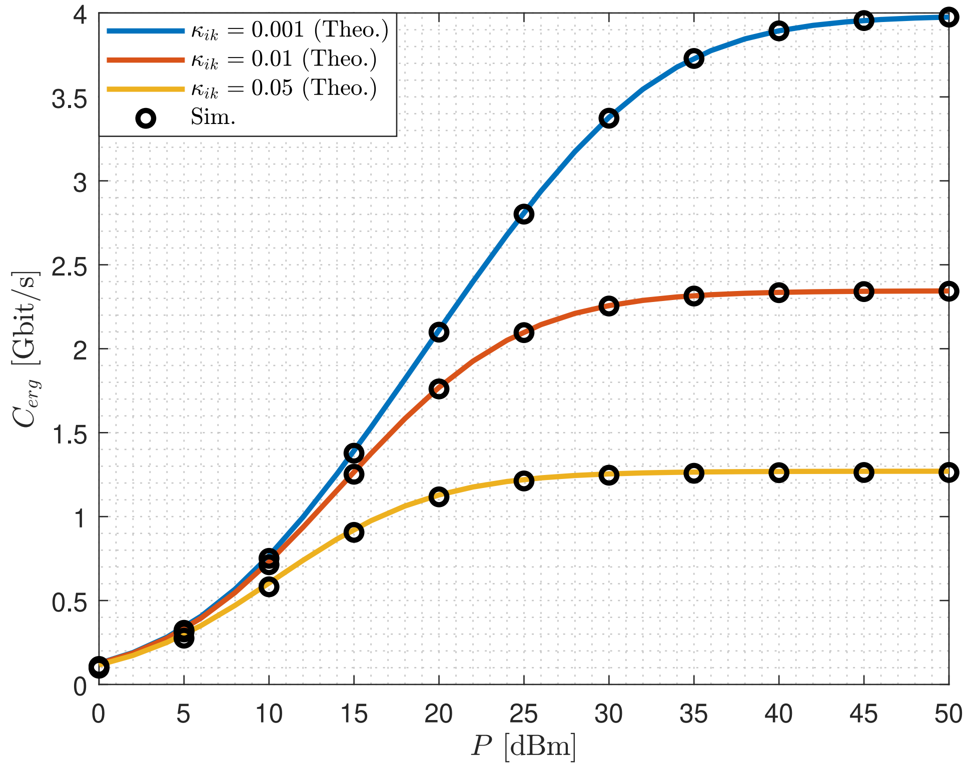

Figure 7.6 : Ergodic capacity curves for $K = 2$ and humid atmosphere.

is assumed that variable-gain AF is employed at the HAPS nodes, and the ground station selects the HAPS system which offers the maximum end-to-end SNR for transmission. It is considered that THz channels experience α-μ fading, pointing errors, and absorption loss. To obtain the closed-form outage probability and capacity expressions, the PDF, CDF, and asymptotic CDF of the upper bound for the end-to-end SNR are derived. Impacts of total hardware impairment level, number of HAPS systems, zenith angles, and humidity conditions on the system performance are examined. The results have demonstrated that hardware impairments lead to ~ 1 dBm power loss in outage performance, which can be tolerated by increasing the number of HAPS systems. The asymptotic analysis revealed that the system performance is determined by either fading or pointing error characteristics at high SNRs. It is also shown that the outage probability depends on the humidity conditions for zenith angles higher than 30° in HAPS-to-ground links. Furthermore, this highlights the importance of atmospheric modeling in THz communication system design. Moreover, it is illustrated that hardware impairments result in lower capacity limits and also that

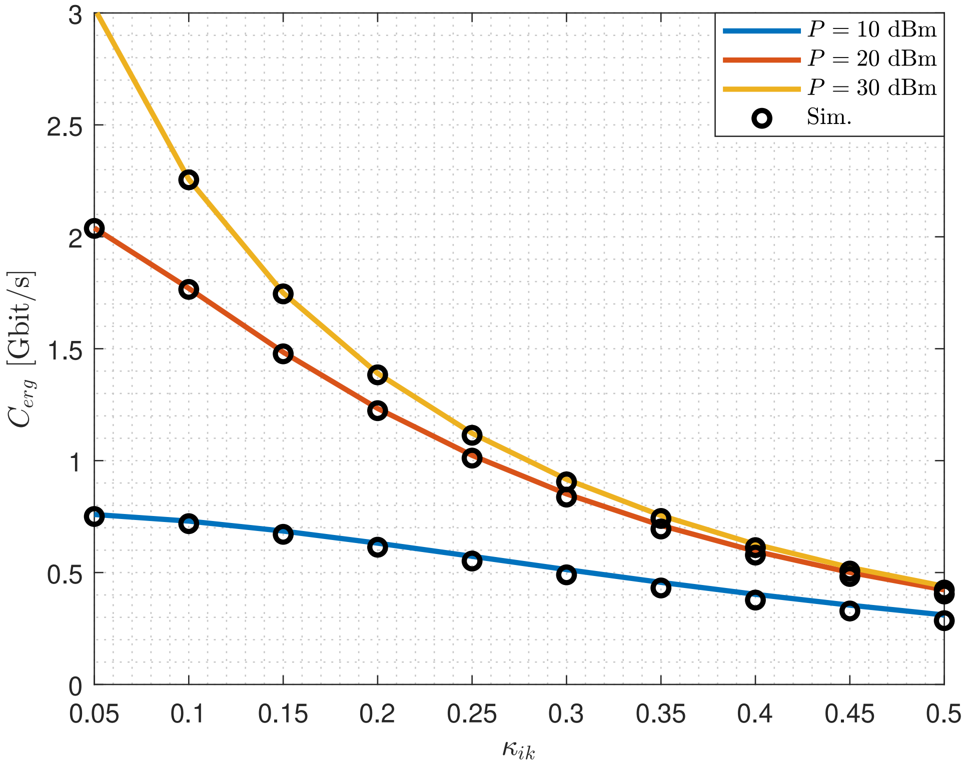

Figure 7.7 : Ergodic capacity curves under humid atmospheric conditions for $P = 10, 20, 30$ dBm, $K = 2$, and different κ_{ik} values.

the maximum achievable capacity is 4 Gbit/s for a total hardware impairment level of 0.001.

8. NTNs IN THE THz BAND WITH I/Q IMBALANCE

As mentioned in the previous chapters, NTNs are one of the most important enablers of 6G and beyond systems as they provide global connectivity. Utilizing THz frequencies in NTNs can offer incredibly wide bands to achieve extreme data rates. However, together with the challenges due to free-space loss, atmospheric absorption, and pointing errors, hardware imperfections, such as in-phase and quadrature (I/Q) imbalance, have a non-negligible impact on system performance. I/Q imbalance is observed in these systems due to the mismatches in the amplitude and/or phase between the in-phase and quadrature components. This leads to distortion in the transmitted and received signals, resulting in significant performance loss and limitations. In the current literature, the impact of I/Q imbalance on the performance of dual-hop THz NTN system remains unexplored. Therefore, in this chapter, SER for M-PSK modulation and ergodic capacity analyses of a dual-hop multi-HAPS THz NTN system are presented.[1] Throughout the derivations, statistics of the end-to-end SNR are obtained. By using these statistics, SER and capacity expressions are derived.

8.1 System Model

In this chapter, a downlink NTN utilizing THz frequencies is investigated. In the considered setup, it is assumed that the LOS link is not available between satellite (S) and destination (D). Therefore, K number of HAPS systems (H_k, $k = 1, 2, ...K$) are employed to connect S with D, forming a dual-hop K-branch communication system as depicted in Fig. 8.1. In this system, the transmission is completed in orthogonal time slots, and in the first time slot, S transmits information signal to all HAPS systems. Thereafter, each HAPS system transmits its data to D by using the variable-gain AF relaying [6] while S remains silent. The received signals at D are combined with the

[1]This chapter is based on the paper entitled "Multi-HAPS THz satellite communication: Error and capacity analyses under I/Q imbalance" published in *IEEE Sensors Journal* [59].

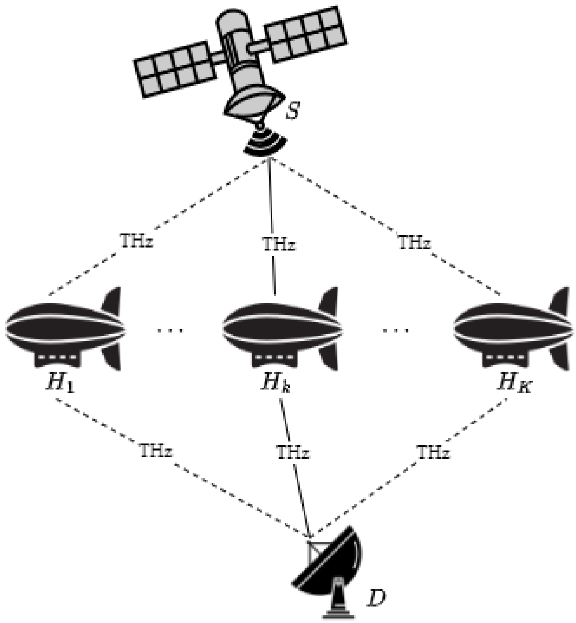

Figure 8.1 : Multi-HAPS aided THz NTN.

MRC technique. Also, it is assumed that perfect synchronization in both time and frequency domains is established. In the considered system, it is assumed that M-PSK modulation is utilized. In the i-th hop of the k-th branch for $i \in \{1,2\}$ and $1 \leq k \leq K$, the received signal can be written as

$$y_{ik} = \sqrt{\frac{P_{ik}}{L_{ik}}} h_{ik}^{\mathrm{fp}} x_{ik} + n_{ik}, \tag{8.1}$$

where P_{ik} and L_{ik} are the transmit power and the signal attenuation, respectively. $n_{ik} \sim \mathcal{CN}\left(0, \sigma_{n_{ik}}^2\right)$ is the additive Gaussian noise observed at the receiver, where $\sigma_{n_{ik}}^2$ denotes the noise power. Moreover, h_{ik}^{fp} represents the independent identically distributed joint channel coefficient which depends on the small-scale fading term h_{ik}^{f} and the pointing error term h_{ik}^{p}. Furthermore, x_{ik} is the transmitted complex signal of unit power. For the first hop, x_{1k} is modulated signal transmitted from S, and for the second hop, $x_{2k} = G_k y_{1k}$ is the amplified and re-transmitted signal from H_k. Here, $G_k = 1/\sqrt{\frac{P_{1k}}{L_{1k}} \left| h_{1k}^{\mathrm{fp}} \right|^2 + \sigma_{n_{ik}}^2}$ stands for the amplification factor in the k-th branch, depending on the channel coefficient h_{1k}^{fp}.

In the system of interest, end-to-end SNR for the k-th branch can be written as $\gamma_{e2e,k} = \frac{\gamma_{1k}\gamma_{2k}}{\gamma_{1k}+\gamma_{2k}}$, where $\gamma_{ik} = \frac{P_{ik}}{L_{ik}\sigma^2_{n_{ik}}}\left|h^{\text{fp}}_{ik}\right|^2$ shows the received signal's SNR for the i-th hop of the k-th branch. The overall SNR is expressed as

$$\gamma_{\text{MRC}} = \sum_{k=1}^{K} \gamma_{e2e,k}. \tag{8.2}$$

8.1.1 I/Q imbalance at the destination

At the destination, phase and/or amplitude mismatch cause I/Q imbalance, resulting in a performance degradation. In the presence of I/Q imbalance, the received signal at the destination from the k-th HAPS system can be written as

$$\begin{aligned} y^{\text{IQ}}_{2k} &= U_1\left(\sqrt{\frac{P_{2k}}{L_{2k}}}h^{\text{fp}}_{2k}x_{2k}+n_{2k}\right)+U_2\left(\sqrt{\frac{P_{2k}}{L_{2k}}}h^{\text{fp}}_{2k}x_{2k}+n_{2k}\right)^* \\ &= U_1\sqrt{\frac{P_{1k}}{L_{1k}}}\sqrt{\frac{P_{2k}}{L_{2k}}}G_k h^{\text{fp}}_{1k}h^{\text{fp}}_{2k}x_{1k}+U_1\sqrt{\frac{P_{2k}}{L_{2k}}}G_k h^{\text{fp}}_{2k}n_{1k} \\ &+U_2\sqrt{\frac{P_{1k}}{L_{1k}}}\sqrt{\frac{P_{2k}}{L_{2k}}}G_k h^{\text{fp}}_{1k}h^{\text{fp}}_{2k}x^*_{1k} \\ &+U_2\sqrt{\frac{P_{2k}}{L_{2k}}}G_k h^{\text{fp}}_{2k}n^*_{1k}+U_2 n^*_{2k}, \end{aligned} \tag{8.3}$$

where $U_1 = \frac{1+g_D e^{-j\theta_D}}{2}$ and $U_2 = \frac{1-g_D e^{j\theta_D}}{2}$ [63]. In this formulation, g_D and θ_D are the amplitude and phase mismatches, respectively. From (8.3), the end-to-end SNR under I/Q imbalance can be obtained after some manipulations as

$$\gamma^{\text{IQ}}_{e2e,k} \approx \frac{\gamma_{1k}\gamma_{2k}}{\frac{|U_2|^2}{|U_1|^2}\gamma_{1k}\gamma_{2k}+\frac{|U_1|^2+|U_2|^2}{|U_1|^2}\gamma_{1k}+\frac{|U_1|^2+|U_2|^2}{|U_1|^2}\gamma_{2k}}. \tag{8.4}$$

Please notice here that for $g_D = 1$ and $\theta = 0$ (or equivalently $U_1 = 1$ and $U_2 = 0$), the SNR expression in (8.4) reduces to the perfect hardware scenario, i.e. $\gamma^{\text{IQ}}_{e2e,k} = \gamma_{e2e,k}$. The overall SNR in the presence of I/Q imbalance $\gamma^{\text{IQ}}_{\text{MRC}}$ can be expressed as in (8.2) by replacing $\gamma_{e2e,k}$ by $\gamma^{\text{IQ}}_{e2e,k}$.

8.1.2 Attenuation

Signal attenuation can be divided into two groups: free-space loss and absorption loss. The free-space loss occurs due to the propagation of the EM waves, whereas absorption loss is caused by the content of the transmission medium which contains water vapour and oxygen as the principal absorbers. By taking the transmitter and receiver antenna gains ($\mathcal{G}_{ik}^{\mathrm{t}}$ and $\mathcal{G}_{ik}^{\mathrm{r}}$, respectively) into account, total attenuation observed in the i-th hop of the k-th branch can be written as

$$L_{ik} = \frac{L_{ik}^{\mathrm{fsl}} L_{ik}^{\mathrm{abs}}}{\mathcal{G}_{ik}^{\mathrm{t}} \mathcal{G}_{ik}^{\mathrm{r}}}. \tag{8.5}$$

In this formulation, L_{ik}^{fsl} denotes the free-space loss, and it is directly related to frequency f (or wavelength λ) and link distance d_{ik} as $L_{ik}^{\mathrm{fsl}} = \left(\frac{4\pi d_{ik}}{\lambda}\right)^2$. Here, the link distance d_{ik} is found depending on the zenith angle ζ_{ik} and vertical distance between transmitter and receiver.[2] Furthermore, L_{ik}^{abs} is the absorption loss which can be modeled as a function of atmospheric humidity, pressure, and temperature which depend on altitude. In the literature, several models are proposed to evaluate the absorption loss [72, 126]. In this chapter, [13] is considered in the calculation of atmospheric absorption loss with the standard atmospheric conditions provided in [73].

8.1.3 Fading and pointing error

In this study, the small-scale fading coefficients ($h_{ik}^{\mathrm{f}},\ k = 1,2,...,K,\ i = 1,2$) are modelled as independent identically distributed α-μ random variables [58], where α and μ are the distribution parameters. Besides small scale fading, in THz communication systems, pointing errors are observed due to misalignment between transmitter and receiver antennas. When the antennas are not perfectly aligned, received power decreases, resulting in performance degradation. Here, the pointing error coefficient is denoted as h_{ik}^{p}, and its PDF is given as $f_{h_{ik}^{\mathrm{p}}}(z) = z^{\psi^2-1}\psi^2/A_0^{\psi^2}$, for $0 \leq z \leq A_0$ [84], where $\psi = \frac{\sigma_{eq}}{2\sigma_s}$. In this formulation, σ_s is the distribution parameter of Rayleigh distributed misalignment vector. $\sigma_{eq} = \sqrt{\sigma_d^2 \frac{\sqrt{\pi}\mathrm{erf}(c)}{2c\exp(-c^2)}}$ and $A_0 = \mathrm{erf}^2(c)$ represent the equivalent beamwidth and the fraction of the power received in the presence of perfect alignment, respectively, and $c = \frac{\sqrt{\pi}a}{\sqrt{2}\sigma_d}$. Here, a and σ_d are receiver aperture and transmitter's beam footprint at the receiver plane, respectively. Hence, the joint channel coefficient can be expressed as $h_{ik}^{\mathrm{fp}} = h_{ik}^{\mathrm{f}} h_{ik}^{\mathrm{p}}$. The PDF of the envelope

[2]The zenith angle is the angle between the propagation path and the vertical axis.

of h_{ik}^{fp} can be given by [50, Eq. (26)]

$$f_{|h_{ik}^{\mathrm{fp}}|}(z) = \frac{\mu^{\psi^2/\alpha}\psi^2 A_0^{-\psi^2}}{(\hat{h}_{ik}^{\mathrm{f}})^{\psi^2}\Gamma(\mu)} z^{\psi^2-1}\Gamma\left(\mu - \frac{\psi^2}{\alpha}, \frac{\mu z^\alpha}{(\hat{h}_{ik}^{\mathrm{f}})^\alpha A_0^\alpha}\right), \ z \geq 0, \tag{8.6}$$

where $\hat{h}_{ik}^{\mathrm{f}} = \sqrt[\alpha]{E\left[\left|h_{ik}^{\mathrm{f}}\right|^\alpha\right]}$ is the α-root mean value of the small-scale fading coefficient. Accordingly, the statistics of γ_{ik} can be derived through the statistics of h_{ik}^{fp}. The PDF of γ_{ik} is found by using (8.6) as

$$f_{\gamma_{ik}}(z) = A_{ik} z^{\frac{\psi^2}{2}-1}\Gamma\left(B_{ik}, C_{ik} z^{\frac{\alpha}{2}}\right), \ z \geq 0, \tag{8.7}$$

where $A_{ik} = \frac{\psi^2\mu^{\psi^2/\alpha}\left(L_{ik}\sigma_{n_{ik}}^2/P_{ik}\right)^{\frac{\psi^2}{2}}}{2A_0^{\psi^2}(\hat{h}_{ik}^{\mathrm{f}})^{\psi^2}\Gamma(\mu)}$, $B_{ik} = \mu - \frac{\psi^2}{\alpha}$ and $C_{ik} = \frac{\mu\left(L_{ik}\sigma_{n_{ik}}^2/P_{ik}\right)^{\frac{\alpha}{2}}}{(\hat{h}_{ik}^{\mathrm{f}})^\alpha A_0^\alpha}$. From (8.7), the CDF of γ_{ik} can be obtained as [114, Eq. (14)]

$$F_{\gamma_{ik}}(z) = \frac{\gamma\left(\mu, C_{ik} z^{\frac{\alpha}{2}}\right)}{\Gamma(\mu)} + \frac{C_{ik}^{\frac{\psi^2}{\alpha}}}{\Gamma(\mu)} z^{\frac{\psi^2}{2}}\Gamma\left(B_{ik}, C_{ik} z^{\frac{\alpha}{2}}\right), \ z \geq 0. \tag{8.8}$$

8.2 Performance Analyses

In this subsection, error and capacity analyses are performed in the presence of perfect hardware and I/Q imbalance at the destination.

8.2.1 Error analysis

8.2.1.1 Exact SER

SER of an M-PSK system can be found by the following well-known formula [57]

$$P_e = \frac{1}{\pi}\int_0^\Theta \mathcal{M}_{\gamma_{\mathrm{MRC}}}\left(\frac{c_{\mathrm{MPSK}}}{\sin^2(\theta)}\right) d\theta, \tag{8.9}$$

where $\Theta = \pi\frac{M-1}{M}$ and $c_{\mathrm{MPSK}} = \sin^2(\pi/M)$. Here, the MGF of γ_{MRC} can be rewritten by using (8.2) as

$$\mathcal{M}_{\gamma_{\mathrm{MRC}}}(s) = \prod_{k=1}^{K}\mathcal{M}_{\gamma_{e2e,k}}(s), \tag{8.10}$$

where the exact expressions for the MGF of $\gamma_{e2e,k}$ can be found by using its CDF which is given by the following theorem.[3]

[3]It is important to note that the CDF expression given in Theorem 1 allows studying the proposed system for different diversity combining techniques including SC and MRC.

Theorem 1: The CDF of $\gamma_{e2e,k}$ can be written as

$$
\begin{aligned}
F_{\gamma_{e2e,k}}(z) &= \frac{\gamma\left(\mu, C_{2k} z^{\alpha/2}\right)}{\Gamma(\mu)} + \frac{C_{2k}^{\psi^2/\alpha}}{\Gamma(\mu)} z^{\psi^2/2} \Gamma\left(B_{2k}, C_{2k} z^{\alpha/2}\right) \\
&+ \frac{A_{2k}}{\Gamma(\mu)} z^{\frac{\psi^2}{2}} \mathrm{H}^{0,0:2,1:3,0}_{1,0:1,3:1,3}\left[\begin{matrix} C_{1k} z^{\frac{\alpha}{2}} \\ C_{2k} z^{\frac{\alpha}{2}} \end{matrix} \middle| \begin{matrix} V_1 \\ V_2 \end{matrix}\right] \\
&+ \frac{C_{1k}^{\frac{\psi^2}{\alpha}} A_{2k} z^{\psi^2}}{\Gamma(\mu)} \mathrm{H}^{0,0:3,0:3,0}_{1,0:1,3:1,3}\left[\begin{matrix} C_{1k} z^{\frac{\alpha}{2}} \\ C_{2k} z^{\frac{\alpha}{2}} \end{matrix} \middle| \begin{matrix} V_3 \\ V_4 \end{matrix}\right], \; z \geq 0,
\end{aligned}
\tag{8.11}
$$

where $V_1 = \{(1-\frac{\psi^2}{2}, \frac{\alpha}{2}, \frac{\alpha}{2})\} : \{(1,1)\} : \{(1,1)\}$, $V_2 = \{-\} : \{(\mu,1), (1,\frac{\alpha}{2}), (0,1)\} : \{(B_{2k},1), (0,1), (-\frac{\psi^2}{2}, \frac{\alpha}{2})\}$, $V_3 = \{(1-\psi^2, \frac{\alpha}{2}, \frac{\alpha}{2})\} : \{(1,1)\} : \{(1,1)\}$, $V_4 = \{-\} : \{(B_{1k},1), (0,1), (1-\frac{\psi^2}{2}, \frac{\alpha}{2})\} : \{(B_{2k},1), (0,1), (-\frac{\psi^2}{2}, \frac{\alpha}{2})\}$.

Proof: Please see Appendix A.

By employing (8.11), the exact expression for $\mathcal{M}_{\gamma_{e2e,k}}(s)$ can be given by the following theorem.

Theorem 2: The MGF of $\gamma_{e2e,k}$ can be expressed as

$$
\begin{aligned}
\mathcal{M}_{\gamma_{e2e,k}}(s) &= \frac{1}{\Gamma(\mu)} \mathrm{H}^{1,2}_{2,2}\left[\frac{C_{2k}}{s^{\frac{\alpha}{2}}} \middle| \begin{matrix} (1,1), (0,\frac{\alpha}{2}) \\ (\mu,1), (0,1) \end{matrix}\right] \\
&+ \frac{C_{2k}^{\frac{\psi^2}{\alpha}}}{\Gamma(\mu)} \left(\frac{1}{s}\right)^{\frac{\psi^2}{2}} \mathrm{H}^{2,1}_{2,2}\left[\frac{C_{2k}}{s^{\frac{\alpha}{2}}} \middle| \begin{matrix} (-\frac{\psi^2}{2}, \frac{\alpha}{2}), (1,1) \\ (B_{2k},1), (0,1) \end{matrix}\right] \\
&+ \frac{A_{2k}}{\Gamma(\mu)} \left(\frac{1}{s}\right)^{\frac{\psi^2}{2}} \mathrm{H}^{0,1:2,1:3,0}_{2,0:1,3:1,3}\left[\begin{matrix} C_{1k} s^{-\alpha/2} \\ C_{2k} s^{-\alpha/2} \end{matrix} \middle| \begin{matrix} V_5 \\ V_6 \end{matrix}\right] \\
&+ \frac{C_{1k}^{\frac{\psi^2}{\alpha}} A_{2k}}{\Gamma(\mu)} \left(\frac{1}{s}\right)^{\psi^2} \mathrm{H}^{0,1:3,0:3,0}_{2,0:1,3:1,3}\left[\begin{matrix} C_{1k} s^{-\alpha/2} \\ C_{2k} s^{-\alpha/2} \end{matrix} \middle| \begin{matrix} V_7 \\ V_8 \end{matrix}\right],
\end{aligned}
\tag{8.12}
$$

where $V_5 = \{(-\frac{\psi^2}{2}, \frac{\alpha}{2}, \frac{\alpha}{2}), (1-\frac{\psi^2}{2}, \frac{\alpha}{2}, \frac{\alpha}{2})\} : \{(1,1)\} : \{(1,1)\}$, $V_6 = \{-\} : \{(\mu,1), (1,\frac{\alpha}{2}), (0,1)\} : \{(B_{2k},1), (0,1), (-\frac{\psi^2}{2}, \frac{\alpha}{2})\}$, $V_7 = \{(-\psi^2, \frac{\alpha}{2}, \frac{\alpha}{2}), (1-\psi^2, \frac{\alpha}{2}, \frac{\alpha}{2})\} : \{(1,1)\} : \{(1,1)\}$, $V_8 = \{-\} : \{(B_{1k},1), (0,1), (1-\frac{\psi^2}{2}, \frac{\alpha}{2})\} : \{(B_{2k},1), (0,1), (-\frac{\psi^2}{2}, \frac{\alpha}{2})\}$.

Proof: Please see Appendix B.

By substituting (8.12) in (8.10), the MGF of the overall SNR can be found. In order to evaluate the SER for M-PSK modulation in the closed form, following simplified expression can be used [117, Eq. (10)]:

$$P_e \approx \left(\frac{\Theta}{2\pi}-\frac{1}{6}\right)\mathcal{M}_{\gamma_{\mathrm{MRC}}}(c_{\mathrm{MPSK}})+\frac{1}{4}\mathcal{M}_{\gamma_{\mathrm{MRC}}}\left(\frac{4}{3}c_{\mathrm{MPSK}}\right)+\left(\frac{\Theta}{2\pi}-\frac{1}{4}\right)\mathcal{M}_{\gamma_{\mathrm{MRC}}}\left(\frac{c_{\mathrm{MPSK}}}{\sin^2\Theta}\right). \tag{8.13}$$

It is worth mentioning that (8.13) can be accurately evaluated by using the implementations for the uni-variate Fox-H function and bi-variate Fox-H function in MATLAB or MATHEMATICA [127–129].

8.2.1.2 SER lower bound

The overall SNR can be upper bounded as $\gamma_{\mathrm{MRC}} \leq \gamma_{\mathrm{MRC}}^{b_1} = \sum_{k=1}^{K}\gamma_{e2e,k}^{b_1}$, where $\gamma_{e2e,k}^{b_1} = \min(\gamma_{1k},\gamma_{2k})$ shows the upper bound for the end-to-end SNR. The approximate CDF of $\gamma_{e2e,k}^{b_1}$ is given by $F_{\gamma_{e2e,k}^{b_1}}(z) \approx F_{\gamma_{1k}}(z)+F_{\gamma_{2k}}(z)$, and the corresponding MGF is expressed as

$$\mathcal{M}_{\gamma_{e2e,k}^{b_1}}(s) \approx s\mathcal{L}\{F_{\gamma_{1k}}(z)\}+s\mathcal{L}\{F_{\gamma_{2k}}(z)\}. \tag{8.14}$$

Here, the Laplace transform of $F_{\gamma_{ik}}(z)$ for $i\in\{1,2\}$ can be obtained as

$$\mathcal{L}\{F_{\gamma_{ik}}(z)\} = \frac{\mathcal{T}_1}{\Gamma(\mu)}+C_{ik}^{\psi^2/\alpha}\frac{\mathcal{T}_2}{\Gamma(\mu)}, \tag{8.15}$$

where $\mathcal{T}_1 = \int_0^\infty \gamma\left(\mu, C_{ik}z^{\frac{\alpha}{2}}\right)e^{-sz}dz$, $\mathcal{T}_2 = \int_0^\infty z^{\frac{\psi^2}{2}}\Gamma\left(B_{ik}, C_{ik}z^{\frac{\alpha}{2}}\right)e^{-sz}dz$. By using the Meijer-G representations of the exponential function [118, Eq. (01.03.26.0004.01)] and lower incomplete Gamma function [118, Eq. (06.06.26.0004.01)], [116, Eq. (45.0.1)], $\mathcal{T}_1$ can be evaluated with the aid of [118, Eq. (07.34.21.0013.01)] as

$$\mathcal{T}_1 = \int_0^\infty \mathrm{G}_{0,1}^{1,0}\left[sz\,\middle|\,\begin{matrix}-\\0\end{matrix}\right]\mathrm{G}_{1,2}^{1,1}\left[C_{ik}z^{\frac{\ell}{\rho}}\,\middle|\,\begin{matrix}1\\\mu,0\end{matrix}\right]dz = \frac{\rho^{\mu-0.5}\ell^{0.5}}{(2\pi)^{\frac{\ell}{2}+\frac{\rho}{2}-1}s}\mathrm{G}_{\rho+\ell,2\rho}^{\rho,\rho+\ell}\left[\frac{C_{ik}^{\rho}\ell^{\ell}}{s^{\ell}\rho^{\rho}}\,\middle|\,\begin{matrix}V_9\\V_{10}\end{matrix}\right], \tag{8.16}$$

where $V_9 = \{\frac{1}{\rho},\frac{2}{\rho},\cdots,1,0,\frac{1}{\ell},\cdots,\frac{\ell-1}{\ell}\}$ and $V_{10} = \{\frac{\mu}{\rho},\frac{\mu+1}{\rho},\cdots,\frac{\mu+\rho-1}{\rho},0,\frac{1}{\rho},\cdots,\frac{\rho-1}{\rho}\}$. Here, the variables ℓ and ρ are positive integers such that $\frac{\ell}{\rho}=\frac{\alpha}{2}$ and $\gcd(\ell,\rho)=1$ to satisfy the convergence conditions of the integral in (8.16). Similarly, by employing [118, Eq. (07.34.21.0013.01)] and by using [118, Eq. (01.03.26.0004.01)] and [118, Eq. (06.06.26.0005.01)], $\mathcal{T}_2$ can be rewritten as

$$\mathcal{T}_2 = \int_0^\infty z^{\psi^2/2}\mathrm{G}_{0,1}^{1,0}\left[sz\,\middle|\,\begin{matrix}-\\0\end{matrix}\right]\mathrm{G}_{1,2}^{2,0}\left[C_{ik}z^{\frac{\ell}{\rho}}\,\middle|\,\begin{matrix}1\\B_{ik},0\end{matrix}\right]dz = \frac{\rho^{B_{ik}-0.5}\ell^{\frac{\psi^2}{2}+0.5}}{(2\pi)^{\frac{\ell}{2}+\frac{\rho}{2}-1}s^{\frac{\psi^2}{2}+1}}\mathrm{G}_{\rho+\ell,2\rho}^{2\rho,\ell}\left[\frac{C_{ik}^{\rho}\ell^{\ell}}{s^{\ell}\rho^{\rho}}\,\middle|\,\begin{matrix}V_{11}\\V_{12}\end{matrix}\right], \tag{8.17}$$

where $V_{11} = \{\frac{-\psi^2/2}{\ell}, \frac{1-\psi^2/2}{\ell}, \cdots, \frac{\ell-\psi^2/2-1}{\ell}, \frac{1}{\rho}, \frac{2}{\rho}, \cdots, 1\}$, $V_{12} = \{\frac{B_{ik}}{\rho}, \frac{B_{ik}+1}{\rho}, \cdots, \frac{B_{ik}+\rho-1}{\rho}, 0, \frac{1}{\rho}, \cdots, \frac{\rho-1}{\rho}\}$. By substituting (8.16) and (8.17) in (8.15) and by inserting (8.15) in (8.14), $\mathcal{M}_{\gamma^{b_1}_{e2e,k}}(s)$ can be found. Then, by using $\mathcal{M}_{\gamma^{b_1}_{e2e,k}}(s)$, the MGF of $\gamma^{b_1}_{\mathrm{MRC}}$ can be obtained similar to (8.10). Thereafter, by replacing $\mathcal{M}_{\gamma_{\mathrm{MRC}}}(s)$ in (8.9) by $\mathcal{M}_{\gamma^{b_1}_{\mathrm{MRC}}}(s)$, a lower bound for the SER can be found. Please note that (8.9) can be easily evaluated by using the Meijer-G implementation in the standard library in MATLAB or MATHEMATICA. It is worth mentioning that an approximated lower bound for the SER can also be calculated by using (8.13).

8.2.1.3 High SNR analysis

In high SNR analysis, the CDF of $\gamma^{b_1}_{e2e,k}$ can be written as $F^{\infty}_{\gamma^{b_1}_{e2e,k}}(z) \approx F^{\infty}_{\gamma_{1k}}(z) + F^{\infty}_{\gamma_{2k}}(z)$ where the CDF of γ_{ik} in high SNR region for $i \in \{1, 2\}$ can be expressed by employing [116, Eq. (45.9.1)] and [116, Eq. (45.9.6)] as

$$F^{\infty}_{\gamma_{ik}}(z) = \left(\frac{C^{\mu}_{ik}}{\Gamma(\mu+1)} - \frac{C^{\mu}_{ik}}{\Gamma(\mu)B_{ik}}\right) z^{\frac{\alpha\mu}{2}} + \frac{\Gamma(B_{ik})C^{\psi^2/\alpha}_{ik}}{\Gamma(\mu)} z^{\frac{\psi^2}{2}}. \tag{8.18}$$

By using (8.18) and [55, Eq. (17.13.3)], the asymptotic MGF of $\gamma^{b_1}_{e2e,k}$ is obtained as

$$\mathcal{M}^{\infty}_{\gamma^{b_1}_{e2e,k}}(s) = (E_{1k} + E_{2k})\, s^{-\frac{\alpha\mu}{2}} + (J_{1k} + J_{2k})\, s^{-\frac{\psi^2}{2}}, \tag{8.19}$$

where $E_{ik} = \left(\frac{C^{\mu}_{ik}}{\Gamma(\mu+1)} - \frac{C^{\mu}_{ik}}{\Gamma(\mu)B_{ik}}\right)\Gamma(\frac{\alpha\mu}{2}+1)$ and $J_{ik} = \frac{\Gamma(B_{ik})C^{\psi^2/\alpha}_{ik}}{\Gamma(\mu)}\Gamma(\frac{\psi^2}{2}+1)$. From (8.19), the MGF of overall SNR can be written similar to (8.10). The closed-form expression for SER performance of the M-PSK system for high SNR values can be found similar to (8.13).

Remark 7.1: By using the asymptotic MGF of $\gamma^{b_1}_{e2e,k}$, the high SNR expression for the SER can be obtained as $P^{\infty}_{e} = \mathcal{G}_c\left(\frac{P}{\sigma^2_{n_{ik}}}\right)^{-\mathcal{G}_d}$, where $P = P_{1k} = P_{2k}$. In this formulation, $\mathcal{G}_c$ denotes the array gain, and $\mathcal{G}_d$ represents the diversity order which can be found as $\mathcal{G}_d = \min\left(\frac{\alpha\mu K}{2}, \frac{\psi^2 K}{2}\right)$. Here, it can be observed that the diversity order increases with the increasing number of HAPS systems. Moreover, asymptotic analysis reveals that the diversity order is either related with the fading parameters (α and μ) or the pointing error distribution parameter ψ.

8.2.1.4 Impact of I/Q imbalance on SER

To evaluate SER in the presence of I/Q imbalance, the following upper bound is proposed: $\gamma_{\mathrm{MRC}}^{\mathrm{IQ}} \leq \gamma_{\mathrm{MRC}}^{\mathrm{IQ},b_2} = \sum_{k=1}^{K} \gamma_{e2e,k}^{\mathrm{IQ},b_2}$, where $\gamma_{e2e,k}^{\mathrm{IQ},b_2} = \min\left(c_1, c_2 \frac{\gamma_{1k}\gamma_{2k}}{\gamma_{1k}+\gamma_{2k}}\right)$ denotes the SNR upper bound. Here, $c_1 = \frac{|U_1|^2}{|U_2|^2}$ and $c_2 = \frac{|U_1|^2}{|U_1|^2+|U_2|^2}$ simplify the notation. The approximate CDF of $\gamma_{e2e,k}^{\mathrm{IQ},b_2}$ can be given by

$$F_{\gamma_{e2e,k}^{\mathrm{IQ},b_2}}(z) \approx F_{c_1}(z) + F_{c_2\gamma_{e2e,k}}(z). \tag{8.20}$$

By taking the Laplace transform of $F_{\gamma_{e2e,k}^{\mathrm{IQ},b_2}}(z)$, the approximate MGF of $\gamma_{e2e,k}^{\mathrm{IQ},b_2}$ can be found as

$$\mathcal{M}_{\gamma_{e2e,k}^{\mathrm{IQ},b_2}}(s) \approx s\mathcal{L}\{F_{c_1}(z)\} + s\mathcal{L}\{F_{c_2\gamma_{e2e,k}}(z)\}. \tag{8.21}$$

Here, the first summation term in (8.21) is related to the constant c_1, hence, $s\mathcal{L}\{F_{c_1}(z)\} = e^{-c_1 s}$. The second term in (8.21) is obtained as $s\mathcal{L}\{F_{c_2\gamma_{e2e,k}}(z)\} = \mathcal{M}_{\gamma_{e2e,k}}(sc_2)$, which can be easily evaluated by employing (8.12). By using $\mathcal{M}_{\gamma_{e2e,k}^{\mathrm{IQ},b_2}}(s)$, the MGF of $\gamma_{\mathrm{MRC}}^{\mathrm{IQ},b_2}$ can be written similar to (8.10). Afterwards, a lower bound for the SER in the presence of I/Q imbalance can be found by replacing $\mathcal{M}_{\gamma_{\mathrm{MRC}}}(s)$ in (8.13) by $\mathcal{M}_{\gamma_{\mathrm{MRC}}^{\mathrm{IQ},b_2}}(s)$.

Remark 7.2: Here, it can be inferred that the SNR upper bound $\gamma_{e2e,k}^{\mathrm{IQ},b_2} = \min\left(c_1, c_2 \frac{\gamma_{1k}\gamma_{2k}}{\gamma_{1k}+\gamma_{2k}}\right)$ implies a maximum achievable SNR depending on c_1. Thus, the system performance can only be improved up to a certain level due to I/Q imbalance.

8.2.2 Capacity analysis

The average achievable data rate in a wireless channel is defined as ergodic channel capacity. For the system of interest, ergodic channel capacity can be written as $C_{erg} = \frac{W}{K+1} E\left[\log_2\left(1+\gamma_{\mathrm{MRC}}\right)\right]$, where W is the system bandwidth. By using (8.2) together with the Jensen's inequality, C_{erg} can be upper bounded as

$$C_{erg} \leq \frac{W}{K+1} \log_2\left(1 + \sum_{k=1}^{K} E\left[\gamma_{e2e,k}\right]\right). \tag{8.22}$$

In this formulation, the expected value of $\gamma_{e2e,k}$ can also be upper bounded by using the Jensen's inequality as $E\left[\gamma_{e2e,k}\right] \leq E\left[\gamma_{e2e,k}^{b_1}\right] \leq \min\left(E\left[\gamma_{1k}\right], E\left[\gamma_{2k}\right]\right)$. Hence, the upper bound for the system capacity can be given as

$$C_{erg} \leq \frac{W}{K+1}\log_2\left(1+\sum_{k=1}^{K}\min\left(E\left[\gamma_{1k}\right],E\left[\gamma_{2k}\right]\right)\right). \tag{8.23}$$

Here, $E\left[\gamma_{ik}\right]$ can be obtained via squared expected value of $h_{ik}^{\mathrm{fp}} = h_{ik}^{\mathrm{f}} h_{ik}^{\mathrm{p}}$ for $i \in \{1,2\}$ as [50, Eq. (106)]

$$E\left[\gamma_{ik}\right] = \frac{P_{ik}}{L_{ik}\sigma_{n_{ik}}^2}\frac{\psi^2 A_0^2}{2+\psi^2}\frac{(\hat{h}_{ik}^{\mathrm{f}})^2}{\mu^{\frac{2}{\alpha}}}\frac{\Gamma\left(\frac{2}{\alpha}+\mu\right)}{\Gamma(\mu)}. \tag{8.24}$$

By substituting (8.24) in (8.23), the upper bound for C_{erg} can be obtained.

Impact of I/Q Imbalance on Capacity: Ergodic capacity in the presence of I/Q imbalance can be evaluated by replacing $\gamma_{e2e,k}$ by $\gamma_{e2e,k}^{\mathrm{IQ}}$ in (8.22). In this case, the expected value of $\gamma_{e2e,k}^{\mathrm{IQ}}$ can be upper bounded as $E\left[\gamma_{e2e,k}^{\mathrm{IQ}}\right] \leq E\left[\gamma_{e2e,k}^{\mathrm{IQ},b_2}\right]$. By employing Jensen's inequality, expected value of $\gamma_{e2e,k}^{\mathrm{IQ},b_2}$ can be obtained as

$$E\left[\gamma_{e2e,k}^{\mathrm{IQ},b_2}\right] \leq \min\left(c_1, c_2\min\left(E\left[\frac{\gamma_{1k}\gamma_{2k}}{\gamma_{1k}+\gamma_{2k}}\right]\right)\right). \tag{8.25}$$

Here, using the upper bound $\frac{\gamma_{1k}\gamma_{2k}}{\gamma_{1k}+\gamma_{2k}} \leq \min(\gamma_{1k},\gamma_{2k})$ and invoking the Jensen's inequality again result in

$$E\left[\gamma_{e2e,k}^{\mathrm{IQ},b_2}\right] \leq \min\left(c_1, c_2\min\left(E\left[\gamma_{1k}\right],E\left[\gamma_{2k}\right]\right)\right), \tag{8.26}$$

where $E\left[\gamma_{ik}\right]$ for $i \in \{1,2\}$ can be found as in (8.24). Finally, by substituting (8.24) in (8.26), $E\left[\gamma_{e2e,k}^{\mathrm{IQ},b_2}\right]$ can be evaluated. By replacing $\gamma_{e2e,k}$ by $\gamma_{e2e,k}^{\mathrm{IQ}}$ in (8.22), the upper bound for the ergodic capacity under receiver I/Q imbalance at ground station can be obtained.

8.3 Numerical Results

In this section, error and capacity performance of the system are illustrated, and theoretical expressions are validated through Monte-Carlo simulations. Unless otherwise stated, it is assumed that altitudes of S, H_k, and D are set to 500 km, 30 km, and 0 km, respectively. In the first hop, zenith angle ζ_{1k}, $\forall k$, is set to $10°$. For the zenith angle in the second hop, three different values, i.e. $\zeta_{2k} = 30°, 60°, 75°$, $\forall k$,

Table 8.1 : Parameters for the proposed system

Parameter	Value
Satellite S altitude	500 km
HAPS H_k altitude	30 km
Ground station D altitude	0 km
Zenith angle in S-to-H_k link	$\zeta_{1k} = 10°$
Zenith angle in H_k-to-D link	$\zeta_{2k} = 30°, 60°, 75°$
Antenna gains	$\mathcal{G}^{\mathrm{t}}_{ik} = \mathcal{G}^{\mathrm{r}}_{ik} = 60$ dBi
Fading parameters	$\alpha = 3$, $\mu = 2$
Pointing error parameters	$\psi = 4.422$, $A_0 = 0.74$

are considered.[4] Moreover, the carrier frequency is set to 295 GHz, and the transmitter and receiver antenna gains are $\mathcal{G}^{\mathrm{t}}_{ik} = \mathcal{G}^{\mathrm{r}}_{ik} = 60$ dBi, $i \in \{1,2\}$, $1 \leq k \leq K$. Also, it is assumed that the system's bandwidth is $W = 0.5$ GHz. In addition, fading parameters are set to $\alpha = 3$ and $\mu = 2$ and the parameters related to the pointing errors are taken as $\psi = 4.422$ and $A_0 = 0.74$. It is assumed that binary phase shift keying (BPSK, $M = 2$) and/or 8-PSK modulations are utilized in the system. Finally, transmit powers and the noise power are taken as $P_{1k} = P_{2k} = P$ and $\sigma^2_{n_{ik}} = -70$ dBm, respectively. All the parameters used in simulations are provided in Table 8.1.

8.3.1 Attenuation in dry and humid atmosphere

In Table 8.2, free-space loss and atmospheric absorption loss values are shown for $\zeta_{2k} = 30°, 60°, 75°$, $\forall k$, under dry and humid atmospheric conditions [13, 73]. It can be seen from the table that atmospheric absorption loss values for the first hop are negligible since the densities of water vapour and oxygen are very low at high altitudes. Additionally, it can be seen that increased humidity causes higher absorption loss, especially in the second hop, as the humidity significantly increases the densities of absorber particles at the lower altitudes, resulting in higher attenuation. The table also shows that the total attenuation in the second hop is higher than that in the first hop, i.e. $L_{1k} < L_{2k}$, only when $\zeta_{2k} = 75°$ under humid atmosphere since the total attenuation level in the second hop increases with higher zenith angle and longer propagation

[4]Considering the altitude difference between H_k and S, values of ζ_{1k}, $\forall k$, are almost the same. Furthermore, HAPS systems can be deployed in such a way that the values of ζ_{2k}, $\forall k$, are exactly the same.

Table 8.2 : Free-space loss and absorption loss values for $\zeta_{2k} = 30°, 60°, 75°$, $\forall k$, under dry and humid atmospheric conditions [13, 73]

	Dry	Humid
$\zeta_{2k} = 30°$	$L_{1k}^{\text{fsl}} = 195.41$ dB	$L_{1k}^{\text{fsl}} = 195.41$ dB
	$L_{1k}^{\text{abs}} = 2.75 \times 10^{-5}$ dB	$L_{1k}^{\text{abs}} = 2.76 \times 10^{-5}$ dB
	$L_{2k}^{\text{fsl}} = 172.63$ dB	$L_{2k}^{\text{fsl}} = 172.63$ dB
	$L_{2k}^{\text{abs}} = 0.16$ dB	$L_{2k}^{\text{abs}} = 10.33$ dB
$\zeta_{2k} = 60°$	$L_{1k}^{\text{fsl}} = 195.41$ dB	$L_{1k}^{\text{fsl}} = 195.41$ dB
	$L_{1k}^{\text{abs}} = 2.75 \times 10^{-5}$ dB	$L_{1k}^{\text{abs}} = 2.76 \times 10^{-5}$ dB
	$L_{2k}^{\text{fsl}} = 177.40$ dB	$L_{2k}^{\text{fsl}} = 177.40$ dB
	$L_{2k}^{\text{abs}} = 0.28$ dB	$L_{2k}^{\text{abs}} = 17.88$ dB
$\zeta_{2k} = 75°$	$L_{1k}^{\text{fsl}} = 195.41$ dB	$L_{1k}^{\text{fsl}} = 195.41$ dB
	$L_{1k}^{\text{abs}} = 2.75 \times 10^{-5}$ dB	$L_{1k}^{\text{abs}} = 2.76 \times 10^{-5}$ dB
	$L_{2k}^{\text{fsl}} = 183.12$ dB	$L_{2k}^{\text{fsl}} = 183.12$ dB
	$L_{2k}^{\text{abs}} = 0.53$ dB	$L_{2k}^{\text{abs}} = 34.46$ dB

distance under humid atmosphere. For $\zeta_{2k} = 60°$ under humid atmosphere, the total attenuation values in the first and second hop are almost the same, i.e. $L_{1k} \approx L_{2k}$. For other cases, $L_{1k} > L_{2k}$. Although such loss values can be observed, taking the transmit power, antenna gains, and noise power into account, it can be concluded that it is still feasible to maintain high SNR levels.

8.3.2 Verification of the theoretical results

In Fig. 8.2, the BPSK and 8-PSK SER curves are illustrated for the proposed system and a reference dual THz/Ka band transmission system (direct communication from S to G) [130]. In this figure, $K = 1{,}3$ number of HAPS systems and $\zeta_{2k} = 60°$, $\forall k$ are considered for the proposed system. Also, antenna gains for dual THz/Ka band transmission are taken as specified in [130]. Here, (8.13) is used for the theoretical curves with the statistics of $\gamma_{e2e,k}$, and (8.9) is employed for the lower bound curves with the statistics of $\gamma_{e2e,k}^{b_1}$. It can be seen from the figure that results of (8.9) and (8.13) match well with the simulations. Additionally, asymptotic curves accurately depict the system performance in high SNR region. Moreover, comparing the dual THz/Ka band transmission directly from S to D [130] and the proposed system, it can be inferred that the system performance is improved by deploying HAPS systems. This performance

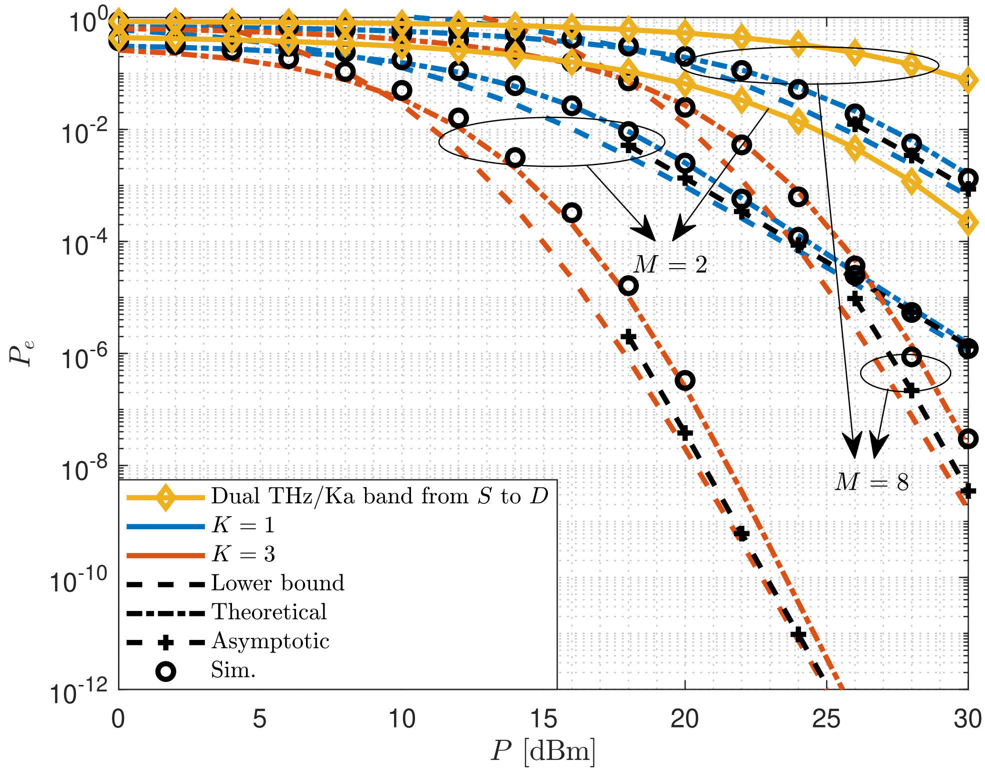

Figure 8.2 : Comparison of BPSK and 8-PSK SER performance of the proposed system (for $K = 1,3$ and $\zeta_{2k} = 60^{\circ}$) and dual THz/Ka band transmission (direct communication from S to D) [130] under humid atmosphere.

improvement originates from the fact that the total transmission distance is divided into two hops, resulting in lower free-space loss and absorption loss levels. Therefore, the system becomes more resilient to attenuation. It can be observed that the system performance is enhanced when the number of HAPS systems increases. Also, SER performance is degraded as the modulation order M increases.

In Fig. 8.3, the effect of ζ_{2k} on the BPSK SER performance of the system is presented for $P = 20$ dBm and $K = 1,2,3$ under humid atmosphere. In this figure, the theoretical and lower bound curves are plotted by using (8.13) with the statistics of $\gamma_{e2e,k}$ and (8.9) with the statistics of $\gamma_{e2e,k}^{b_1}$, respectively. It is evident that increasing the number of HAPS systems enhances the minimum achievable error rate. When the number of HAPS systems is increased from 1 to 2, minimum achievable SER reduces from 5×10^{-4} to $\sim 1 \times 10^{-6}$ for $P = 20$ dBm. It can also be deduced from the figure that SER lower bound provides close results to P_e for low and high ζ_{2k} values. However,

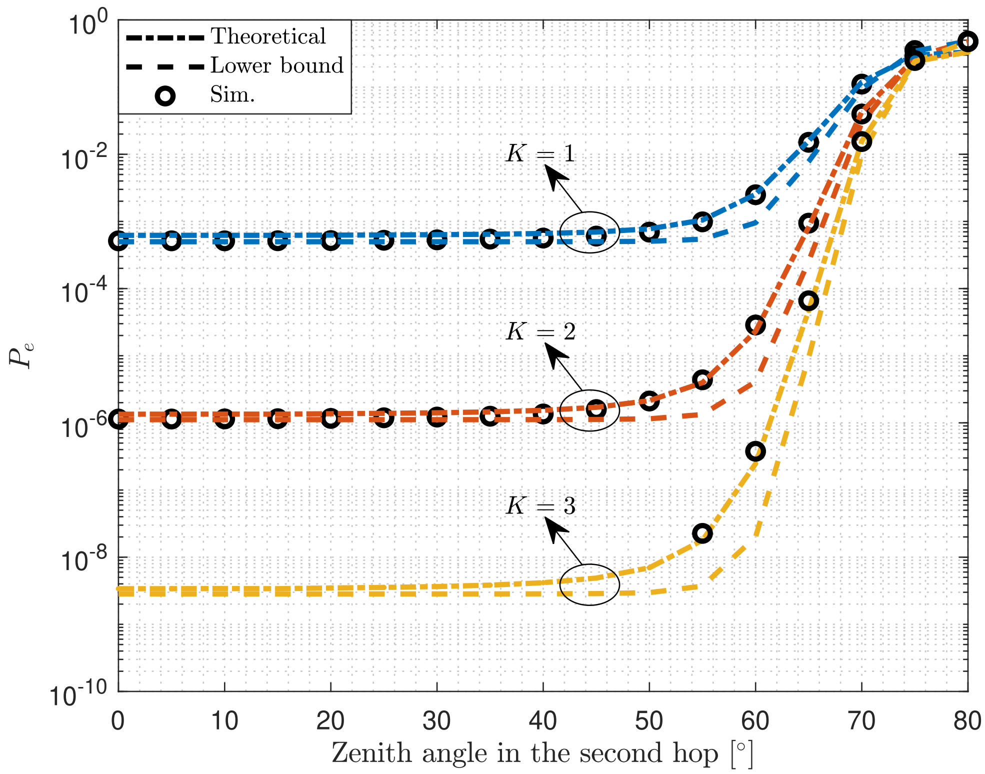

Figure 8.3 : BPSK SER performance of the system with respect to zenith angle in the second hop for $P = 20$ dBm and $K = 1,2,3$ under humid atmosphere.

it offers slightly looser lower bound to P_e for medium ζ_{2k} values (from 40° to 70°). Furthermore, it can be inferred that at least 3 HAPS systems are required to achieve 10^{-8} SER performance.

8.3.3 Impact of humidity

In Fig. 8.4, BPSK SER performance of the system is illustrated for $\zeta_{2k} = 30^\circ, 75^\circ$ and $K = 2$ under dry and humid atmospheric conditions. Here, (8.13) is used to illustrate the SER performance. It can be observed from the figure that error performance remains almost the same under dry and humid atmosphere when $\zeta_{2k} = 30^\circ$. This can be explained by the fact that the dominant loss factor for $\zeta_{2k} = 30^\circ$ is L_{1k}, and it is not affected from the humidity (see Table 8.2) since the first hop is in the upper layer of the atmosphere. As the attenuation in the first hop is higher than that in the second hop for both dry and humid atmosphere, γ_{1k} is more likely to be less than γ_{2k}. Consequently, SNR in the first hop dominates the error performance under dry/humid atmosphere

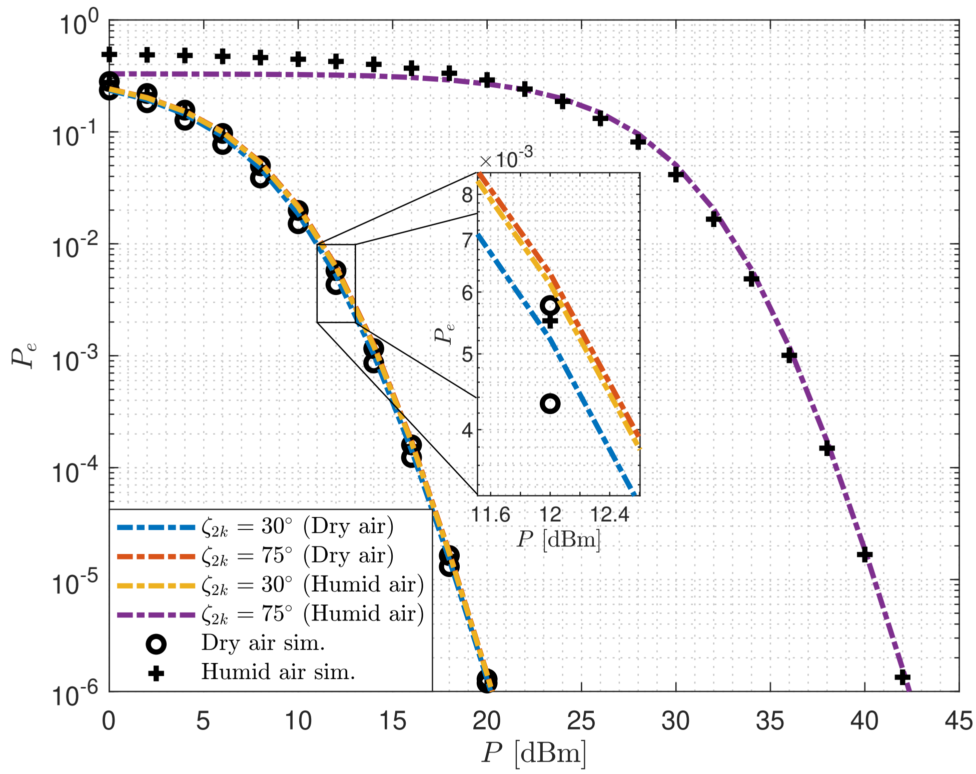

Figure 8.4 : BPSK SER curves for $\zeta_{2k} = 30^\circ, 75^\circ$ under dry and humid atmospheric conditions for $K = 2$.

when $\zeta_{2k} = 30^\circ$. Hence, it can be concluded that whether the atmosphere is dry or humid, the SER performance remains almost the same for low zenith angles in the second hop. It can also be observed that humidity introduces ~ 22 dBm power loss at 10^{-6} error probability when $\zeta_{2k} = 75^\circ$, which arises from the fact that absorption loss is increased dramatically for humid atmosphere and high ζ_{2k} values. This is because the total attenuation in the second hop is higher than that in the first hop when $\zeta_{2k} = 75^\circ$ under humid atmospheric conditions, and γ_{2k} dominates the SER performance. It can be concluded that for high ζ_{2k} values, humidity significantly affects the performance.

In Fig. 8.5, BPSK SER performance is presented with respect to ζ_{2k} under dry and humid atmospheric conditions for $K = 2$ and $P = 20$ dBm. In this figure, (8.13) is used to plot the theoretical SER curves. Here, the figure shows that the SER performance remains the same up to 70° of zenith angle for dry atmospheric conditions as the total attenuation in the first hop is higher ($L_{1k} > L_{2k}$), and γ_{1k} dominates the error performance. However, the SER performance is degraded for

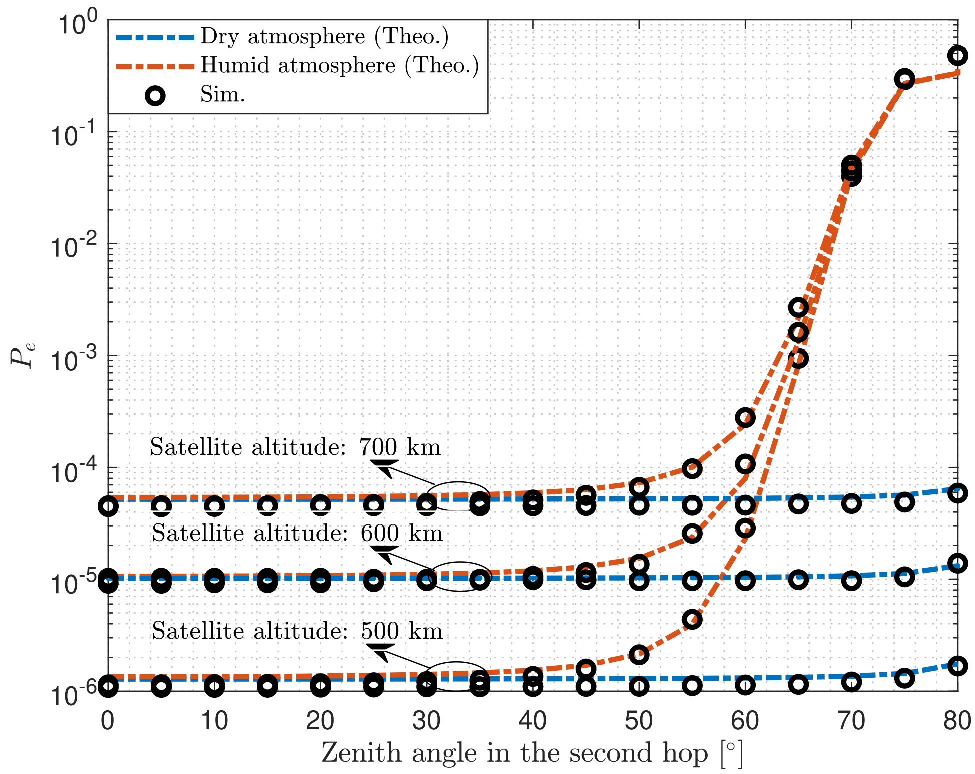

Figure 8.5 : BPSK SER curves with respect to the zenith angle in the second hop for different satellite altitudes under dry and humid atmospheric conditions for $K = 2$ and $P = 20$ dBm.

zenith angles greater than 30° for humid air as γ_{2k} becomes the dominant factor in the error performance owing to extreme level of absorption loss and long propagation distance in the second hop. Moreover, it can be deduced that increment in satellite altitude results in performance degradation for low ζ_{2k} regardless of the atmospheric condition. Additionally, since the system performance is predominantly determined by the HAPS-to-ground station link for high ζ_{2k} under humid atmosphere (see Table 8.2), satellite altitude has negligible impact on the system performance, i.e. all red curves meet for $\zeta_{2k} \geq 70°$.

8.3.4 Impact of I/Q imbalance on SER

In Fig. 8.6, 8-PSK SER performance of the proposed system is illustrated for different numbers of HAPS systems ($K = 1, 2$) in the presence of I/Q imbalance ($g_D = 0.75$ and $\theta_D = 10°$) and ideal hardware ($g_D = 1$ and $\theta_D = 0$). Here, (8.13) is utilized for the theoretical curves. It can be observed from the figure that I/Q imbalance causes error

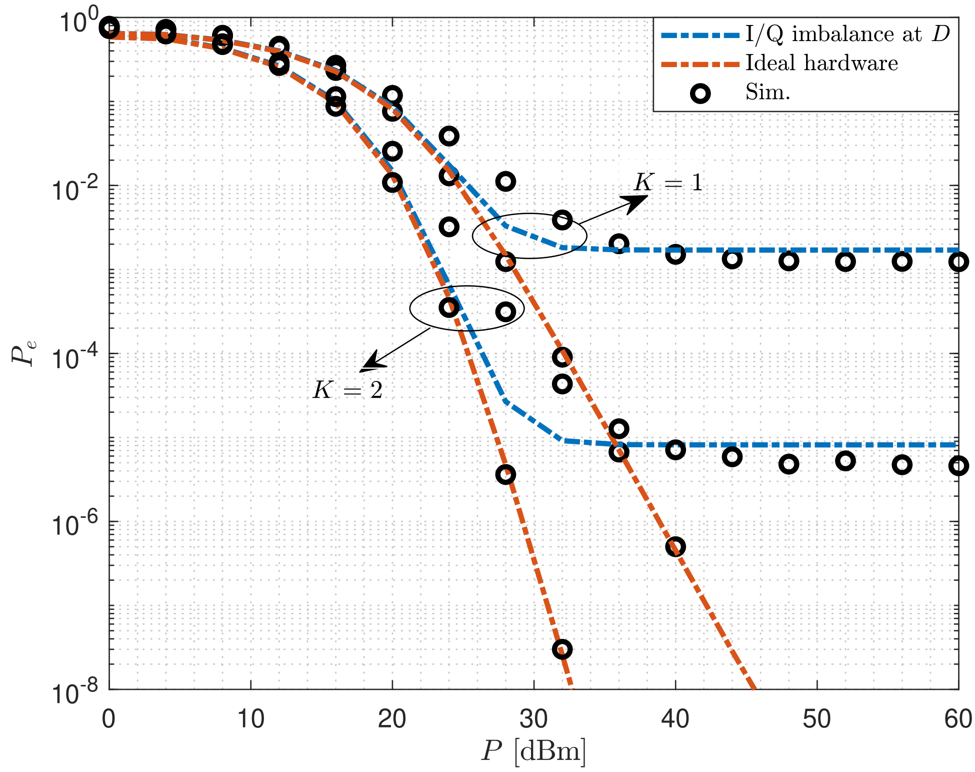

Figure 8.6 : 8-PSK SER curves in the presence of I/Q imbalance ($g_D = 0.75$ and $\theta_D = 10°$) and ideal hardware ($g_D = 1$ and $\theta_D = 0$) for $K = 1, 2$.

floors, limiting the achievable SER performance. Furthermore, the results reveal that the achievable SER in the presence of I/Q imbalance is around 10^{-3} for $K = 1$, whereas it is enhanced to around 10^{-5} for $K = 2$. This stems from the diversity introduced by the deployment of multiple HAPS systems. In other words, by increasing the number of HAPS systems, the achievable SER performance can be improved which emphasizes the advantage of HAPS deployment in THz NTNs.

8.3.5 Ergodic capacity

Ergodic capacity performance of the system is illustrated in Fig. 8.7 for $\zeta_{2k} = 75°$ and $K = 1, 2, 3$ under dry and humid atmospheric conditions. It is obtained that theoretical capacity curves provide a tight upper bound to simulation curves, verifying the analytical derivations. Additionally, it can be seen from the figure that ergodic channel capacity decreases with the increasing number of HAPS systems since the transmission is completed in $K + 1$ transmission intervals. Also, with the increased

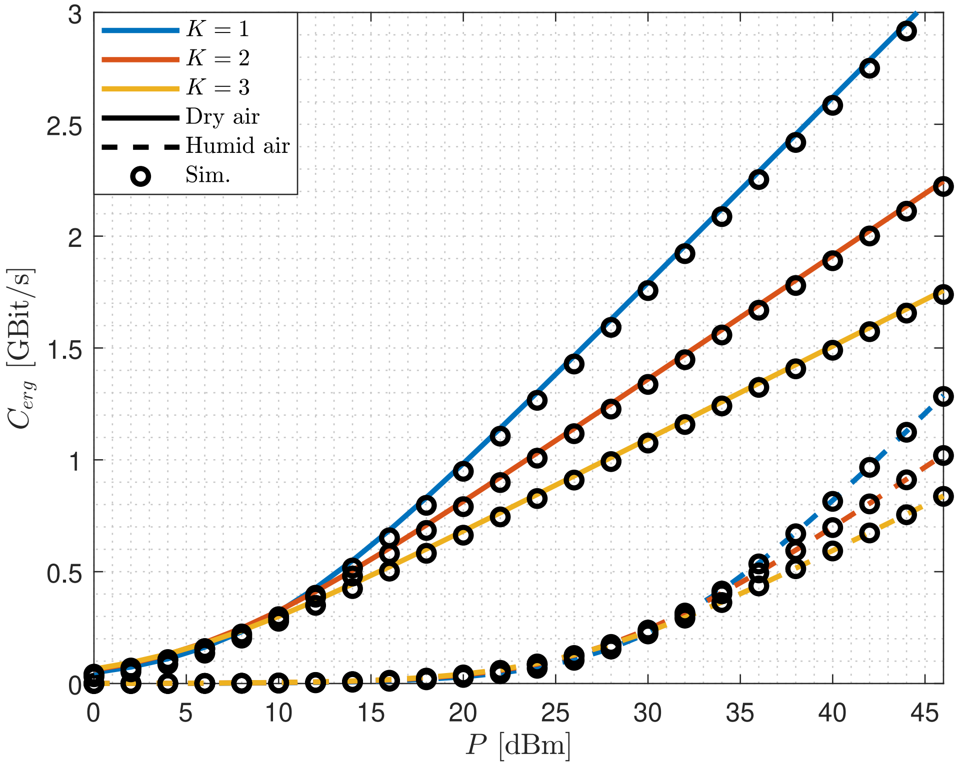

Figure 8.7 : Ergodic capacity curves for $\zeta_{2k} = 75°$ under dry and humid atmospheric conditions for $K = 1, 2, 3$.

humidity, $\sim$ 22 dBm power loss is observed in the capacity performance, similar to the SER performance for $\zeta_{2k} = 75°$ (see Fig. 8.4). This clearly demonstrates the critical impact of atmospheric conditions on high-frequency link performance.

In Fig. 8.8, ergodic capacity performance of the system is depicted with respect to ζ_{2k} for $K = 1, 2, 3$ and $P = 30$ dBm under humid atmosphere. It can be seen from the figure that the maximum achievable capacity decreases when the number of HAPS systems increases as the total transmission time increases due to additional relay intervals. Also, for low and high zenith angles, theoretical curves provide a tight upper bound to the simulation curves, validating the analytical expressions. However, for medium zenith angle values, the total attenuation factors in the first and second hop (L_{1k} and L_{2k}) are very close to each other (see Table 8.2), making the distributions of γ_{1k} and γ_{2k} in (8.7) almost the same. Hence, Jensen's inequality used in (8.23) provides a slightly looser upper bound in this region, as the approximation becomes less accurate.

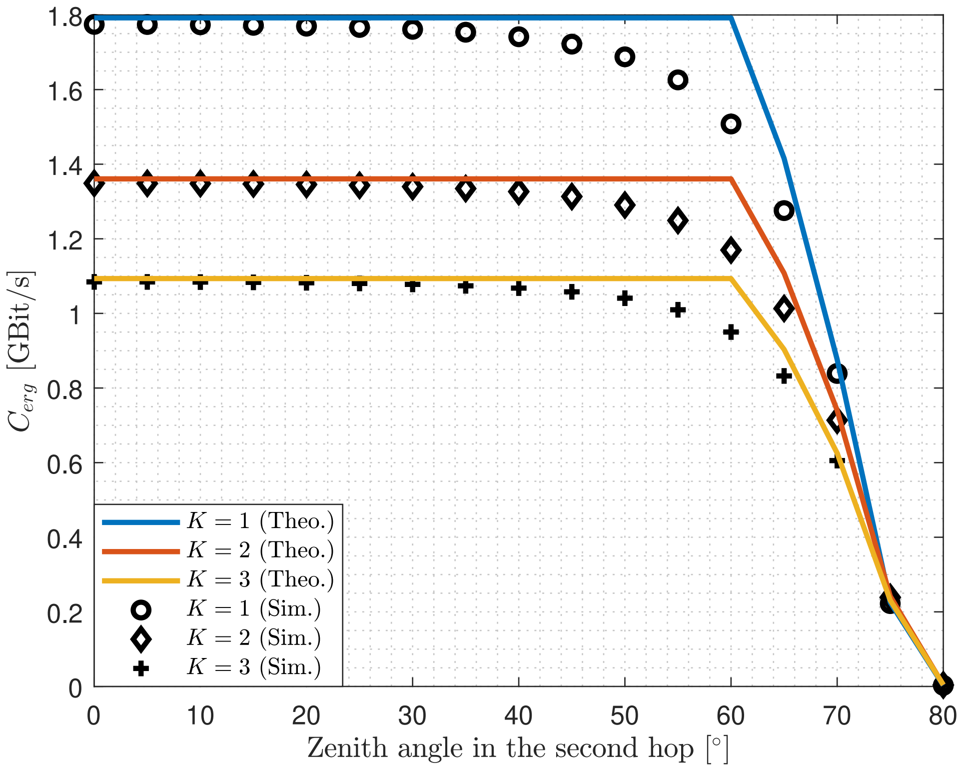

Figure 8.8 : Ergodic capacity curves with respect to the zenith angle in the second hop for $K = 1, 2$ and $P = 30$ dBm under humid atmospheric conditions.

8.3.6 Impact of I/Q imbalance on capacity

In Fig. 8.9, ergodic capacity curves are shown in the presence of I/Q imbalance ($g_D = 0.75$ and $\theta_D = 10°$) and ideal hardware ($g_D = 1$ and $\theta_D = 0$) for $K = 1, 2$ and $\zeta_{2k} = 75°$. It can be deduced from the figure that I/Q imbalance limits the system performance significantly. Formally, this limit emerges from the term c_1 in (8.26) since it is independent of transmit power. Thus, system capacity can be improved up to a certain level in the presence of I/Q imbalance.

8.4 Concluding Remarks

In this chapter, a THz NTN's SER and also ergodic capacity performance are analyzed where HAPS systems are deployed to assist transmission by using variable-gain AF relaying. It is assumed that the received signals are combined by using MRC at the ground station. In order to perform the analyses, the CDF and MGF of the end-to-end

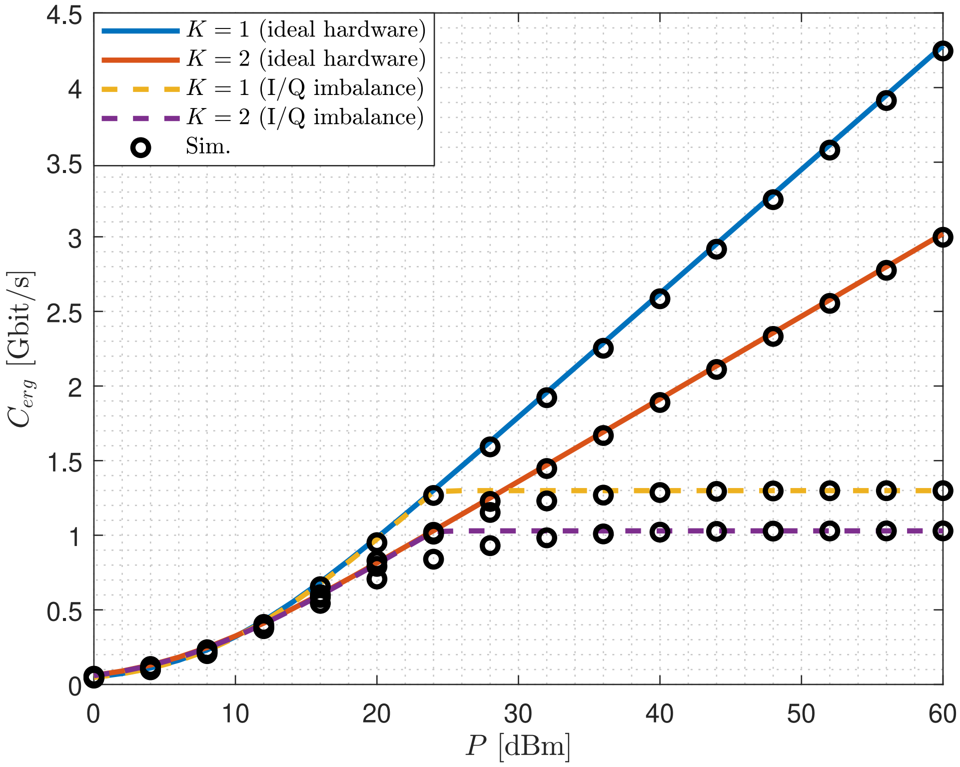

Figure 8.9 : Ergodic capacity curves in the presence of I/Q imbalance ($g_D = 0.75$ and $\theta_D = 10°$) and ideal hardware ($g_D = 1$ and $\theta_D = 0$) for $K = 1, 2$ and $\zeta_{2k} = 75°$.

SNR are found in the presence of atmospheric absorption loss, fading, and pointing errors. The exact and asymptotic expressions for SER are derived together with SER lower bound in the case of M-PSK modulation. Also, ergodic capacity expression is obtained. It is shown that the theoretical results are accurate. Moreover, the effects of zenith angle and atmospheric absorption loss under different atmospheric conditions are presented. It is found out that for lower zenith angles in the second hop, the SER performance remains almost the same regardless of the humidity level. However, for higher zenith angles, humid atmospheric conditions introduce ~ 22 dBm power loss both for error and capacity performance of the system.

9. CONCLUSION

In this thesis, an in-depth investigation on the utilization of the THz band within the NTN architecture is provided. Throughout the thesis, a statistical model for the pointing error characteristics in mmWave/THz transmission is proposed, and performance analyses for various communication scenarios, including HAPS-to-HAPS, inter-satellite, satellite-to-HAPS-to-ground station communications, are presented. The performance of the considered setups are quantified in terms of the outage probability, asymptotic outage probability, SER, and capacity, and the derived theoretical results are validated through Monte-Carlo simulations.

First, a simple analytical pointing error model for highly directional mmWave/THz transmission is proposed. By utilizing the Gaussian beam approximation for both the array element radiation pattern and the array factor, the presented model incorporates antenna design parameters (maximum gain and 3 dB beamwidth) and array design parameters (number of array elements, element spacing, and 3 dB beamwidth). This approximation is validated via EM simulations in CST Microwave Studio. Afterwards, the statistics of the pointing error are derived according to the Gaussian beam approximation, and it is demonstrated that the pointing error follows a special case of the negative log-Gamma distribution with the shape parameter of 2 and the scale parameter depending on antenna/array design and jitter variance. It is shown that the proposed model aligns perfectly with the simulation results. Moreover, the outage performance of an aerial communication scenario is analyzed to examine the impact of the pointing errors. The results have revealed that the antenna and array design parameters are as influential as the jitter variance, and they cannot be neglected.

Secondly, the feasibility of mmWave/THz NTNs is investigated by performing the link budget analysis for all possible communication scenarios within the NTN architecture. To accomplish this, the main channel effects in mmWave/THz transmission, such as the free-space loss, absorption loss under dry/humid atmospheric conditions, weather-induced losses, ionospheric effects, polarization mismatches between antennas, feeder losses, antenna requirements, fading and pointing errors, and frequency-dependent noise characteristics, are taken into consideration. The achievable data rate is evaluated for uplink/downlink inter-layer and intra-layer links to quantify the system performance. It is shown that the frequent absorption and weather events cause high loss factors in transmission in the lower layers of the atmosphere, affecting the ground-aerial and ground-satellite links, and that the transmission in the upper layers (as in aerial-satellite links) exhibits almost frequency-independent channel characteristics. This suggests that the excessive loss levels in ground-satellite links can be reduced to a compensable level by leveraging the multi-layer structure of the NTN architecture, which makes the mmWave/THz NTNs a strong enabler to support extreme data rates in future communication systems.

Thirdly, the performance analysis is performed for a dual-hop inter-satellite THz communication system, where the connectivity between two LEO satellites is established via another variable-gain AF relay LEO satellite at a higher altitude. For the considered setup, the statistics of the received SNR are derived in the presence of free-space loss, absorption loss, ionospheric loss, fading, and pointing errors. Then the outage probability and SER expressions are derived in terms of the bi-variate Fox-H function and the Meijer-G function, respectively. Also, the asymptotic outage probability analysis is provided to gain insights about the system performance in the high SNR region. It is illustrated that satisfactory outage and SER performance are achievable below 30 dBm transmit power, enabling reliable inter-satellite connectivity in the THz band.

Fourthly, the impact of hardware impairment noise on the outage and capacity performance of a downlink multi-HAPS THz NTN is investigated. In the system of interest, it is assumed that the variable-gain AF protocol is utilized at HAPS nodes (systems), and the HAPS system, which provides the maximum end-to-end SNR, is selected for transmission. To evaluate the outage, asymptotic outage, and ergodic capacity bounds for the system, the PDF, CDF, and asymptotic CDF related to the upper bound of the end-to-end SNR are obtained. By using these statistics, the effects of hardware impairment levels, zenith angles, and atmospheric conditions on the system performance are examined. The results have shown that hardware impairments cause power loss in outage performance and reduce the system capacity, while increasing the number of HAPS systems can tolerate the power loss in the outage performance. Moreover, it is demonstrated that the outage probability depends on either fading or pointing error characteristics in high SNR region and also that the system performance almost remains the same for lower zenith angles in HAPS-to-ground link regardless of the atmospheric conditions.

Finally, a downlink multi-HAPS THz NTN's SER and ergodic capacity performance are analyzed in the presence of the free-space loss, absorption loss, fading, pointing errors, and receiver I/Q imbalance at the ground station. For the considered setup, it is assumed that all HAPS systems aid the transmission from the satellite to the ground station by utilizing the variable-gain AF relaying and that the ground station employs the MRC technique. To obtain the SER and capacity expressions, the CDF and MGF related to the received SNR are derived in terms of the uni-variate and bi-variate Fox-H functions. The system performance is illustrated for various zenith angle values in HAPS-to-ground station link, satellite altitudes, amplitude and phase mismatches. It is shown that the receiver I/Q imbalance introduces error floors, limiting the system performance. Moreover, it is demonstrated that the system performance determined by either fading or the pointing error characteristics in the high SNR region. Additionally, it is found out that for low zenith angles in HAPS-to-ground station link, the system performance is highly dependent on the satellite-to-HAPS link, and the SER performance remains almost the same regardless of the humidity level.

REFERENCES

[1] **Vaezi, M.**, **Azari, A.**, **Khosravirad, S.R.**, **Shirvanimoghaddam, M.**, **Azari, M.M.**, **Chasaki, D. and Popovski, P.** (2022). Cellular, wide-area, and non-terrestrial IoT: A survey on 5G advances and the road toward 6G, *IEEE Communications Surveys Tutorials*, *24*(2), 1117–1174.

[2] **Xie, H.**, **Zhan, Y.**, **Zeng, G. and Pan, X.** (2021). LEO mega-constellations for 6G global coverage: Challenges and opportunities, *IEEE Access*, *9*, 164223–164244.

[3] **Mohammed, A.**, **Mehmood, A.**, **Pavlidou, F.N. and Mohorcic, M.** (2011). The role of high-altitude platforms (HAPs) in the global wireless connectivity, *Proceedings of the IEEE*, *99*(11), 1939–1953.

[4] **Azari, M.M.**, **Solanki, S.**, **Chatzinotas, S.**, **Kodheli, O.**, **Sallouha, H.**, **Colpaert, A.**, **Mendoza Montoya, J.F.**, **Pollin, S.**, **Haqiqatnejad, A.**, **Mostaani, A.**, **Lagunas, E. and Ottersten, B.** (2022). Evolution of non-terrestrial networks from 5G to 6G: A survey, *IEEE Communications Surveys Tutorials*, *24*(4), 2633–2672.

[5] **Karabulut Kurt, G.**, **Khoshkholgh, M.G.**, **Alfattani, S.**, **Ibrahim, A.**, **Darwish, T.S.J.**, **Alam, M.S.**, **Yanikomeroglu, H. and Yongacoglu, A.** (2021). A Vision and framework for the high altitude platform station (HAPS) networks of the future, *IEEE Communications Surveys Tutorials*, *23*(2), 729–779.

[6] **Li, H. and Zhao, Q.** (2006). Distributed modulation for cooperative wireless communications, *IEEE Signal Processing Magazine*, *23*(5), 30–36.

[7] **Cao, X.**, **Yang, P.**, **Alzenad, M.**, **Xi, X.**, **Wu, D. and Yanikomeroglu, H.** (2018). Airborne communication networks: A survey, *IEEE Journal on Selected Areas in Communications*, *36*(9), 1907–1926.

[8] **Chaccour, C.**, **Soorki, M.N.**, **Saad, W.**, **Bennis, M.**, **Popovski, P. and Debbah, M.** (2022). Seven defining features of terahertz (THz) wireless systems: A fellowship of communication and sensing, *IEEE Communications Surveys Tutorials*, *24*(2), 967–993.

[9] **Huang, K.C. and Wang, Z.** (2011). Terahertz terabit wireless communication, *IEEE Microwave Magazine*, *12*(4), 108–116.

[10] **Chen, Z.**, **Ma, X.**, **Zhang, B.**, **Zhang, Y.**, **Niu, Z.**, **Kuang, N.**, **Chen, W.**, **Li, L. and Li, S.** (2019). A survey on terahertz communications, *China Communications*, *16*(2), 1–35.

[11] **Jornet, J.M. and Akyildiz, I.F.** (2011). Channel modeling and capacity analysis for electromagnetic wireless nanonetworks in the terahertz band, *IEEE Transactions on Wireless Communications*, *10*(10), 3211–3221.

[12] **Rinaldi, F.**, **Maattanen, H.L.**, **Torsner, J.**, **Pizzi, S.**, **Andreev, S.**, **Iera, A.**, **Koucheryavy, Y. and Araniti, G.** (2020). Non-terrestrial networks in 5G beyond: A survey, *IEEE Access*, *8*, 165178–165200.

[13] **International Telecommunication Union** (2022). Attenuation by atmospheric gases and related effects, Recommendation ITU–R P.676–13.

[14] **Akyildiz, I.F.**, **Han, C.**, **Hu, Z.**, **Nie, S. and Jornet, J.M.** (2022). Terahertz band communication: An old problem revisited and research directions for the next decade, *IEEE Transactions on Communications*, *70*(6), 4250–4285.

[15] **Schneider, T.**, **Wiatrek, A.**, **Preussler, S.**, **Grigat, M. and Braun, R.P.** (2012). Link budget analysis for terahertz fixed wireless links, *IEEE Transactions on Terahertz Science and Technology*, *2*(2), 250–256.

[16] **Hossain, Z.**, **Li, Q.C.**, **Ying, D.**, **Wu, G. and Xiong, C.** (2021). THz channel model for 6G communications, *2021 IEEE 32nd Annual International Symposium on Personal, Indoor and Mobile Radio Communications (PIMRC)*, pp.1–7.

[17] **Kunisawa, Y. and Amano, Y.** (2022). Virtualized terminal utilizing terahertz band radio waves for Beyond 5G: Link budget analysis, *2022 IEEE 95th Vehicular Technology Conference: (VTC2022-Spring)*, pp.1–5.

[18] **Weng, Z.K.**, **Kanno, A.**, **Dat, P.T.**, **Inagaki, K.**, **Tanabe, K.**, **Sasaki, E.**, **Kürner, T.**, **Jung, B.K. and Kawanishi, T.** (2021). Millimeter-wave and terahertz fixed wireless link budget evaluation for extreme weather conditions, *IEEE Access*, *9*, 163476–163491.

[19] **Rikkinen, K.**, **Kyosti, P.**, **Leinonen, M.E.**, **Berg, M. and Parssinen, A.** (2020). THz radio communication: Link budget analysis toward 6G, *IEEE Communications Magazine*, *58*(11), 22–27.

[20] **Varotsos, G.K.**, **Aidinis, K.**, **Katsis, A. and Nistazakis, H.E.** (2023). Capacity performance analysis for terrestrial THz channels, *Electronics*, *12*(6), 1336.

[21] **Ye, J.**, **Dang, S.**, **Ma, G.**, **Amin, O.**, **Shihada, B. and Alouini, M.S.** (2022). On outage performance of terahertz wireless communication systems, *IEEE Transactions on Communications*, *70*(1), 649–663.

[22] **Badarneh, O.S.** (2022). Performance analysis of Terahertz communications in random fog conditions with misalignment, *IEEE Wireless Communications Letters*, *11*(5), 962–966.

[23] **Boulogeorgos, A.A.A. and Alexiou, A.** (2020). Outage probability analysis of THz relaying systems, *2020 IEEE 31st Annual International Symposium on Personal, Indoor and Mobile Radio Communications*, pp.1–7.

[24] **Ahmed, M.**, **Althunibat, S. and Zorba, N.** (2022). Outage analysis of mobile users in terahertz bands in the presence of relays, *ICC 2022 - IEEE International Conference on Communications*, pp.716–720.

[25] **Bilgiç, B.**, **Basaran, S.T.**, **Hökelek, and Görçin, A.** (2023). Performance analysis of dual-hop THz communication under foggy weather, *2023 IEEE International Black Sea Conference on Communications and Networking (BlackSeaCom)*, pp.155–160.

[26] **Bhardwaj, P. and Zafaruddin, S.M.** (2022). On the performance of multihop THz wireless system over mixed channel fading with shadowing and antenna misalignment, *IEEE Transactions on Communications*, *70*(11), 7748–7763.

[27] **Pai, V.U.**, **Bhardwaj, P. and Zafaruddin, S.M.** (2021). Performance analysis of dual-hop THz wireless transmission for backhaul applications, *2021 IEEE International Conference on Advanced Networks and Telecommunications Systems (ANTS)*, pp.438–443.

[28] **Li, S. and Yang, L.** (2022). Performance analysis of dual-hop THz transmission systems over α-μ fading channels with pointing errors, *IEEE Internet of Things Journal*, *9*(14), 11772–11783.

[29] **Yadav, S.**, **Gour, R.**, **Gurjar, D.S. and Pandey, A.** (2023). Exploiting direct link in dual-hop AF relaying for THz wireless systems, *2023 6th International Conference on Advanced Communication Technologies and Networking (CommNet)*, pp.1–6.

[30] **Stratidakis, G.**, **Papasotiriou, E.N.**, **Konstantinis, H.**, **Boulogeorgos, A.A.A. and Alexiou, A.** (2020). Relay-based blockage and antenna misalignment mitigation in THz wireless communications, *2020 2nd 6G Wireless Summit (6G SUMMIT)*, pp.1–4.

[31] **Mir, T.**, **Waqas, M.**, **Mir, U.**, **Hussain, S.M.**, **Elbir, A.M. and Tu, S.** (2020). Hybrid precoding design for two-way relay-assisted terahertz massive MIMO systems, *IEEE Access*, *8*, 222660–222671.

[32] **Varotsos, G.K.**, **Aidinis, K. and Nistazakis, H.E.** (2022). Average BER performance estimation of relayed THz links with losses, molecular attenuation, adverse weather conditions, turbulence and generalized pointing errors, *Photonics*, volume 9, MDPI, p.671.

[33] **Amodu, O.A.**, **Jarray, C.**, **Busari, S.A. and Othman, M.** (2023). THz-enabled UAV communications: Motivations, results, applications, challenges, and future considerations, *Ad Hoc Networks*, *140*, 103073.

[34] **Azari, M.M.**, **Solanki, S.**, **Chatzinotas, S. and Bennis, M.** (2022). THz-empowered UAVs in 6G: Opportunities, challenges, and trade-offs, *IEEE Communications Magazine*, *60*(5), 24–30.

[35] **Siegel, P.H.** (2010). THz for space: The golden age, *2010 IEEE MTT-S International Microwave Symposium*, pp.816–819.

[36] **Suen, J.Y.** (2016). Terabit-per-second satellite links: A path toward ubiquitous terahertz communication, *Journal of Infrared, Millimeter, and Terahertz Waves*, *37*(7), 615–639.

[37] **Tamesue, K. and Sato, T.**, (2024). THz communication for non-terrestrial networks, Handbook of Radio and Optical Networks Convergence, Springer, pp.1–21.

[38] **Zhen, R. and Han, C.** (2018). Link budget analysis for massive-antenna-array-enabled terahertz satellite communications, *Journal of Shanghai Jiaotong University (Science)*, *23*, 20–27.

[39] **Song, S.**, **Zhang, H.**, **Song, R.**, **Li, J.**, **Duan, W.**, **Zheng, X. and Cai, J.** (2023). Analysis of THz communication in satellite constellation, *2023 IEEE 3rd International Conference on Information Technology, Big Data and Artificial Intelligence (ICIBA)*, volume 3, IEEE, pp.184–187.

[40] **Nie, S. and Akyildiz, I.F.** (2021). Channel modeling and analysis of inter-small-satellite links in terahertz band space networks, *IEEE Transactions on Communications*, *69*(12), 8585–8599.

[41] **Yadav, A. and Mallik, R.K.** (2023). Terahertz communications between unstable transceivers with pointing errors over FTR fading, *IEEE Open Journal of the Communications Society*, *4*, 2939–2951.

[42] **Saeed, A.**, **Gurbuz, O. and Alagoz, F.** (2023). Outage performance analysis of Terahertz band drone-to-ground communications, *2023 International Balkan Conference on Communications and Networking (BalkanCom)*, pp.1–6.

[43] **Farrag, S.**, **Maher, E.**, **El-Mahdy, A. and Dressler, F.** (2021). Outage probability analysis of UAV assisted mobile communications in THz channel, *2021 16th Annual Conference on Wireless On-demand Network Systems and Services Conference (WONS)*, pp.1–8.

[44] **Farrag, S.**, **Maher, E.**, **El-Mahdy, A. and Dressler, F.** (2021). Performance Analysis of UAV assisted mobile communications in THz channel, *IEEE Access*, *9*, 160104–160115.

[45] **Yadav, A. and Mallik, R.K.** (2024). A performance study of relay-assisted double-hop hybrid RF-THz wireless systems, *IEEE Transactions on Communications*, 1–1.

[46] **Saeed, A.**, **Yaldiz, H. and Alagoz, F.** (2023). GHz-to-THz broadband communications for 6G non-terrestrial networks, *ITU Journal on Future and Evolving Technologies*, *4*(1), 241–250.

[47] **Saqlain, M.**, **Idrees, N.M.**, **Wang, S.**, **Zhang, L. and Yu, X.** (2021). Analysis of THz earth-satellite link capacity in the mid-latitude regions, *2021 IEEE 6th Optoelectronics Global Conference (OGC)*, pp.63–67.

[48] **Tekbiyik, K.**, **Kurt, G.K.**, **Ektı, A.R. and Yanikomeroglu, H.** (2022). Reconfigurable intelligent surfaces empowered THz communication in LEO satellite networks, *IEEE Access*, *10*, 121957–121969.

[49] **Schenk, T.** (2008). *RF imperfections in high-rate wireless systems: Impact and digital compensation*, Springer Science & Business Media.

[50] **Boulogeorgos, A.A.A.**, **Papasotiriou, E.N. and Alexiou, A.** (2019). Analytical performance assessment of THz wireless systems, *IEEE Access*, *7*, 11436–11453.

[51] **Bhardwaj, P. and Zafaruddin, S.M.** (2023). Exact performance analysis of THz link under transceiver hardware impairments, *IEEE Communications Letters*, *27*(8), 2197–2201.

[52] **Ramadan, Y.R.**, **Minn, H. and Abdelgelil, M.E.** (2018). Precompensation and system parameters estimation for low-cost nonlinear Tera-Hertz transmitters in the presence of I/Q imbalance, *IEEE Access*, *6*, 51814–51833.

[53] **Vincent, M. and R.T., R.** (2024). On the impact of hardware impairments on performance of terahertz communication systems utilizing hybrid beamforming techniques, *2024 IEEE Region 10 Symposium (TENSYMP)*, pp.1–6.

[54] **Papasotiriou, E.N.**, **Boulogeorgos, A.A.A. and Alexiou, A.** (2020). Performance analysis of THz wireless systems in the presence of antenna misalignment and phase noise, *IEEE Communications Letters*, *24*(6), 1211–1215.

[55] **Gradshteyn, I.S. and Ryzhik, I.M.** (2014). *Table of integrals, series, and products,* 7th ed., Academic Press.

[56] **Mathai, A.M.**, **Saxena, R.K. and Haubold, H.J.** (2009). *The H-function: Theory and applications*, Springer Science & Business Media.

[57] **Simon, M.K. and Alouini, M.S.** (2007). *Digital communication over fading channels*, New York: Wiley.

[58] **Yacoub, M.D.** (2007). The α-μ Distribution: A physical fading model for the Stacy distribution, *IEEE Transactions on Vehicular Technology*, *56*(1), 27–34.

[59] **Ahrazoglu, E.S.**, **Altunbas, I. and Erdogan, E.** (2024). Multi-HAPS THz satellite communication: Error and capacity analyses under I/Q imbalance, *IEEE Sensors Journal*, *24*(23), 39845–39855.

[60] **Shynk, J.J.** (2012). *Probability, random variables, and random processes: Theory and signal processing applications*, John Wiley & Sons.

[61] **Vucetic, B. and Yuan, J.** (2003). *Space-time coding*, John Wiley & Sons.

[62] **Bjornson, E.**, **Matthaiou, M. and Debbah, M.** (2013). A new look at dual-hop relaying: Performance limits with hardware impairments, *IEEE Transactions on Communications*, *61*(11), 4512–4525.

[63] **T. Schenk** (2008). *RF imperfections in high-rate wireless systems: Impact and digital compensation*, Springer.

[64] **Jiang, W.**, **Han, B.**, **Habibi, M.A. and Schotten, H.D.** (2021). The road towards 6G: A comprehensive survey, *IEEE Open Journal of the Communications Society*, *2*, 334–366.

[65] **Alsaedi, W.K.**, **Ahmadi, H.**, **Khan, Z. and Grace, D.** (2023). Spectrum options and allocations for 6G: A regulatory and standardization review, *IEEE Open Journal of the Communications Society*, *4*, 1787–1812.

[66] **Balanis, C.A.** (2016). *Antenna theory: Analysis and design*, John Wiley & Sons.

[67] **Clough, S.**, **Shephard, M.**, **Mlawer, E.**, **Delamere, J.**, **Iacono, M.**, **Cady-Pereira, K.**, **Boukabara, S. and Brown, P.** (2005). Atmospheric radiative transfer modeling: A summary of the AER codes, *Journal of Quantitative Spectroscopy and Radiative Transfer*, *91*(2), 233–244.

[68] **Paine, S.** (2022). The *am* atmospheric model [Online]. Available: https://www.cfa.harvard.edu/spaine/am/.

[69] **Saeed, A.**, **Gurbuz, O. and Akkas, M.A.** (2020). Terahertz communications at various atmospheric altitudes, *Physical Communication*, *41*, 101113.

[70] **Erdem, M.**, **Saleem, A.**, **Gurbuz, O.**, **Ecemis, C. and Saeed, A.** (2023). A simple analytical model for THz band path loss, *IEEE Communications Letters*, *27*(3), 996–1000.

[71] **Kokkoniemi, J.**, **Lehtomäki, J. and Juntti, M.** (2018). Simplified molecular absorption loss model for 275–400 gigahertz frequency band, *12th European Conference on Antennas and Propagation (EuCAP 2018)*, pp.1–5.

[72] **Kokkoniemi, J.**, **Jornet, J.M.**, **Petrov, V.**, **Koucheryavy, Y. and Juntti, M.** (2021). Channel modeling and performance analysis of airplane-satellite terahertz band communications, *IEEE Transactions on Vehicular Technology*, *70*(3), 2047–2061.

[73] **International Telecommunication Union** (2017). Reference standard atmospheres, Recommendation ITU–R P.835–6.

[74] **Norouzian, F.**, **Marchetti, E.**, **Gashinova, M.**, **Hoare, E.**, **Constantinou, C.**, **Gardner, P. and Cherniakov, M.** (2020). Rain attenuation at millimeter wave and low-THz frequencies, *IEEE Transactions on Antennas and Propagation*, *68*(1), 421–431.

[75] **Liao, X.**, **Fan, L.**, **Wang, Y.**, **Yu, Z.**, **Wang, G.**, **Li, X. and Zhang, J.** (2023). Attenuation characterization of terahertz waves in foggy and rainy conditions at 0.1–1 THz frequencies, *Electronics*, *12*(7), 1684.

[76] **International Telecommunication Union** (2005). Specific attenuation model for rain for use in prediction methods, Recommendation ITU–R P.838–3.

[77] **International Telecommunication Union** (2023). Attenuation due to clouds and fog, Recommendation ITU–R P.840–9.

[78] **Budden, K.G.** (1988). *The propagation of radio waves: The theory of radio waves of low power in the ionosphere and magnetosphere*, Cambridge University Press.

[79] **Kelley, M.C.** (2009). *The Earth's ionosphere: Plasma physics and electrodynamics*, Academic Press.

[80] **Richardson, A.S.** (2019). *2019 NRL plasma formulary*, Naval Research Laboratory Washington, DC.

[81] **Chukhno, N.**, **Chukhno, O.**, **Moltchanov, D.**, **Pizzi, S.**, **Gaydamaka, A.**, **Samuylov, A.**, **Molinaro, A.**, **Koucheryavy, Y.**, **Iera, A. and Araniti, G.** (2024). Models, methods, and solutions for multicasting in 5G/6G mmWave and sub-THz systems, *IEEE Communications Surveys Tutorials*, *26*(1), 119–159.

[82] **Tekbıyık, K.**, **Ekti, A.R.**, **Kurt, G.K.**, **Görçin, A. and Yarkan, S.** (2021). Modeling and analysis of short distance sub-terahertz communication channel via mixture of Gamma distribution, *IEEE Transactions on Vehicular Technology*, *70*(4), 2945–2954.

[83] **Papasotiriou, E.N.**, **Boulogeorgos, A.A.A.**, **Haneda, K.**, **de Guzman, M.F. and Alexiou, A.** (2021). An experimentally validated fading model for THz wireless systems, *Scientific Reports*, *11*(1), 18717.

[84] **Farid, A.A. and Hranilovic, S.** (2007). Outage capacity optimization for free-space optical links with pointing errors, *Journal of Lightwave Technology*, *25*(7), 1702–1710.

[85] **Dabiri, M.T. and Hasna, M.** (2022). Pointing error modeling of mmWave to THz high-directional antenna arrays, *IEEE Wireless Communications Letters*, *11*(11), 2435–2439.

[86] **Dabiri, M.T.**, **Hasna, M.**, **Zorba, N.**, **Khattab, T. and Qaraqe, K.A.** (2022). A general model for pointing error of high frequency directional antennas, *IEEE Open Journal of the Communications Society*, *3*, 1978–1990.

[87] **Jornet, J.M.**, **Petrov, V.**, **Wang, H.**, **Popović, Z.**, **Shakya, D.**, **Siles, J.V. and Rappaport, T.S.** (2024). The evolution of applications, hardware design, and channel modeling for terahertz (THz) band communications and sensing: Ready for 6G?, *Proceedings of the IEEE*, 1–32.

[88] **Ahrazoglu, E.S.**, **Gul, A.C.**, **Akinci, M.N.**, **Altunbas, I. and Erdogan, E.** (2025). An improved pointing error model for mmWave and THz links: Antenna and array design impact, *IEEE Communications Letters*, 1–1.

[89] **Bhardwaj, P. and Zafaruddin, S.M.** (2023). Performance of hybrid THz and multiantenna RF system with diversity combining, *IEEE Systems Journal*, *17*(2), 2546–2557.

[90] **Li, S.**, **Yang, L.**, **Zhang, J.**, **Bithas, P.S.**, **Tsiftsis, T.A. and Alouini, M.S.** (2022). Mixed THz/FSO relaying systems: Statistical analysis and performance evaluation, *IEEE Transactions on Wireless Communications*, *21*(12), 10996–11010.

[91] **Varotsos, G.K.**, **Chatzikontis, E.V.**, **Kapotis, E.**, **Nistazakis, H.E.**, **Aidinis, K. and Christofilakis, V.** (2022). THz links performance study for Gamma turbulence links with path loss and pointing errors, *2022 11th International Conference on Modern Circuits and Systems Technologies (MOCAST)*, pp.1–4.

[92] **International Telecommunication Union** (2024). Radio Regulations, [Online]. Available: http://www.itu.int/pub/R–REG–RR–2024.

[93] **Mailloux, R.J.** (2017). *Phased array antenna handbook*, Artech house.

[94] **Vaughan, R. and Andersen, J.B.** (2003). *Channels, propagation and antennas for mobile communications*, IET.

[95] **Buttazzoni, G. and Vescovo, R.** (2017). Density tapering of linear arrays radiating pencil beams: A new extremely fast Gaussian approach, *IEEE Transactions on Antennas and Propagation*, *65*(12), 7372–7377.

[96] **B. Baharom, et al.** (2023). 2 × 2 lens array antenna using square-bottom concave-convex lens in 300-GHz band, *IEEE Open J. Antennas Propag.*, *4*, 1074–1086.

[97] **J. Zhao, F. Gao, Q. Wu, S. Jin, Y. Wu, and W. Jia** (2018). Beam tracking for UAV mounted SatCom on-the-move with massive antenna array, *IEEE Journal on Selected Areas in Communications*, *36*(2), 363–375.

[98] **Zheng, Z.Y.**, **Shao, Z.J. and Mao, J.F.** (2018). A 300-GHz step-profiled corrugated horn antenna array, *2018 IEEE International Symposium on Antennas and Propagation USNC/URSI National Radio Science Meeting*, pp.1037–1038.

[99] **Zoh, R.S.** (2012). Using the negative log-Gamma distribution for Bayesian system reliability assessment, *Ph.D. thesis*, Iowa State University.

[100] **International Telecommunication Union** (2023). Ionospheric propagation data and prediction methods required for the design of satellite networks and systems, Recommendation ITU–R P.531–15.

[101] **International Telecommunication Union** (2015). Propagation data and prediction methods required for the design of Earth-space telecommunication systems, Recommendation ITU–R P.618–12.

[102] **Lumpp, J.E.**, **Karam, A.K.**, **Erb, D.M.**, **Bratcher, J.R.**, **Rawashdeh, S.A.**, **Clements, T.**, **Fite, N.**, **Kruth, J.**, **Malphrus, B.**, **Bland, I.**, **Munakata, R.**, **Coelho, R.**, **Puig-Suari, J.**, **Reese, J.**, **Brodell, C. and Schaire, S.** (2010). SOCEM: Sub-orbital CubeSat experimental mission, *2010 IEEE Aerospace Conference*, pp.1–9.

[103] **Zhou, P.**, **Chen, J.**, **Yan, P.**, **Yu, J.**, **Li, H.**, **Hou, D.**, **Gao, H. and Hong, W.** (2020). A 150-GHz transmitter with 12-dBm peak output power using 130-nm SiGe:C BiCMOS process, *IEEE Transactions on Microwave Theory and Techniques*, *68*(7), 3056–3067.

[104] **Mortazavi, M.**, **Shen, Y.**, **Mul, D.**, **de Vreede, L.C.N.**, **Spirito, M. and Babaie, M.** (2022). A four-way series Doherty digital polar transmitter at mm-Wave frequencies, *IEEE Journal of Solid-State Circuits*, *57*(3), 803–817.

[105] **Buckwalter, J.F.**, **Rodwell, M.J.W.**, **Ning, K.**, **Ahmed, A.**, **Arias-Purdue, A.**, **Chien, J.**, **O'Malley, E. and Lam, E.** (2021). Prospects for high-efficiency silicon and III-V power amplifiers and transmitters in 100-300 GHz bands, *2021 IEEE Custom Integrated Circuits Conference (CICC)*, pp.1–7.

[106] **Heller, T.**, **Cohen, E. and Socher, E.** (2016). A 102–129-GHz 39-dB gain 8.4-dB noise figure I/Q receiver frontend in 28-nm CMOS, *IEEE Transactions on Microwave Theory and Techniques*, *64*(5), 1535–1543.

[107] **Laskin, E., Khanpour, M., Nicolson, S.T., Tomkins, A., Garcia, P., Cathelin, A., Belot, D. and Voinigescu, S.P.** (2009). Nanoscale CMOS transceiver design in the 90–170-GHz range, *IEEE Transactions on Microwave Theory and Techniques*, *57*(12), 3477–3490.

[108] **Deal, W.R., Leong, K., Zamora, A., Yoshida, W., Lange, M., Gorospe, B., Nguyen, K. and Mei, G.X.B.** (2016). A low-power 670-GHz InP HEMT receiver, *IEEE Transactions on Terahertz Science and Technology*, *6*(6), 862–864.

[109] **Alwis, C.D., Kalla, A., Pham, Q.V., Kumar, P., Dev, K., Hwang, W.J. and Liyanage, M.** (2021). Survey on 6G frontiers: Trends, applications, requirements, technologies and future research, *IEEE Open Journal of the Communications Society*, *2*, 836–886.

[110] **Sheng, M., Zhou, D., Bai, W., Liu, J. and Li, J.** (2022). 6G service coverage with mega satellite constellations, *China Communications*, *19*(1), 64–76.

[111] **Zhang, S., Zhu, D. and Wang, Y.** (2020). A survey on space-aerial-terrestrial integrated 5G networks, *Computer Networks*, *174*, 107212.

[112] **Dabiri, M.T., Hasna, M. and Khattab, T.** (2023). THz vs. FSO: An outage probability and channel capacity performance comparison study, *2023 International Symposium on Networks, Computers and Communications (ISNCC)*, pp.1–6.

[113] **Ahrazoglu, E.S., Erdogan, E. and Altunbas, I.** (2024). Outage and SER analyses for dual-hop inter-satellite THz communication, *2024 6th International Conference on Communications, Signal Processing, and their Applications (ICCSPA)*, pp.1–5.

[114] **Bhardwaj, P. and Zafaruddin, S.M.** (2021). Performance of dual-hop relaying for THz-RF wireless link over asymmetrical α-μ fading, *IEEE Transactions on Vehicular Technology*, *70*(10), 10031–10047.

[115] **Hasna, M. and Alouini, M.S.** (2003). End-to-end performance of transmission systems with relays over Rayleigh-fading channels, *IEEE Transactions on Wireless Communications*, *2*(6), 1126–1131.

[116] **Oldham, K.B., Myland, J. and Spanier, J.** (2009). *An atlas of functions: With equator, the atlas function calculator*, Springer.

[117] **McKay, M.R., Zanella, A., Collings, I.B. and Chiani, M.** (2009). Error probability and SINR analysis of optimum combining in Rician fading, *IEEE Transactions on Communications*, *57*(3), 676–687.

[118] **Wolfram research**. *The Wolfram functions site*, Accessed: Sep. 20, 2024. [Online]. Available: http://www.functions.wolfram.com.

[119] **Asgaran, S. and Deen, M.J.** (2004). RF noise models of MOSFETs-A Review, *Proc. Nanotechnology Conf.*, volume 2, pp.96–101.

[120] **Ahrazoglu, E.S.**, **Can, M.**, **Erdogan, E. and Altunbas, I.** (2023). Outage probability analysis of dual-hop multi-HAPS THz satellite communication systems, *2023 31st Signal Processing and Communications Applications Conference (SIU)*, pp.1–4.

[121] **Björnson, E.**, **Papadogiannis, A.**, **Matthaiou, M. and Debbah, M.** (2013). On the impact of transceiver impairments on AF relaying, *2013 IEEE International Conference on Acoustics, Speech and Signal Processing*, pp.4948–4952.

[122] **Karatza, G.P.**, **Peppas, K.P.**, **Sagias, N.C. and Tsoulos, G.V.** (2019). Unified ergodic capacity expressions for AF dual-Hop systems with hardware impairments, *IEEE Communications Letters*, *23*(6), 1057–1060.

[123] **Kilbas, A.**, (2004), H-Transforms, Theory and Applications.

[124] **Hwu, S.U.**, **deSilva, K.B. and Jih, C.T.** (2013). Terahertz (THz) wireless systems for space applications, *2013 IEEE Sensors Applications Symposium Proceedings*, pp.171–175.

[125] **Saqlain, M.**, **Idrees, N.M.**, **Zhang, L. and Yu, X.** (2019). Capacity analysis of opto-electronic THz earth-satellite links, *2019 Asia Communications and Photonics Conference (ACP)*, pp.1–3.

[126] **Cao, X.C.**, **Hao, J.H.**, **Zhao, Q.**, **Zhang, F.**, **Fan, J.Q. and Dong, Z.W.** (2022). Analysis of high-frequency atmospheric windows for terahertz transmission along Earth-space paths, *IEEE Transactions on Antennas and Propagation*, *70*(7), 5715–5724.

[127] **Soulimani, A.**, **Benjillali, M.**, **Chergui, H. and da Costa, D.B.** (2021). Multihop Weibull-fading communications: Performance analysis framework and applications, *Journal of the Franklin Institute*, *358*(15), 8012–8044.

[128] **Illi, E.**, **El Bouanani, F. and Ayoub, F.** (2017). A performance study of a hybrid 5G RF/FSO transmission system, *2017 International Conference on Wireless Networks and Mobile Communications (WINCOM)*, IEEE, pp.1–7.

[129] **Yilmaz, F. and Alouini, M.S.** (2009). Product of the powers of generalized Nakagami-m variates and performance of cascaded fading channels, *GLOBECOM 2009-2009 IEEE Global Telecommunications Conference*, IEEE, pp.1–8.

[130] **Alqaraghuli, A.J.**, **Abdellatif, H. and Jornet, J.M.** (2021). Performance analysis of a dual terahertz/Ka band communication system for satellite mega-constellations, *2021 IEEE 22nd International Symposium on a*

World of Wireless, Mobile and Multimedia Networks (WoWMoM), pp.316–322.

APPENDICES

APPENDIX A : Derivation of (8.11)
APPENDIX B : Derivation of (8.12)

APPENDIX A

The CDF of $\gamma_{e2e,k}$ can be found by

$$F_{\gamma_{e2e,k}}(z) = \int_0^\infty \Pr\left[\frac{\gamma_{1k}\gamma_{2k}}{\gamma_{1k}+\gamma_{2k}} < z \middle| \gamma_{2k}\right] f_{\gamma_{2k}}(\upsilon)d\upsilon, \tag{A.1}$$

where the CDF of $\frac{\gamma_1\gamma_2}{\gamma_1+\gamma_2}$ conditioned on γ_2 can be obtained as

$$\Pr\left[\frac{\gamma_{1k}\gamma_{2k}}{\gamma_{1k}+\gamma_{2k}} < z \middle| \gamma_{2k}\right] = \begin{cases} F_{\gamma_{1k}}\left(\frac{\gamma_{2k}z}{\gamma_{2k}-z}\right) & ,\gamma_{2k} > z \\ 1 & ,\gamma_{2k} \leq z \end{cases}. \tag{A.2}$$

By substituting (A.2) in (A.1), the CDF of $\gamma_{e2e,k}$ can be written as

$$F_{\gamma_{e2e,k}}(z) = F_{\gamma_{2k}}(z) + \int_z^\infty F_{\gamma_{1k}}\left(\frac{\upsilon z}{\upsilon - z}\right) f_{\gamma_{2k}}(\upsilon)\, d\upsilon. \tag{A.3}$$

By substituting (8.7) and (8.8) in (A.3), $F_{\gamma_{e2e,k}}(z)$ is expressed as

$$F_{\gamma_{e2e,k}}(z) = F_{\gamma_{2k}}(z) + \frac{A_{2k}}{\Gamma(\mu)}\mathcal{T}_3 + \frac{C_{1k}^{\frac{q^2}{\alpha}} A_{2k} z^{\frac{q^2}{2}}}{\Gamma(\mu)}\mathcal{T}_4, \tag{A.4}$$

where $\mathcal{T}_3$ and $\mathcal{T}_4$ are defined as

$$\mathcal{T}_3 = \int_z^\infty \upsilon^{\frac{q^2}{2}-1}\gamma\left(\mu, C_{1k}\left(\frac{\upsilon z}{\upsilon - z}\right)^{\frac{\alpha}{2}}\right)\Gamma\left(B_{2k}, C_{2k}\upsilon^{\frac{\alpha}{2}}\right)d\upsilon \tag{A.5}$$

and

$$\mathcal{T}_4 = \int_z^\infty \left(\frac{\upsilon}{\upsilon - z}\right)^{\frac{q^2}{2}}\Gamma\left(B_{1k}, C_{1k}\left(\frac{\upsilon z}{\upsilon - z}\right)^{\frac{\alpha}{2}}\right)\upsilon^{\frac{q^2}{2}-1}\Gamma\left(B_{2k}, C_{2k}\upsilon^{\frac{\alpha}{2}}\right)d\upsilon. \tag{A.6}$$

By using integral forms of the Meijer-G representations of the incomplete Gamma functions in (A.5) and by changing the order of integrals, $\mathcal{T}_3$ can be written as

$$\mathcal{T}_3 = \frac{1}{(2\pi j)^2}\int_{\mathcal{L}_1}\int_{\mathcal{L}_2}\phi_1(\xi_1)\phi_2(\xi_2)C_{1k}^{\xi_1}C_{2k}^{\xi_2}z^{\frac{\alpha\xi_1}{2}}\mathcal{I}_1 d\xi_1 d\xi_2, \tag{A.7}$$

where $\phi_1(\xi_1) = \frac{\Gamma(\mu-\xi_1)\Gamma(\xi_1)}{\Gamma(1+\xi_1)}$ and $\phi_2(\xi_2) = \frac{\Gamma(B_{2k}-\xi_2)\Gamma(-\xi_2)}{\Gamma(1-\xi_2)}$. The inner term $\mathcal{I}_1$ is expressed as

$$\begin{aligned}\mathcal{I}_1 &= \int_z^\infty \upsilon^{\frac{q^2}{2}-1+\frac{\alpha\xi_1}{2}+\frac{\alpha\xi_2}{2}}(\upsilon - z)^{-\frac{\alpha\xi_1}{2}}d\upsilon \\ &= z^{\frac{q^2}{2}+\frac{\alpha\xi_2}{2}}\frac{\Gamma\left(-\frac{q^2}{2}-\frac{\alpha}{2}\xi_2\right)\Gamma\left(1-\frac{\alpha}{2}\xi_1\right)}{\Gamma\left(1-\frac{q^2}{2}-\frac{\alpha}{2}\xi_1-\frac{\alpha}{2}\xi_2\right)},\end{aligned} \tag{A.8}$$

under the condition of $\mathcal{C}_1 : \mathcal{R}\{1-\frac{q^2}{2}-\frac{\alpha\xi_1}{2}-\frac{\alpha\xi_2}{2}\} > \mathcal{R}\{1-\frac{\alpha\xi_1}{2}\} > 0$ [55, Eq. (3.191.2)]. Please note that this condition can always be satisfied by a proper choice of integration paths as described in [56]. On the other hand, to find a closed form expression for $\mathcal{T}_4$, integral forms of the Meijer-G representation for upper incomplete Gamma function can be used. After changing the integral orders, $\mathcal{T}_4$ can be expressed as

$$\mathcal{T}_4 = \frac{1}{(2\pi j)^2}\int_{\mathcal{L}_3}\int_{\mathcal{L}_4}\phi_3(\xi_3)\phi_4(\xi_4)C_{1k}^{\xi_3}C_{2k}^{\xi_4}z^{\frac{\alpha\xi_3}{2}}\mathcal{I}_2 d\xi_3 d\xi_4, \tag{A.9}$$

where $\phi_3(\xi_3) = \frac{\Gamma(B_{1k}-\xi_3)\Gamma(-\xi_3)}{\Gamma(1-\xi_3)}$ and $\phi_4(\xi_4) = \frac{\Gamma(B_{2k}-\xi_4)\Gamma(-\xi_4)}{\Gamma(1-\xi_4)}$. Similarly, $\mathcal{I}_2$ is given as

$$\begin{aligned}\mathcal{I}_2 &= \int_z^\infty \upsilon^{q^2-1+\frac{\alpha\xi_3}{2}+\frac{\alpha\xi_4}{2}}(\upsilon-z)^{-\frac{q^2}{2}-\frac{\alpha\xi_3}{2}}d\upsilon \\ &= z^{\frac{q^2}{2}+\frac{\alpha\xi_4}{2}}\frac{\Gamma\left(-\frac{q^2}{2}-\frac{\alpha}{2}\xi_4\right)\Gamma\left(1-\frac{q^2}{2}-\frac{\alpha}{2}\xi_3\right)}{\Gamma\left(1-q^2-\frac{\alpha}{2}\xi_3-\frac{\alpha}{2}\xi_4\right)},\end{aligned} \tag{A.10}$$

under the condition of $\mathcal{C}_2 : \mathcal{R}\{1-q^2-\frac{\alpha\xi_3}{2}-\frac{\alpha\xi_4}{2}\} > \mathcal{R}\{1-\frac{q^2}{2}-\frac{\alpha\xi_3}{2}\} > 0$ [55, Eq. (3.191.2)]. $\mathcal{T}_3$ and $\mathcal{T}_4$ can be found by substituting (A.8) and (A.10) in (A.7) and (A.9), respectively. Then, by inserting these expressions in (A.4) with the definition of the bi-variate Fox-H function [56] for $\mathcal{T}_3$ and $\mathcal{T}_4$, the CDF of $\gamma_{e2e,k}$ can be found as in (8.11).

APPENDIX B

The MGF of $\gamma_{e2e,k}$ can be written as

$$\mathcal{M}_{\gamma_{e2e,k}}(s) = s\int_0^\infty F_{\gamma_{e2e,k}}(z)e^{-sz}dz. \tag{B.1}$$

By using the CDF of $\gamma_{e2e,k}$ in (8.11), $\mathcal{M}_{\gamma_{e2e,k}}(s)$ can be rewritten as

$$\mathcal{M}_{\gamma_{e2e,k}}(s) = \mathcal{T}_5+\mathcal{T}_6+\mathcal{T}_7+\mathcal{T}_8, \tag{B.2}$$

where

$$\mathcal{T}_5 = \frac{s}{\Gamma(\mu)}\int_0^\infty \gamma\left(\mu, C_{2k}z^{\alpha/2}\right)e^{-sz}dz, \tag{B.3a}$$

$$\mathcal{T}_6 = \frac{sC_{2k}^{q^2/\alpha}}{\Gamma(\mu)}\int_0^\infty z^{q^2/2}\Gamma\left(B_{2k}, C_{2k}z^{\alpha/2}\right)e^{-sz}dz, \tag{B.3b}$$

$$\mathcal{T}_7 = \frac{sA_{2k}}{\Gamma(\mu)}\int_0^\infty z^{\frac{q^2}{2}}\mathrm{H}_{1,0:1,3:1,3}^{0,0:2,1:3,0}\left[\begin{matrix}C_{1k}z^{\frac{\alpha}{2}}\\C_{2k}z^{\frac{\alpha}{2}}\end{matrix}\middle|\begin{matrix}V_1\\V_2\end{matrix}\right]e^{-sz}dz, \tag{B.3c}$$

$$\mathcal{T}_8 = \frac{sC_{1k}^{\frac{q^2}{\alpha}}A_{2k}}{\Gamma(\mu)}\int_0^\infty z^{q^2}\mathrm{H}_{1,0:1,3:1,3}^{0,0:3,0:3,0}\left[\begin{matrix}C_{1k}z^{\frac{\alpha}{2}}\\C_{2k}z^{\frac{\alpha}{2}}\end{matrix}\middle|\begin{matrix}V_3\\V_4\end{matrix}\right]e^{-sz}dz. \tag{B.3d}$$

For $\mathcal{T}_5$, expressing the lower incomplete Gamma function in terms of the Meijer-G's integral form results in

$$\mathcal{T}_5 = \frac{s}{\Gamma(\mu)} \frac{1}{2\pi j} \int_{\mathcal{L}_5} \phi_5(\xi_5) C_{2k}^{\xi_5} \int_0^\infty z^{\frac{\alpha\xi_5}{2}} e^{-sz} dz d\xi_5, \tag{B.4}$$

where $\phi_5(\xi_5) = \frac{\Gamma(\mu-\xi_5)\Gamma(\xi_5)}{\Gamma(1+\xi_5)}$. By employing [55, Eq. (17.13.3)] and by using the definition of Fox-H function in (B.4), $\mathcal{T}_5$ can be obtained as

$$\mathcal{T}_5 = \frac{1}{\Gamma(\mu)} \mathrm{H}_{2,2}^{1,2} \left[\frac{C_{2k}}{s^{\frac{\alpha}{2}}} \middle| \begin{matrix} (1,1),(0,\frac{\alpha}{2}) \\ (\mu,1),(0,1) \end{matrix} \right], \tag{B.5}$$

under the condition of $\mathcal{C}_3 : \mathcal{R}\{\frac{\alpha}{2}\xi_5\} > -1$. Similarly, with the integral form of the upper incomplete Gamma function's Meijer-G representation, $\mathcal{T}_6$ can be obtained as

$$\mathcal{T}_6 = \frac{sC_{2k}^{\frac{q^2}{\alpha}}}{\Gamma(\mu)} \frac{1}{2\pi j} \int_{\mathcal{L}_6} \phi_6(\xi_6) C_{2k}^{\xi_6} \int_0^\infty z^{\frac{q^2}{2}+\frac{\alpha\xi_6}{2}} e^{-sz} dz d\xi_6, \tag{B.6}$$

where $\phi_6(\xi_6) = \frac{\Gamma(B_{2k}-\xi_6)\Gamma(-\xi_6)}{\Gamma(1-\xi_6)}$. Taking the Laplace transform of a power function with the inner integral yields

$$\mathcal{T}_6 = \frac{C_{2k}^{\frac{q^2}{\alpha}}}{\Gamma(\mu)} \left(\frac{1}{s}\right)^{\frac{q^2}{2}} \mathrm{H}_{2,2}^{2,1} \left[\frac{C_{2k}}{s^{\frac{\alpha}{2}}} \middle| \begin{matrix} (-\frac{q^2}{2},\frac{\alpha}{2}),(1,1) \\ (B_{2k},1),(0,1) \end{matrix} \right], \tag{B.7}$$

under the condition of $\mathcal{C}_4 : \mathcal{R}\{\frac{q^2}{2} + \frac{\alpha}{2}\xi_6\} > -1$. By using the same steps, $\mathcal{T}_7$ can be obtained as

$$\mathcal{T}_7 = \frac{sA_{2k}}{\Gamma(\mu)} \frac{1}{(2\pi j)^2} \int_{\mathcal{L}_1} \int_{\mathcal{L}_2} \phi_{7,8}(\xi_1,\xi_2)\phi_7(\xi_1)\phi_8(\xi_2) C_{1k}^{\xi_1} C_{2k}^{\xi_2} \int_0^\infty z^{\frac{\alpha\xi_1}{2}+\frac{\alpha\xi_2}{2}+\frac{q^2}{2}} e^{-sz} dz d\xi_1 d\xi_2, \tag{B.8}$$

where $\phi_{7,8}(\xi_1,\xi_2) = \frac{1}{\Gamma(1-\frac{q^2}{2}-\frac{\alpha}{2}\xi_1-\frac{\alpha}{2}\xi_2)}$, $\phi_7(\xi_1) = \frac{\Gamma(\mu-\xi_1)\Gamma(\xi_1)\Gamma(1-\frac{\alpha}{2}\xi_1)}{\Gamma(1+\xi_1)}$, $\phi_8(\xi_2) = \frac{\Gamma(B_{2k}-\xi_2)\Gamma(-\xi_2)\Gamma(-\frac{q^2}{2}-\frac{\alpha}{2}\xi_2)}{\Gamma(1-\xi_2)}$. By employing [55, Eq. (17.13.3)] and by using the bi-variate Fox-H function's definition, (B.8) can be rewritten as

$$\mathcal{T}_7 = \frac{A_{2k}}{\Gamma(\mu)} \left(\frac{1}{s}\right)^{\frac{q^2}{2}} \mathrm{H}_{2,0:1,3:1,3}^{0,1:2,1:3,0} \left[\begin{matrix} C_{1k}s^{-\alpha/2} \\ C_{2k}s^{-\alpha/2} \end{matrix} \middle| \begin{matrix} V_5 \\ V_6 \end{matrix} \right], \tag{B.9}$$

under the condition of $\mathcal{C}_5 : \mathcal{R}\{\frac{q^2}{2} + \frac{\alpha}{2}\xi_1 + \frac{\alpha}{2}\xi_2\} > -1$. Notice here that $\mathcal{C}_5$ does not contradict with $\mathcal{C}_1$ which is the convergence condition of the bi-variate Fox-H function in (B.3c). Here, V_5 and V_6 are given as $V_5 = \{(-\frac{q^2}{2},\frac{\alpha}{2},\frac{\alpha}{2}),(1-\frac{q^2}{2},\frac{\alpha}{2},\frac{\alpha}{2})\} : \{(1,1)\} : \{(1,1)\}$ and $V_6 = \{-\} : \{(\mu,1),(1,\frac{\alpha}{2}),(0,1)\} : \{(B_{2k},1),(0,1),(-\frac{q^2}{2},\frac{\alpha}{2})\}$, respectively. Finally, $\mathcal{T}_8$ can be expressed in integral form as

$$\mathcal{T}_8 = \frac{sC_{1k}^{\frac{q^2}{\alpha}}A_{2k}}{\Gamma(\mu)} \frac{1}{(2\pi j)^2} \int_{\mathcal{L}_3} \int_{\mathcal{L}_4} \phi_{9,10}(\xi_3,\xi_4)\phi_9(\xi_3)\phi_{10}(\xi_4) C_{1k}^{\xi_3} C_{2k}^{\xi_4} \int_0^\infty z^{q^2+\frac{\alpha}{2}\xi_3+\frac{\alpha}{2}\xi_4} e^{-sz} dz d\xi_3 d\xi_4, \tag{B.10}$$

where $\phi_{9,10}(\xi_3,\xi_4) = \frac{1}{\Gamma(1-q^2-\frac{\alpha}{2}\xi_3-\frac{\alpha}{2}\xi_4)}$, $\phi_9(\xi_3) = \frac{\Gamma(B_{1k}-\xi_3)\Gamma(-\xi_3)\Gamma(1-\frac{q^2}{2}-\frac{\alpha}{2}\xi_3)}{\Gamma(1-\xi_3)}$, and $\phi_{10}(\xi_4) = \frac{\Gamma(B_{2k}-\xi_4)\Gamma(-\xi_4)\Gamma(-\frac{q^2}{2}-\frac{\alpha}{2}\xi_4)}{\Gamma(1-\xi_4)}$. Taking the inner integral by employing [55, Eq. (17.13.3)] yields

$$\mathcal{T}_8 = \frac{C_{1k}^{\frac{q^2}{\alpha}} A_{2k}}{\Gamma(\mu)} \left(\frac{1}{s}\right)^{q^2} \mathrm{H}_{2,0:1,3:1,3}^{0,1:3,0:3,0} \left[\begin{matrix} C_{1k}s^{-\alpha/2} \\ C_{2k}s^{-\alpha/2} \end{matrix} \middle| \begin{matrix} V_7 \\ V_8 \end{matrix} \right], \tag{B.11}$$

where $V_7 = \{(-q^2, \frac{\alpha}{2}, \frac{\alpha}{2}), (1-q^2, \frac{\alpha}{2}, \frac{\alpha}{2})\} : \{(1,1)\} : \{(1,1)\}$ and $V_8 = \{-\} : \{(B_{1k},1),(0,1),(1-\frac{q^2}{2},\frac{\alpha}{2})\} : \{(B_{2k},1),(0,1),(-\frac{q^2}{2},\frac{\alpha}{2})\}$, under the condition of $\mathcal{C}_6 : \mathcal{R}\{q^2 + \frac{\alpha}{2}\xi_3 + \frac{\alpha}{2}\xi_4\} > -1$. Here, $\mathcal{C}_6$ does not contradict with $\mathcal{C}_2$ which is the convergence condition of the bi-variate Fox-H function in (B.3d). By substituting (B.5), (B.7), (B.9), and (B.11) in (B.2), the MGF of $\gamma_{e2e,k}$ can be found as in (8.12).

CURRICULUM VITAE

Name Surname: Evla Safahan AHRAZOĞLU

EDUCATION:

- **B.Sc.:** 2022, Istanbul Technical University, Faculty of Electrical and Electronics Engineering, Department of Electronics and Communication Engineering.

PROFESSIONAL EXPERIENCE AND REWARDS:

- **2022 - ... :** Research & Teaching Assistant at Istanbul Technical University

PUBLICATIONS, PRESENTATIONS AND PATENTS ON THE THESIS:

International Journal Papers

- **Ahrazoglu, E.S.**, Altunbas, I., and Erdogan, E. (2024) Multi-HAPS THz satellite communication: Error and capacity analyses under I/Q imbalance, *IEEE Sensors Journal, 24*(23), 39845-39855.

- **Ahrazoglu, E.S.**, Gul, A.C., Akinci, M.N., Altunbas, I., and Erdogan, E. (2025) An improved pointing error model for mmWave and THz links: Antenna and array design impact, *IEEE Communications Letters, 29*(3), 532-536.

- **Ahrazoglu, E.S.**, Erdogan, E., and Altunbas, I. (2025) HAPS-aided THz satellite communication systems with hardware impairments, Submitted to *Transactions on Emerging Telecommunications Technologies*.

- **Ahrazoglu, E.S.**, Erdogan, E., Altunbas, I., and Yanikomeroglu, H. (2025) A holistic link budget analysis for mmWave and THz communication in non-terrestrial networks, Submitted to *IEEE Transactions on Vehicular Technology.*

International Conference Papers

- **Ahrazoglu, E.S.**, Erdogan, E., Altunbas, I. (2024) Outage and SER analyses for dual-hop inter-satellite THz communication, *International Conference on Communications, Signal Processing, and their Applications (ICCSPA 2024).*

National Conference Papers

- **Ahrazoglu, E.S.**, Can, M., Erdogan, E., and Altunbas, I. (2023) Outage probability analysis of dual-hop multi-HAPS THz satellite communication systems (In Turkish), *31st Signal Processing and Communication Applications Conference (SIU 2023).*

OTHER PUBLICATIONS, PRESENTATIONS AND PATENTS:

International Journal Papers

- Turk, S.E., **Ahrazoglu, E.S.**, Erdogan, E., and Altunbas, I. (2024) Design of energy efficient multi-HAPS assisted hybrid RF/FSO satellite communication systems with optimal placement, accepted for publication in *IEEE Transactions on Green Communications and Networking*.

National Journal Papers

- Erdogan, E., **Ahrazoglu, E.S.**, Bakirci, E.B., and Altunbas, I. (2025) Improving secrecy performance in optical HAPS communications through site selection under harsh weather conditions, *ITU Journal of Wireless Communications and Cybersecurity, 2*(1), 1-10.

International Conference Papers

- **Ahrazoglu, E.S.**, Erdogan, E., Ozbek, B., and Altunbas, I. (2025) Toward seamless connectivity: HAPS-assisted hybrid THz/FSO bidirectional communication for multi-satellite multi-ground station network, Accepted for presentation at *International Symposium on Personal, Indoor and Mobile Radio Communications (PIMRC 2025).*

National Conference Papers

- Bakirci, E.B., **Ahrazoglu, E.S.**, Altunbas, I., and Erdogan, E. (2024) Outage probability analysis of triple-hybrid RF/FSO/THz communication system (In Turkish), *32nd Signal Processing and Communication Applications Conference (SIU 2024).*

- Ozbirecikli, D.E., **Ahrazoglu, E.S.**, Peker, E.T., Erturk, O., and Altunbas, I. (2025) Implementation of SM MIMO systems on GNU Radio platform (In Turkish), Accepted for presentation at *33rd Signal Processing and Communication Applications Conference (SIU 2025).*

- Bakirci, E.B., **Ahrazoglu, E.S.**, Erdogan, E., and Altunbas, I. (2025) Outage and intercept performance in THz LEO-ground communication with satellite selection (In Turkish), Accepted for presentation at *33rd Signal Processing and Communication Applications Conference (SIU 2025).*

AWARDS AND SCHOLARSHIPS:

- **2020:** ERASMUS Scholarship for B.Sc. Students, European Union (EU).
- **2023:** IEEE Best Paper Award in 31st Signal Processing and Communications Applications Conference with the paper entitled "Outage probability analysis of dual-hop multi-HAPS THz satellite communication systems."
- **2024:** Recognition Award for Top Research Productivity (publication-based) among research assistants, Istanbul Technical University.